Members of the jury

Chairman

Prof. dr. Ivo Lambrichts, Universiteit Hasselt, Diepenbeek, Belgium.

Promoter

Prof. dr. Marcel Ameloot, Universiteit Hasselt, Diepenbeek, Belgium.

Co-promoters

Prof. dr. Jef Hooyberghs, VITO, Mol, Belgium.

Prof. dr. Niels Hellings, Universiteit Hasselt, Diepenbeek, Belgium.

Other members

Dr. Inge Nelissen, VITO, Mol, Belgium.

Prof. dr. Milos Nesladek, Universiteit Hasselt, Diepenbeek, Belgium.

Prof. dr. Peter Hoet, Katholieke Universiteit Leuven, Leuven, Belgium.

Dr. Anna Salvati, Rijksuniversiteit Groningen, Groningen, The Netherlands.

Preface

Nanoparticles have an extensive history which is not restricted to man-made materials and modern research. Applications using naturally occurring nanoparticles can be traced back to the ancient years. However, due to the advances in the controlled synthesis and surface functionalization of nanomaterials in the last decades, nanotechnology and new applications for engineered nanoparticles are growing extensively in a wide range of fields.

The usage of engineered nanoparticles for biomedical and commercial applications is expanding enormously. Due to their size-related properties, they have been utilized in consumer products for their antimicrobial properties, self-cleaning characteristics, durability and resistance to the environmental conditions. Nanotechnology offers the unprecedented capacity to manipulate cells with nanoscale precision. This opens up tremendous opportunities to exploit the interactions at the nano-bio interface for therapeutic purposes. In order to take full advantage of this promise, it is necessary that the interactions of nanoparticles and living cells are characterized in advance. This allows the assessment of the safety of nanotechnology-based applications, but also provides insights to the nano-bio interactions for health applications.

Recent investigations have shown that nanoparticles can interfere with the immune system, which can result in adverse immune reactions including the development and/or progression of allergic responses. In contrast, the specific targeting of nanoparticles to the cells of the immune system can be used to modulate the immune response for therapeutic approaches. Dendritic cells, one of the key players of the immune system, act as specialized sentinel cells that scan the interfaces of the body which are in contact with the external environment. From this point of view, they are expected to encounter the nanoparticles in the human body. Since dendritic cells are involved in many diseases, they also provide a target for disease prevention and therapy.

Although efforts have been made in understanding how nanoparticles interact with biological systems, there is still a lack of well-adjusted tools to evaluate the nano-bio interaction. For that reason, part of this dissertation focuses on the implementation of technologies to assess this interaction. In that part, advanced fluorimetric techniques are used to study the uptake, the intracellular behaviour and the fate of nanoparticles in biological cells. In the second part, the impact of nanoparticles on the biological function of dendritic cells is investigated.

This dissertation is a composition of five manuscripts, preceded by an introduction and followed by a general discussion. The general discussion first handles the applications and conclusions with regard to the characterization of the nano-bio interactions. Thereafter, the interactions of nanoparticles on biological function of dendritic cells are discussed. Finally, a section is devoted to the future perspectives with regard to nano-bio interaction studies.

Table of content

List of figures

Chapter 1

Chapter 2

Chapter 3

Chapter 4

Chapter 5

Chapter 6

List of tables

Chapter 2

Chapter 3

Chapter 4

Chapter 5

Chapter 6

List of abbreviations

APCs	Antigen presenting cells
BSA	Bovine serum albumin
CCM	Complete cell culture medium
CD34-DCs	$CD34^+$ HPC-derived dendritic cells
cDCs	Conventional DCs
CDPs	Common DC progenitors
CLSM	Confocal laser scanning microscopy
DAPI	4',6-diamidino-2-phenylindole
DCs	Dendritic cells
DLS	Dynamic light scattering
DMPC	1,2-dimyristoyl-sn-glycero-3-phosphocholine
DNA	Deoxyribonucleic acid
DNCB	Dinitrochlorobenzene
DOPC	1,2-dioleoyl-sn-glycero-3-phosphocholine
FBS	Fetal bovine serum
FCS	Fluorescence correlation spectroscopy
FDA	Food and Drug Administration
FLIM	Fluorescence lifetime imaging microscopy
GM-CSF	Granulocyte-macrophage colony-stimulating factor
GMDPs	Granulocyte, monocyte and DC progenitor cells
GMFI	Geometric mean of the fluorescence intensity
GNPs	Gold nanoparticles
HBSS	Hank's Balanced Salt Solution
HDM	House dust mite
HSCs	Hematopoietic stem cells
HPCs	Hematopoietic progenitor cells
ICS	Image correlation spectroscopy
ICCS	Image cross-correlation spectroscopy
IL-4	Interleukin 4
IMDM	Iscove’s Modified Dulbecco’s Medium

LCs	Langerhans cells
MDPs	Monocyte and DC progenitors
MHC	Major histocompatibility complex
MSD	Mean square displacement
NPs	Nanoparticles
NTA	Nanoparticle tracking analysis
PBS	Phosphate buffered saline
PBS-T	PBS with 0.05% Tween®20
PC	Positive control
PDI	Polydispersity index
pDCs	Plasmacytoid DCs
PDD	Photodynamic diagnosis
PDT	Photodynamic therapy
PFC	Perfluorobutane
PI	Propidium iodide
PLLA	Poly lactic-co-glycolic acid
PM	Particulate matter
PMT	Photomultiplier tube
pre-cDCs	Precursor cells of circulating conventional DCs
PS	Polystyrene
P/S	Penicillin/streptomycin
PSF	Point spread function
PVP	Polyvinylpyrrolidone
ROI	Region of interest
ROS	Reactive oxygen species
SC	Sodium citrate
SCF	Stem cell factor
SD	Standard derivation
SDCLM	Spinning disk confocal laser microscopy
SDS	Sodium dodecyl sulphate
SDS-PAGE	Sodium dodecyl sulfate polyacrylamide gel electrophoresis
SEM	Standard error of the mean

SI	Stimulation indices
SIN-1	3-morpholinosydnonimine hydrochloride
SPIO	Superparamagnetic iron oxide
SPR	Surface plasmon resonance
SPT	Single particle tracking
STACF	Spatiotemporal autocorrelation function
STED	Stimulated emission depletion microscopy
STICS	Spatiotemporal image correlation spectroscopy
STICCS	Spatiotemporal image cross-correlation spectroscopy
TACF	Temporal autocorrelation function
TEM	Transmission electron microscopy
T_H1	T helper 1 cell
T_H2	T helper 2 cell
THF	Tetrahydrofuran
TICS	Temporal image correlation spectroscopy
TIRF	Total internal reflectance fluorescence microscopy
TLCM	Time-lapse fluorescence confocal microscopy
TNF-α	Tumor necrosis factor alpha
UFP	Ultrafine Particulate Matter
WGA	Wheat germ agglutinin

1 Introduction

1.1 Nanoparticles

Nanotechnology is science, engineering and technology conducted at the nanoscale. The prefix nano derives from the Greek word “nanos”, which means dwarf. The term nanometer is a metric unit of length and denotes to 10^{-9} or one billionth of a meter.

Nanoparticles (NPs) have an amazingly extensive history, which is not restricted to man-made materials and modern research. Naturally occurring NPs include organic and inorganic compounds, such as polysaccharides, viruses, metals and iron oxyhydroxides. They can be generated by microbial processes, weathering, volcano eruptions and wildfires among others [1]. NPs existed in nature for a long time and therefore their applications can be traced back to ancient times. More than 4500 years ago, natural asbestos nanofibers were used for the controlled reinforcement of a ceramic matrix [2]. Gold NPs (GNPs) have been employed in sculptures and paintings for their extraordinary optical properties even before the 4th century [3]. Silver and copper NPs were used for generating glitter effects on Mesopotamian metallic lustres during the 9th century [4]. In addition, GNPs and silver NPs were applied in stained glass windows of churches during the Middle Ages [2].

Approximately 150 years ago, research on the interaction of light and colloidal gold by Michael Faraday in 1857 gave rise to an emergence in the field of nanoscience. The ideas and concepts behind nanotechnology were established with a lecture by Richard Feynman in 1959. In *‘There is plenty of room at the bottom’* he described a process by which scientists would be able to manipulate and control individual atoms and molecules. The term nanotechnology was first used by Norio Taniguchi in 1974 in order to specify the processing of separation, consolidation and deformation of individual atoms or molecules. Subsequent technological progresses including the development of the scanning tunnelling microscope in 1981 resulted in a rapid expansion of the modern nanotechnology.

The field has evolved from molecular manufacturing to multidisciplinary research in many different fields including chemistry, material sciences, medicine, toxicology, ecotoxicology and industrial hygiene [5]. Nowadays nanotechnology is expanding dramatically. NPs have a great potential for new innovative technological applications, however, they also poses great challenges which should be addressed to take its full advantages.

1.1.1 Small is different

NPs are defined as particles of any shape which for 50% or more of the particles in the number size distribution have at least one external dimension in the size range between 1 and 100 nm [6]. NPs are commonly categorized based on their (i) dimensionality, (ii) morphology, (iii) uniformity and (iv) agglomeration [7]. These parameters highly influence the NPs' properties and reactivity.

NPs react very differently in comparison to their corresponding bulk material. Two primary factors are responsible for this phenomenon: (i) surface effects and (ii) quantum effects [7]. When the size of the particle decreases, the surface area to volume ratio of the particle increases and therefore, the fraction of atoms present at the surface rather than the interior of the particle will be enlarged [8, 9] (Figure 1-1a). Moreover, when comparing the same mass of microparticles in the nanoparticulate form, the total surface area increases tremendously. When considering a 60-µm sized carbon microparticle with a mass of 0.30 µg and a surface area of 0.01 mm^2, the same mass of carbon NPs with a diameter of 60 nm corresponds with 11.3 mm^2 and comprises 1 billion NPs (Figure 1-1b) [7]. In addition, once particles become small enough, they exhibit a quantum mechanical behaviour [10]. Both the surface and quantum effects change the chemical reactivity of the NP, as well as their mechanical, optical, electric and magnetic properties [9, 10].

Due to the advances in the NP synthesis and their surface functionalization, NPs can be specifically designed with favourable characteristics depended on the application of interest. Since NPs possess unique physicochemical properties compared to their bulk materials, they can be used to improve the functionality

of products in many fields. Examples include the addition of NPs in sunscreens, cosmetics, clothes, building materials and paintings among others [7]. Moreover, NPs offer great opportunities for the biomedical sciences. Because of their small dimensions, which are in the same order of magnitude as biomolecules and viruses, NPs have the potential to enter living cells [11, 12]. Here they can act as an instrument to unravel molecular processes and can be used for therapeutic purposes. Because of their extremely high surface-to-volume ratio and their enhanced surface reactivity, NPs can interact with biological and chemical entities and, therefore, can lead to desirable effects but also unwanted side-effects [13].

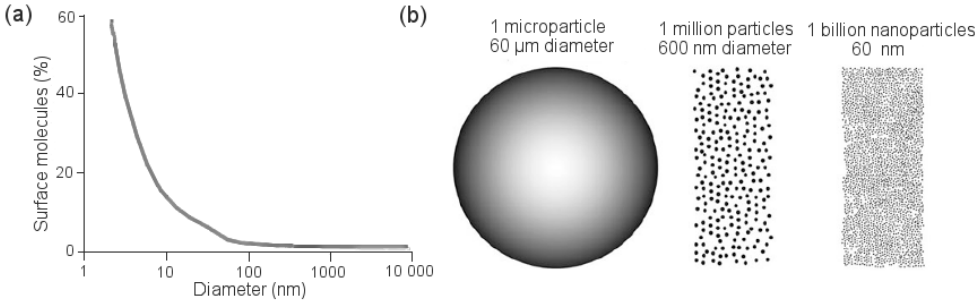

Figure 1-1: Surface effects of nanomaterials. (a) The inverse relationship between the percentage of molecules located at the surface and the particle size. When the particle size decreases below 100 nm, the number of the surface molecules increases exponentially. (b) Illustration of a microparticle of 60 µm and the corresponding number of NPs with a diameter of 600 nm and 60 nm having the same mass as one microparticle. (Figure based on Oberdörster et al. *2005* [9] and Buzea et al. *2007* [7].)

1.1.2 Nanoparticles and protein corona

NPs present in the external environment are able to enter the body spontaneously through the lung, gut or skin [14, 15]. For biomedical applications, NPs are mainly injected intravenously [14]. When NPs come in contact with biological fluids (e.g. blood, plasma or interstitial fluid), mainly proteins and some other minor biomolecules will adhere to the NP and a layer, the *protein corona*, will be formed which can completely cover the NPs' surface

[13, 16]. Initially, the surface of the NP will be covered by the most abundant proteins present in the biological medium. These proteins, however, will be rapidly exchanged with proteins with a higher binding affinity to the NP surface. This phenomenon is called the *Vroman effect* [17-19]. Over time, these proteins will evolve from a loosely bond to the NP surface to a relatively irreversible protein bond [20]. From this perspective, the protein corona is often subdivided into two components, i.e. the "soft" component and the "hard" component. The *soft corona* is recognized as the component in which a dynamic exchange between the NPs and the proteins in the surrounding medium exist. The *hard corona*, however, represents the fraction of adhered proteins having a high affinity for the NPs' surface resulting in a relatively immobile layer [21, 22]. The NP-protein complexes are considered as a dynamic system, with a lifetime ranging from seconds to days, due to a continuously changing micro-environment for instance caused by the cellular homeostasis and environmental influences [16, 22, 23]. The hard corona typically has long exchange times (i.e. many hours), whereas the soft corona is much faster replaced [21].

The nature of the protein corona is governed by both the NPs' chemical composition, hydrophobicity, size, surface charge, curvature and the composition of the biological environment including the proteins present, and the pH and ionic strength of the solution [22, 23]. The adsorption of proteins can induce alterations in the overall NPs' charge, NP aggregation properties and its hydrodynamic radius [21, 22]. Therefore, the formation of the protein corona on the NP surface will give the NP a new identity, changing the interaction of the NP with biological cells and inducing changes in their physiological responses including their cellular uptake, intracellular signalling, transport and toxicity [24]. Because the lifetime of the hard corona has been shown to be appropriately long for the biomedical context, it is this component of the corona which principally determines the biological identity of the NPs [21, 25].

The composition of the protein corona has been the subject of many investigations. The majority of the protein corona was found to consist of mainly serum proteins such as albumin, fibrinogen and IgG molecules [16, 22, 26].

Albumin and fibrinogen, being the most abundant serum proteins, principally dominate the particle surface for short periods (i.e. in the first 30 minutes) [16, 22]. Other proteins, including complement factors, apolipoproteins, alpha-1-antitrypsin and immunoglobulins, have also been identified in protein corona [16, 21, 25, 26].

1.1.3 Cellular uptake of nanoparticles

The physicochemical characteristics of the NP, the nature of the target cell and its micro-environment will affect how the NPs are internalized. Two main internalization mechanisms occur: either phagocytic or non-phagocytic pathways (Figure 1-2). Non-phagocytic pathways include clathrin-mediated endocytosis, caveolae-mediated endocytosis, macropinocytosis and diffusion through the membrane [27, 28].

Phagocytosis is an actin-mediated mechanism, which primarily occurs in professional phagocytes including macrophages and DCs. Other cell types including fibroblasts, epithelial cells and endothelial cells only display a limited amount of phagocytic activity [29, 30]. The uptake by phagocytosis comprises three steps: (i) opsonisation, (ii) adhesion of the opsonized NPs to the cell and (iii) ingestion [28]. Opsonisation describes the process of tagging the NPs with opsonins to make it visible for phagocytes. These opsosins include immunoglobulins, complement components, laminin and fibronectin among others. After that, NPs become recognisable by specific cell surface receptors [31, 32]. Receptor binding activates a signalling cascade which triggers the actin-assembly, the formation of surface extensions, the engulfing of the NP and internalization [28]. The resulting endocytic vesicles, which are called phagosomes, fuse with the lysosomal compartment and leads to the formation of phagolysosomes [33]. The uptake of larger NPs or agglomerates (> 500 nm) is often favoured by phagocytic mechanisms [26].

Clathrin-mediated endocytosis occurs in all mammalian cells where it plays crucial physiological roles, such as intracellular communication and nutrient uptake [28]. Clathrin-mediated endocytosis can both be receptor-mediated or independent, and involves the formation of vesicles from triskelion clathrin-coated regions of the plasma membrane [33]. The NP-containing vesicles will mature and form the early endosomes and late endosomes, and finally they will fuse with lysosomes. The clathrin-coated vesicle has been reported to have an average size of 100 to 120 nm [34, 35].

Caveolae-mediated endocytosis involves clustering of lipid raft components on the plasma membrane into caveolae [27]. Caveolae are flask-shaped invaginations made of caveolin dimers that form vesicles which translocate through the cell or fuse with the endoplasmic reticulum and the Golgi complex [28, 33]. The caveolae have a size between 50 and 100 nm [34-37].

Macropinocytosis is a clathrin- and caveolin-independent pathway which involves the internalisation of large areas of the plasma membrane together with the surrounding fluid [28]. The resulting vesicles called macropinosomes are formed through actin filament driven plasma membrane protrusions [33]. As these macropinosomes are uncoated, they can become bigger than the coated ones and thus allow the endocytosis of objects larger than 150 nm [27].

Diffusion through the plasma membrane can occur in certain conditions [38-40]. The capability of the NPs to adhere and passively penetrate the cell membrane is highly dependent on their physical properties, including size, surface composition and surface charge [41-46]. Especially small, positively charged NPs have been observed to enter the cell through the cell membrane by diffusion [40, 47-49].

NPs are shown to enter very different cell types with ease and NP uptake is principally energy-dependent [27, 50-54]. Pharmacological treatments demonstrated that inhibition of one uptake mechanism is not sufficient to fully inhibit NP uptake. This suggests that cells use multiple parallel pathways to simultaneously internalise the same kind of NPs [27, 51, 54].

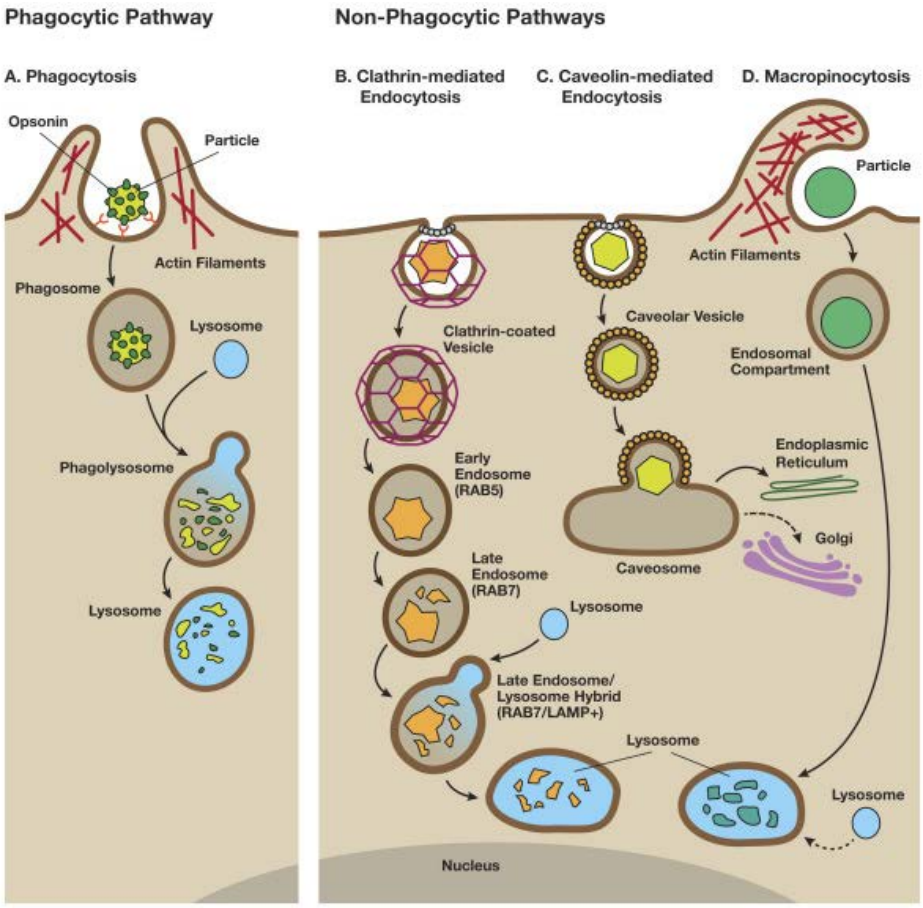

Figure 1-2: Principal NP internalization pathways in mammalian cells. (a) Phagocytosis involves the interaction with specialized cell surface receptors. NPs are recognized and internalized to form endocytic vesicles (phagosomes). Fusion of phagosomes and lysosomes leads to the formation of phagolysosomes, in which the cells attempts to degrade the NPs. (b) Clathrin-mediated endocytosis in which NP are loaded in clathrin-coated vesicles. The NPs move from the early endosomes to late endosomes and lysosomes. (c) Caveolae-mediated endocytosis in which NPs are internalized through caveolin-enriched invaginations. The resultant vesicle delivers its content to endosomes and forms the caveosomes. They are transported to the endoplasmic reticulum or Golgi complex. (d) Macropinocytosis involves the formation of large vesicles (macropinosomes). NPs are transported and degraded through the endolysosomal pathway. (Figure adapted from Stern et al. *2012* (BioMed Central®) [33].)

NP size is an important parameter that affects the internalization mechanisms and, therefore, its uptake efficiency and kinetics [55]. Size-dependent interactions between the cell membrane and the NPs are related to the membrane-wrapping process. For receptor-mediated internalization it is crucial that multiple NP-receptor interactions occur [56, 57]. Smaller sized NPs have less ligand-to-receptor interactions compared to their larger counterparts [55]. For small NPs to be internalized, multiple small NPs have to interact simultaneously with the receptor in order to trigger membrane wrapping [55]. Large NPs, however, can act as a cross-linking agent which clusters receptors and therefore facilitates its uptake [55]. Though, beyond a certain size threshold (>200 nm) NPs are getting much slower internalized as clathrin-mediated and caveolae-mediated endocytosis are not feasible anymore to any further extent [28, 33, 58]. Multiple studies have demonstrated the uptake rate is the maximum with NPs of 50 nm in diameter [56, 59-64].

1.1.4 Protein corona influences nanoparticle uptake

Protein adsorption and the protein corona of the NPs also significantly impact on the cellular uptake of NPs. In non-specific uptake (macropinocytosis and diffusion), which is the uptake of NPs without specific biomolecular control by the cells, the extent of NP internalization is greatly dependent on the presence of the protein corona [65]. Cells exposed to NPs without serum have a significantly higher NP uptake [66-73]. Furthermore, the thickness of the NP corona is shown to be inversely related to the degree of NP uptake [74, 75]. These observations are explained by a reduction of NPs adhering to the cell membrane when the protein corona has formed [65, 71, 76].

Specific internalization (phagocytosis, clathrin-mediated and caveolae-mediated endocytosis) involves the binding of the NP and the activation of membrane receptor through receptor-specific ligands in the protein corona which trigger NP uptake [65]. The presence of proteins in the corona such as immunoglobulins and components of the complement systems can result in opsonisation of the NPs, and can lead to an increased phagocytosis rate [22, 31].

Through the recognition of lipoproteins and unfolded proteins present in the protein corona, scavenger receptor mediated phagocytosis of NPs is also promoted [76, 77]. In addition, the presence of the protein corona can promote interaction with the folate receptor, which facilitates NP endocytosis [78].

1.1.5 Nanotoxicology

The advantages of nanotechnology have been offset by discussions concerning the toxicology and associated health issues associated with the use of nanomaterials [5, 9, 79, 80]. Cellular exposure to NPs affect its cellular, subcellular and genetic behaviour. Furthermore, NPs can cause cell death through mitochondrial damage, impairment of the nucleus or disruption of the plasma membrane's integrity [22, 81].

Exposure to NPs is able to trigger the generation of reactive oxygen species (ROS) as the NPs' large surface area and reactive surface molecules give rise to multiple oxidizing capabilities [7, 81]. Different mechanisms have been described in which NPs can possibly generate ROS: (i) exposure of NPs to an acidic environment can directly result to ROS production either from the NPs surface or from leached ions [82, 83], (ii) interaction of NPs with cellular organelles [84], (iii) interaction of NPs with redox active proteins [81] and (iv) interaction of NPs with cell surface receptors and the subsequent activation of intracellular signalling pathways [81]. ROS generation is dependent on (i) the chemical composition and reactivity of the NPs, (ii) the impurities in the NP dispersion and (iii) the physical interaction of NPs with cellular structures involved in the cellular reduction-oxidation processes [22, 81]. Although ROS have beneficial physiological roles, overproduction induces oxidative stress in which cells fail to preserve their normal physiological redox-regulated functions [85-89]. This results in cytotoxic and genotoxic effects through the generation of deoxyribonucleic acid (DNA) strand breaks, lipid peroxidation, the production of protein radicals, modulation of the gene expression and modulation of inflammatory responses among others [85, 90-96].

Besides the ROS induced toxicity, NPs can affect cellular functioning through other mechanisms. The perinuclear localization of large numbers of NP-loaded lysosomes and effects mediated by ions leached from the NPs such as iron (II) and cadmium(II) ions can hamper the cellular transcription and translation machinery disturbing the cellular protein synthesis [81, 97-99]. Leached ions can travel to the cytoplasm where they can interfere with mRNA stabilizing proteins which have metal response domains [100, 101]. This can result in the release and degradation of mRNA. Released ions can also impair with the translation of mRNA through inhibition of the ribosomes [102, 103]. As NPs can interact with the cell surface receptors, they can activate intracellular signalling pathways. ROS-induced damage and leached ions can also indirectly change gene expression patterns through the activation of stress response genes or repair genes [88, 89, 97, 98, 104]. Furthermore, small NPs can penetrate through the nuclear pore and directly interact with the DNA [81, 105]. Additionally, leached ions can bind to the DNA and directly induce DNA damage [106, 107] (Figure 1-3).

In addition, the formation of the protein corona on the NP surface can induce structural and functional perturbations of adsorbed proteins [22, 108, 109]. This can possibly result in functional effects (e.g. interference with the proteins' enzymatic activity), which consequently can cause disturbance of biological processes or precipitation of polymeric assemblies. These polymeric assemblies can induce diseases such as amyloidosis [22, 109, 110].

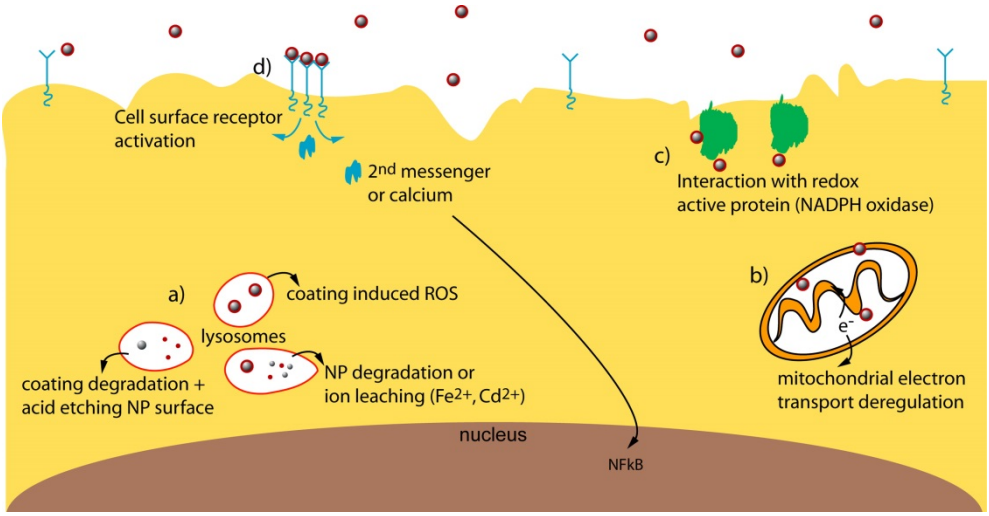

Figure 1-3: Different mechanisms by which NPs are able to affect the cellular behaviour. (a) ROS induction in the present of acidic environment of the lysosomes through the NP coating, degradation of the NP coating or NP degradation and ion leaching. (b) Deregulation of mitochondrial electron transport. (c) Interaction of NPs with redox active proteins. (d) Interaction of NP with cell surface receptors, resulting in the activation of intracellular signalling pathways. (Figure adapted from Soenen et al. *2011* (Elsevier®) *[81]*)

1.2 Dendritic cells

The immune system has evolved complex and distinct mechanisms to protect the human body from disease or potential harmful agents. This defence system consists of the innate and adaptive immunity. The innate immune system includes protective tissue (including skin, mucosa and the epithelial layers), cellular mediated protection and the complement system. Through activation of germline encoded receptors which recognize components of micro-organisms and viruses, a prompt non-specific response to pathogens and tissue damage is initiated. Moreover, the innate immune system facilitates and enhances an antigen-specific immune response through antigen presenting cells (APCs). APCs induce a cascade of events that results in the activation of specialized T and B lymphocytes, which are the key components of the adaptive immunity. This results in the generation of a highly specific action, adjusted to defeat the particular pathogen. Upon re-exposure, the adaptive immunity allows for a rapid and antigen-specific response in order to eliminate the harmful agents and to provide the long-term immunological memory [111]. Dendritic cells (DCs), which are known as the most potent APCs, play an important role as bridge between the innate and the adaptive immunity through the secretion of pro-inflammatory and immuno-regulatory cytokines [112-117]. DCs are capable in inducing T lymphocyte activation and differentiation into T helper and cytotoxic T cells. Moreover, they promote B lymphocyte activation and differentiation through the production of signal molecules.

1.2.1 Characteristics

DCs are stellate-like cells, whose name is derived from “dendron", the Greek word for tree. They consist of numerous long and dynamic finger-like cytoplasmic processes. DCs were first described by Ralph Steinman in 1973. They act as specialized sentinel cells and are found in the lymphoid tissues and at the interfaces of the body which are in contact with the external environment [112, 118].

1.2.2 Origin and dendritic cell subsets

All the different cells of the immune system are produced by a controlled process of differentiation and proliferation of multipotent hematopoietic stem cells (HSCs) and of hematopoietic progenitor cells (HPCs) [119]. DC hematopoiesis is initiated in the bone marrow were granulocyte, monocyte and DC progenitor cells (GMDPs) differentiate into more restricted monocyte and DC progenitors (MDPs) [120, 121] (Figure 1-4). MDPs develop in either monocytes or common DC progenitors (CDPs), which lose the potential to mature into monocytes. CDPs reside in the bone marrow and in the cord blood, but not in the blood or lymphoid tissues [122]. CDPs give rise to precursor cells of circulating conventional DCs (pre-cDCs) or plasmacytoid DCs (pDCs). Pre-cDCs and pDCs migrate from the bone marrow through the blood into the periphery, where the pre-cDCs give rise to the cDCs [121-123]. DCs are divided into two main groups: (i) pDCs and (ii) cDCs. cDCs comprise several DCs subsets including Langerhans cells (LCs) and myeloid DCs [121-124].

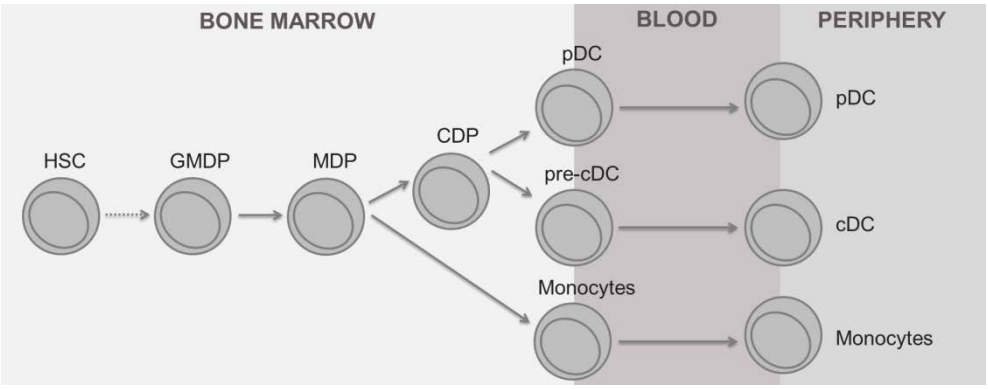

Figure 1-4 DC hematopoiesis. DC hematopoiesis is initiated in the bone marrow where granulocyte, monocyte and DC progenitors (GMDPs) differentiate in monocyte and DC progenitors (MDPs). MDPs develop in monocytes or a common DC progenitors (CDPs), which lose the potential to mature into monocytes. CDPs give rise to circulating conventional DCs (cDCs) precursor cells (pre-cDCs) or plasmacytoid DCs (pDCs). Pre-cDCs and pDCs migrate from the bone marrow through the blood into the periphery, where the pre-cDCs give rise to the cDCs [121-123]. (Figure based on Breton et al. *2015* [121])

pDCs are expert in type I interferon synthesis in response to viral infections, whereas cDCs are specialized in antigen capture, processing and presentation for T-cell priming [124, 125]. In addition, human monocytes can also be a source for the precursor population of DCs, though, the role of monocyte-derived DCs and their biological significance remains imprecise [125-127]. Monocyte-derived DCs have been suggested to represent a crucial reservoir of APCs, which are recruited in immune responses to certain pathogens and can serve as an emergency back-up mechanisms in acute inflammation [125]. The intrinsic DC subset properties and the local microenvironment regulate their actions in controlling the immune response [128].

1.2.3 Antigen uptake, processing and presentation

Immature DCs sense pathogens through the recognition of pathogen-associated molecular patterns by germline encoded pattern recognition receptors or through inflammatory cytokines present in the microenvironment [113, 124, 129]. After recognition DCs make use of several features that allow them to capture antigens: (i) phagocytosis, (ii) receptor-mediated endocytosis and (iii) macropinocytosis [130]. Subsequently, the captured antigens are processed and displayed on the cell surface in association with major histocompatibility complex (MHC) molecules. DCs have functional MHC class I and MHC class II presentation pathways. MHC class I molecules present peptides that result from protein degradation in the cytosol. In contrast, MHC class II molecules are loaded with cargo through proteolytic degradation in the endosomal compartments [130, 131]. The type of MHC class on which antigen peptides are presented determines the type of T cells to be primed [132]. MHC class I presentation results in the activation of $CD8^+$ cytotoxic T lymphocytes. MHC class II presentation can lead to the activation of $CD4^+$ T helper cells, and thereby eliciting either a T helper 1 (T_H1) or T helper 2 (T_H2) response. A T_H1 response is characterized by the activation of macrophages, cytotoxic T lymphocytes and other effector cells. A T_H2 response, on the other hand, induces the activation of B lymphocytes with the following formation of immunoglobulins [113, 130, 132].

In addition, DCs have the unique capability to present exogenous peptides on MHC class I molecules. This process is called 'cross-presentation' and represents an important feature of DCs. Through cross-presentation DCs are able to present antigens from pathogens or tumours that are otherwise not accessible to the classical MHC class I pathway. In this way $CD8^+$ cytotoxic T lymphocytes can be activated [130, 131].

1.2.4 Maturation

DC maturation refers to the process whereby DCs react to an environmental stimulus and become capable in activating the adaptive immunity [133]. Upon maturation DCs completely change their phenotype and function [113]. Microbial-derived stimuli, pro-inflammatory mediators and T-cell derived signals among others can induce DC maturation [133, 134].

DC maturation is characterized by upregulation of surface costimulatory molecules, such as the expression of CD80 and CD86, as well as an amplified expression of CD83 and MHC class molecules, the secretion of signal molecules, and the surface expression of adhesion molecules and chemokine receptors [113, 133]. During maturation, DCs initially augment the uptake of antigens in order to scan their surroundings for pathogens. Thereafter, antigen uptake quickly declines [135]. In addition, DCs undergo cytoskeletal reorganisation in which they transform to their typical distinct stellate morphology [136].

Maturation of DCs render them capable in migrating to the lymph nodes and there inducing the clonal expansion of antigen-specific naïve T lymphocytes and the associated differentiation into effector T cells. Depending on the stimuli, DCs produce distinct cytokines and trigger the differentiation of distinct subsets of T lymphocytes. In this way the T lymphocyte response will be adjusted to the specific nature of the pathogen [113, 137].

1.2.5 Role in disease

While DCs are important to protect us by regulating the immune system, they are also involved in the development of infectious diseases, immune-mediated diseases and cancer.

Certain pathogens have learned to subvert DC physiological role in controlling the immune response [138]. Some pathogens can invade DCs in peripheral tissues and replicate intracellularly. The agents can spread locally through a productive non-lytic infection and/or by killing the DCs. Moreover, infected DCs can carry the agent to the lymph nodes. In addition, pathogens can interfere with MHC class I and class II processing and presentation pathways or they can activate T cells indiscriminately through the presentation of superantigens [113, 138-142]. Examples of pathogens who can circumvent DC function include the viruses human immunodeficiency virus I, Epstein-Barr virus and herpes viruses, the bacteria *mycobacterium tuberculosis* and *Salmonella species*, and the parasite *Leishmania major* [138, 143].

Altered function of DCs is also known to be involved in the initiation and perpetuation of immune-mediated diseases including autoimmune diseases (e.g. Systemic Lupus Erythematosus, Multiple Sclerosis, Inflammatory Bowel Diseases and Rheumatoid Arthritis) and allergies [112, 138, 143, 144]. DCs may induce immune-mediated diseases through an altered antigen processing, which lead to the presentation of self-antigens, skewing of the T_H1 and T_H2 balances, failure to delete autoreactive T lymphocytes, overproduction of inflammatory cytokines, or incorrectly migrating and presenting antigens in peripheral sites [143-145].

DC dysfunction has been recognized as well as a mechanism for cancer escape. Tumour-derived products such as cytokines, inflammatory mediators and metabolic products can hamper DC differentiation, maturation and survival. As a result, antitumour responses are insufficiently induced and tumour progression will be promoted [143, 146].

1.2.6 Opportunities for disease prevention and therapy

Although DCs are involved in the pathogenesis of multiple diseases, they also have a promising role in clinical medicine in order to counteract the aforementioned mechanisms [143]. DC manipulation offers an interesting approach to prevent and treat infectious diseases. By considering DCs in the designs of vaccines, it can contribute to protective immunity against the pathogen [147-149].

Activated DCs are an hopeful alternative for the treatment of cancer as an immunostimulatory vaccine. DCs can induce effective cancer immunity through targeting T_H1 cells and cytotoxic T lymphocytes and natural killer cells to tumour antigens [147, 150, 151]. Furthermore, as anti-cancer vaccines have the potential to stimulate long-lasting memory T lymphocytes to tumour antigens, it can contribute to long-term cancer remission [143, 147, 152].

The manipulation of DCs in order to induce immune silencing in an antigen-specific manner can contribute to the prevention of graft versus host disease in transplantations, autoimmune diseases and allergic diseases. Different approaches including genetic, biological and pharmacologic manipulation can program DCs towards tolerogenic DCs which functions in inducing T cell apoptosis, anergy and regulatory T cells [143, 153-155].

1.3 Dendritic cells and nanoparticles

DCs play a prominent role in various diseases and conditions which involve the immune system. Exposure to NPs can interfere with DCs' immune regulatory functions which can contribute to unwanted side effects [156, 157]. On the other hand, the targeting of NPs to DCs offers a promising method for developing a well-adjusted and protective immune response which can be useful for novel therapeutic approaches [158].

1.3.1 Immune toxicity

Ambiguities concerning the interaction of NPs and their impact on the immune system still remain. The effect of NPs on the development of allergic disorders is not yet clarified. Air pollution particulate matter (PM) including ultrafine PM (UFP), which is PM smaller than 100 nm, exhibit an adjuvant activity on allergic airway sensitization. UFP is typically composed from a carbonaceous core coated with metals, sulphates and polyaromatic hydrocarbons, and has the potential for binding allergens and adsorbing lipopolysaccharides [159, 160]. Accordingly, UFP acts as an adjuvant in provoking primary allergic sensitization and are able to exacerbate secondary immune responses [161, 162]. Noteworthy, a significant component of UFP adjuvant effects has been attributed exclusively to impurities in the UFP mixture or adsorbed toxic chemicals on the UFPs' surface rather than the nanosized character of the material itself [8, 163-165].

Recent studies propose that engineered NPs can exert similar effects on the immune system [166, 167]. For example, TiO_2 (titanium dioxide) NPs have been shown to act as an adjuvant for the skin sensitizer dinitrochlorobenzene (DNCB), where it increases the dermal sensitization potency of DNCB [168]. Moreover, both TiO_2 and GNPs aggravate the inflammatory response in a mouse model of diisocyanate-induced asthma [169]. Studies showed inconclusiveness on the involvement of and the effects on DCs upon NP exposure. DCs accumulate NPs in their intracellular compartments dedicated to antigen processing. NP uptake therefore can potentially hamper antigen presentation [170]. GNPs were shown to induce either pro-inflammatory or anti-inflammatory effects in DCs [171],

whereas GNPs were shown to inhibit cytokine secretion after LPS stimulation [170]. Functionalized polystyrene (PS) NPs were shown to trigger DC maturation [172]. On the other hand, superparamagnetic iron oxide (SPIO) NPs can revert mature DCs to a functional immature phenotype [173]. Moreover, amino-functionalized PS NPs did not alter the phenotype and functionality of matured DCs [174]. The detailed mechanism behind the possible NP-induced maturation effects by various NPs are not yet identified. Recent studies suggest the involvement of NP surface modifications and NP size [171, 175, 176]. Hydrophobic regions on the NP surface have been proposed as well to play an important role as they can act as danger signals triggering an immune response [172, 176, 177]. In addition, there is a high need to address the interaction of DCs with NPs in the context of mixed exposure situation, combined exposures are highly relevant for human subjection to NPs and risk assessment of nanomaterials.

1.3.2 Target-oriented therapeutic approaches

Cancer immunotherapy is one important field in which the application of NPs is extensively under investigation. Here, DCs are provided with tumour-specific antigens in order to induce tumour-specific effector T cells that eliminate tumour cells specifically and induce immunological memory in order to control tumour relapse [178]. NPs are an attractive vehicle for the synchronized delivery of tumour antigens and adjuvants to DCs [179]. Especially NPs (e.g. poly-lactic-co-glycolic acid NPs) which possess immunomodulatory properties are promising as they can act as an adjuvant by themselves [172, 176].

Specific immunotherapy in order to induce immunologic hyporesponsiveness for the treatment of autoimmune diseases and allergies using NPs is also being explored [176, 180-182]. Allergen and adjuvant NPs can modulate the DCs and the resulting allergen-specific T-cell responses inducing tolerance against the particular allergen [176, 183]. Other therapeutic approaches targeting NPs to DCs include NPs for the treatment of infectious diseases [184-187] and autoimmune diseases [182, 188, 189] amongst others.

1.4 Characterization of nanoparticle-bio interaction

There is a high need for a better understanding of the processes occurring at the interface between nanomaterials and biological systems. This nano-bio interface covers a wide range of interactions between the NP surface and the biomolecular surface. Processes such as the protein corona formation, cellular contact, endocytosis and intracellular trafficking of NPs are influenced by a variety of forces taking place, including long-range forces such as attractive van der Waals forces and repulsive electrostatic double-layer interactions, or short-range forces such as charge, steric, depletion and solvent interactions [26, 190]. In order to study the processes that take place at the nano-interface, it is crucial to have customized tools to assess the behaviour of the nanomaterials in biological systems. Fluorescence-based methods are being appreciated as reliable and quantitative tools. Due to advances in the nanotechnology in the recent years, a wide range of intrinsically fluorescent NPs have become available including fluorescently stained polymeric NPs, dye-doped silica NPs, quantum dots, nanodiamonds and metal nanoclusters [190, 191]. Fluorescence-based methods including fluorescence microscopy and flow cytometry allow for live-cell, long-term follow-up of the nano-bio interactions.

1.4.1 Fluorescence microscopy

One approach to extent the knowledge of how fluorescent NPs interact with biological systems including their uptake and transport pathways, their intracellular fate and their effects on cellular function is the usage of fluorescence microscopy. The usage of fluorescent NPs allows to directly visualize and quantify the uptake processes and track NPs within living cells [192]. Spatially sensitive detection of NPs can be accomplished by a number of optical microscopy techniques including confocal laser scanning microscopy (CLSM), spinning disk confocal laser microscopy (SDCLM), super-resolution methods and total internal reflectance fluorescence microscopy (TIRF) [190, 193].

CLSM is a classical technique which can generate images by means of laser scanning on an optical platform. Through the usage of a pinhole, optical sectioning of the specimen can be obtained [194]. CLSM is an important tool to enhance the identification and localization of NPs in the cell [193, 195], but also in tissues such as the skin [194, 196]. SDCLM has a high image acquisition rate compared to CLSM with a minimum illumination. Therefore, this method is well suited to visualize NP uptake in cells in real time [197, 198]. Super-resolution methods, including stimulated emission depletion microscopy (STED), reduce the limits of optical imaging down to the molecular scale [199, 200]. By depleting fluorophores in the outer area of the point-spread function in STED, the focus is sharpened and the resolution of the lateral and/or axial plane is increased. Penetration of the nucleus by silica NPs and the absolute quantification of the intracellular load of silica NPs have been established by STED [201, 202]. In contrast to the aforementioned microscopy techniques, TIRF has a considerably less bleaching effect and reduced photo-induced toxicity as only the area very near the cell membrane is specifically illuminated [203]. Hereby TIRF provides crucial information concerning the cellular internalization kinetics and diffusion in the cell as described for quantum dots [204].

Besides the image acquisition, the ensuing data analyses can reveal important facts on the intracellular trafficking and interactions of the NPs within the cell. The dynamics of intracellular NP transport have been quantified by single particle tracking (SPT) [205-207], image correlation spectroscopy (ICS) [193, 207-212], fluorescence correlation spectroscopy (FCS) [212, 213], fluorescence recovery after photobleaching [212] among others. Interactions of NPs within the cells have been quantified using static two-dimensional [193, 207, 211, 214-216] and static three-dimensional [217] colocalization analyses. Dynamic colocalization analysis take into account the kinetic behaviour of the NPs together with for instance an intracellular organelle by determining their correlated motions [207, 210, 211, 218].

In addition, fluorescence microscopy based tools can clarify the interaction of fluorescent NPs with its environment. In FCS temporal fluctuations from individual fluorescent emitters in a small, observation volume are used to describe the processes giving rise to these fluctuations [190]. FCS can provide quantitative information on NP-protein interactions, such as protein adsorption, protein binding affinity and protein orientation on the NP surface [24, 68, 219, 220]. SPT, on the other hand, gives also spatial information and has the ability to characterize nano-bio interactions at a single particle level [221]. Moreover, SPT reveals crucial information with regard to NP mobility and penetration in complex biological mixtures being significant for drug delivery [222, 223].

1.4.2 Flow cytometry

Flow cytometry is a fluorescence-based method in which a suspension of cells are passed through one or more laser beams [224]. As they pass through the lasers, the light scattered by each individual cell in the forward and side directions is measured together with the fluorescence signal emitted by the fluorescent species, such as fluorescent NPs. Flow cytometry is a high-throughput method in which large numbers of cells can be assessed at once on a cell-by-cell basis. Extensive work has been performed in order to quantify NP uptake and their uptake kinetics [27, 50, 225].

1.5 Research outline

Although efforts have been made in understanding how NPs interact with biological systems, well-adjusted tools to evaluate the nano-bio interaction are still missing. For that reason, part of this dissertation focuses on the implementation of technologies to assess this interaction. In this part, the aim is to investigate whether advanced fluorimetric techniques are suitable to retrieve quantitative information on the uptake, the intracellular behaviour and the fate of NPs in biological cells. In the second part, the aim is to examine the impact of NPs on the biological function of DCs. In the next chapters of this dissertation, following aspects are addressed: (i) the intracellular transport and fate of NPs, (ii) the uptake and release of drug-loaded nanocarriers, (iii) the uptake kinetics of NPs and (iv) co-exposure effects of NPs and allergens on the DC sensitization response.

1.5.1 Intracellular transport and fate of NPs

Various aspects of the intracellular trafficking of NPs inside biological cells remain largely unknown. In **chapter 2** and **chapter 3** the applicability of ICS-based techniques and SPT are explored in order to measure the intracellular dynamics of NPs, as this can be considered as a fundamental step in understanding their complex behaviour. The intracellular transport and fate of 100-nm sized fluorescently stained PS NPs and 200-nm sized biodegradable poly-l-lactic acid (PLLA) NPs containing the photosensitizer Hypericin are studied. The dynamic interactions of the NPs within several subcellular compartments are also assessed and quantified. In addition, the involvement of the cytoskeleton in the NP transport is explored.

1.5.2 Uptake and release of drug-loaded nanocarriers

Theranostic NPs have the potential of carrying loads such as imaging and therapeutic agents and deliver it to the target tissue of interest. In **chapter 3** the uptake and intracellular release of the photosensitizer Hypericin encapsulated in biodegradable PLLA NPs is assessed. ICS and fluorescence

lifetime imaging microscopy (FLIM) are performed in order to monitor the dynamics of the encapsulated and released Hypericin in the cell. By using FLIM a map of the fluorescence lifetime of Hypericin over the cell is obtained. The fluorescence lifetime is highly dependent on the surrounding microenvironment and, as a result, reports on the local intracellular interactions of the encapsulated and released Hypericin. Passive interactions of PPLA NPs with a lipophilic surrounding are assessed by investigating the passive transfer of the fluorescent cargo to microbubbles using CLSM.

1.5.3 Uptake kinetics of NPs

The uptake and its time kinetics of 40-nm sized fluorescently stained carboxylated PS NPs are studied in $CD34^+$ HPCs and $CD34^+$ derived DCs (**chapter 4**). PS NPs are chosen for their convenient commercial availability, high quality, low cellular toxicity, wide variety of sizes and surface chemistries. Flow cytometry and CLSM are used to determine NP uptake. Differentiation of HPCs into DCs significantly changes the cellular response to 40 nm PS NPs. The uptake kinetics of naïve HPCs propose the opportunity of transient NP loading.

1.5.4 Co-exposure effects of NPs and allergens on DC sensitization response

Immunomodulatory effects of 50-nm sized GNPs on the phenotype of immature DCs are studied in **chapter 5** and **chapter 6**. GNPs are very promising in different kinds of fields due to their chemical inertness, high biocompatibility and optical properties, which make them attractive for electronics, sensors but also anticancer therapy. Immunomodulatory properties of GNPs have been described before, therefore, flow cytometric analyses of the exposed cells are performed to characterize their surface marker expression. NP uptake is quantified by ICP-MS analyses in which the gold content is chemically determined. The combined exposure of allergens and GNPs on the allergenic sensitization response of DCs is further explored to elucidate if GNPs interfere with allergic responses. Two major allergens, nickel (II) sulphate ($NiSO_4$) **(chapter 5)** and house dust mite

(HDM) extract **(chapter 6)** are used. DCs are exposed to an allergen, 50-nm sized GNPs or a mixture of both. A detailed physicochemical characterization of the GNPs in contact with the allergen is performed including nanoparticle tracking analysis (NTA), disc centrifugation, UV-Visible spectroscopy, ζ-potential determination and proteomics.

2 Intracellular dynamics and fate of polystyrene nanoparticles by image (cross-) correlation spectroscopy and single particle tracking

This chapter is based on:

Intracellular dynamics and fate of polystyrene nanoparticles in A549 Lung epithelial cells monitored by image (cross-) correlation spectroscopy and single particle tracking.

Sarah Deville, Rozhin Penjweini, Nick Smisdom, Kristof Notelaers, Inge Nelissen, Jef Hooyberghs, Marcel Ameloot.

Biochimica et Biophysica Acta – Molecular Cell Research 2015
Volume 1853, Issue 10, Pages 2411-2419
doi: 10.1016/j.bbamcr.2015.07.004

2.1 Abstract

Novel insights in NPs uptake routes of cells, their intracellular trafficking and subcellular targeting can be obtained through the investigation of their temporal and spatial behaviour. In this work, we present the application of ICS-ICCS and SPT to monitor the intracellular dynamics of PS NPs in the human lung carcinoma A549 cell line. The ensemble kinetic behaviour of NPs inside the cell was characterized by temporal and spatiotemporal image correlation spectroscopy (TICS and STICS). Moreover, a more direct interpretation of the diffusion and flow detected in the NPs motion was obtained by SPT by monitoring individual NPs. Both techniques demonstrate that the PS NPs transport in A549 cells is mainly dependent on microtubule-assisted transport. By applying spatiotemporal image cross-correlation spectroscopy (STICCS), the correlated motions of NPs with the early endosomes, late endosomes and lysosomes are identified. PS NPs were equally distributed among the endolysosomal compartment during the time interval of the experiments. The cotransport of the NPs with the lysosomes is significantly larger compared to the other cell organelles. In the present study we show that the complementarity of ICS-based techniques and SPT enables a consistent elaborate model of the complex behaviour of NPs inside biological systems.

2.2 Introduction

NPs are defined as particles with at least 50% in the number size distribution having one or more external dimensions in the size range between 1 nm and 100 nm [120]. The study of the interaction of NPs with living systems is of steadily growing interest. Since NPs are in the same order of magnitude as biomolecules and viruses, they can easily enter cells and interact with the cellular machinery [50, 59, 60, 226]. Although NPs hold great promise for new nanoscaled diagnostics and targeted drug delivery in biological systems [227], they may also provoke toxic side effects [228]. NPs enter cells predominantly through a complex interplay of endocytic pathways and thereafter travel

throughout the cell by using its endocytic machinery [27, 221]. Primary endocytic vesicles can fuse together with the early endosomes to deliver the cargo for further cellular processing [37]. Early endosomes move towards the perinuclear space, where the transition towards the late endosomes takes place. Finally, the late endosomes fuse with the lysosomes [229]. The intracellular transport of vesicles and cell organelles is mediated through both the microtubules and the actin microfilaments [230]. By studying the trafficking of NPs within living cells and cell organelles, novel insights in NPs uptake processes, intracellular transport and their multiple outcomes can be obtained [231].

In the present study, the application of ICS for the determination of interactions of fluorescently stained carboxylated PS NPs within the cell is presented. PS NPs are commonly used as model NPs to study interaction with biological systems due to their commercial availability, high quality and wide variety of sizes and surface chemistries [221]. ICS is a fluorescence-based microscopic technique suitable for defining the diffusion and directed motion on time scales ranging from microseconds to milliseconds [232-234]. This information is obtained from the fluctuations of the fluorescence intensity within a region of interest (ROI) of a time-lapse image series. Various ICS variants exist which differ in the way how the fluorescence fluctuations in the image series are analysed. Where in TICS, fluorescence fluctuations in time for the recorded pixels of an image series are exploited for the correlation analysis [233, 235], STICS correlates fluorescence fluctuations both in space and time [208, 233, 236]. With these techniques the diffusion and/or flow (magnitude and direction) of molecular complexes can be monitored. They have been used in previous studies to quantify the intracellular transport of the photosensitizer polyvinylpyrrolidone (PVP)-hypericin, polyplexes, lipoplexes and silica NPs [193, 209, 210, 237]. Interaction between molecular complexes is investigated by STICCS in which space-time correlation functions from the fluorescence intensity fluctuations within a two-channel fluorescence image series are correlated [238]. This approach is used here to study the association of NPs complexes with cell organelles. Besides these ensemble

averaging techniques, SPT can be used to quantify the individual NP motions, which registers and tracks the NP frame by frame [239], as demonstrated for gene nanocarriers and polymeric NPs [205, 206].

Here we report on the intracellular dynamics of fluorescently stained carboxylated PS NPs in human alveolar epithelial A549 cells, mimicking the biological responses of lung cells to NPs exposure, which is highly relevant for both nanomedicine and nanotoxicology as inhalation is one the major entry routes of NPs to the human body. TICS and STICS were used to characterize the diffusion and map the flow magnitude and direction of PS NP inside the cell. PS NP motions were also analysed by SPT, which facilitated in the translation of these general motion models to effective NP dynamics created by biological processes. This was corroborated by dynamic interactions of NPs with the early endosomes, late endosomes and lysosomes established and quantified with STICCS. In addition, the role of cytoskeleton in the NPs transport was explored by means of ICS and SPT.

2.3 Materials and methods

2.3.1 Cell culture

The human alveolar epithelial A549 cell line was routinely maintained in modified eagle's medium with glutamax (MEM, Gibco, Paisley, United Kingdom) supplemented with 10% non-heat inactivated fetal bovine serum (FBS, Biochrom AG, Berlin, Germany) and 1% penicillin/streptomycin (P/S, Gibco) at 37°C under 5% CO_2. Before reaching confluence, cells were washed with versene (Gibco) and detached using 0.05% trypsin containing 0.02% EDTA (Sigma-Aldrich, Ayrshire, United Kingdom).

2.3.2 Nanoparticles

Dark red (λ^{Ex} 660, λ^{Em} 680) fluorescent carboxylated PS NPs were purchased from Molecular Probes (Invitrogen, Merelbeke, Belgium). PS NPs were characterized by dynamic light scattering (DLS, ZetaPALS, Brookhaven

Instruments Corporation, Holtsville, USA), yielding a mean hydrodynamic diameter of 116 ± 1 nm (polydispersity index (PDI) of 0.19) in water and 152 ± 2 nm (PDI of 0.18) in complete cell culture medium (CCM).

2.3.3 Cell exposure

The cells used for microscopic observation were plated one day before the experiment in 8 well µ-Slide (Ibidi GmbH, Martinsried, Germany) at a density of 30×10^3 cells/cm². Cells were exposed for 30 minutes to 50 µg/ml of PS NPs diluted in MEM containing 10% FBS, but without phenol red and without P/S at 37°C under 5% CO_2. After exposure, cells were washed 3 times to remove the PS NPs that were not taken up by the cells and STICS/TICS measurements were conducted. In order to disturb the cytoskeleton mediated transport within the cell, 1 µM latrunculin A (Merck Millipore, Overijse, Belgium) and 20 µM nocodazole (Sigma-Aldrich) were added to the culture medium after NPs treatment and washing. After incubation for 30 minutes, STICS/TICS measurements were performed. For the STICCS measurements, the cells were labelled prior to PS NPs exposure with organelle specific dyes. 1 µM LysoTracker® Green DND-26 (Molecular Probes) was added for 30 minutes. CellLight® Early Endosomes-GFP (Molecular Probes) or CellLight® Late Endosomes-GFP (Molecular Probes) were added to the cultures in a final concentration of 25 particles per cell 24 hours prior to the experiments, according to the manufacturer's protocol.

2.3.4 Immunofluorescence

For visualization of the tubulin and F-actin cytoskeleton, cells exposed to PS NPs, latrunculin A and/or nocodazole were fixed with 4% formalin (Sigma-Aldrich). Cells were permeabilized with 0.5% Tween®20 (Sigma-Aldrich) in PBS for 10 minutes, and blocked with 0.1% Tween®20 and 2% bovine serum albumin (BSA, Sigma-Aldrich) for 30 minutes. Subsequently, cells were incubated with mouse anti-tubulin antibodies (T9026, Sigma-Aldrich) for 30 minutes. After washing the unbound fraction, donkey anti-mouse antibodies conjugated with Alexa Fluor® 488 and CytoPainter Phalloidin-iFluor 555 Reagent (Abcam, Cambridge, UK)

were applied for 30 minutes. Finally, after rinsing the sections extensively, Vectashield® mounting medium containing 4',6-diamidino-2-phenylindole (DAPI) (Vector Laboratories, Peterborough, United Kingdom) was added.

2.3.5 Confocal microscopy

Image time-series were acquired using an epifluorescence Axiovert 200M equipped with a Zeiss LSM 510 Meta CLSM (Zeiss, Jena, Germany) and a LD C-Apochromat 40x/1.1 W Korr UV-VIS-IR water immersion objective (Zeiss), placed on a vibration isolation table in an air-conditioned room kept at constant temperature. Cells were kept at 37°C by the means of a stage incubator (Tempcontrol 37-2 digital, PeCon, Erbach, Germany).

Alexa Fluor® 488, CellLight® Early Endosomes-GFP, CellLight® Late Endosomes-GFP and LysoTracker® Green DND-26 were excited with the 488 nm line of an argon ion laser. CytoPainter Phalloidin-iFluor 555 was excited with a 543 nm helium-neon laser. Dark red PS NPs were excited a 633 nm helium-neon laser. DAPI was excited using a 150 fs pulsed laser light of a Ti:Sapphire laser (MaiTai DeepSee, Spectra-Physics, California, USA) tuned at an output wavelength of 730 nm. The excitation light was directed to the sample by a dichroic beam splitter (HFT UV/488/543/633).

For the detection and separation of the different emitted fluorescence signals, a secondary dichroic beam splitter NFT 545, as well as four band-pass filters BP 390-465 (DAPI), BP500-550 (Alexa Fluor® 488, CellLight® Early Endosomes-GFP, CellLight® Late Endosomes-GFP, LysoTracker® Green DND-26), BP565-615 (CytoPainter Phalloidin-iFluor 555) or BP650-710 (dark red PS NPs) were used. Signals were directed towards an internal analog photomultiplier tube (PMT) of the confocal unit. Confocal pinhole was set to a maximum of 1.5 Airy units to provide sufficient z-sectioning. Each image time-series comprised typically 100 frames with a 512 by 512 resolution, a pixel size between 40 and 120 nm, a frame rate of 0.63 Hz without extra time delay between subsequent frames, and a pixel dwell time of 2.51 µs.

2.3.6 Image (cross-) correlation spectroscopy and colocalization analyses

A brief review of ICS is given in *2.6.1. Autocorrelation functions*. Image (cross-) correlation spectroscopy analysis was performed using custom written MATLAB routines (The MathWorks, Eindhoven, The Netherlands), based on the original work of the Wiseman Research Group (McGill University, Canada). The original routines and details of analysis have been published before [208, 236, 238, 240-243]. Immobile populations within the image series were removed by the means of Fourier-filtering [236]. Due to the flat morphology of the A549 cells, only two-dimensional dynamics were considered.

The central subregion of the spatial autocorrelation of each image in the time series was fit by a two-dimensional Gaussian function yielding the zero-lag amplitude $G(0,0,0)$ and the e^{-2} radius of the point spread function (PSF) of the laser beam ω_0 [236, 243]:

$$G(\xi,\eta,0) = G(0,0,0)\exp\left\{-\frac{\xi^2+\eta^2}{\omega_0^2}\right\} + G_\infty \qquad \text{(Eq. 2-1)}$$

where ξ and η denote to the spatial lags in x and y directions, respectively, and where G_∞ is the longtime offset.

In TICS, the temporal autocorrelation function (TACF), $G(0,0,\tau)$, was fit to the decay models introduced by *Hebert et al* for two-dimensional diffusion and/or flow [236]. Among these models, one single species undergoing both diffusion and flow gave the best fit to $G(0,0,\tau)$:

$$G(0,0,\tau) = G(0,0,0)\left(1+\frac{\tau}{\tau_D}\right)^{-1} \times \exp\left\{-\left(\frac{|v_f|\tau}{\langle\omega_0\rangle}\right)^2\left(1+\frac{\tau}{\tau_D}\right)^{-1}\right\} + G_\infty \qquad \text{(Eq. 2-2)}$$

where v_f and τ_D refer to the flow velocity and the characteristic diffusion time, respectively.

$<\omega_0>$ represents the average of e^{-2} radius of the PSF of the optical setup. The value of $<\omega_0>$ was calculated by averaging the individual ω_0 obtained from fitting (Eq. 2-1) for every image in the time series.

The diffusion coefficient (D) was obtained from the characteristic diffusion time, τ_D and $<\omega_0>$ according to:

$$D = \frac{\langle \omega_0 \rangle^2}{4\tau_D} \qquad \text{(Eq. 2-3)}$$

For all pairs of images separated by lag-time τ, the spatiotemporal autocorrelation function (STACF) in STICS is defined by:

$$G(\xi - \Delta\xi, \eta - \Delta\eta, \tau) = G(\Delta\xi, \Delta\eta, \tau) \exp\left\{ - \frac{(\xi - \Delta\xi)^2 + (\eta - \Delta\eta)^2}{\omega_0(\tau)^2} \right\} + G_\infty \qquad \text{(Eq. 2-4)}$$

The time-dependent amplitude $G(\Delta\xi, \Delta\eta, \tau)$, the position of the Gaussian peak ($\Delta\xi$, $\Delta\eta$) in lag-space and the spatial offset parameter G_∞ were obtained by fitting the experimental data. The displacement of the Gaussian peak over time provides vectorial information about the flow (V_{STICS}) and was always fit to the first linear part detected [236]. The determination of the magnitude of the flow by STICS is more accurate than by TICS [210].

The fitting scheme weights the correlation from each pair of images equally. As photobleaching can affect the primary data [235, 244], the autocorrelation function in the presence of photobleaching, $G_{pb}(0,0,\tau)$, was corrected as follows [244]:

$$G_{pb-corrected}(0,0,\tau) = \frac{G_{pb}(0,0,\tau)}{\left\langle [b(t)b(t+\tau)]^{-1/2} \right\rangle_T} \quad , \quad b(t) = e^{-kt} \qquad \text{(Eq. 2-5)}$$

where $b(t)$ is the time course of particle number concentration during the measurement normalized to the initial concentration; k is the bleaching rate constant with reciprocal time units.

In order to investigate the association between PS NPs and cell organelles, the cross-correlation scheme (STICCS) was employed [208, 236, 238]. STICCS is based on the image time series in space and time collected in two fluorescence detection channels, *a* from the PS NPs and *b* from labelling of the cell organelle, yielding the cross-correlation function $G_{ab}(\xi,\eta,\tau)$ (see *2.6.1 Autocorrelation functions*) [233].

The space-time evolution of the cross-correlation function was characterized by locating the maximum of $G_{ab}(\xi,\eta,\tau)$ and fitting with a Gaussian function as presented in (Eq. 2-4). If at zero time-lag the cross-correlation between the two detection channels is non-zero, the two species (PS NPs and organelle specific dye) are in association [236]. However, non-zero cross-correlation values do not automatically imply direct interaction [236]. In the case of stationary particles, the cross-correlation stays unchanged for all values of τ and centers at (ξ = 0, η = 0). Changes over time in the number of interacting and/or correlating particles that are at the same location in space will be reflected in the cross-correlation function as described for STICS.

From the recorded confocal time-lapse movies image subsections of 64 × 64 pixels in size were selected from different regions in the cell for STICS, TICS and STICCS analyses. Median values were taken from at least 10 regions inside the cell as an estimate for the average motion per cell. For STICCS, the absence of cross-talk between the fluorescently labelled cell organelles and the NPs was verified.

Stage drift was assessed by performing the STICS analysis to fixed beads (Invitrogen, PS-Speck Microscope Point Source Kit, nominal diameter 175 nm) mounted on a coverslip under the same environment and set-up as in the actual experiments. The magnitude of the stage drift was about $(1.5 \pm 0.1)\times10^{-3}$µm/s. STICS analysis was performed on the entire image (512×512 pixels) giving an estimate of the experimental cell motions and stage drift. Velocities obtained from individual regions within cells were corrected accordingly.

Colocalization analyses of NPs with organelles was also performed by calculating the Manders' overlap coefficients M1 and M2 by using the JACoP plugin in ImageJ (National Institutes of Health, Bethesda, United States) [245, 246]. Prior to the colocalization analysis, the threshold was set to the estimated value of the background. Subsequently, the M1 and M2 colocalization coefficients were defined by (Eq. 2-6) and (Eq. 2-7) with A_i and B_i the signal intensity above a selected threshold of pixel number i obtained from the channel representing respectively the organelle type and NPs:

$$M_1 = \frac{\sum_i A_{i,coloc}}{\sum_i A_i} \qquad \text{(Eq. 2-6)}$$

where $A_{i,coloc} = A_i$ if $B_i > 0$ and $A_{i,coloc} = 0$ if $B_i = 0$ and

$$M_2 = \frac{\sum_i B_{i,coloc}}{\sum_i B_i} \qquad \text{(Eq. 2-7)}$$

where $B_{i,coloc} = B_i$ if $A_i > 0$ and $B_{i,coloc} = 0$ if $A_i = 0$. Obtained overlap coefficients are not dependent on the relative intensities of each channel [245]. Cross-talk between the double labelled cells was found to be negligible.

2.3.7 Single particle tracking

SPT analysis was performed on the same experimental data of PS NPs as used for ICS analysis. Particles were localized in each frame by automated thresholding and Gaussian fitting [247]. Trajectories were constructed by connecting particle locations in subsequent frames, while minimizing the total square displacement [248]. For all trajectories, containing at least 12 displacements, the mean square displacement (MSD) $<r^2>$ was determined over all pairs of points for the available time lags. Each trajectory provided an estimator of the diffusion coefficient D_{est} by linear least squares fitting of the MSD in function of the first three time lags ($t_{1\text{-}3}$) according to 2D Brownian motion:

$$\langle r^2 \rangle = 4 D_{est} t_{1-3} \qquad \text{(Eq. 2-8)}$$

Particle trajectories not displaying an increase in MSD over increasing time lags were considered to be *immobile* (I) and the corresponding values were excluded from the distribution of D_{est}. Segments of directed motion were identified in particle trajectories by a scanning window analysis [249]. Elongated trajectory sections were identified based on the radius of gyration and identified as directed motion if the net displacement (R) was sufficient according to:

$$R > \sqrt{4D_e t} \qquad \text{(Eq. 2-9)}$$

where D_e represents the diffusion coefficient D_{est} averaged over all trajectories of the non-treated, control condition (0.011 ± 0.001 µm²/s) and t is the *duration* of the time section. The *distance* of the section was quantified as the scalar sum of all first order displacements within t. The *speed* was obtained by dividing the *distance* by *duration*. All image processing and consequent analysis were performed by in-house developed MATLAB routines.

2.3.8 Statistical analysis

Statistical analyses were performed by GraphPad Prism version 5.00 (GraphPad Software, San Diego, California, USA). Student's t-tests were performed in order to investigate the effect of nocodazole and latrunculin A on the flow and diffusion values obtained from STICS, TICS and SPT. A Kruskal-Wallis test was performed to compare the correlated motion velocities of PS NPs with the cell organelles. Results with p-values smaller than 0.05 were considered to be statistically significant.

2.4 Results and discussion

2.4.1 Nanoparticle dynamics within cytosol

The subsequent phenomena of non-directed and possible directed motion of PS NPs within the cytosol of A549 was investigated by STICS and TICS. Figure 2-1 displays for a typical cellular region (region 1 from Figure 2-3a) the STICS STACF at τ = 0, 20 and 40 s (Figure 2-1a), the time evolution of its peak position (Figure 2-1b) and the TICS TACF (Figure 2-1c). Fitting for the displacement of the Gaussian peak yielded the velocity V_{STICS} = 7.4×10^{-3} µm/s (v_ξ = 6.2 ×10^{-3} µm/s; v_η = 4.1×10^{-3} µm/s) (Figure 2-1b, using only the linear part of the traces). Fitting the TACF with a model for diffusion and flow yields the diffusion coefficient D_{TICS} = 0.8 ×10^{-3} µm²/s when the flow magnitude was fixed at the obtained value for V_{STICS} (Figure 2-1c). The same STICS and TICS analyses were executed for the different regions inside the cell (Figure 2-3). The velocity mapping shows locally directed motion of different magnitudes for intracellular NPs transport, where the median of the flow and diffusion values inside the cell equals to V_{STICS} (N=1) = 9.9×10^{-3} µm/s and D_{TICS} (N=1) = 18.5×10^{-3} µm²/s. Values obtained from different biological cells (N = 5) were averaged over the median of each cell, resulting in V_{STICS} (N=5) = (9 ± 2)×10^{-3} µm/s and D_{TICS} (N=5) = (8 ± 3)×10^{-3} µm²/s (average ± SEM); Table 2-1).

These values are in close agreement with the velocity and diffusion acquired from polyplexes in CHO-K1 cells studied with STICS [209]. In contrast, the values are respectively 10 times and 5 times smaller than the results obtained with STICS for SiO_2 NPs in A549 cells and polyplexes in HeLa [193, 237]. Little is known about the influence of NP exposure on the regulation of the endocytic pathways and the speed of vesicle trafficking. For that reason, the divergence can possibly be attributed to the differences in exposure time, the type of NPs or their uptake pathways.

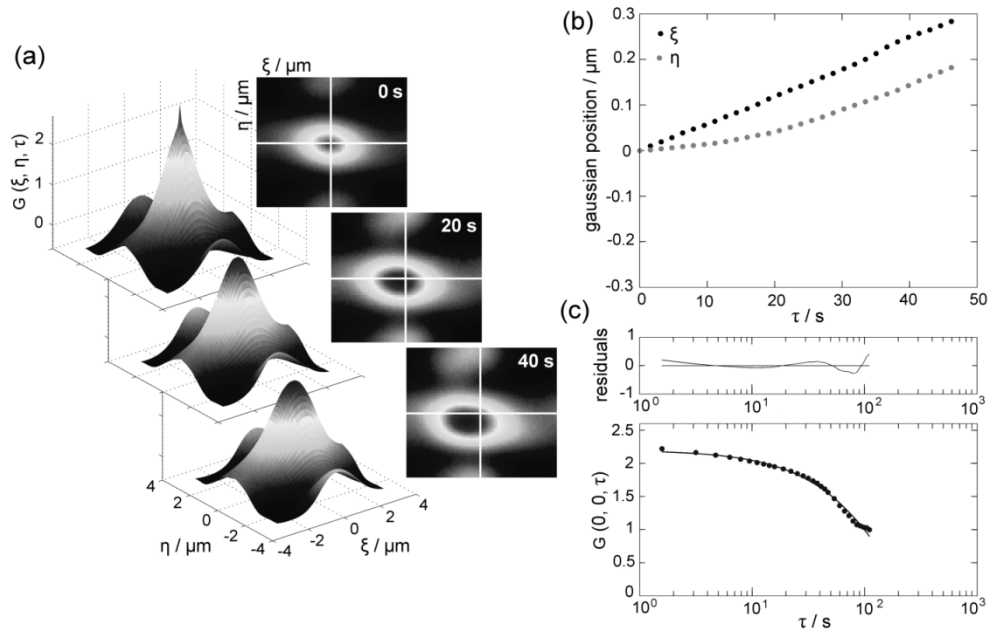

Figure 2-1: STICS and TICS analyses of PS NPs in A549 cells. Image subsections of 64×64 pixels were selected from different regions of the cells shown in Figure 2-3a. Here region 1 is presented. (a) The STACF G (ξ,η,τ) (STACF) and their contour plot at different time points. (b) Time dependence of the position of the peak of the STACF. (c) The TACF G(0,0,τ) was fitted using a diffusion model, considering a fixed flow component as determined by STICS.

Table 2-1: Parameters of NP motions extracted by STICS and TICS analysis. Reported values are averaged over the median of the parameter values obtained for the different regions of each cell (N = 5) and represented with standard error of the mean (SEM). The asterix denotes significant differences of treatment compared to control conditions (* p-value < 0.05).

motion type	A549 cell treatment		
	control	nocodazole	latrunculin A
diffusion [µm²/s]	$(8 \pm 3)\times10^{-3}$	$(1.3 \pm 0.3)\times10^{-3}$ *	$(2 \pm 1)\times10^{-3}$
velocity [µm/s]	$(9 \pm 2)\times10^{-3}$	$(2.7 \pm 0.2)\times10^{-3}$ *	$(8 \pm 2)\times10^{-3}$

The intracellular transport of vesicles and cell organelles is mediated through both the microtubules and the actin microfilaments [230]. In order to explore the role of these cytoskeleton assemblies in PS NPs dynamics, nocodazole and latrunculin A were added to the cultures after NP internalization. Nocodazole and latrunculin A interfere with the polymerization of the tubulin and actin cytoskeleton respectively, significantly reducing the transport that they mediate [237, 250]. Effectivity of nocodazole and latrunculin A inhibition was verified by means of immunofluorescence (Figure 2-2). Flow velocities and diffusion values from 5 independent cells were compared to evaluate the effects of nocodazole and latrunculin A (Figure 2-3, Table 2-1). Nocodazole treatment dramatically reduced the motion of the PS NPs when compared to the untreated cells.

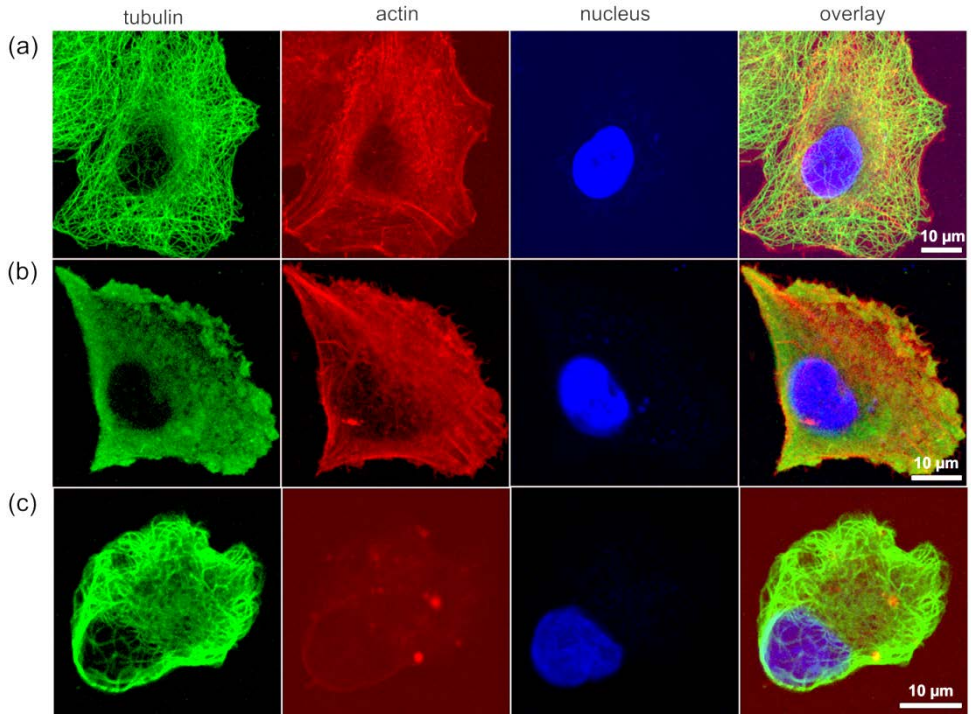

Figure 2-2: Immunofluorescence of tubulin and F-actin cytoskeleton after treatment with cytoskeleton inhibitors: control (a), 20 µM nocodazole (b) and 500 nM latrunculin A (c).

The flow velocity dropped significantly from (9 ± 2)×10^{-3} µm/s to (2.7 ± 0.2)×10^{-3} µm/s (p = 0.0141), whereas the diffusion coefficient decreased significantly from (8 ± 3)×10^{-3} µm²/s to (1.3 ± 0.3)×10^{-3} µm²/s (p-value = 0.029). In contrast, latrunculin A treatment did not affect the velocity ((8 ± 2)×10^{-3} µm/s). The diffusion coefficient was reduced ((2 ± 1)×10^{-3} µm²/s), although this reduction is not significant (p = 0.0543). These findings suggest that the microtubules play a key role in mediating the directed transport of the PS NPs within the cell. Moreover, it indicates that the obtained velocity from STICS represents the activity of the microtubule motors when the PS NPs are transported through the cell [49].

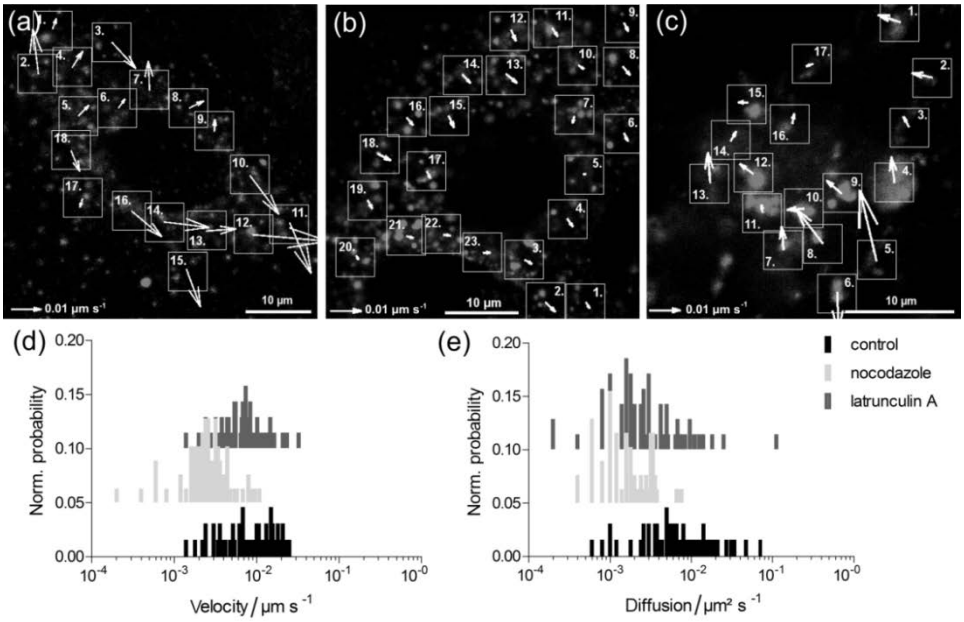

Figure 2-3: The role of the cytoskeleton in the intracellular dynamics of PS NPs transport within A549 cells based on STICS and TICS analyses. Velocity mapping of NP dynamics without treatment (a), and after treatment with 20 µM nocodazole (b) and 500 nM latrunculin A (c). Flow velocities and diffusion coefficients of the presented cells are shown in Table 2-2. (d-e) Frequency distribution histograms of NPs velocity and diffusion coefficient from ROIs of 5 independent cells (expressed as the normalized probability) without (control) and after treatment with cytoskeletal inhibitors.

Table 2-2: Effective flow velocities and diffusion coefficients of PS NPs motions for different regions inside A549 cell without treatment, or treatment with 20 µM nocodazole and 500 nM latrunculin A, as shown in Figure 2-3a-c.

Region	Control		Nocodazole		Latrunculin A	
	V_{STICS} [a] [10^{-3} µm/s]	D_{TICS} [b] [10^{-3} µm²/s]	V_{STICS} [10^{-3} µm/s]	D_{TICS} [10^{-3} µm²/s]	V_{STICS} [10^{-3} µm/s]	D_{TICS} [10^{-3} µm²/s]
1	3.84	0.8	2.3	0.3	7.5	1.0
2	15.0	17.8	4.4	0.5	6.9	1.7
3	11.7	27.3	2.7	0.2	3.8	1.7
4	6.5	18.3	3.1	0.1	8.4	1.1
5	5.1	6.0	8.4	0.1	23.4	9.7
6	3.7	9.4	2.9	1.8	12.6	3.1
7	9.8	21.3	2.2	0.6	7.47	1.8
8	5.3	47.3	3.7	1.6	13.8	2.6
9	4.2	14.1	3.0	0.3	6.4	2.6
10	15.8	18.7	2.1	3.1	5.6	0.7
11	18.2	16.7	3.3	1.9	2.4	1.5
12	24.9	19.5	3.9	1.1	5.3	4.1
13	9.9	5.5	4.6	0.2	9.8	6.7
14	15.0	33.5	3.8	6.7	3.6	4.7
15	13.3	19.9	4.2	2.3	3.2	4.2
16	13.1	34.1	3.1	1.1	3.4	7.6
17	3.0	70.9	2.5	0.1	2.2	1.7
18	7.6	13.0	4.8	0.3		
19			3.1	3.3		
20			1.5	1.3		
21			2.2	0.6		
22			2.1	0.1		
23			2.3	0.3		
Median	9.9	18.5	3.0	0.6	6.4	2.6

[a] Magnitude of flow velocity measured by STICS from velocities in the *x* and *y* plane. Velocities are corrected for stage drift and cell movement.

[b] Diffusion coefficient measured by TICS, considering a fixed flow component as determined by STICS.

In accordance with our findings, nocodazole treatment of cells exposed to quantum dots and polyplexes was shown to abolish the microtubule associated active transport [198, 237, 251], while prevention of the F-actin cytoskeleton polymerization with cytochalasin D did not interfere with the active transport [198]. In order to pursue a more direct interpretation of the diffusion and flow detected in the NP motion, SPT was applied on the same data sets (Figure 2-4).

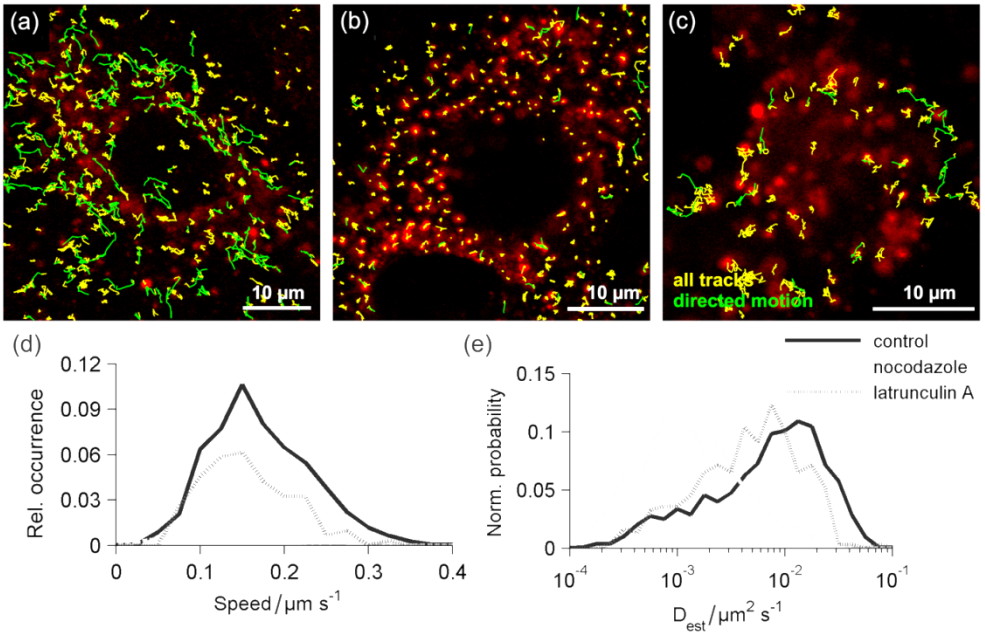

Figure 2-4: Tracking and quantification of PS NP intracellular dynamics and the role of the cytoskeleton in A549 cells using SPT analysis. (a-c) All PS NPs identified tracks (yellow), the identified directed motion sections (green) and PS NPs (red) in cells without treatment (a), or treated with 20 µM nocodazole (b) and 500 nM latrunculin A (c) are displayed. The first image of the time series is presented. (d) The distribution of the speed of NP transport over the sections is shown per treatment. The area under the curve represents the relative contribution of directed motion to the overall PS NPs dynamics in each condition. (e) From each trajectory an estimator of the diffusion coefficient (D_{est}) was determined and the corresponding distribution over all trajectories from each treatment is shown. The normalization is with respect to the total number of trajectories in each condition.

NPs were traced and these traces were analyzed for diffusion and directed motion. Analysis of the MSDs reveals a broad distribution of diffusion coefficient estimators, spanning four orders of magnitude (Figure 2-4e), which is analogous to the distribution of the diffusion coefficient estimators obtained by TICS (Figure 2-3e). This finding suggests anomalous diffusion and/or multiple diffusion modes [42]. Furthermore, compared to the control, the distribution of the diffusion coefficient estimators shows a slight shift for latrunculin A and a large shift for nocodazole treatment towards lower values. This is also reflected in the average diffusion coefficient estimators: control (11 ± 1)×10-3 µm²/s, nocodazole (2.7 ± 0.2)×10-3 µm²/s and latrunculin A (7.0 ± 0.5)×10-3 µm²/s, yielding a significant difference between control and nocodazole ($p = 0.002$) (Table 2-1).

Table 2-3: Parameters of NP motion extracted by SPT analysis. Diffusion parameters were determined by analyzing the MSD in function of time using a linear model *(Eq. 2-8)*. Sections of directed motion were also extracted from the trajectories and individually quantified. Values reported here are averaged over mean parameter values of each cell *(N = 5)* and represented with SEM. The asterix denotes significant differences of treatment compared to control conditions (** p-value < 0.01)

motion type	parameter	A549 cell treatment		
		control	nocodazole	latrunculin A
diffusion	D_{est} [µm²/s] [a]	$(11 \pm 1)\times10^{-3}$	$(2.7 \pm 0.2)\times10^{-3}$ **	$(7.0 \pm 0.5)\times10^{-3}$
	I [%] [b]	8 ± 2	7 ± 1	4 ± 1
directed motion	prevalence [%]	38 ± 4	9 ± 1 **	25 ± 3
	duration [s]	16.4 ± 0.6	15 ± 1	13.4 ± 0.8
	distance [µm]	2.71 ± 0.08	1.9 ± 0.2 **	2.0 ± 0.2 **
	speed [µm/s]	$(169 \pm 7)\times10^{-3}$	$(127 \pm 5)\times10^{-3}$ **	$(150 \pm 10)\times10^{-3}$

[a] Estimated diffusion coefficient by linear least squares fitting of the MSD.

[b] Immobile fraction.

These diffusion coefficients are in the same order of magnitude as the mean values of TICS. However, diffusion is considered to be a thermal process and should thereby be independent of treatment conditions [252-254]. The results of TICS and SPT therefore suggest that the random walk-like behaviour of the NPs is part of an active cellular capture process linked to microtubules and can be attributed to diffusive interphases present in the directed transport. This phenomenon has been described before for the cytoskeletal transport of early endosomes [255, 256]. Disruption of the cytoskeleton can, consequently, impair track switching and therefore contribute to a change in the PS NPs apparent diffusion. The presence of directed motion supports the notion of cellular control over intracellular particle dynamics.

Using trajectory analysis, sections of directed motion could be identified in the particle traces (Figure 2-4a-c). Direct investigation of the trajectories shows that particles often display saltatory motion without any overall directionality [257]. Consistent analysis of all conditions shows that this motion type occurs frequently in control conditions 38 ± 4%, but is strongly abolished under influence of nocodazole 9 ± 1% (p-value < 0.0001) (Table 2-3). The approximate range of the SPT-measured directed motion speed (0.1 µm/s to 0.3 µm/s) under control conditions (Figure 2-4d) is overlapping with results of microtubule-assisted transport speeds of organelles and NPs reported in the literature [251, 258, 259]. Also, values between 0.2 µm/s and 1.5 µm/s have been reported for the active intracellular transport of quantum dots in A549 cells [251]. The *speed* and *distance* of the remaining directed motion under nocodazole conditions is also significantly decreased compared to the control, 0.127 ± 0.005 µm/s *vs* 0.169 ± 0.007 µm/s (p = 0.0013) and 1.9 ± 0.2 µm *vs* 2.71 ± 0.08 µm (p = 0.0011), suggesting less efficient NP transport (Table 2-3). Under latrunculin A influence, the directed motion of the NPs mainly seems to vary as a consequence of cell morphology changes (Figure 2-4e).

This is corroborated by the directed motion *distance* being the only significantly decreased parameter under latrunculin A treatment compared to control, 2.0 ± 0.2 µm *vs* 2.71 ± 0.08 µm ($p = 0.0082$). Latrunculin A induced cell shrinking can be expected to reduce NP transport distance [260].

2.4.2 Colocalization of polystyrene nanoparticles with cell organelles

In order to investigate the accumulation and transport of PS NPs within the early endosomes, late endosomes and lysosomes, the fluorescent signals of the PS NPs were correlated with the signals of, respectively, Early Endosomes-GFP, Late Endosomes-GFP and LysoTracker® Green DND-26. The distribution and localization of PS NPs within the endolysosomal compartment was investigated by static colocalization analyses using Manders' overlap coefficients (Table 2-4, Figure 2-5). The Manders' overlap coefficients M1 and M2 describe the colocalization of PS NPs with the cell organelle of interest [245]. M1 represents the fraction of the labelled organelle containing PS NPs, whereas M2 represents the fraction of PS NPs associated with the labelled organelle. PS NPs were almost equally distributed among the early endosomes (18 ± 2 %), late endosomes (28 ± 3 %) and lysosomes (20 ± 3 %) during the time interval of the experiments.

Table 2-4: Distribution of PS NPs within early endosomes, late endosomes and lysosomes using Manders' overlap coefficients, together with the SEM over N cells. M1 represents the fraction of labelled organelle colocalizing with the PS NPs, whereas M2 represents the fraction of PS NPs colocalizing with the labelled organelle.

	M1	M2	*N*
early endosomes	0.15 ± 0.01	0.18 ± 0.02	29
late endosomes	0.16 ± 0.02	0.28 ± 0.03	21
lysosomes	0.12 ± 0.02	0.20 ± 0.03	18

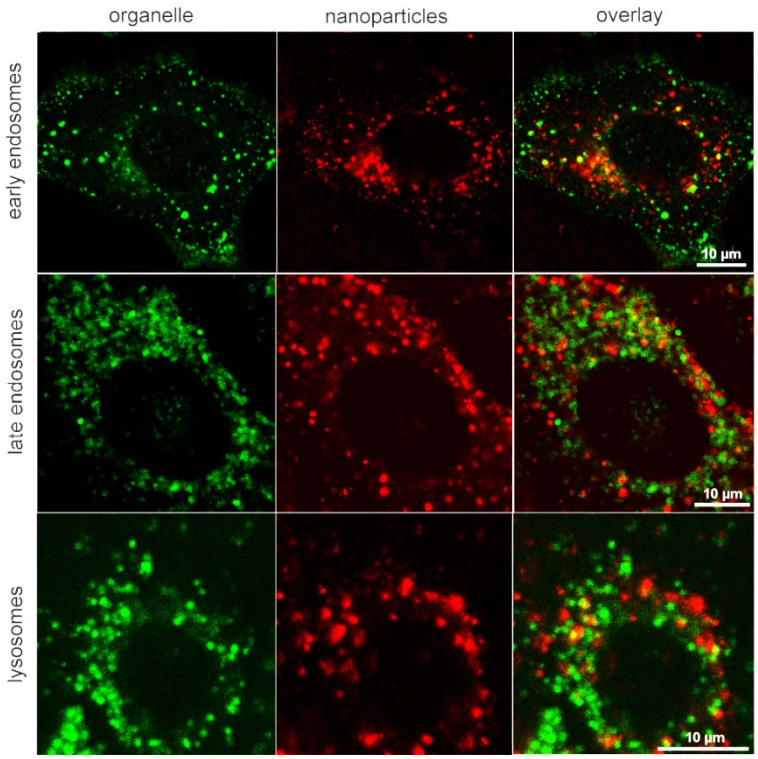

Figure 2-5: Dual-channel image of A549 cells incubated with PS NPs (in red) and labelled for cell organelles (in green): early endosomes, late endosomes and lysosomes. Scalebar: 10 µm.

Conventional static dual-color colocalization imaging has been applied before to study the accumulation of NPs in specific cell organelles [193, 234, 237]. Quantitative analysis often suffers from intrinsic user bias in defining an intensity threshold. STICCS overcomes the limitations of conventional colocalization analyses by analyzing the correlated motion of NPs and cellular organelles. Therefore, the kinetics of potentially correlated motions (dynamic colocalization) of NPs within the endosomes and lysosomes were further explored by STICCS. Although STICCS reveals comigrating complexes, it has to be noted however that this does not indicate whether they are necessarily in direct contact [238].

For each cell organelle type, a typical STICCS analysis is presented in Figure 2-6 with an image from the time-series, the contour plot of the Gaussian cross-correlation peak $G(\xi,\eta,\tau)$ for τ = 0, 20 and 40 seconds, the position of $G(\xi,\eta,\tau)$ peak as a function of time, and the velocity mapping of the cotransport inside the whole cell (values are given in Table 2-5). The Gaussian cross-correlation peak $G(\xi,\eta,\tau)$ for both endosomes and lysosomes is very strong, indicating that correlated motions between the PS NPs and these cell organelles were detected. The peak appears to be mobile as a function of time and broadens by increasing time lags, indicating that the mobile population of PS NPs cotransported with the organelles exhibits a combination of directed movement interspersed with diffusive pauses. Fitting the displacement of $G(\xi,\eta,\tau)$ yields directional flow information of the colocalized PS NPs and the cell organelle of interest (Figure 2-6b-c). The STICCS analyses results show an asymmetric peak, which could be attributed to the spatial distribution of the PS NPs and/or the asymmetric shape of the cell organelles.

STICCS analyses of the complete A549 cell, considering 512 × 512 pixels, labelled with the organelle specific dye and the fluorescently labelled PS NPs were performed. Lysosomes had a significantly higher cotransport velocity ((212 ± 45)×10^{-3} µm/s, N = 18) compared to early endosomes ((52 ± 9)×10^{-3} µm/s, N = 15) and late endosomes ((35 ± 7)×10^{-3} µm/s, N = 15) ($p < 0.0001$). STICS analyses on the organelle population were performed as well. Early endosomes presented V_{STICS} = (6 ± 2)×10^{-3} µm/s), late endosomes V_{STICS} = (4 ± 1)×10^{-3} µm/s) and lysosomes V_{STICS} = (5 ± 1)×10^{-3} µm/s). Compared to literature, the acquired velocities for the PS NPs cotransport with the endosomal transport resemble the average velocity of the early endosomes (approximately 12×10^{-3} µm/s) [261]. On the contrary, others report velocities of early endosomes between approximately 400 – 800×10^{-3} µm/s [262]. Vesicle speed of late endosomes was reported approximately 250×10^{-3} µm/s [263]. The velocities obtained for the PS NPs cotransport with the lysosomes are in close approximation to the reported active transport velocities of the lysosomes approximately 200 – 700×10^{-3} µm/s [264-266]. Correlated flow velocities of PS

NPs together with cell organelles obtained by STICCS are remarkably higher than the velocities obtained for PS NPs and cell organelles with STICS. Similar effects have been observed with biodegradable poly L-lactic acid nanocarriers (~ 200 nm size) also in A549 cells.

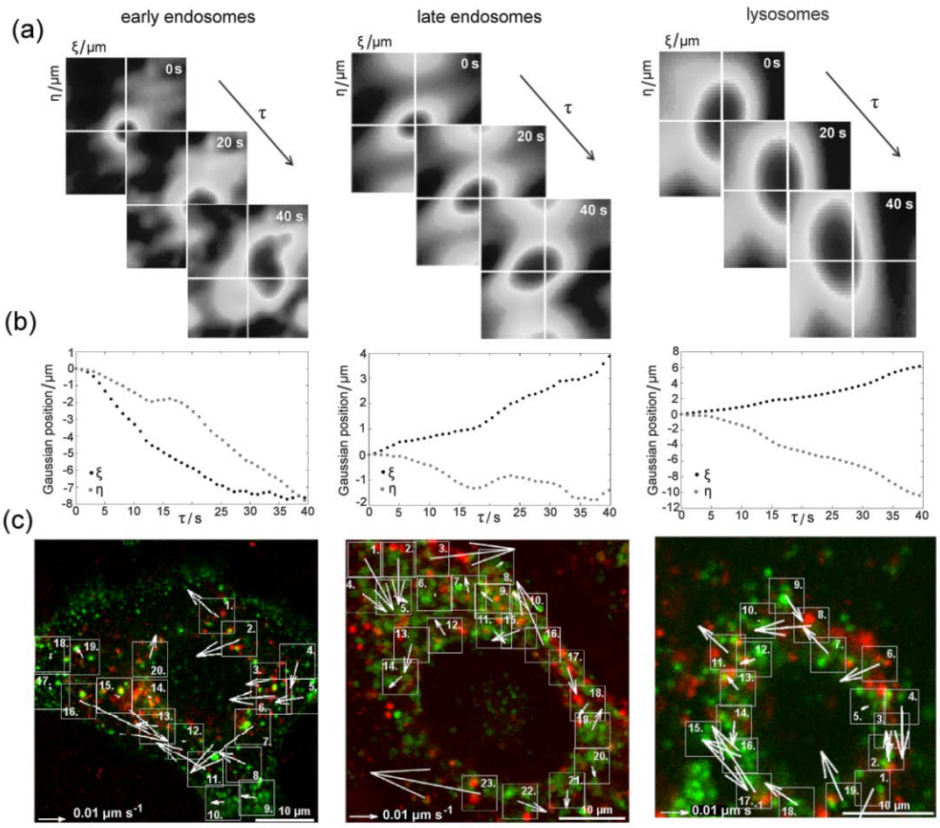

Figure 2-6: STICCS analyses of correlated motions of PS NPs with early endosomes, late endosomes and lysosomes within A549 cells. (a) Contour plot of the cross-correlation peak G (ξ,η,τ) for τ = 0, 20 or 40 s for early endosomes (ROI 16), late endosomes (ROI 17) and lysosomes (ROI 1). (b) Position of G (ξ,η,τ) as a function of τ. (c) Dual-channel time series image with PS NPs (in red) and cell organelle (in green) together with velocity mapping of NP correlated motions (Figure 2-5). Effective flow velocities of the cotransport in all ROIs (numbered boxes) are presented in Table 2-5.

Table 2-5: Effective flow velocities of STICCS analyses for PS NPs in early endosomes, late endosomes and lysosomes, as shown in Figure 2-6.

Region	Early endosomes	Late endosomes	Lysosomes
	V_{STICCS} [a)] [10^{-3} µm/s]	V_{STICCS} [10^{-3} µm/s]	V_{STICCS} [10^{-3} µm/s]
1	148.0	212.1	279.9
2	168.6	166.0	110.2
3	81.7	305.8	94.5
4	93.4	108.2	187.3
5	108.4	54.4	24.2
6	164.0	10.2	153.3
7	288.7	56.6	129.5
8	109.3	28.4	204.4
9	48.3	54.6	109.1
10	44.7	88.8	3.7
11	203.4	58.4	55.4
12	9.3	66.2	140.6
13	83.6	106.4	59.8
14	13.4	60.4	89.1
15	32.0	108.7	238.6
16	371.3	247.5	150.1
17	9.5	102.7	283.6
18	21.1	55.8	150.1
19	40.5	83.6	238.4
20	88.9	39.0	139.9
21		67.1	192.0
22		110.5	
23		400.7	
Median	86.2	83.6	139.9

a) Magnitude of flow velocity measured by STICCS from velocities in the *x* and *y* plane. Velocities are corrected for stage drift and cell movement.

STICS provides the most accurate information on transport dynamics if the process exhibits a unidirectional flow pattern which can be averaged over a sufficient number of particles [236]. If, on the other hand, the organelle mediated transport is not unidirectional, the averaged velocity determined by STICS will underestimate the actual transport velocities. Furthermore, if only the PS NPs associated with the organelles of interest are considered, as achieved through cross-correlation, the averaging effect is reduced. This results in more representative values of the velocity. These values as obtained by STICCS resemble those as recovered by SPT when analysing individual tracks of PS NPs. Therefore, both STICCS and SPT provide reliable information on specific organelle mediated transport of PS NPs. Despite the averaging effect in STICS, both STICS and SPT indicate diminished PS NP dynamics upon nocodazole treatment. This demonstrates the significance of the microtubule cytoskeleton in PS NPs transport.

2.5 Conclusion

Various aspects of the trafficking of NPs inside the cells remain largely unknown. Measuring their intracellular dynamics is considered as a fundamental step in understanding their complex behaviour. In this work, we presented the application of ICS-based techniques and SPT to characterize the directed motion and diffusion characteristics of internalized PS NPs in A549 lung cells. We applied TICS and STICS to characterize the diffusion, and map the flow magnitude and direction of PS NPs inside the cell. STICS and TICS analyses were shown to be a powerful tool for determining the ensemble kinetic behaviour of NPs inside the cell. Moreover, when NPs are not clearly resolved, the employed techniques can reveal information concerning their intracellular movement. In addition, SPT was used in order to retrieve a more direct interpretation of the diffusion and flow detected in NP motion by defining the trajectories of NPs. STICS and SPT in combination with cytoskeleton inhibitors revealed that PS NP directed motions were strongly dependent on microtubule-assisted transport. Moreover, by applying STICCS, we were able to detect the correlated motions of PS NPs with

the early endosomes, late endosomes and lysosomes. Both SPT and STICCS provided information on specific organelle mediated transport of PS NPs in A549 cells. In summary, the combination of ICS-based techniques and SPT can obtain novel insights into the complex behavior of NPs inside biological systems and represents a valuable tool for both nanosafety assessment and nanomedicine.

2.6 Supplementary material

2.6.1 Autocorrelation functions

All variants of image correlation and cross-correlation spectroscopy are based on the analysis of fluorescence fluctuations measured from an observation area defined by the diffraction-limited focal spot of the exciting laser beam in a laser-scanning microscope [235, 236, 242]. The fluctuations of fluorescence intensity, δi, that are recorded in the image series are defined by:

$$\delta i\,(x,y,t) = i(x,y,t) \quad \langle i(x,y,t) \rangle_{XY} \qquad \text{(Eq. 2-10)}$$

where $\langle \ldots \rangle_{XY}$ indicates the spatial averaging of the stack of images; x and y represent the spatial coordinates of the considered pixel, t is the time of the considered image in the time series, and $i(x, y, t)$ denotes the intensity at (x,y) and time t.

Depending on the variant of the applied image correlation technique, the fluctuations can be defined as spatial intensity fluctuations across a given image and/or temporal intensity fluctuations between images taken at different times in a time series stack. The spatial fluctuations reflect the variations in the numbers of static or slowly moving fluorophores distributed in space, whereas the temporal fluctuations arise from dynamic changes in the number of fluorophores at a given spot over time as the fluorescent molecules undergo transport. The dynamics of interest can be investigated by considering the appropriate time scale through the use of a suitable variant of the ICS technique.

TICS was introduced as an alternative to FCS for measuring the magnitude of the diffusion coefficient and/or flow speed of slowly moving particles from an image time series [233, 235-237, 242, 243]. Each pixel location yields an autocorrelation function, which all are averaged to obtain a single temporal autocorrelation function *G (0,0,τ)*:

$$G(0,0,\tau) = \left\langle \frac{\left\langle \delta i(x,y,t)\, \delta i(x,y,t+\tau) \right\rangle_{XY}}{\left\langle i(x,y,t) \right\rangle_{XY} \left\langle i(x,y,t+\tau) \right\rangle_{XY}} \right\rangle_{T} \qquad \text{(Eq. 2-11)}$$

where <…> denotes the averaging of the stack of images in space ($_{XY}$) or time ($_{T}$); and τ represents the time-lag.

In STICS, the spatial information embedded in the two-dimensional spatial correlations is combined with the time-dependent transport measured by the temporal correlation. $G(\xi,\eta,\tau)$ represents the average correlation function for all pairs of images separated by the time lag τ [235, 236, 242]:

$$G(\xi,\eta,\tau) = \left\langle \frac{\left\langle \delta i(x,y,t)\, \delta i(x+\xi,y+\eta,t+\tau) \right\rangle_{XY}}{\left\langle i(x,y,t) \right\rangle_{XY} \left\langle i(x+\xi,y+\eta,t+\tau) \right\rangle_{XY}} \right\rangle_{T} \qquad \text{(Eq. 2-12)}$$

with ξ and η the spatial lag variables in x and y, respectively.

STICCS requires the image time series in space and time from two fluorescence detection channels, a from the NPs and b from labelling of the cell organelle. An adapted version of G(ξ,η,τ) shown in is used for the cross-correlation function[233]:

$$G_{ab}(\xi,\eta,\tau) = \left\langle \frac{\left\langle \delta i_a(x,y,t)\, \delta i_b(x+\xi,y+\eta,t+\tau) \right\rangle_{XY}}{\left\langle i_a(x,y,t) \right\rangle_{XY} \left\langle i_b(x+\xi,y+\eta,t+\tau) \right\rangle_{XY}} \right\rangle_{T} \qquad \text{(Eq. 2-13)}$$

3 Intracellular localization and dynamics of Hypericin loaded PLLA nanocarriers by image correlation spectroscopy

This chapter is based on:

Intracellular localization and dynamics of Hypericin loaded PLLA nanocarriers by image correlation spectroscopy.

Rozhin Penjweini, Sarah Deville, Lien D'Olieslaeger, Mandy Berden, Marcel Ameloot, Anitha Ethirajan

Journal of Controlled Release 2015
Volume 218, Pages 82-93
doi: 10.1016/j.jconrel.2015.09.064

Declaration of contribution: Sarah Deville performed the cell preparations, cell exposure and leakage experiments. She was involved in the data acquisition and data analysis of cell organelle dynamics and reviewing of the manuscript.

3.1 Abstract

The study of cell-NP interactions is an important aspect for understanding drug delivery using nanocarriers. In this regard, advances in fluorescence based microscopy are useful for the investigation of temporal and spatial behaviour of NPs within the intracellular environment. In this work, we focus on the delivery of the naturally-occurring hydrophobic photosensitizer Hypericin in human lung carcinoma A549 cells by using biodegradable PLLA NPs. For the first time, Hypericin containing NPs are prepared by combining the miniemulsion technique with the solvent evaporation method. This approach yields an efficient loading of the NPs with Hypericin and allows for additional cargo molecules. To monitor the release of Hypericin from the NPs, an additional fluorescent lipophilic dye Coumarin-6 is incorporated in the NPs. TICS and STICS are used to determine the fate of the NPs carrying the potential cargo. Both directed and non-directed motions are detected. By using ICCS and specific fluorescent labelling of endosomes, lysosomes and mitochondria, the dynamics of the cargo loaded NPs in association with the organelles is studied.

3.2 Introduction

Engineered NPs create a coherent interest to develop nanomaterials for biomedical applications such as imaging, diagnostics and therapeutics [267, 268]. Theranostic nanomedicine takes advantage of the high capacity of nanosystems to carry loads like imaging and therapeutic agents [269]. The theranostic nanocarriers capable of diagnosis and therapy have the potential to revolutionize the drug development process and change the landscape of the pharmaceutical industry [267-270]. They can travel through complex biological environments full of steric and adhesive obstacles and increase the selective drug delivery [270]. However, the therapeutic efficacy and intracellular behaviour of NPs depend primarily on how they interface to biomolecules and their surroundings [212, 271, 272]. NPs interact not only passively with cells but also actively modulate the molecular processes that are essential for regulating cell functions [231, 271]. These perturbed activities may or may not, late in

time, reveal to be stressful for the cells. Understanding NPs-bio-interactions requires knowledge about the dynamic behaviour of nanomaterials during their cellular uptake, intracellular traffic, mutual reactions with cell organelles, fate of nanomaterials and respective cellular end points [193, 206, 209, 212, 231, 237, 272-275]. The nanocarrier pharmacology at the microscale can shed light on the uptake mechanisms and intracellular trafficking of the nanocarriers [210, 276]. As intracellular location and interactions of NPs correlate with their characteristics [277, 278], every (new) nanomaterial has to be tested separately [212, 231]. In this regard, fluorescence based techniques, proteomics mass spectrometry and pH-reporting (in the physiological range of 5.0–7.4) nanosensors provide insights on the NPs uptake mechanisms and intracellular trafficking [210, 232, 233, 236, 241, 242, 279-281]. Recently, combination of complimentary techniques such as mass spectrometry and imaging analysis has been used to shed valuable insight on the intracellular trafficking of NPs [210, 279].

Photodynamic therapy and diagnosis (PDT and PDD) are currently undergoing intensive clinical investigations as adjuvant treatment for oncological diseases [282-286]. PDT is based on the use of photochemical reactions mediated through an interaction between a photosensitizer, photoexcitation at a characteristic wavelengths of light and production of ROS [282-284, 287-289]. Studies have also shown that PDD enhances the visual contrast between benign and malignant tissue because of selective emission of fluorescence from the cancer cells [285, 286]. Hypericin is a naturally-occurring, potent photosensitizer with several advantages over common photosensitizers, such as a broad excitation spectrum in the visible region, a high quantum yield of fluorescence and singlet oxygen generation upon photoexcitation, good photostability and a relatively low dark toxicity [282-284]. However, bioavailability is limited by its hydrophobic nature [282-284]. The efficacy of PLLA NPs to carry Hypericin (henceforth PLLA-Hyp NPs) for the benefit of improving PDD and PDT of ovarian cancer has been reported [284]. PLLA has been approved by U.S. Food and Drug Administration (FDA) for clinical use [290] due to its unique properties such as established safety, and

biocompatibility suitable for drug delivery applications [277, 278]. PLLA being an ester can be degraded in an acidic environment as well as by enzymes such as esterases. The various cellular components maintain their own characteristic pH values ranging from 4.5 in the lysosome to about 8 in the mitochondria [231, 280, 281]. Therefore, the inherent pH conditions in addition to the presence of enzymes has influence on the degradation of the PLLA-Hyp NPs within the cells. Some studies have shown that PLLA-Hyp NPs exhibit cancer selective targeting, enhanced reduction of cancer cell viability together with no significant reduction in viability of normal cells [277, 278, 284, 291, 292].

Although PLLA NPs have been previously well investigated for the medical applications, more attention has to be devoted specifically to understand their intracellular dynamics [231, 293, 294]. The goal of the present study is to investigate the intracellular dynamics and localization of PLLA-Hyp NPs in living human lung carcinoma A549 cells. To the best of our knowledge, no other attempts to study this aspect have been reported and for the first time different variants of ICS [233, 241, 243] will be used for this NP platform.

ICS is a fluorescence based microscopic technique most appropriate for the study of biomolecular interactions and the measurement of molecular diffusion and directed transport (flow) on time scales ranging from microseconds to milliseconds [232-234, 241]. Whereas FCS is based on the temporal fluctuations at a single spot, ICS also utilizes the spatial information within a significant, homogeneous area of the specimen [233, 235, 236, 243, 295]. ICS allows for relatively slow intracellular dynamics as compared to FCS [233, 296], and to determine the flow and diffusion of small particles at a higher density as compared to SPT [210]. ICS implementations are subdivided according to whether fluorescence fluctuation information in space and/or time is analysed within the image series. TICS involves the correlation analysis of the fluorescence fluctuations in time recorded in the pixels of an image time series allowing for the determination of diffusion related processes [209, 235, 237, 243]. ICS extended for STICS correlates fluorescence fluctuations in space and time. STICS depends on both diffusion and flow directions of fluorescently

tagged macromolecules or particles enabling the mapping of the velocity vectors [208, 236, 238].

The intracellular trafficking of NPs and their association with cell organelles is essential for understanding the dynamics of the intracellular drug delivery process. Therefore, the intracellular motions of PLLA-Hyp NPs and released Hypericin in association with individual early endosomes, late endosomes, lysosomes, mitochondria and nucleus contents are explored. To assess the dynamics of the associated motions of the loaded NPs and organelles, STICS is used via cross-correlation analyses (STICCS) of two fluorescence detection channels [236, 242].

The fluorescence lifetime is highly dependent on the surrounding microenvironment and can therefore report on local interactions of the fluorophores [297]. The fluorescence lifetime is independent of concentration and artifacts such as photobleaching. In FLIM a map of the fluorescence lifetime over space is obtained [298]. FLIM experiments have been reported for Hypericin in pharmaceutical preparations [297]. Although the aim of the present study is not to elaborate on the phototoxicity of the Hypericin itself but to study the dynamics of the NPs carrying the Hypericin, we use FLIM in this work as a tool to monitor Hypericin release from the NPs.

To monitor the degradation of the PLLA-Hyp NPs and subsequent release of Hypericin, a suitable control dye that can be co-localized at the beginning of the observations is required. To achieve the aforementioned goal, a careful design of nanocarrier with mono- and dual-labelling is crucial; here dual-labelled particles allow for the co-localization of Hypericin and the control dye. Previously, PLLA-Hyp particles were prepared by nanoprecipitation method, where, despite small Hypericin loading, low entrapment efficiency was reported [284]. For the present study, sufficiently high loading of dyes with decent encapsulation efficiency and homogeneous distribution of dye in the particle dispersion (especially considering dual-labelling options) are required. Therefore, to overcome the aforementioned challenges, in this work labelled polymer particles are prepared by combining the versatile miniemulsion technique with the emulsion/solvent

evaporation method [299-301]. This procedure allows for reliable entrapment of the different hydrophobic dyes in case of both mono- and dual-labelled particles. It is worth to note that such a dual-labelled NP design containing therapeutic Hypericin has not been envisaged before. In this work, the green-fluorescent lipophilic dye Coumarin-6 was chosen as a control. Although, this dye has been used as a drug model before [299-301], in here, the inclusion of the dye is only to mark the onset of the Hypericin release as it can be discriminated spectrally from Hypericin.

As lung cancer is the leading cause of cancer-related mortality worldwide and patients with this cancer have a poor five-year survival rate less than 20% [302], the human lung cancer carcinoma A549 cell line was employed here. The latter serves as a good model cell line, as translational research can be relied upon for the diagnostic and therapy of lung cancer [302, 303]. Moreover, as A549 cells are adherent and flat, they are suitable cells for imaging [303].

3.3 Materials and methods

3.3.1 Materials

The anionic surfactant sodium dodecyl sulphate (SDS) was purchased from Merck. PLLA (Mw = 101,700 g/mol, inherent viscosity: 1.0 dl/g) was delivered by Sigma Aldrich. Chloroform ($CHCl_3$) was bought from AnalaR NORMAPUR. Hypericin was obtained from HWI analytic GMBH pharma solutions and Coumarin-6 from Sigma Aldrich. PVP (Mw = 40,000 g/mol) was delivered by Sigma-Aldrich Corporation. The Amicon ultra filter membrane tubes, which are used for washing the NPs, were acquired from Millipore. Milli-Q water was used for the sample preparation. The transmission electron microscopy (TEM) grids were bought from Electron Microscopy Science.

For the cell preparation, MEM and P/S were purchased from Gibco, Paisley, UK. FBS was obtained from Biochrom AG, Germany. µ-Slide 8 well petridishes were bought from Ibidi GmbH, Martinsried, Germany. Organelle specific dyes, Early Endosomes (Rab5a –GFP) and Late Endosomes (Rab7a –GFP) (CellLight®

Reagents, BacMam 2.0), LysoTracker® Green DND-22 and MitoTracker® Green FM were purchased from Molecular Probes. Hoechst 33442 and nocodazole were delivered by Sigma-Aldrich Corporation.

3.3.2 Nanoparticle characterization methods

The solid content of the samples were determined thermogravimetrically. The size and size distribution of all NPs were characterized by DLS using a Brookhaven Instruments ZetaPALS. The morphology of the NPs was imaged using a TECNAI spirit TEM of FEI operating at an accelerating voltage of 120 kV. The sample was prepared by air drying the diluted sample in water on a carbon-coated copper grid. The absorption spectra of the NPs was measured using the Agilent Cary500 Scan UV-Vis-NIR spectrophotometer. The emission spectrum of the NPs was obtained using the Horiba-JobinYvon FluoroLog-3 spectrofluorometer. The optical spectra were measured from the NP dispersions of known solid content in order to determine the amount of encapsulated dye (see Table 3-3, Table 3-4, Figure 3-5 and Figure 3-6 in *3.6 Supplementary information*).

3.3.3 Synthesis of nanoparticles

Polymer particles were prepared by combining the miniemulsion technique with the emulsion/solvent evaporation method. PLLA and hydrophobic fluorescent dye(s) were dissolved in $CHCl_3$ (5g) and mixed with an aqueous surfactant solution. After stirring for 1-h, the miniemulsion was prepared by ultrasonication under ice cooling for 180s (30s pulse, 10s pause) at 65% using a (Branson Mylar) 1/4" tip. The miniemulsion was transferred to a round bottom flask with a wide neck and heated at 40°C for 4-h. The excess surfactant in the samples was removed by multiple washing steps using Milipore membrane tubes. To remove unencapsulated dye, washing with ethanol solution was carried out by centrifugation (10,000 rpm, 30 min) and redispersion of the pellet. After the final washing step, the particles were redispersed in Milli-Q water with the final solid content about 1-1.3%. The washed samples were characterized using DLS,

TEM and optical spectroscopy (detailed properties of the NPs in *3.6 Supplementary information*).

3.3.4 Cell preparation

A549 cells were maintained in MEM supplemented with 10% non-heat inactivated FBS and 1% P/S. One day before the experiments, the cells were plated in µ-Slide 8 well with a density of 5×10^4 cells/chamber at 37°C and 5% CO_2.

3.3.5 Intracellular nanoparticle distribution

Freshly prepared PLLA-based NPs were diluted in CCM at a final concentration of 130 µg/ml. Then, the cells were incubated for 1-h with the NPs solution in a standard incubator (SANYO CO_2 incubator MCO-18AIC(UV), Massachusetts, USA) at 37°C and 5% CO_2. The staining was stopped by washing three times with phosphate buffered saline (PBS) and finally the cells were maintained in the culture medium with 10% FBS.

For STICCS, several organelles were additionally labelled by staining with organelle specific dyes diluted in complete culture medium: lysosomes with 5µM LysoTracker® Green DND-22 for 30 min, mitochondria with 200 nM MitoTracker® Green FM for 20 min and nucleus with 1µg/ml Hoechst 33442 for 10 min. Cells were transduced with 25 particles per cell Rab5a- or Rab7a- GFP 24-h prior to the imaging experiments. The transduction uses an insect cell virus (baculovirus) containing fusions construct of Rab5a and GFP or Rab7a and GFP coupled with a mammalian promoter for visualization of the early and late endosomes, respectively. Transgenes under the mammalian promoter are expressed, while baculoviral genes and their promoters are not recognized. After labelling, the cells were washed several times by PBS maintained at 37°C and then incubated in the culture medium. Using these dyes, the behavior of labelled organells can be studied in living cells independently of organelle pH and label with multiple tracking or tracing dyes to image dynamic cellular processes.

3.3.6 Incubation of the cells with Hypericin

Hypericin was solved in water by the formulation of the photosensitizer with PVP, in a ratio of 1:100 [210, 304, 305]. The photosensitizer was diluted in CCM at a final concentration of 10 μM. Then, the cells were incubated for 20 min with the photosensitizer solution at 37°C and 5% CO_2.

3.3.7 Inhibiting microtubules directed motion

After 1-h incubation of A549 cells with PLLA-Hyp NPs, the cells were exposed to nocodazole at a final concentration of 25 μM in culture medium for a duration of 30 min. Different drug concentrations and incubation times have been tested and explored to find this appropriate protocol [306]. Prolonged incubation of the cells with higher concentration of nocodazole resulted in cell death by apoptosis.

3.3.8 Imaging setup

For ICS and FLIM, various image series were acquired with a commercial Zeiss LSM 510 Meta CLSM (Jena, Germany) on an inverted epifluorescence Axiovert 200M motorized frame equipped with a LD C-Apochromat 40×/1.1 W Corr UV-VIS-IR water immersion objective. During the live cell imaging, to provide an environment that is non-perturbing and suitable for the metabolism and growth of the cells, a chamber (Tempcontrol 37-2 digital, PeCon, Erbach, Germany) was fitted to the microscope, with temperature (37°C) and 5% CO_2 control. For imaging of the PLLA-based NPs, GFP-labelled early and late endosomes (i.e. fluorescently tagged Rab proteins) as well as labelled mitochondria and lysosomes, the microscope was coupled to a 30 mW air-cooled argon ion laser emitting at 488 nm under the control of an acousto-optic modulator (~3 μW maximum radiant power at the sample position). The laser light was directed to the sample using a dichroic mirror and beam splitters NFT 545 and HFT UV/488/543/633. For detection and separation of the different emitted fluorescence signals, three band-pass filters BP 650-710 IR and BP 565-615 IR (for Hypericin) as well as BP 500-550 IR (for Coumarin-6 and organelle specific dyes) were used. The filter selection avoided bleed-through artifacts (see Figure 3-11 in *3.6 Supplementary information*). In all cases, point detection was

achieved using one or two analog PMTs (proprietary Zeiss information). The images (512×512 pixels) of each series were collected with no time delays between the sequential frames. The individual frames were acquired with the pixel size of 0.1 µm and pixel dwell times of 1.6 and 2.5 µs. Fluorescence photobleaching and cytotoxicity (due to the ROS) of Hypericin limited the maximum continuous observation of the healthy cells to 250 frames.

A femtosecond pulsed titanium-sapphire laser (MaiTai DeepSee, Spectra-Physics, Irvine, California, USA) tuned at an output wavelength of 730 nm and ~0.6 mW radiant power at the sample position was used for two-photon excitation of Hoechst and FLIM. The images of the cells stained with Hoechst were collected with the identical dichroic mirror and beam splitters as used for ICS and a band-pass filter BP 390-465 IR. The images of the cells stained with PLLA-Cou-Hyp NPs and Hoechst, shown in Figure 3-1, were taken each 20 min; the overall acquisition time per each image was about 1-1.6 s. In FLIM, the emission light was detected using non-descanned detection: the fluorescence was directed using a dichroic mirror KP650, a short-pass KP685 and a band-pass BP565-615 IR towards a PMT (Hamamatsu 7422, Herrsching am Ammersee, Germany). This PMT was connected to an SPC830 card (Becker and Hickl, Berlin, Germany) synchronized by the scan pulses from the CLSM (12.5 ns laser repetition time). The image series for FLIM were collected each 15 min and the overall acquisition time per each image series was 1000 s (dead time 150 ns). The resulting images have a 512×512 pixel resolution, a pixel size of 0.3 µm, and a pixel dwell time of 51.2 µs (Figure 3-9 and Figure 3-10 in *3.6 Supplementary information*).

The light exposure time in TLCM (about 1-1.6 s acquisition time for each image taken every 20 min in Figure 3-1) was substantially lower than in FLIM (1000 s acquisition time for each image series taken every 15 min). Therefore, there was no indication of the morphological changes of the cells due to the cytotoxicity even after 4 h TLCM while the changes were very pronounced in FLIM after 120 min (*Figure 3-9 in Supplementary information*).

3.3.9 Image correlation spectroscopy

The intracellular dynamics of the NPs and cell organelles in the x,y-plane perpendicular to the microscope stage was investigated by using TICS, STICS and STICCS. The analyses were performed using custom written MATLAB (The MathWorks, The Netherlands) routines, which have been published previously by Wiseman Research Group, McGill University [233, 235, 236, 242, 243, 307].

3.3.10 Correction for cell movement and stage drift

All the flow velocities presented in this paper are corrected for the stage drift and cell movement. For each individual cell, STICS analysis was performed on the whole cell itself, which yields $|v_x|$ = (2.2± 0.2)×10^{-3} µm/s and $|v_y|$ = (2.3 ± 0.2)×10^{-3} µm/s. These values, which take the motions of the cell and the stage into account are reported as mean ± SEM for 72 cells. The stage drift, assessed by applying the STICS analysis to fixed beads (Invitrogen, PS-Speck Microscope Point Source Kit, nominal diameter 175 nm) on a cover slip with the same environment and set-up as in the actual experiments, gives $|v_x|$ = (1.5± 0.1)×10^{-3}µm/s and $|v_y|$ = (4.2 ± 0.5)×10^{-4} µm/s; SEM is calculated from the results of 20 measurements.

3.3.11 Co-localization analysis

To investigate the integrity of NPs and penetration of the released Hypericin within the nucleus, co-localization analyses were performed on fluorescence images of PLLA-Cou-Hyp NPs and Hoechst in A549 cells by using a freely available JACoP toolbox [246] under ImageJ. For the co-localization analyses of the images A_i and B_i, Manders' coefficients $M_{A\text{-}B}$ were defined as follows [245, 246, 308]:

$$M_1 = \frac{\sum_i A_{i,coloc}}{\sum_i A_i} \qquad \text{(Eq. 3-1)}$$

where $A_{i,coloc} = A_i$ if $B_i > 0$ and $A_{i,coloc} = 0$ if $B_i = 0$.

M-values are ranging from 0 to 1, the former corresponding to non-overlapping images and the latter reflecting absolute co-localization between both images.

M-values do not depend on the instrumental amplifier settings or labelling densities [245, 246, 308].

3.3.12 Statistical analysis

To assess the consistency of the results of STICS and TICS, flow and diffusion values of the NPs and cell organelles were compared in five cells by using Kruskal-Wallis tests; 22 regions of interest were considered for each cell (see Table 3-6 and Table 3-7 in *3.6 Supplementary information*). Mann-Whitney tests were also used to evaluate whether the flow velocity in each two independent groups of samples, with and without NPs or nocodazole treatments (all possible pair-wise combinations), are significantly different from each other. Analyses were carried out using the SPSS 14.0 software. Statistical significance was defined at $p < 0.05$ level (95% confidence level).

3.4 Results and discussion

Mono-labelled PLLA NPs containing Hypericin (PLLA-Hyp) or Coumarin-6 (PLLA-Cou) and dual-labelled particles containing both dyes (PLLA-Cou-Hyp) were synthesized and washed thoroughly to remove any surface bound dye. The washed particles were systematically characterized for their size, size distribution, morphology, dye entrapment efficiency and optical properties (Table 3-3, Table 3-4, Figure 3-5 and Figure 3-6 in *3.6 Supplementary information*).

To minimize the NPs degradation within A549 cells before the start of the ICS measurements and at the same time to strike a balance between a decent signal to noise ratio in the fluorescence intensity and a sufficient cellular uptake of NPs, different concentrations of the freshly prepared NPs and incubation times have been explored. Among different protocols, incubation of the cells with 130 µg/ml NPs in CCM for 1 h at 37°C have been chosen as the optimum conditions for time-lapse fluorescence confocal microscopy (TLCM) and FLIM experiments. The time point after the subsequent washing steps is taken to be time zero in reporting the experimental results. The non-cytotoxicity of PLLA-Hyp NPs in

darkness for the used concentrations were confirmed by using an MTS assay (3-(4,5-dimethylthiazol-2-yl)-5-(3-carboxymethoxyphenyl)-2-(4-sulfophenyl)-2H-tetrazolium) (Figure 3-7 in *3.6 Supplementary information*).

As release of Hypericin is foreseen due to the biodegradability of PLLA NPs within the cellular environment, the dual-labelled NPs (PLLA-Cou-Hyp) containing the control dye Coumarin-6 was used to study the integrity of NPs and the release of Hypericin via co-localization of the respective fluorescence signals. It has been previously reported that with non-covalently labelled hydrophobic fluorescent dye, the NPs carrying the dye on brief interaction with the phospholipid bilayer of cells and vesicles releases the hydrophobic dye by a kiss-and-run mechanism [246, 309]. In light of this, in our study, the leakage of the used hydrophobic dyes from the NPs on contact with lipophilic surrounding was tested using lipid microbubbles as model system. The data related to this study is presented in the supporting information (Figure 3-8 in *3.6 Supplementary information*). It was found that the washing procedures used during the synthesis of the NPs ensured that there was no leakage from the NPs on contact with the lipophilic surrounding. Therefore, in the present study, as the particles were washed to remove the surface bound dyes, both dyes are presumably buried underneath the surface of the particles as long as the PLLA particles are intact. Within the cellular environment, the exposure of the dyes to the outside environment of the NPs is dictated by the degradation ability of the polymer particle itself. The escaping tendency of the dyes into the environment is associated with the physicochemical properties of the respective dyes.

Image series using TLCM were acquired in three different channels: green fluorescence (λ_{em}= 494nm) of Coumarin-6, red fluorescence (λ_{em}= 590nm) of Hypericin, blue emission (λ_{em}= 486nm) of Hoechst (a cell-permeant nuclear counterstain that emits blue fluorescence when bound to DNA [310]). The green and red channels and the overlay of the three channels are presented in Figure 3-1A. It can be seen that the Coumarin-6 signal decreases over time whereas the Hypericin signals intensifies.

It is worth noting that the Coumarin-6 fluorescence of the NPs outside the cells and attached to the surface of the cell chamber indicate that the disappearance of the Coumarin-6 emission is not due to the photobleaching. On the one hand, it has been shown previously that the emission of Coumarin-6 entrapped in liposomal nanocarriers disappears -360 minutes after the administration into the retina- due to the disintegration of the NPs structure; however, disappearance of the fluorescence due to the photobleaching has not been reported [311, 312]. The observed variation in fluorescence intensity can well be due to a change in environment upon degradation of the PLLA NPs. A substantial drop in fluorescence quantum yield of Coumarin-6 when going from pure ethanol to aqueous ethanol solutions or upon complexation with poly (methacrylic) acid in its hypercoiled form has been reported [57].

The time evolution of Hypericin fluorescence can be rationalized by relying on the following observations. It is known that Hypericin can form non-fluorescent aggregates in water [210, 313, 314]. Interaction with proteins leads to the dissociation of the aggregates into fluorescent monomers [315, 316]. The initial low Hypericin fluorescence might indicate that a fraction of the PLLA NPs contains Hypericin aggregates. Upon degradation of the NPs, Hypericin aggregates can associate with macromolecules yielding fluorescent monomers. Hypericin is well retained in the cell. This is also in agreement with the previous studies where it has been shown that 24-h after the administration of Hypericin, the tumours still exhibit bright red fluorescence after excitation [315]. It is reported that free Hypericin interacts with DNA [210, 313], while the PLLA NPs are not able to enter the cell nuclei [293].

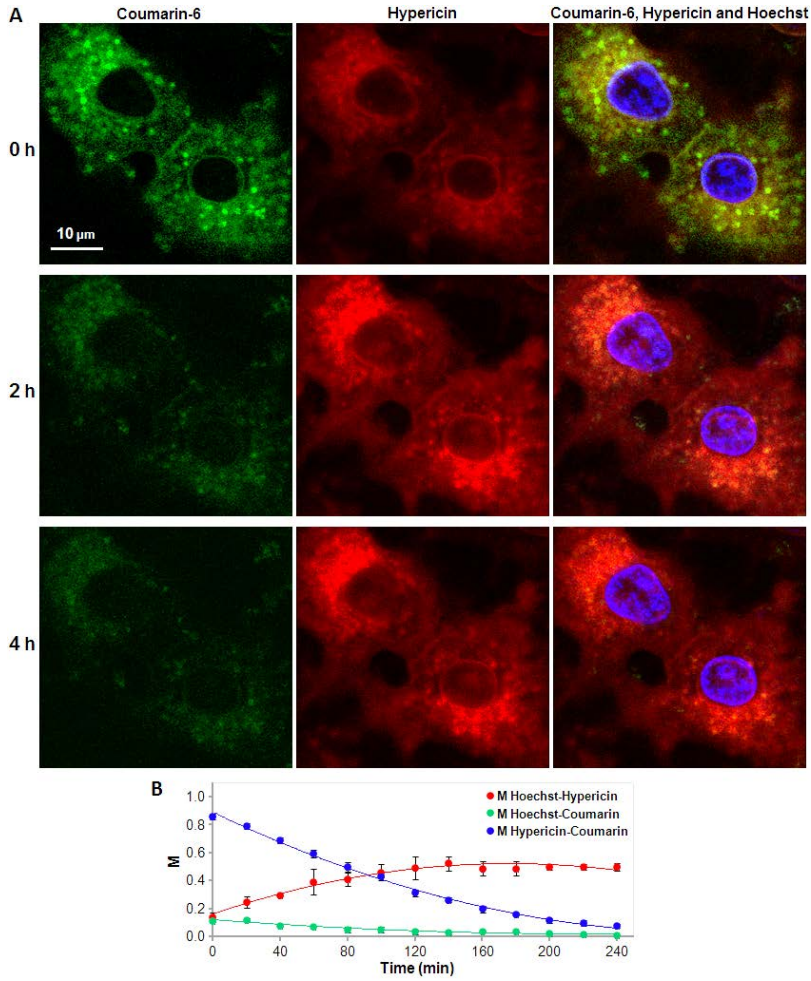

Figure 3-1: (a) Fluorescence time-lapse imaging of A549 cells stained with PLLA-Cou-Hyp NPs and Hoechst. The end of the incubation period is indicated by t = 0. (b) The co-localization analyses based on the calculation of the Manders' overlap coefficients (M): Hoechst-Hypericin ($M_{Hoechst\text{-}Hypericin}$), Hoechst-Coumarin ($M_{Hoechst\text{-}Coumarin}$) and Hypericin-Coumarin ($M_{Hypericin\text{-}Coumarin}$). To minimize fluorescence photobleaching and cytotoxicity, images were collected with 20 min time delay between the sequential frames. Individual frames were recorded with the pixel dwell time of 1.6 µs. The experiments were repeated for five cells and error bars represent the SEM. Error bars are smaller than the symbol for $M_{Hoechst\text{-}Coumarin}$.

The changes in the mutual co-localization of Hypericin and Coumarin, and their location at the nucleus through the overlap with the Hoechst dye can be quantified by Manders' overlap coefficients, M [246, 308]. $M_{Hypericin\text{-}Coumarin}$ is used to study the proportion of the Hypericin (red) pixels coincident with Coumarin (green) pixels (Figure 3-1A). The fractions of pixels related to the nucleus (blue) co-localized with Hypericin and Coumarin-6 are, respectively, given by $M_{Hoechst\text{-}Hypericin}$ and $M_{Hoechst\text{-}Coumarin}$. The time evolution of these Manders' coefficients is shown in Figure 3-1B. Given the small size of the PLLA NPs and the limited resolution of the optical system one can expect that the $M_{Hypericin\text{-}Coumarin}$ coefficient will take high values at the end of the incubation period, denoted as t = 0. Assuming that all PLLA NPs contain both Hypericin and Coumarin-6 a value near unity could be expected. However, some fast degradation of the PLLA NPs during the incubation cannot be excluded. This explains the somewhat lower value of $M_{Hypericin\text{-}Coumarin}$ and the non-zero value of $M_{Hoechst\text{-}Hypericin}$ and $M_{Hoechst\text{-}Coumarin}$ immediately after the incubation period, with the latter being essentially equal.

The decrease of $M_{Hypericin\text{-}Coumarin}$ over time is indicative of the separation of the dyes and the disintegration of the PLLA-NPs. The value of $M_{Hoechst\text{-}Hypericin}$ increases with time and reaches a plateau value of about 0.5 around two hours after the incubation period. The initial $M_{Hoechst\text{-}Coumarin}$ value is rather low 0.1 and decreases over time suggesting an increase in average distance between nuclear components and the free Coumarin-6 dye. These findings are in accordance with the observation that free Coumarin-6 does not enter the nucleus and can only be found perinuclear [299-301].

The fluorescence lifetime of Hypericin is sensitive to its environment [297, 298, 317, 318]. We applied FLIM as a tool to monitor the degradation of the PLLA NPs over time through the changes of the fluorescence lifetime of Hypericin (see *3.6 Supplementary information* for more detail). The time-resolved fluorescence decays of Hypericin are multi-exponential in each condition. The average fluorescence lifetime τ_M of Hypericin in intact NPs in medium is 3.4 ns. Essentially the same value is obtained immediately after incubation (τ_M = 3.6 ns).

Thereafter, τ_M decreases and reaches the value of 2.1 ns after 90 min. This value is also obtained when A549 cells are directly loaded with Hypericin (τ_M = 1.9 ns). At longer incubation times τ_M remains essentially constant at this value (Table 3-5 in *3.6 Supplementary information*).Therefore, it can be stated that the results obtained by TLCM and FLIM are in mutual agreement in describing the time evolution of the release of Hypericin associated with the degradation of the PLLA NPs. As no substantial release of Hypericin was observed within the first 15 min (τ_M ranges from 3.4-3.6 ns), no significant degradation of the PLLA NPs is expected within the first 15 min after incubation.

The dynamics of the essentially intact PLLA NPs in the cells has been investigated by ICS based methods within these first 15 minutes. The intracellular non-directed and possible directed transport of PLLA-Hyp NPs were studied by using TICS and STICS. Image subsections with the immobile population removed were selected from different regions of the cells. In all selected regions, the STACF $r(\xi,\eta,\tau)$ broaden and move with time, indicating diffusive and guided motion, respectively [231]. The symbols ξ and η represent the spatial lag variables in x and y directions respectively and τ the time lag in the STACF $r(\xi,\eta,\tau)$.

Fitting for the displacement of the Gaussian peaks of $r(\xi,\eta,\tau)$ yields flow vectors of the NPs with magnitudes and directions presented in Figure 3-2A (left image). The directed movements of the NPs, whether free or associated with cell organelles, can be related to microtubules, actions of the proteins such as Rab family of small GTPases, motor proteins such as myosin, intracellular contraction systems and differences of the viscosity among cytoplasmic regions [217, 319, 320]. In order to evaluate the microtubules role in the flow of organelles we exposed the cells to nocodazole, an anti-neoplastic agent that interferes with the polymerization of microtubules [320, 321]. As shown in Figure 3-2A (right image) the application of nocodazole results in a substantially different distribution of the NPs and a strong reduction of the flow.

It has been reported that microtubules are involved in the endocytic process, and thus nocodazole as a microtubule disruptor, affected NPs internalization by the panel of cells [27, 319, 320].

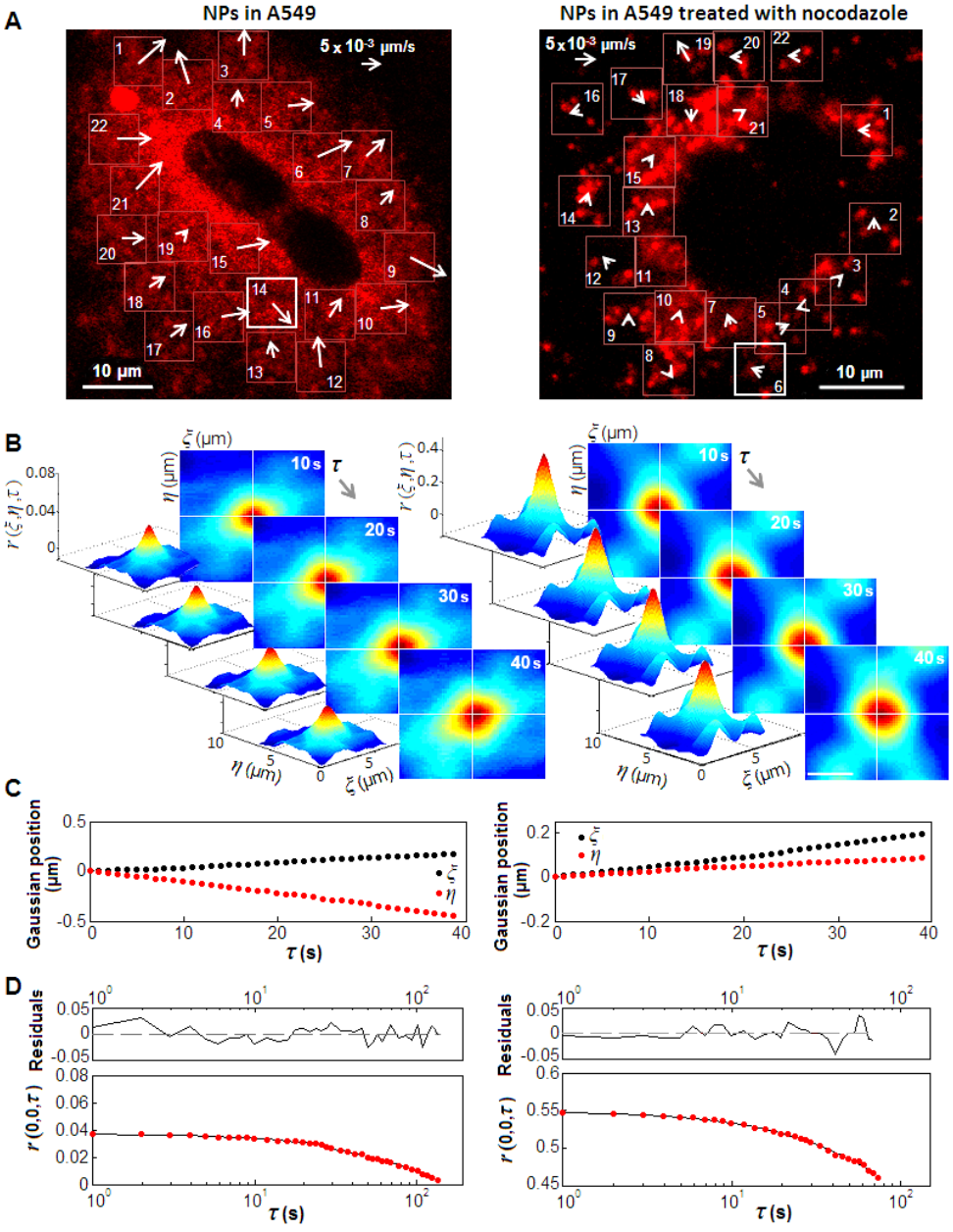

Figure 3-2 (p.72): (a) Collected images after removal of the immobile population with flow mapping resulting from STICS analysis of the PLLA-Hyp NPs in A549 cells without (left image) and with nocodazole treatment (right image). The 64×64 pixels region for which the STICS and TICS analyses are shown in panels B, C and D is marked with a bold white square. (b) STACF $r(\xi,\eta,\tau)$ and their contour plot. (c) Plots of the position of the $r(\xi,\eta,\tau)$ peak as a function of time. (d) TICS fit to temporal autocorrelation peak $r(0,0,\tau)$, which gives an estimate of the particles diffusion coefficient for the cell without nocodazole treatment and the treated cell. The flow velocity and diffusion coefficient of each region are presented in Table 3-8 in *3.6 Supplementary information*.

Table 3-1: Flow velocities and diffusion coefficients of PLLA-Hyp NPs in A549 cells with and without nocodazole treatment.

	A549 cell		Nocodazole-treated A549 cell		Statistics
	V_{STICS} [a] × 10^{-3} (μm/s)	D_{TICS} [b] × 10^{-3} ($\mu m^2/s$)	V_{STICS} × 10^{-3} (μm/s)	D_{TICS} × 10^{-3} ($\mu m^2/s$)	p values [c]
PLLA-Hyp	7.0± 0.5[d]	5.1 ± 1.3	2.1 ± 0.2	4 ± 1	< 0.002

[a] Flow velocity measured by STICS.

[b] Diffusion coefficient measured by TICS.

[c] p values are generated by comparing the velocities or diffusion coefficients of A549 cells with and without nocodazole treatment. In all combinations $p < 0.002$ showing a statistically significant difference with 95% confidence level.

[d] Flow velocities and diffusion coefficients are reported as mean ± SEM for 22 regions inside the cells. The magnitude of the flow velocity and diffusion coefficient of each individual region is presented in *3.6 Supplementary information*, Table 3-9.

For a typical region discriminated in Figure 3-2A with a bold white square, $r(\xi,\eta,\tau)$ for τ = 10, 20, 30 and 40s, the peak position of $r(\xi,\eta,\tau)$ at different time lags and TACF $r(0,0,\tau)$ are presented in B, C and D, respectively. The mean values of the velocities and diffusion coefficients of the PLLA-Hyp NPs in the absence and in the presence of nocodazole are shown in Table 3-1. The effect of nocodazole on the velocity is statistically significant. The magnitude of the flow velocity and diffusion coefficient of PLLA-Hyp NPs for each individual region in Figure 3-2A are presented in Table 3-8 in *3.6 Supplementary information*. The dynamics of PLLA-Cou NPs as a non-phototoxic control was identical to the dynamics observed for PLLA-Hyp NPs (Table 3-8). The agreement between the results obtained for PLLA-Hyp and control shows that ICS was not affected by the Hypericin cytotoxicity.

As the directed motion of the NPs can well be due to association with organelles, the motion of the latter was studied in detail. Time-lapse live-imaging of endosomes, lysosomes and mitochondria combined with STICCS was used to investigate co-transport of PLLA-Hyp NPs with individual organelles after 1-h administration of the NPs. Lysosomes and mitochondria were labelled with LysoTracker and MitoTracker Green, respectively. Early and late endosomes were visualized by transduction of the cells with GFP fused to Rab5a and Rab7a proteins, respectively. Previously the role of Rab proteins in the intracellular trafficking of nanocarriers has been reported [210, 279, 321]. However, no interference of the transduction procedure of Rab5a and Rab7a on intracellular trafficking has been reported [217, 293, 322-324].

For each type of organelle, image subsections were selected from different regions of the cells. Spatiotemporal cross-correlation functions of two image time-series collected for PLLA-Hyp and labelled organelles were calculated. The velocity mapping of the NPs flowing with the cell organelles are shown in Figure 3-3A. Appearance of the strong Gaussian cross-correlation peaks, $r(\xi,\eta,\tau)$ in all selected regions, reveals association of NPs with early endosomes, late endosomes, lysosomes and mitochondria.

The peaks, $r(\xi,\eta,\tau)$ broaden and appear to be mobile as a function of time, which represents a flow biased diffusion of the NPs associated with the aforementioned organelles. For a typical region shown in Figure 3-3A, the STICCS STACF $r(\xi,\eta,\tau)$ for τ = 1, 20 and 40s and the peak position of $r(\xi,\eta,\tau)$ at different time lags are presented in B and C, respectively. Fitting for the displacement of $r(\xi,\eta,\tau)$ yields the flow velocity of the co-localized Hypericin (red) and the specifically labelled organelles (green) populations with average values presented in Table 3-2. The magnitude of the co-transport of PLLA-Hyp NPs with organelles for each individual region is presented in Table 3-9 in *3.6 Supplementary information*. In most regions of the cells, the velocities of the co-transport populations are about 10 times bigger than those estimated for the whole population of the NPs in cytosol. To understand how intracellular organelle interactions impact directed transport of the NPs, the directed motion of labelled endosomes, lysosomes and mitochondria was characterized by STICS and presented in Figure 3-4 and Table 3-2. The magnitude of the velocity for each individual region is presented in Table 3-10 in *3.6 Supplementary information*. To measure the average velocity of the organelles without NP exposure (as controls) we used STICS, which yields an ensemble average velocity in a ROI. As shown in Table 3-1 and Table 3-2, the average flow velocities obtained for the entire population of the organelles within the cells treated with NPs (8×10^{-3}-12×10^{-3} µm/s) are in close agreement with velocities estimated for PLLA-Hyp NPs in the cytosol (7×10^{-3}µm/s). In most regions of the cells, the flow values show larger average velocities for the co-transport populations (organelles co-transport with NPs) compared to the entire population of the concerned organelles treated with NPs and the concerned organelles without NP exposure (controls with flow velocity of 5×10^{-3}-6×10^{-3} µm/s).

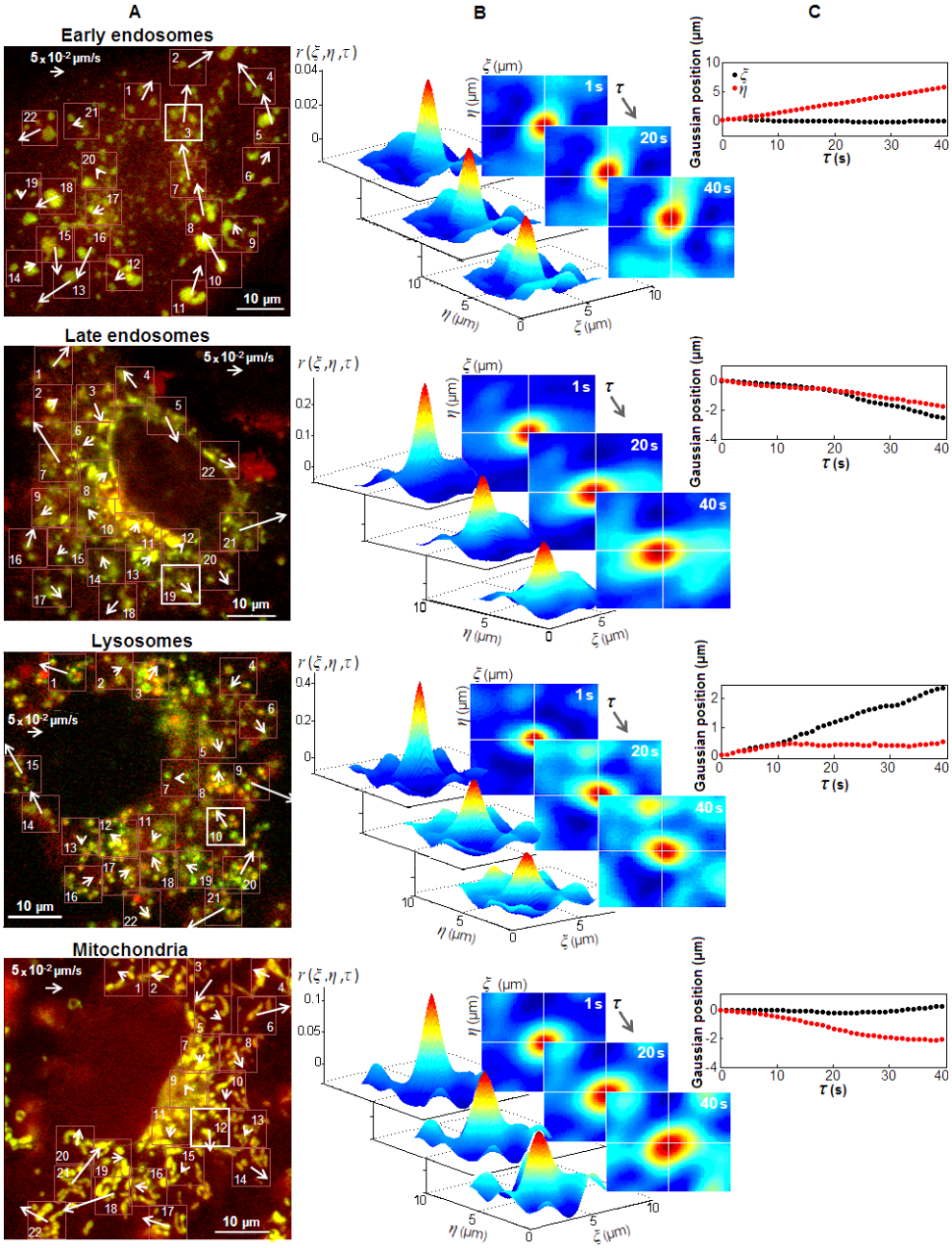
A
B
C
Early endosomes
Late endosomes
Lysosomes
Mitochondria
5x10-2 µm/s
10 µm
r(ξ,η,τ)
ξ (µm)
η (µm)
1 s
20 s
40 s
τ
Gaussian position (µm)
τ (s)

Figure 3-3 (p. 76): Collected image after removal of the immobile population with flow mapping of PLLA-Hyp NPs co-transport with early endosomes, late endosomes, lysosomes and mitochondria of A549 cells. For STICCS analyses, the cells incubated with NPs (red color) were stained with the respective organelle specific dyes (green color) Early Endosomes-GFP, Late Endosomes-GFP, LysoTracker green or MitoTracker green. The first column (a) presents a typical figure of the merged channels (yellow color) of the labelled cells from the image time-series. The 64×64 pixels region for which the STICCS analyses are shown in panels (b) and (c) is marked with a bold white square. The central column (b), represents the STICCS cross-correlation function $r(\xi,\eta,\tau)$ for τ = 1, 20 and 40s. The right column (c) shows the position of cross-correlation peak $r(\xi,\eta,\tau)$ as a function of τ. The magnitude of the co-transport velocity in each region is presented in Table 3-9 in 3.6 Supporting information.

Figure 3-4 (p. 78): Collected images after removal of the immobile population with indication of the directed movement characteristics of the early endosomes, late endosomes, lysosomes and mitochondria of A549 cells without NPs (A), with PLLA-Hyp NPs (B) and with exposure to PLLA-Hyp NPs and nocodazole (C). For STICS analyses, the cells were stained with organelle specific dyes. More details concerning the magnitude of the flow velocity in each region is presented in Table 3-10 in *3.6 Supplementary information*.

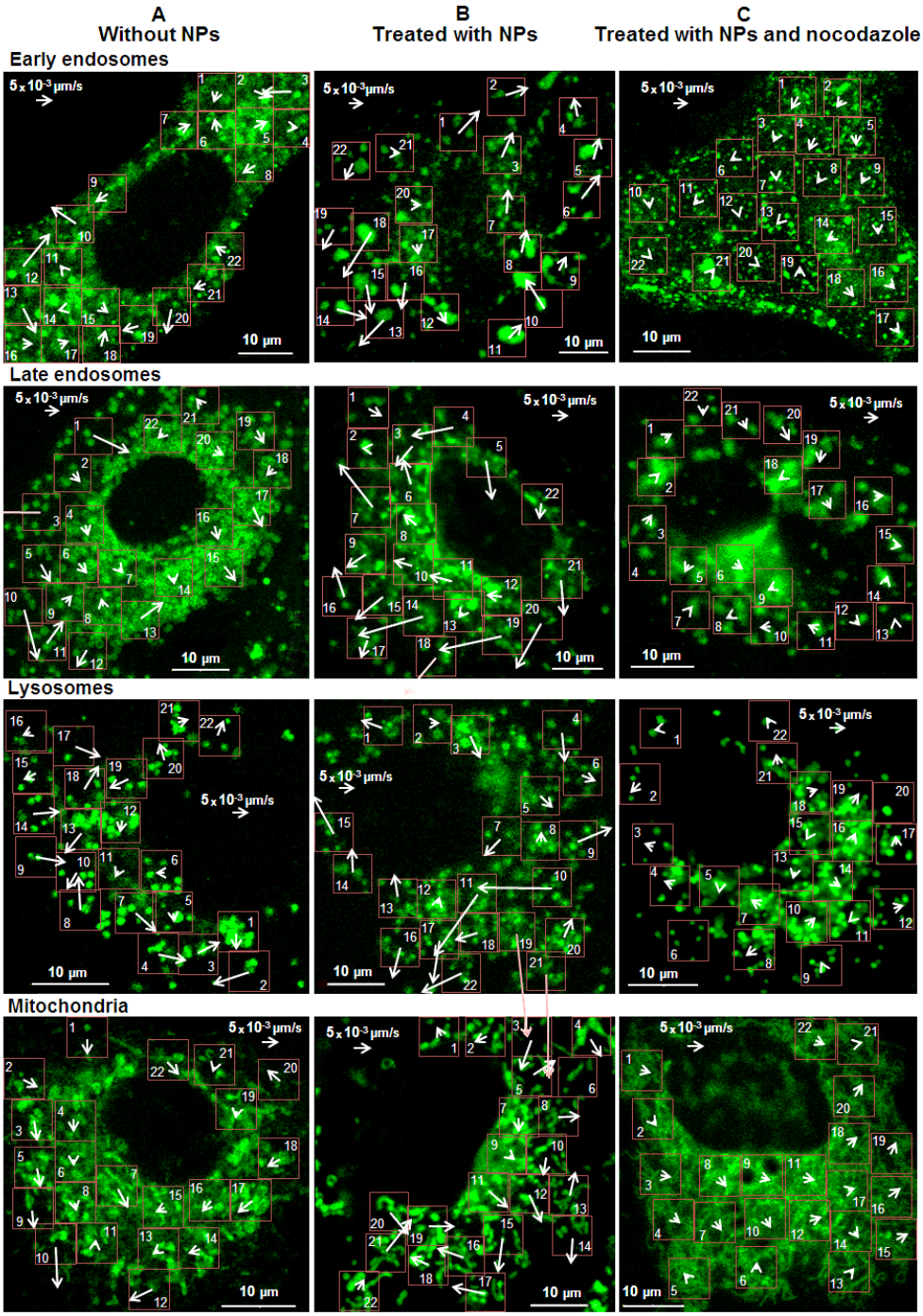
A
Without NPs
B
Treated with NPs
C
Treated with NPs and nocodazole
Early endosomes
Late endosomes
Lysosomes
Mitochondria
5x10-3 µm/s
10 µm

Table 3-2: Flow velocities of organelles in A549 cells that were all incubated with PLLA-Hyp NPs for 1-h. Cells without NPs were considered as controls.

Organelles	*M*[a]	V_{STICCS}[b] × 10^{-3} (μm/s)	V_{STICS} × 10^{-3} (μm/s)			Statistics
		Co-transport population[c]	Organelle population[d]	Control population[e]	Nocodazole-treated population[f]	p values[g]
Early endosomes	0.30	85 ± 9[h]	8 ± 1	5 ± 1	1.8 ± 0.2	< 0.001
Late endosomes	0.30	62 ± 8	7 ± 1	6 ± 1	2.2 ± 0.3	< 0.001
Lysosomes	0.16	58 ± 9	12 ± 2	6 ± 1	2.0 ± 0.2	< 0.001
Mitochondria	0.20	65 ± 10	8 ± 1	5 ± 1	2.6 ± 0.2	< 0.001

[a] Manders' overlap coefficient, which shows the fractions of pixels related to PLLA-Hyp NPs (red) co-localized with organelle specific dyes (green).

[b] Average velocity of the co-transport measured by STICCS.

[c] Organelles co-transport with PLLA-Hyp NPs

[d] Average velocity of the entire population of the organelles treated with PLLA-Hyp NPs

[e] Average velocity of the organelles without NPs.

[f] The cell population treated with both PLLA-Hyp NPs and nocodazole.

[g] p values obtained by Mann-Whitney tests are generated by comparing the velocities of each two independent groups (columns in the table) in all possible pair-wise combinations. In all cases $p < 0.001$ showing a statistically significant difference with 95% confidence level.

[h] Velocity values are reported as mean ± SEM for 22 regions inside the cells. The magnitude of the flow velocity of each individual region is presented in Table 3-9 and Table 3-10 in *3.6 Supplementary information*.

The use of STICCS implicitly selects the subpopulations of NPs and organelles that undergo a correlated motion. These subpopulations are smaller as compared to the corresponding populations as considered in STICS. Although there is a reduced averaging effect in STICCS the considered autocorrelation functions still exhibited a good signal to noise ratio (Figure 3-3). The fraction of PLLA-Hyp NPs localized at different cell organelles have been additionally investigated by calculating Manders' overlap coefficients (Table 3-2, M values). The maximum Manders' overlap coefficient of 0.30 has been obtained for PLLA-Hyp NPs co-localized with early and late endosomes. The M values indicate different amounts of NP association with various organelles, which might be attributed to the optimized time duration of the experiments (taking into account 1-h incubation and that the measurements were finalized 20 min after ending the incubation). Despite the variations within the respective fractions of the NPs associated within the different organelles, we can clearly see a significant increase in the co-transport flow values for all associated motions irrespective of the fact that different cells were used for studying the individual associations. In general, high flow values are not unusual as it has been already reported that the velocities of the endosomes, lysosomes and mitochondria are respectively 30×10^{-3}, 300×10^{-3} and 16×10^{-3} µm/s for those flowing continuously between diffusive pauses using other techniques [255, 321, 325]. As these techniques do not rely on Rab mediated labelling, we think that our labelling strategy did not introduce artefactual effects on the trafficking kinetics. Our reproducible observations, though not rationalized at this point with any physiological means, are also consistent with our study using another kind of NPs employing an independent methodology [207, 284]. As the values obtained with STICS are consistent for all populations (organelles only with or without NP treatment as in Table 3-2 and that of NPs in Table 3-6), the interesting STICCS observations certainly necessitates further studies involving modelling to shed light on the averaging effects for different population sizes. Also, combination of different methodologies to seek complimentary information is required to elucidate the underlying effects.

As abrupted intracellular directed motion of the NPs was seen in the cells treated with nocodazole (see Table 3-1), the effects of the microtubule cytoskeleton on the organelle dynamics were studied in detail. As shown in Table 3-2 and Figure 3-4 (right image), nocodazole abolished the directed long-range NPs associated motions of the endosomes, lysosomes and mitochondria.

Mann-Whitney tests showed a statistically significant difference between the flow velocities of each two independent groups in all possible pair-wise combinations (in Table 3-2). In all combinations, the maximum p-value of the considered differences between the flow velocities was < 0.001, which means a statistical significance. Based on the statistical analyses on five cells for each type of experiment, TICS, STICS and STICCS yielded reproducible flow velocities and diffusion coefficients (more details in *3.6 Supplementary information*, Table 3-6 and Table 3-7).

3.5 Conclusion

Systematically designed mono-labelled (Hypericin or Coumarin-6 only) and dual-labelled (Hypericin and Coumarin-6) PLLA NPs were synthesized for the first time by combining the miniemulsion and solvent evaporation method. These NPs allowed for a detailed study of the intracellular dynamics and localization of Hypericin loaded NPs in A549 cancer cells. The fate of the cargo, directed motion of the NPs, association of NPs with different cell organelles and their related motions were studied using TLCM, FLIM and different variants of ICS.

The correlated findings from the different experiments are summarized as follows:

- Using dual-labelled particles with Coumarin-6 as a colocalization probe with respect to Hypericin, clear evidence for the release of Hypericin was observed. The Manders' coefficient determined for Hypercin in correlation with the Hoechst and the Coumarin-6 strongly supports this observation. In addition, the average fluorescence decay time determined for Hypericin clearly shows the change in environment of

Hypericin upon release from the NPs. Subsequently, the occurrence of cell death associated with the release of Hypericin and the changes in the time-resolved fluorescence of Hypericin as observed by FLIM validated the TLCM findings. The optimal conditions and the time duration for the unambiguous ICS studies were obtained from the FLIM and TLCM observations.

- The intracellular transports of mono-labelled PLLA-Hyp NPs were studied by using TICS and STICS. The mean values of the flow velocities and the diffusion coefficient were about $(7.0 \pm 0.5) \times 10^{-3}$ μm/s and $(5.1 \pm 1.3) \times 10^{-3}$ $\mu m^2/s$, respectively. It was found that the presence of nocodazole, an anti-neoplastic agent known to interfere with the microtubule dynamics, resulted in the disruption of the directed motion leading to a drastic reduction of the flow velocity to $(2.1 \pm 0.2) \times 10^{-3}$ μm/s.
- A fraction of the NPs associate with the respective organelle under consideration as indicated by the Manders' overlap coefficient. The correlated motion of these NPs and the organelles has been quantified by STICCS. The related flow velocity values extracted from their associated motion with the concerned organelles are higher than that for all other populations considered (organelles only with or without NP treatment and that of NPs), the interesting STICCS observations certainly necessitates further studies involving modelling to shed light on the averaging effects for different population sizes. Also, combination of different methodologies to seek complimentary information is required to illucudate the underlying effects. The disruption of the directed NPs associated motions of the endosomes, lysosomes and mitochondria in presence of nocodazole clearly indicates the influential role of the dynamics along the microtubule network.

Despite the complexity involved in the study of intracellular dynamics associated with NP uptake, this study provides insight into the inherent transport characteristics of the NPs and different organelles using a powerful and systematic combination of methods. The results of this study can be extended to

explore new avenues for unraveling the intricacies involved in the cellular uptake of the nanocarriers as well as the fate of the cargo and the carrier. This can subsequently lead to a substantial contribution to the understanding of the interaction of the drug at the sub-cellular level and in realizing a thoughtful design of the drug carriers for an improved efficacy of the involved therapy. Currently, further studies are in progress in our laboratory to validate our results with other NPs as well as drugs and to shine light on the different mechanisms involved in co-transport.

3.6 Supplementary information

3.6.1 Detailed properties of the PLLA-based nanoparticles

Qualitative and quantitative information on physical properties of the PLLA-based NPs including size, solid content, absorption and emission wavelengths of their encapsulated dye and photosensitizer is presented in Table 3-3, Table 3-4, Figure 3-5 and Figure 3-6.

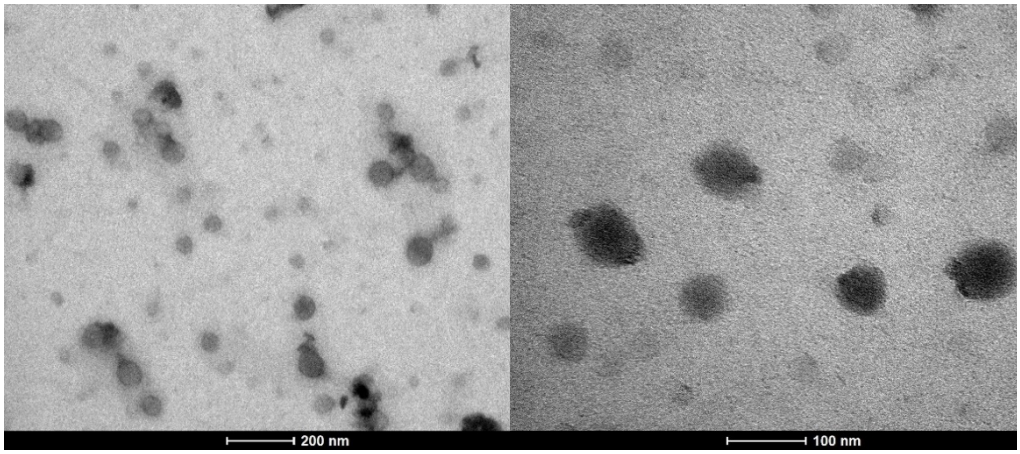

Figure 3-5: TEM at different magnifications (scale bars: left image - 200 nm and right image - 100 nm) images showing the morphology of PLLA-Hyp NPs.

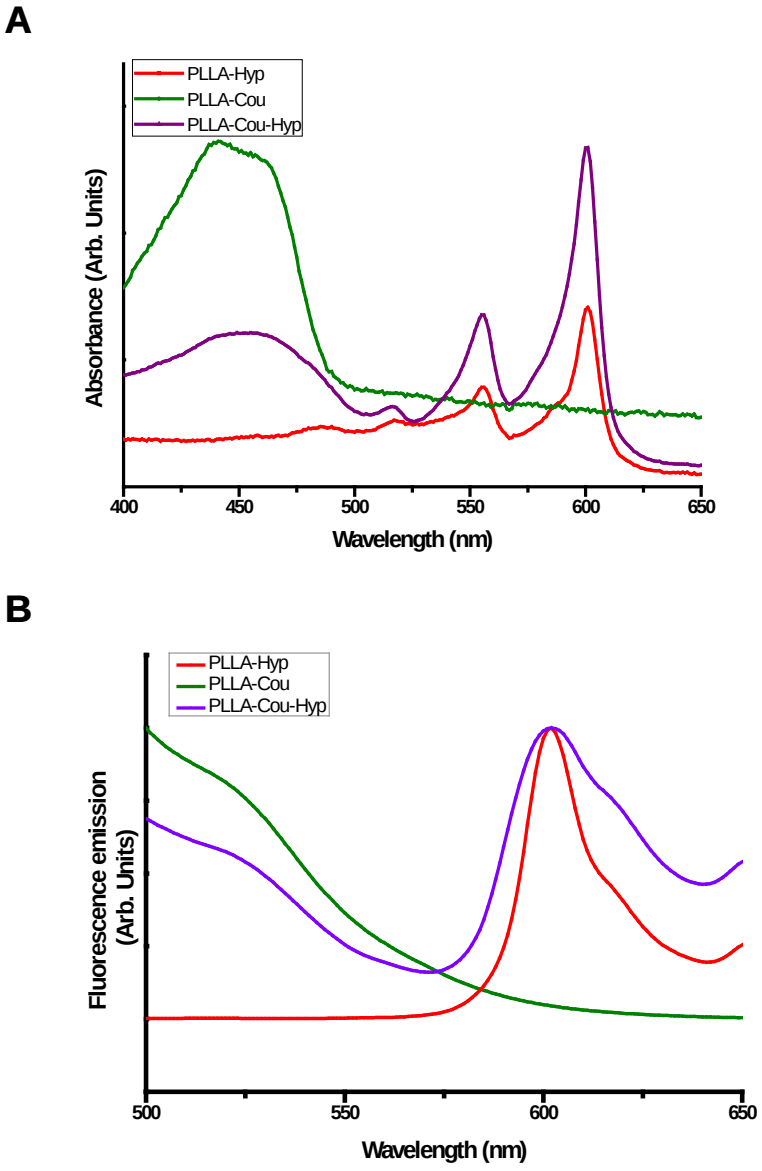

Figure 3-6: A UV-Vis absorbance and B fluorescence emission spectra (λex= 488 nm) of different NPs in THF. PLLA-Hyp (only Hypericin), PLLA-Cou (only Coumarin-6) and PLLA-Cou-Hyp (Coumarin-6 and Hypericin).

Table 3-3: Synthesis and characterization of NPs. For the synthesis of all the samples, 150 mg of polymer, 36 mg of the anionic surfactant SDS and 12 g of Milli-Q water was used. The incorporated fluorescent dye or photosensitizer amount was 5 wt% with respect to the polymer. In case of dual-labelled particles, the combined amount of dye and photosensitizer was 5 wt% with respect to the polymer.

Samples	Components continuous phase	Components dispersed phase	Diameter [a] (nm)	PDI [b]	Solid content (%)	
					Before washing	After washing
PLLA-Hyp	SDS H_2O	PLLA Hypericin $CHCl_3$	204.6	0.3	1.7	1.3
PLLA-Cou	SDS H_2O	PLLA Coumarin-6 $CHCl_3$	178.9	0.3	1.7	1.3
PLLA-Cou-Hyp	SDS H_2O	PLLA Coumarin-6 Hypericin $CHCl_3$	266.0	0.3	1.2	1.1

[a] Mean effective diameters (intensity average) are measured by DLS.

[b] PDI values indicating size distribution were obtained by DLS.

Table 3-4: Amount of dye encapsulated determined by fluorescence spectroscopy. The amount of encapsulated dye from the known amount of dried polymer particles was determined using by molecularly dissolving the polymer and the dye in tetrahydrofuran (THF). The unknown amount of entrapped dye was determined using a standard curve plotted using a series of known concentrations of the respective dye also dissolved in THF. (Hypericin: λ_{ex}= 570nm, λ_{em}= 602 nm) (Coumarin-6: λ_{ex}= 425nm, λ_{em}= 475nm). For synthesis about 150 mg of the polymer PLLA was used.

Sample	Theoretical amount incorporated dye (mg)	Experimental amount incorporated dye (mg)	Efficiency incorporated dye (%)
PLLA-Hyp	7.2	1.1	14.5
PLLA-Cou	7.5	1.1	15.3
PLLA-Cou-Hyp (Hyp)*	15.2 (7.6 mg Hyp)	2.7	35.9
PLLA-Cou-Hyp (Cou)*	15.2 (7.6 mg Cou)	0.6	7.2

* The respective dye amounts incorporated are determined for the dual-labelled sample.

3.6.2 Dark cytotoxicity of Hypericin loaded PLLA nanocarriers

A549 cells were incubated in 96 well plates (Cellstar, Greiner Bio-One, Belgium) at a density of 5×10^3 cells/well. After 24 hours of incubation at 37°C and 5% CO_2, the cells were washed and incubated for a further 24 hours with 0, 1, 10, 25, 50 and 100 µg/ml concentrations of Hypericin loaded PLLA NPs (PLLA-Hyp) in culture medium. $ZnSO_4 \cdot 7H_2O$ (Sigma-Aldrich, Belgium) was added to the cells as a positive control for cytotoxicity (PC). After exposure, cell viability was assessed by the CellTiter 96® AQueous One Solution Cell Proliferation Assay (Promega Corporation, USA) according to the manufacturer's protocol.

The resulting formazan crystals, which are directly proportional to the number of metabolic active cells present in the culture, were measured by recording the absorbance at 490 nm by using a microplate reader (FLUOstar Optima, BMG Labtech, Germany). The results are shown in Figure 3-7.

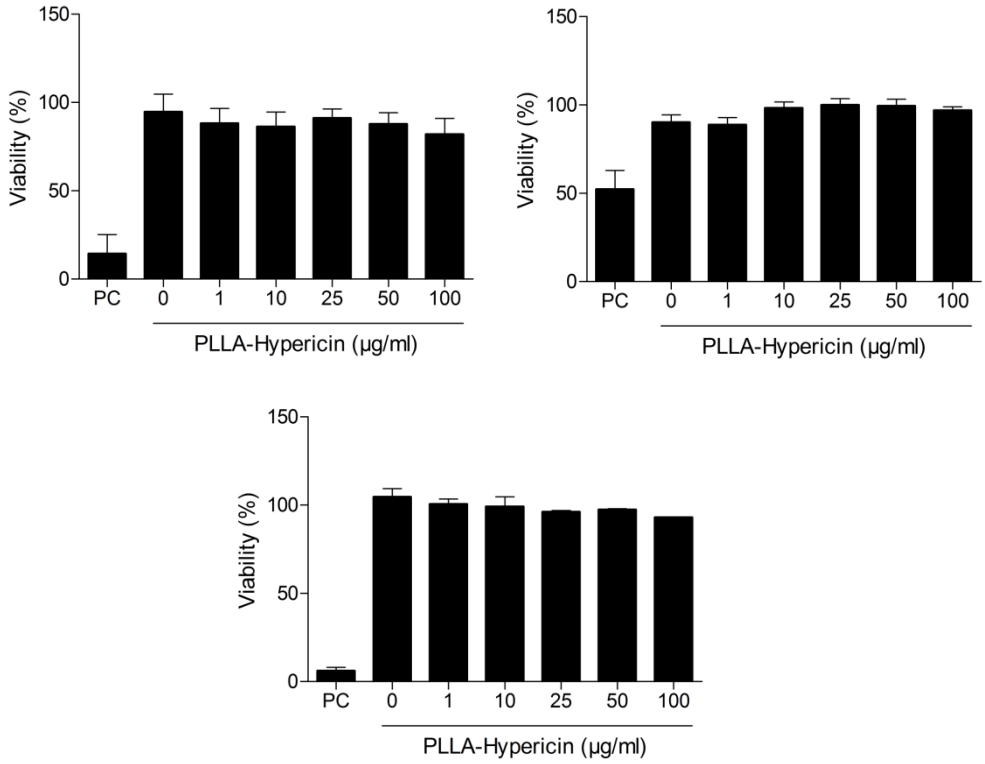

Figure 3-7: Dark cytotoxicity of PLLA-Hyp NPs in A549 cells. Each panel represents a biologically independent cell culture. The cells were exposed for 24-h to different concentrations of PLLA-Hyp NPs (0, 1, 10, 25, 50 and 100 µg/ml) at 37°C. 29 µg/ml ZnSO4 was used as a positive control (PC). Data represent mean ± standard deviation of three replicates.

3.6.3 Leakage experiments using PLLA-Cou-Hyp NPs

The passive interaction of PLLA-Cou-Hyp NPs with the lipophilic surrounding was investigated by evaluating the release and transfer of Coumarin-6 and Hypericin to microbubbles. For that reason 1,2-dioleoyl-sn-glycero-3-phosphocholine (DOPC) – 1,2-dimyristoyl-sn-glycero-3-phosphocholine (DMPC) (70-30 mol%) microbubbles filled with perfluorobutane (PFC) were prepared by dr. Summit Pramanik according to the following procedure: DOPC and DMPC (Avanti Polar Lipids, USA) were co-dissolved in $CHCl_3$ in a borosilicate vial with a screw cap. Thereafter, $CHCl_3$ was evaporated to dryness under a nitrogen stream for 2 hours. The resulting lipid film on the wall of the vial was hydrated with Milli-Q ultrapure water and incubated in an oven for 1 hour at 40°C. Thereafter, the sample was sonicated using a probe sonicator (450W digital sonifier, Branson, USA) employing 1/4" tip and amplitude 30 % for 30 s under a stream of PFC gas (F2 chemicals limited, U.K.).The PLLA-Cou-Hyp NPs washed with water followed by washing with ethanol solution (50% v/v) and finally redispersed in water was incubated with the lipid microbubbles. For all the samples used in this work, the washing step with ethanol solution was performed mainly to remove any unencapsulated dye as both the dyes were soluble in ethanol. To show the significance of the washing step using ethanol solution, the NP sample prior to washing with ethanol solution was also tested with the lipophilic surrounding. Leakage studies were started by adding PLLA-Cou-Hyp NPs (final concentration 130 µg/ml) to 2×10^{10} microbubbles/ml containing solution. This combination was mixed by means of pipetting. Thereafter, 10 µl was transferred to a glass slide with a SecureSeal imaging spacer (Grace Bio-Labs, Sigma-Aldrich, 9 mm x 0.12 mm, GBL654008-100EA) and mounted with a 1.5 coverslip (MenzelGläser, Braunschweig, Germany). Thereafter, release experiments were started immediately. The same microscopic set-up was used as for the cell experiments. Briefly, images were obtained with a commercial Zeiss LSM 510 Meta CLSM (Jena, Germany) on an inverted epifluorescence Axiovert 200M motorized frame equipped with a LD C-Apochromat 40×/1.1 W Corr UV-VIS-IR water immersion objective. PLLA-Cou-Hyp NPs were visualized by means of a 30 mW air-cooled argon ion laser emitting at 488 nm under the control of an acousto-optic

modulator. The laser light was directed to the sample using a dichroic mirror and beam splitters NFT 545 and HFT UV/488/543/633. For detection and separation of the different emitted fluorescence signals, two band-pass filters BP 500-550 IR (for Coumarin-6) as well as 650-710 IR (for Hypericin) were used. The images (512×512 pixels) of each series were collected with 5 minutes between the sequential frames up to 90 minutes. The individual frames were acquired with the pixel size of 0.09 µm and pixel dwell times of 12.8 µs. Images were recorded at room temperature. The images acquired after 90 hours are presented in Figure 3-8.

The results indicate that the washing procedure has a significant effect in our case. The signal from the red channel originating from Hypericin is less intense as compared to the Coumarin-6 signal as Hypericin has reduced fluorescence emission when it is stacked/aggregated (in the intact NPs) as described before.

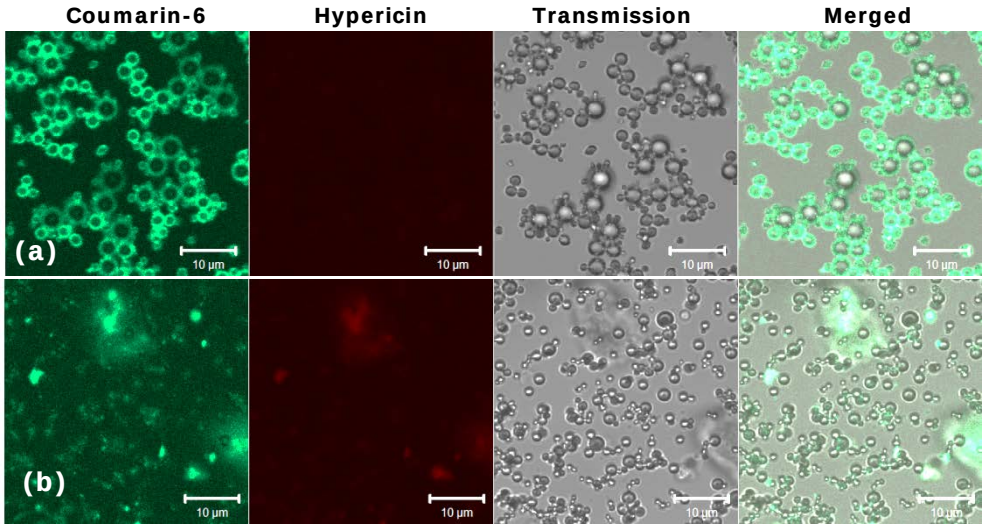

Figure 3-8: DOPC-DMPC (70-30 mol%) microbubbles after 90 hours of exposure to PLLA-Cou-Hyp NPs observed in different channels (a) washed only with water and (b) washed with ethanol solution followed by redispersion in water. The experimental set-up and the settings for imaging were identical to the experiments described in the manuscript. The scale bars are 10 µm.

3.6.4 Studying the intracellular degradation of the NPs by using FLIM

A change in the environment of Hypericin can strongly influence the fluorescence lifetime [297, 298, 317, 318, 326]. Therefore, FLIM was used to monitor the release of Hypericin from the PLLA NPs after 1 h of loading the cells with the NPs (Figure 3-9).

The pseudocolor images, spectra of the fluorescence lifetime and the average values of various lifetime components were obtained using SPCImage 2.9 data analysis software (Becker and Hickl, Germany). By using this software, the decay matrix of the ROI was calculated pixel by pixel. Hypericin fluorescence decay curves do not fully relax between two excitation pulses, which can produce distortions in the lifetime values. Therefore, the information regarding the laser repetition time was provided by the user and the incomplete multi-exponentials fit model of the SPCImage software was used in the all calculations. The estimated time distributions were then interpreted as multi-exponential functions to derive the spatial distribution of fluorescence lifetimes and of their relative (percentage) amplitudes. Finally, a color coded lifetime image was produced which maps the average fluorescence lifetime over the pixels. The data were best fitted with two or three exponential components on the basis of the reduced chi-squared χ^2 value (see Table 3-5), the distribution of the weighted residuals and their autocorrelation function:

$$F(t) = \alpha_1 e^{-t/\tau_1} + \alpha_2 e^{-t/\tau_2} + \alpha_3 e^{-t/\tau_3} \qquad \text{(Eq.3-2)}$$

where, α_1, α_2 and α_3 are the amplitude coefficients. τ_1 , τ_2 and τ_3 represent the fluorescence lifetimes. For two exponential components α_3 is set to zero.

The selected fit parameters show by default the weighted average of the different lifetime components (τ_M) in each pixel over the whole cell including the pixels in the nucleus:

$$\tau_M = \sum_{i=1}^{N} \alpha_i \tau_i / \sum_{i=1}^{N} \alpha_i \qquad \text{(Eq.3-3)}$$

The software also allows analysing all pixels simultaneously for a given number of relaxation times. The number of photons in each decay trace is in the range of 19283-38298.

The FLIM images indicate an evolution over time of the average lifetime from about 3.6 ns to 1.7 ns. The longer average lifetimes observed at the end of the incubation period (t = 0) can be associated with the PLLA-Hyp NPs (blue spots in Figure 3-9A). After 150 min the cells start losing their shape, become round and undergo cell death, indicating that a substantial amount of Hypericin is released from the PLLA NPs and that the excitation intensities during the measurement allow Hypericin to exert the desired effect (Figure 3-9B). To check whether the cell damage is really due to the photoexcited Hypericin, a series of the control experiments under the same experimental conditions were performed with PLLA-Cou NPs. No cell death, damage or deformation was observed in these control experiments (results not shown).

Table 3-5 reports the various lifetime components averaged over the relevant pixels in the image, including those related to the nucleus. The best fits for the fluorescence decay of NPs in A549 cells at t = 0, and for the NPs in culture medium as well (see Figure 3-10A), were obtained by considering two decay times: 0.7 ns and 4.5 ns (average decay time = 3.4-3.6 ns). Thereafter, the fluorescence decay is best described with three decay components of 0.5-0.7 ns, 2.1-4.5 ns and 7.1-7.3 ns (average decay time = 1.9-3.0 ns), which suggest a different cellular environment or condition for Hypericin. This is also the case for the fluorescence decay of Hypericin in direct administration to the A549 cells (see pseudocolor image in Figure 3-10B). The fluorescence decay is then also best described with three decay components of 0.5 ns, 2.3-2.6 ns and 5.1-5.3 ns (average decay time = 1.7-2.1 ns) for the cells damaged by the photoexcited Hypericin. All these fluorescence decay times are comparable with those reported for Hypericin in human retinal pigment epithelial cells [317]. FLIM, performed with the same experimental conditions as in the actual experiments,

did not indicate substantial fluorescence signal in the bathing solution and the untreated cells (Figure 3-10C).

As previously mentioned, Hypericin is an amphiphilic compound, non-soluble in water, where it forms aggregates. The presence of water led to shortening of the fluorescence lifetime of Hypericin [317]. PLLA NPs are like shells around Hypericin and prevent the influence of the water. As NP degradation proceeds more Hypericin molecules escape and enter a more polar environment as compared to the PLLA NPs so that the average lifetime will decrease with time. In addition, Hypericin concentration can increase locally which can result in a shortening of the lifetime, suggesting most likely the self-quenching of aggregated Hypericin [210, 233, 242, 317, 326].

Any change in the intracellular pH can affect the process of the NPs degradation in addition to the Hypericin lifetime [317]. At low photosensitizer concentration, when a small portion of the NPs are degraded, Hypericin might be bound to some specific structure in the cytosol, which could produce a more polar microenvironment as compared to the PLLA NPs. At high Hypericin concentrations, when most of the NPs are degraded, similar binding sites might not be available for all fluorophore molecules, thus leading, on average, to a more polar environment. Local increase of Hypericin concentration decreases the distance between its molecules. This could lead to intermolecular interactions between Hypericin molecules and shortening of the lifetime [317].

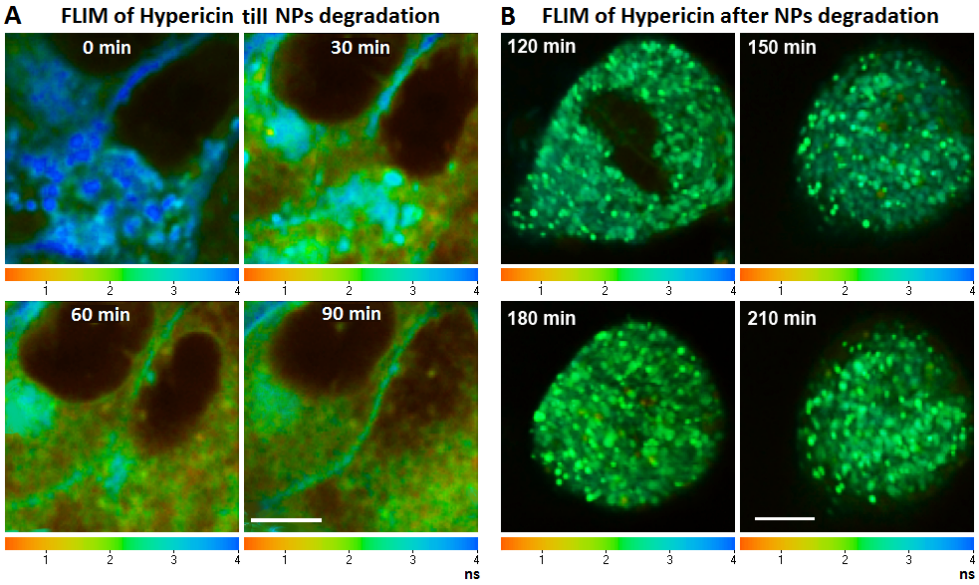

Figure 3-9: FLIM to monitor Hypericin release of the PLLA NPs in A549 cells. The cells were loaded with NPs for 1-h. Pseudocolor images of the mapping of the amplitude averaged Hypericin fluorescence lifetime till NPs degradation (a) and after NPs degradation (b). The photoexcited cells start losing their shape, become round and undergo cell death after NPs released Hypericin. The scale bars are 10 µm.

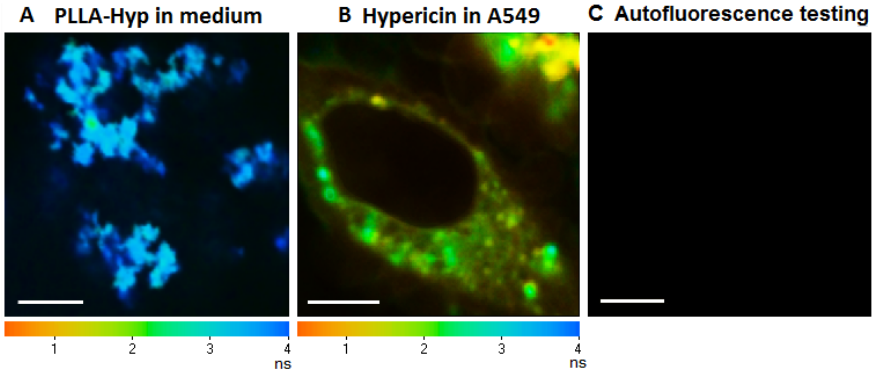

Figure 3-10: Pseudocolor images of fluorescence lifetime of (a) encapsulated Hypericin in the culture medium, (b) free Hypericin in A549 cells and (c) cells' autofluorescence. Average lifetime τ_M decreases from 3.6 ns in its incorporated form to 1.9 ns in its free from. The scale bars represent 10 µm.

Table 3-5: Fluorescence decay times τ (ns) and relative amplitudes α (%) of Hypericin encapsulated into the PLLA NPs in A549 cells. The data shown result from a global analysis over all pixels in the image.

PLLA-Hyp NPs in A549

Time (min)	α1 (%)	τ1 (ns)	α2 (%)	τ2 (ns)	α3 (%)	τ3 (ns)	τM [a] (ns)	χ2 [b]
0	24.5	0.7	75.5	4.5	-	-	3.6	1.6
30	49.5	0.6	33.4	4.5	17.1	7.3	3.0	1.0
60	54.5	0.6	28.5	3.9	17.0	7.2	2.7	1.1
90	58.2	0.5	24.5	2.4	17.3	7.1	2.1	1.0
120	38.1	0.5	48.0	2.6	13.8	5.1	2.1	1.2
150	46.8	0.5	40.6	2.4	12.6	5.3	1.9	1.1
180	57.5	0.5	32.1	2.6	10.4	5.2	1.7	1.0
210	51.3	0.5	35.9	2.3	12.8	5.3	1.8	1.2
NPs in medium	27.9	0.7	72.1	4.5	-	-	3.4	1.4
Hyp in A549	54.5	0.5	31.9	2.1	13.6	7.3	1.9	1.0

[a] The mean decay time as calculated by (Eq. 3-3) and (Eq. 3-4).

[b] The reduced chi-squared, which shows the goodness of the fit.

The last two rows (labelled as NPs in medium and Hyp in A549) are controls that refer to the decay times of the NPs in culture medium and free Hypericin in A549 cells, respectively.

3.6.5 Investigating the bleed-through artifact

For the cells incubated with either PLLA-Hyp NPs or organelle specific dyes, the images of the labelled cells were recorded in each of the channels used under the same conditions as in the actual experiments. Then, the STICCS analyses were performed on the channels to investigate the possible cross-talk.

As shown in Figure 3-11, STICCS did not show bleed-through artifacts.The cellular auto-fluorescence was investigated by recording the images of the non-labelled cells in the different fluorescence channels with the same setup as the actual experiments. The cells did not show any auto-fluorescence as can be seen in Figure 3-11.

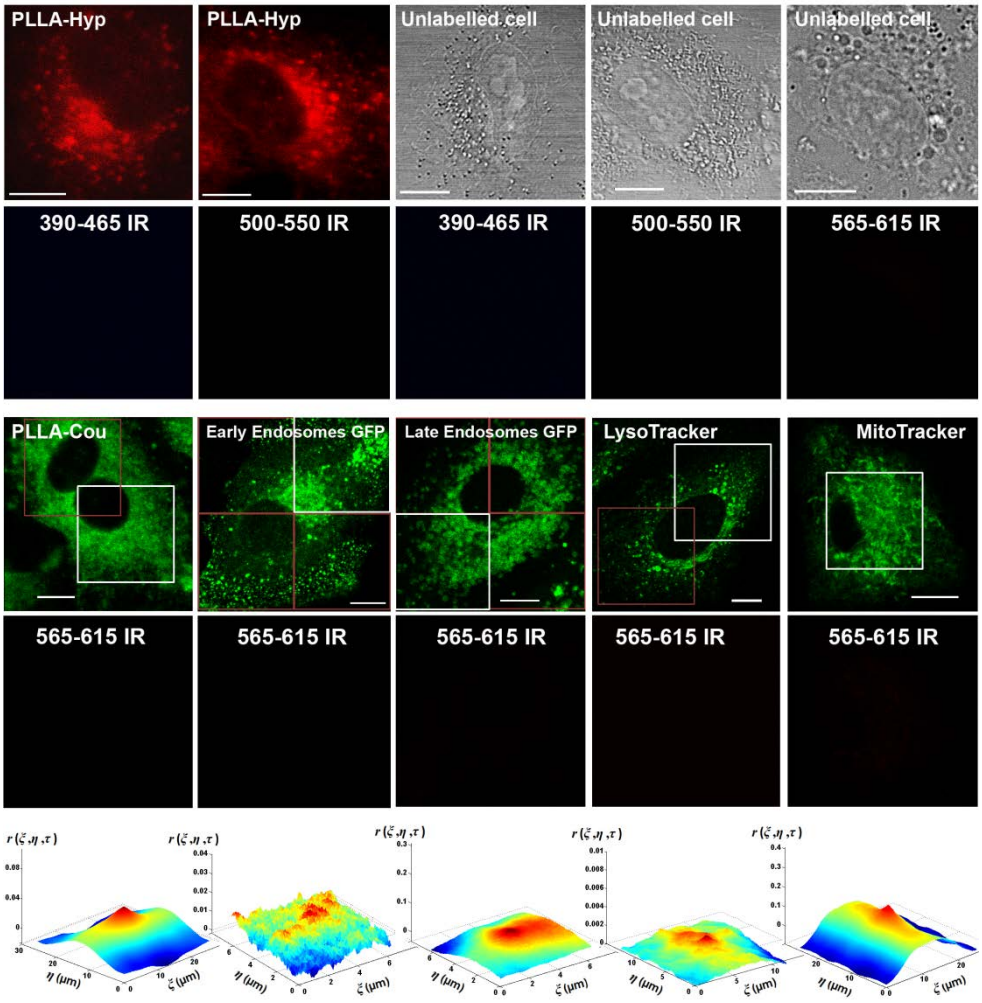

Figure 3-11: Investigating the channel cross-talk and cellular autofluorescence under the same conditions as used for the actual experiments. For detection and separation of the different fluorescence signals, the following band-pass filters are used: 565-615 IR (for Hypericin), 500-550 IR (for Coumarin-6 and organelle specific dyes) and 390-465 IR (for Hoechst). Excitation of Hypericin, Coumarin and the organelle specific labelling is at 488 nm. Hypericin fluorescence does not contribute in the Hoechst and the green channel (organelles, Coumarin) (top row). For studying the autofluorescence, the cells without any fluorescent dye and NPs (unlabelled cells) were used. Using unlabelled cells the absence of autofluorescence in the respective detection channels is shown in the top row. Images of cells when only organelles are labelled have been collected in the Hypericin channel (third row). Regions of 256×256 pixels (white squares) were selected from different parts of the cells and the channel cross-talk was investigated by using STICCS. The images have been cross-correlated with the images of the same cells in the organelle channel. Representative cross-correlation functions shown (bottom row) indicate the absence of significant correlation. Similar observations are obtained when considering PLLA-Cou. The scale bars represent 10 µm.

3.6.6 Immobile population filtering

The intensity of a pixel is a contribution of the fluorescence signals of mobile and immobile components as well as white-noise sources. For a given pixel trace, the signals of dynamic components (flow and diffusion) contribute to intensity fluctuations that change as a function of time. However, immobile components only add a constant intensity offset to the single pixel intensity trace through time. Removing this constant offset eliminates the contribution of the immobile components from the correlation analysis. The corrected intensities for a given pixel location (x,y), are given by [236]:

$$i'(x,y,t) = F_f^{-1}\left\{F_t\left\{i(x,y,t)\right\} \times H_{1/T}(f)\right\} \qquad \text{(Eq. 3-4)}$$

where, f is the pixel temporal frequency variable and T is the total acquisition time of the image series. $F_f^{(-1)}$ denotes the (inverse) Fourier-transform with respect to variable i. $H_{1/T}(f)$ presents the Heavy side function which is 0 for $f < 1/T$ and 1 for $f > 1/T$.

3.6.7 Statistical analysis with Kruskal-Wallis test

To study the consistency of the TICS, STICS and STICCS outcomes, each technique has been performed on 22 regions of five A549 cells. According to the Table 3-6 and Table 3-7, the p values obtained from the Kruskal-Wallis tests indicate that the results of STICS and TICS are consistent.

Table 3-6: Assessment of the consistency of the STICS and TICS results by using Kruskal-Wallis tests. p values are generated by comparing the flow velocities and diffusion coefficients of PLLA-Hyp NPs in 22 regions of five A549 cells.

	V_{STICS} [a] (10^{-3} µm/s)		D_{TICS} [b] (10^{-3} µm²/s)	
Cells number	NPs in cells	NPs in cells treated with nocodazole	NPs in cells	NPs in cells treated with nocodazole
1	6.6 ± 0.7	2.1 ± 0.2	3.5 ± 0.6	3.6 ± 0.7
2	7.0 ± 0.1	2.7 ± 0.4	5.1 ± 0.3	3.7 ± 1.4
3	6.7 ± 0.4	2.8 ± 0.3	4.0 ± 0.6	3.3 ± 1.0
4	6.9 ± 0.8	2.9 ± 0.2	4.5 ± 0.7	3.6 ± 1.2
5	7.1 ± 0.8	2.6 ± 0.3	3.7 ± 1.1	3.8 ± 0.9
p values [c]	0.9	0.2	0.2	0.2

[a] Flow velocities measured by STICS, which are reported as mean ± SEM for 22 regions inside the cells.

[b] Diffusion coefficients measured by TICS, which are reported as mean ± SEM for 22 regions inside the cells.

[c] For 95% confidence level, if $p < 0.05$, the difference is statistically significant, otherwise not.

Table 3-7: Assessment of the consistency of the STICS results by using Kruskal-Wallis tests. The p values are generated by comparing the flow velocities measured in 22 regions of five A549 cells.

	p values [a]			
	Early-Endo	Late-Endo	Lyso	Mito
Organelles without NPs	0.511	0.970	0.815	0.323
Organelles with NPs	0.670	0.496	0.622	0.672
Organelles treated with NPs & nocodazole	0.130	0.313	0.387	0.111
Organelles co-transport with NPs	0.144	0.830	0.252	0.733

[a] For 95% confidence level, if $p < 0.05$, the difference is statistically significant, otherwise not.

Table 3-8: Effective flow velocities and diffusion coefficients of PLLA-Cou and PLLA-Hyp NPs in A549 cells. The dynamics of PLLA-Hyp NPs after nocodazole treatment is also shown in order to evaluate the microtubules roles in the directed movement of the NPs. The magnitude and direction of the velocity has been shown in Figure 3-2 for PLLA-Hyp NPs in cells treated with or without nocodazole.

Regions in A549 cells	PLLA-Cou		PLLA-Hyp		PLLA-Hyp nocodazole-treated	
	V_{STICS} [a] (10^{-3} µm/s)	D_{TICS} [b] (10^{-3} µm²/s)	V_{STICS} [a] (10^{-3} µm/s)	D_{TICS} [b] (10^{-3} µm²/s)	V_{STICS} (10^{-3} µm/s)	D_{TICS} (10^{-3} µm²/s)
1	10.3	13.0	8.6	4.1	2.1	7.2
2	6.2	6.2	8.4	4.8	2.4	1.2
3	8.0	4.1	6.4	0.4	1.2	15.4
4	2.5	2.8	3.9	2.4	1.2	3.8
5	10.1	14.3	6.2	3.3	1.8	2.7
6	3.9	0.6	10.8	29.5	3.4	0.9
7	13.6	16.4	6.2	6.4	3.1	2.6
8	4.5	1.4	5.7	1.0	1.1	2.9
9	7.7	1.2	11.0	0.7	0.9	1.4
10	6.4	0.2	7.5	6.2	1.0	2.7
11	13.2	1.8	6.0	1.6	0.3	3.7
12	5.9	0.2	8.2	10.4	2.1	7.5
13	6.1	21.6	4.8	8.1	1.2	5.6
14	3.6	3.0	6.8	2.3	1.8	2.5
15	4.1	4.0	9.1	1.1	1.9	5.7
16	5.6	1.6	7.6	8.7	2.3	1.0
17	4.7	2.0	4.7	6.9	3.3	3.6
18	9.5	9.1	4.7	4.1	3.2	4.4
19	4.0	1.3	1.8	0.9	5.3	0.5
20	3.2	0.9	6.2	4.2	2.1	1.0
21	4.3	1.1	10.0	3.0	1.4	1.0
22	9.0	13.0	9.0	2.8	2.1	0.7
Mean ± SEM c	7 ± 1	5.4 ± 1.3	7.0 ± 0.5	5.1 ± 1.3	2.1 ± 0.2	4 ± 1

[a] Velocity of the flowing NPs measured by STICS

[b] Diffusion coefficient of the NPs measured by TICS

[c] SEM represents for 22 regions

Table 3-9: Effective velocities of different organelles co-transport with PLLA-Hyp NPs in different regions inside A549 cells. The magnitude and direction of the co-transport has been shown in Figure 3-3.

Regions	Co-transport			
	V_{STICCS} [a] (10^{-3} µm/s)			
	E-E [b]	L-E [c]	Lyso [d]	Mito [e]
1	80.6	83.1	97.3	31.9
2	76.3	23.9	26.2	64.6
3	143.5	70.5	53.2	100.9
4	113.0	75.2	39.9	58.5
5	107.6	95.9	45.8	20.2
6	52.0	33.6	49.2	118.6
7	134.2	169.9	10.6	33.0
8	124.5	26.4	42.1	58.3
9	36.8	32.7	161.2	17.5
10	163.2	28.2	50.6	32.5
11	104.5	26.0	23.9	35.4
12	38.0	15.5	36.8	78.6
13	142.2	32.3	15.5	22.3
14	40.9	37.8	81.8	69.9
15	104.1	18.6	109.7	18.0
16	125.9	59.4	36.9	33.5
17	41.1	56.6	23.1	92.6
18	88.8	56.7	53.1	181.6
19	35.1	50.9	30.9	31.9
20	21.0	60.6	87.9	56.0
21	29.1	172.4	151.1	156.8
22	76.7	60.7	49.2	115.1

[a] Velocity of the co-transport population measured by STICCS

[b] Early-endosomes

[c] Late-endosomes

[d] Lysosomes

[e] Mitochondria

Table 3-10: Effective flow velocities of early-endosomes, late-endosomes, lysosomes and mitochondria of A549 cells. The velocities are measured in 22 different regions inside the cells without or with NPs and nocodazole treatments. Figure 3-4 presents the magnitude and direction of the velocity vectors for different regions inside the cells.

Cell regions	Without treatment				Treated with PLLA-Hyp NPs				Treated with PLLA-Hyp NPs and nocodazole			
	V_{STICS}[a] (10^{-3} µm/s)				V_{STICS} (10^{-3} µm/s)				V_{STICS} (10^{-3} µm/s)			
	E-E[b]	L-E[c]	Lyso[d]	Mit[e]	E-E	L-E	Lyso	Mit	E-E	L-E	Lyso	Mit
1	2.7	14.0	4.6	4.2	9.5	4.2	7.0	3.0	3.6	2.1	0.9	2.2
2	4.1	3.4	10.9	5.1	8.6	1.8	3.0	4.0	2.7	1.7	4.2	1.2
3	10.6	14.9	6.4	6.6	8.5	8.9	7.6	9.9	2.1	3.3	3.1	2.4
4	2.3	3.8	9.0	3.6	6.8	14.8	9.9	6.7	4.1	0.2	2.5	1.7
5	4.6	6.7	2.7	6.3	7.7	12.3	5.5	8.7	2.8	3.0	0.7	1.2
6	3.4	4.0	1.5	1.0	9.9	8.5	5.1	12.2	1.1	2.8	0.1	1.6
7	4.0	0.8	8.4	6.4	8.1	18.0	7.8	4.7	1.6	0.8	3.4	2.2
8	4.9	2.4	10.1	1.5	7.3	5.7	3.0	7.4	2.1	1.0	4.0	2.7
9	4.2	3.4	9.8	5.0	5.6	8.0	10.8	1.1	1.5	1.2	0.9	3.3
10	10.0	16.7	5.7	13.4	9.9	7.1	23.7	5.5	1.4	2.5	3.0	3.4
11	1.7	9.1	2.2	0.9	6.7	7.6	24.5	8.5	1.3	3.7	0.6	3.7
12	13.9	6.3	3.1	8.6	3.5	5.2	1.7	10.3	0.8	1.9	3.3	3.8
13	8.5	9.4	8.1	2.0	12.5	2.4	7.7	8.4	0.9	0.7	2.0	1.3
14	1.5	2.0	7.5	3.5	10.7	23.6	7.6	8.6	1.7	1.2	2.0	1.9
15	2.8	5.1	4.4	2.8	10.5	12.2	14.9	11.7	2.3	1.3	1.0	3.8
16	3.2	4.6	2.9	4.6	8.7	9.9	10.5	9.7	1.5	3.1	1.9	4.2
17	2.8	5.8	8.7	6.1	2.8	6.4	14.2	10.6	1.9	2.5	1.7	2.0
18	5.2	2.6	8.1	4.5	16.8	16.1	7.7	6.4	2.7	1.5	2.1	3.6
19	5.6	4.6	6.5	2.1	8.2	21.7	31.6	8.5	1.3	4.0	2.7	3.6
20	8.1	3.5	5.6	5.6	2.1	17.2	6.4	9.4	0.9	5.3	0.3	3.4

21	4.0	2.3	3.3	2.3	1.6	11.6	30.9	13.1	0.6	2.7	2.6	1.2
22	3.5	2.3	3.4	5.4	4.8	4.5	14.6	3.7	1.0	1.9	1.4	3.0

[a] Velocity measured by STICS

[b] Early-endosomes

[c] Late-endosomes

[d] Lysosomes

[e] Mitochondria

4 Interaction of polystyrene nanoparticles with hematopoietic progenitor cells: uptake and release

This chapter is based on:

Hematopoietic progenitor cells release polystyrene nanoparticles

Sarah Deville, Wahyu Hadiwikarta, Nick Smisdom, Bart Wathiong, Marcel Ameloot, Inge Nelissen, Jef Hooyberghs.

Manuscript in preparation.

4.1 Abstract

$CD34^+$ HPCs offer great opportunities to develop new treatments for numerous malignant and non-malignant diseases. NP-based strategies can further enhance this potential, broadening the scope to new theranostics as well. A thorough understanding of the loading capacity of HPCs towards NPs including the time kinetics involved, is essential to a successful application. Therefore, this study focusses on the interaction kinetics of 40-nm sized carboxylated PS NPs by HPCs. Interestingly, a transient association of the NPs with the cells was observed, reaching a maximum within one hour and declining afterwards. This behaviour was not seen in CD34-DCs differentiated from $CD34^+$ HPCs, which display a monotonic increase in NPs load similar to previous studies in immortalized cancer cell lines. Moreover, we demonstrated that this transient interaction requires an energy-dependent cellular process, suggesting active loading and release of the NPs by the HPCs. This novel observation offers a unique approach to transiently equip therapeutic cells with an active cargo. A simple theoretical approach (modelling NP loading and release) is presented, contributing to a framework to describe the observed transient interaction processes of NPs in HPCs.

4.2 Introduction

HSCs and HPCs offer great opportunities to develop new treatments for numerous malignant and non-malignant diseases. Their ability for self-renewal and to differentiate into all blood lineages is nowadays utilized for stem cell therapies [327]. New strategies utilizing viral vectors or, more recently, NPs attempt to manipulate these cell types, or track or guide them to the place of action [328, 329]. The usage of NPs for HSCs- and HPCs-based cell (and concurrent and/or associated gene) therapies has received considerable attention as it can circumvent efficacy and safety issues of the classical vehicles [330, 331].

Due to their small size, NPs possess new chemical and physical properties as compared to the corresponding bulk material. Since NP size can be in the same order of magnitude as biomolecules and viruses, they are capable to enter cells and interact with the cellular machinery [50, 226]. In the medical field, NP-based strategies offering unprecedented applications are therefore increasingly preferred over the traditional diagnostic and therapeutic methods. Indeed, (i) NPs can easily be loaded with imaging agents, bio-active molecules and drugs due to their large surface area and inner volume, (ii) NPs' surfaces can be easily functionalized and as such have the possibility to allow for specific (sub)cellular targeting, (iii) NPs display an enhanced circulation time in the blood compared to traditional therapeutics, and (iv) NPs can be made multifunctional to exert both diagnostic and therapeutic actions [332]. These features enable a more efficient targeting, guidance and actuation towards HSCs and HPCs. As a result, the utilization of NPs holds great promise for improved cell and gene therapies [328].

Recent studies have focused on directing NPs towards HSCs, however, the use of NPs in combination with HSCs is not yet fully exploited. HSCs have been labelled with SPIO NPs and gadolinium oxide (Gd_2O_3) NPs for MRI contrast enhancement and cell tracking [333-336]. Additionally, the delivery of peptide nucleic acids by poly(lactic-co-glycolic acid) (PLGA) NPs for genome editing in HSCs is currently under investigation [337, 338]. In the available knowledge, limited attention is payed to the loading capacity of HSCs and HPCs with NPs, not to mention the kinetics involved. Since this determines the efficacy and safety of nanotechnology-based applications, it is definitely worthwhile to consider these aspects in more detail.

In the present study, we investigated the interaction, which includes the association with the cell membrane and uptake, and kinetics of human cord blood-derived $CD34^+$ HPCs with well-defined, 40-nm sized fluorescently dyed carboxylated PS NPs. PS NPs are of medical interest as multifunctional carriers for therapy [175, 339]. They are also commonly used as a model NP to study the interaction with biological systems because of their commercial availability,

high quality, and large range of sizes and surface chemistries [221]. A unique transient loading behaviour was observed, suggesting active loading and release of the NPs by HPCs. This behaviour was compared with the PS NPs' interaction with myeloid-type CD34-DCs. DCs are derived by differentiation from $CD34^+$ HPCs and play a key role in initiating, directing and controlling both the innate and adaptive immune response [340]. The CD34-DCs did not exhibit the transient loading.

4.3 Materials and methods

4.3.1 Isolation and culture of $CD34^+$ HPCs and CD34-DCs

$CD34^+$ HPC isolation and culture procedures have been described previously [341]. Briefly, human cord blood samples were collected from umbilical blood vessels of placentas of full-term infants, born at the Heilig Hart hospital in Mol, Belgium and the St. Dimpna hospital in Geel, Belgium. Informed consent was given by the mothers and the study was approved by the ethical commission of both hospitals. Mononuclear cells were separated from the cord blood by density gradient centrifugation (Ficoll-Paque™ plus, GE Healthcare, Uppsala, Sweden). Subsequently, $CD34^+$ HPCs were extracted using positive immunomagnetic selection (EasySep® human CD34 positive selection kit, Stemcell Technologies, Grenoble, France) according to the manufacturer's guidelines.

HPCs were cultured for 12 days in Iscove's Modified Dulbecco's Medium (IMDM, Gibco, Paisley, UK) supplemented with 10% FBS (PAA laboratories, Pasching, Austria), 2% P/S (5000 U/ml-5000 µg/ml, Gibco) and 1% BSA (Sigma-Aldrich, Steinheim, Germany) in the presence of tumor necrosis factor alpha (TNF-α, 250 U/ml, Roche applied science, Upper Bavaria, Germany), granulocyte-macrophage colony-stimulating factor (GM-CSF, 5000 U/ml, Gentaur, Brussels, Belgium), stem cell factor (SCF, 5 U/ml, Biosource, Nivelles, Belgium) and interleukin 4 (IL-4, 1000 U/ml, Biosource) to induce proliferation and differentiation towards immature CD34-DCs.

4.3.2 Nanoparticles and characterization

Yellow-green (λ^{ex} 505 nm, λ^{em} 515 nm) 40-nm carboxylated PS NPs were purchased from Molecular Probes (Invitrogen, Merelbeke, Belgium). NP dispersions were prepared by diluting the concentrated stock solutions in CCM – which is IMDM supplemented with 10% FBS, 2% P/S and 1% BSA – immediately before addition to the cells. PS NPs were characterized in both water and CCM by means of NTA using a Nanosight NS500 instrument (NanoSight Ltd., Wiltshire, United Kingdom) and zeta potential determination using ZetaPALS (Brookhaven instruments corporation, Holtsville, USA).

4.3.3 Dialysis of nanoparticles

PS NPs stock solutions were dialyzed using Slide-A-Lyzer® Mini dialysis units and Slide-A-Lyzer® Gamma Irradiated dialysis cassettes (10 000 MWCO Plus, Thermo Scientific, Rockford, USA) against citric acid – phosphate buffers with a different acidity (pH 5 – pH 7). The fluorescence intensity of the dialysate was monitored using a fluorescence spectrophotometer (LS55, Perkin Elmer, Waltham, Massachusetts, USA). BODIPY® FL (4,4-Difluoro-5,7-Dimethyl-4-Bora-3a,4a-Diaza-s-Indacene-3-Propionic Acid) (Life Technologies) was used for free dye as an control in the dialysis experiments. In order to obtain free dye for the cell exposure experiments, PS NPs were dialyzed against citric acid – phosphate buffer with pH 7 for 48 hours. The dialysate containing only the dye was further diluted and used to expose the cells. This dilution, taking into account the additional dilution due to the dialysis, was performed to obtain an amount of dye equal to the amount of free dye present in the PS NP solution used in the cell experiments.

4.3.4 Flow cytometry

NP uptake was evaluated by means of flow cytometry (FACS Calibur™, Becton Dickinson, San Jose, California, USA). HPCs and CD34-DCs were seeded at a density of 5×10^4 cells/well in 96-well plates and immediately exposed to PS NPs at 37°C and 5% CO_2 until analysis. For the experiments performed at 4°C, cells

were cooled down in the refrigerator (either one hour before exposure or after one hour of exposure) and handled on ice. After the desired exposure time, cells were transferred to polystyrene tubes (Becton Dickinson), washed three times with PBS (without Ca^{2+} and Mg^{2+}, Gibco) to remove loosely adherent NPs and collected by centrifugation. Flow cytometric analyses were performed on fresh cell suspensions directly after the final collection. HPCs and CD34-DCs were identified by light scatter using gates to exclude dead cells and cell debris. Light scattering profiles and fluorescence histograms were evaluated using CellQuest™ (Becton Dickinson) and home-written MATLAB routines (The Mathworks, Eindhoven, The Netherlands). NP uptake was evaluated by the geometric mean of the fluorescence intensity (GMFI) distributions. The same photomultiplier voltages and compensation settings were applied for HPCs and CD34-DCs in order to allow comparison between both.

4.3.5 Confocal microscopy

HPCs and CD34-DCs were exposed to 50 µg ml^{-1} PS NPs for 1, 2, 3, 4, 6 or 24 hours at 37°C and 5% CO_2. After exposure, cells were washed with PBS for three times and cell membranes were labelled with 5 µg/ml Alexa Fluor® 555 conjugated wheat germ agglutinin (WGA, Invitrogen) at 4°C for 30 minutes. After washing, cells were fixed with 4% formalin solution (Sigma-Aldrich) and transferred to a microscope slide by means of cytocentrifugation (Tharmac Cellspin II, Tharmac, Waldsolms, Germany). Cells were mounted with Vectashield® mounting medium containing DAPI (Vector Laboratories, Peterborough, United Kingdom). Images were acquired using an epifluorescence Axiovert 200M equipped with a Zeiss LSM 510 Meta CLSM (Zeiss, Jena, Germany) and a LD C-Apochromat 40x/1.1 W Korr UV-VIS-IR water immersion objective (Zeiss). PS NPs were excited with the 488 nm line of a 30 mW air-cooled argon ion laser (tube current set at 5.9 A) under the control of an acoustic-optic modulator. WGA was excited using a 543 nm helium neon laser. DAPI was excited using 150 fs pulsed laser light of a Ti:Sapphire laser (MaiTai, Spectra-Physics, Utrecht, The Netherlands) tuned at an output wavelength of 730 nm. The excitation light was directed to the sample through a dichroic beam

splitter (HFT UV/488/543/633). For the detection and separation of the different emitted fluorescence signals, a secondary dichroic beam splitter NFT 490 or NFT 545, as well as three band-pass filters BP 390-465 (DAPI), BP500-530 (PS NPs), or BP565-615 (WGA) were used. Signals were directed towards an internal analog PMT (Zeiss).

4.3.6 Cell viability and proliferation

Cytotoxicity of the PS NPs was assessed after 24 hours of cell exposure using Annexin V staining (Life Technologies) according to the manufacturer's protocol. Percentage positive cells was determined by flow cytometry. Staurosporine (0.1 µM, Sigma-Aldrich) was used as a positive control for programmed cell death. Cell proliferation was determined by counting the live cells at different time points using NucleoCassette™ and NucleoCounter® (ChemoMetec, Allenød, Denmark) for HPCs, and trypan blue exclusion (Invitrogen) using a Bürker counting chamber for CD34-DC.

4.4 Results and discussion

4.4.1 Nanoparticle characterization

Fluorescently labelled, carboxylated PS NPs with a nominal diameter of 40 nm were used in present study. Before interaction with cells, proteins and electrolytes present within the cell culture medium may influence the intrinsic physicochemical parameters of the NPs used. Therefore, characterization of PS NPs dispersions in both water and CCM after different incubation periods was performed by means of NTA (Figure 4-1). NP hydrodynamic diameter increased immediately from 50 ± 1 nm to 65 ± 5 nm when diluted in CCM due to adhering biomolecules. The resulting PS NPs dispersions remained stable over the duration of the experiment. No signs of agglomeration or an increase of the biomolecular corona over time were found up to 96 hours. The zeta potential of PS NPs reached a value close to neutrality when dispersed in CCM (from -40 ± 1 mV in water to 2 ± 3 mV in CCM).

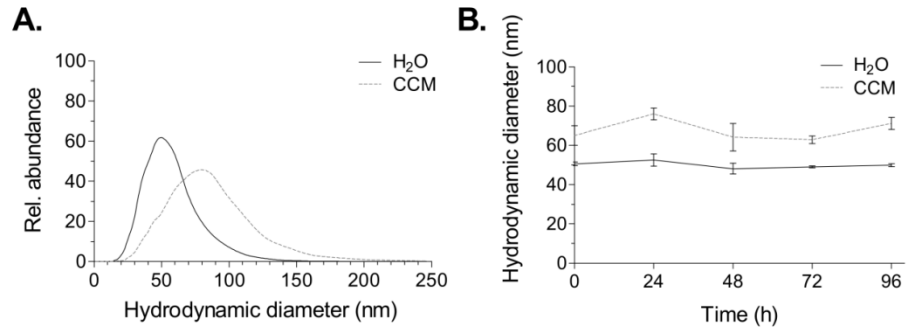

Figure 4-1: PS NPs in cell culture conditions (50 µg/ml) acquire a biomolecular corona and remain colloidally stable. (a) Size distribution of PS NPs after 24 hours of incubation at 37 °C and 5% CO_2 respectively in H_2O and CCM. The NP hydrodynamic diameter increased from 50 ± 1 nm to 76 ± 3 nm when dispersed in CCM. (b) The hydrodynamic diameter does not change over time, indicating a stable dispersion. *All sizes are reported as the average ± SEM of the mode of NP hydrodynamic diameter distributions obtained from 3 replicates.*

4.4.2 Transient nanoparticle loading in HPCs

The interaction of HPCs with NPs was evaluated by exposing the cells to a concentration range of fluorescently labelled PS NPs ranging from 5 to 90 µg ml^{-1}. After 24 hours of continuous exposure, the cellular NP load was evaluated by means of the geometric mean fluorescence intensity (GMFI) measured using flow cytometry (Figure 4-2A). HPCs displayed an almost linear loading profile with increasing NP concentration. However, compared to the differentiated CD34-DCs (Figure 4-2B), HPCs had a smaller NP loading capacity. As HPCs are nonphagocytic cells and have a lower cytoplasmic-to-nuclear ratio, they are expected to be less efficient in engulfing large amounts of extracellular material, such as NPs, than DCs with a prominent phagocytic activity [342]. In order to confirm if the processing of NPs is different by both cell types, the interaction of HPCs and CD34-DCs with NPs was studied as a function of time. The NP load was measured after 1, 2, 3, 4, 5, 6, and 24 hours of exposure to 50 µg ml^{-1} PS NPs (Figure 4-2C, Figure 4-2D).

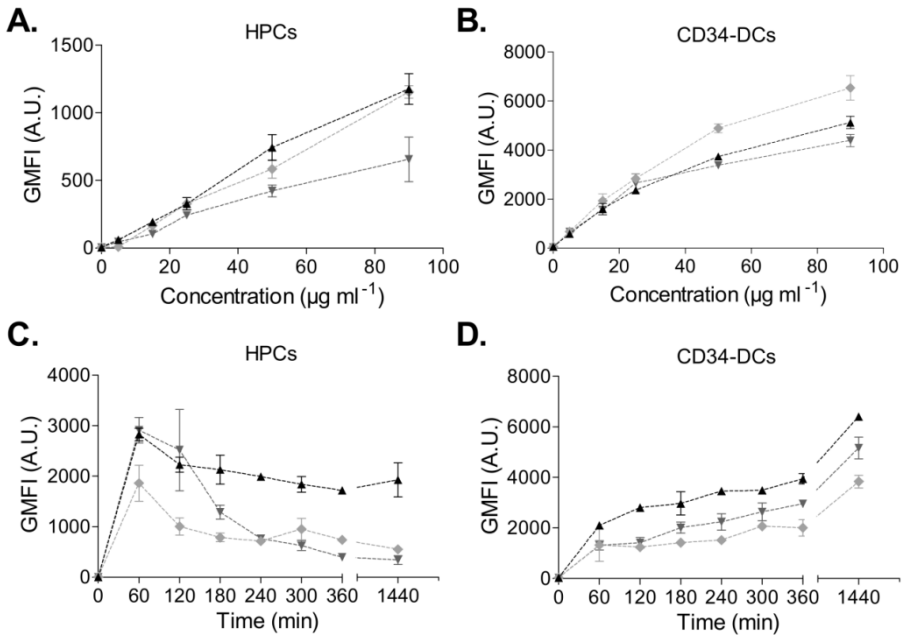

Figure 4-2: CD34$^+$ HPCs show reversible association with 40-nm sized carboxylated PS NPs, a behaviour lost in HPC-derived CD34-DCs . Dose-dependent loading of HPCs (A) and CD34-DCs (B) after 24 hours of exposure to fluorescent 40-nm sized carboxylated PS NPs. The total GMFI of CD34-DCs is larger than the GMFI of HPCs, as expected from the lower cytoplasma-to-nucleus ratio of the latter. In addition, a remarkable discrepancy is observed between the time evolution of NP processing by HPCs (C) and CD34-DCs (D). When exposed to 50 µg ml^{-1} fluorescent 40-nm sized carboxylated PS NPs, HPCs display a transient increase in GMFI in contrast to the steady and continuous increase observed in CD34-DCs. *All values are reported as the average value ± standard derivation (SD) of 3 technical replicates. Different curves represent independent biological experiments from different donors.*

This concentration was chosen because it is still in the (almost) linear range of the concentration-response profile of HPCs while resulting in a strong signal. Surprisingly, within the first hour after exposure, both HPCs and CD34-DCs promptly accumulated NPs, even at a comparable rate. In CD34-DC the NP load continued to increase up to 24 hours post-exposure in a linear behaviour/fashion, similar to what has been published previously for cancer cell

lines [50, 343]. HPCs, however, reached their maximum NP load within one hour of exposure, declining to a stationary state afterwards. Similar observations of decreasing cell-associated PS NPs fluorescence were made using confocal microscopy analyses (Figure 4-6). Although HPCs obtained from different donors reveal variation in the absolute amplitude, all samples demonstrated this transient loading.

4.4.3 Energy dependent loading of HPCs and CD34-DCs with nanoparticles

The NP load of the cells could accumulate in several ways. A discrimination between passive or active processes can be made by performing the NP exposure of the cells at 4°C. This is a common way to assess the involved mechanisms as cooling down the cells inhibits all energy-dependent cellular processes [344]. Pre-incubation at 4°C for 1 hour and exposure of HPCs and CD34-DCs to 50 µg ml^{-1} PS NPs also at 4°C strongly abolished the loading with PS NPs. This was even more obvious when comparing the acquired load with the load accumulated by their cellular counterparts obtained from the same donors but exposed at 37°C (Figure 4-3A, Figure 4-3B). This unambiguously demonstrates the loading process as being an active process.

In addition, cells were exposed to 50 µg ml^{-1} PS NPs for one hour at 37°C and cooled down to 4°C in the presence of PS NPs in order to reveal whether the apparent PS NP release process in HPCs is energy-dependent (Figure 4-3C, Figure 4-3D). Although HPCs at 37°C showed a strong decline in GMFI, cooling down to 4°C completely blocked this process resulting in a constant load. These results clearly demonstrate that both the loading and release processes in HPCs are energy-dependent. Moreover, these observations suggest that an arrest of NP loading occurs over time, or that the release rate of NPs changes over time, or that the signal from the PS NPs declines during the course of the measurement, or a combination of these processes.

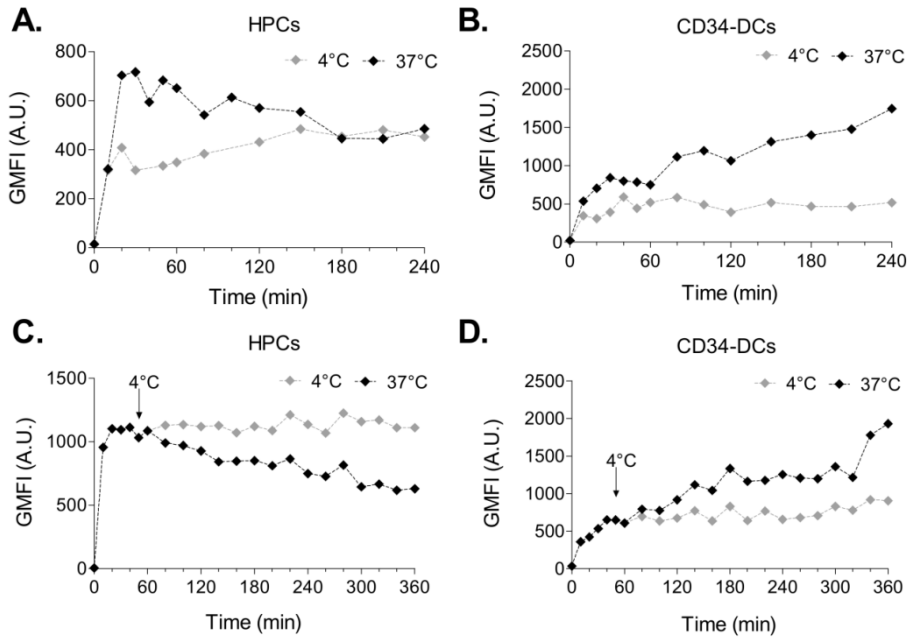

Figure 4-3: PS NPs loading and release are energy-dependent. The loading with fluorescent 40-nm PS NPs is energy-dependent in both HPCs (A) and CD34-DCs (B). Cells were incubated for one hour at 37°C or 4°C prior to exposure to 50 µg ml^{-1} uptake PS NPs at the same temperature. Furthermore, energy-dependent release of NPs is demonstrated in HPCs (C), while CD34-DCs continue to accumulate NPs (D). Here, cells were exposed to 50 µg ml^{-1} PS NPs at 37°C and after 1 hour cells were cooled down to 4°C to block all active processes. *Different curves represent different treatment conditions of cells from one single donor. A representative example is shown.*

4.4.4 The observed transient loading cannot be ascribed to the fluorescent staining of the nanoparticles

In order to support the hypothesis of NP release by HPCs, additional experiments were performed to exclude technical artefacts in the experimental design. A widespread problem with the usage of fluorescently labelled NPs is the presence of residual free dye or labile dye which represents dye leaching out of the NPs [50, 345]. This could confound the obtained results in HPCs but seems, however, not to agree with the results observed in CD34-DCs.

In order to characterize the interference by dye leaching, dialysis experiments were performed to determine the extent of free dye under the experimental circumstances.

NPs are recognized to enter mammalian cells through the endocytosis mechanism [346, 347]. NPs' journey through the endocytic compartment corresponds with an acidification of the NPs' environment. The endosomal acidification was mimicked here by dispersing the PS NPs in a citric acid – phosphate buffer having a pH of 5, 6 or 7, which corresponds to the pH within the endolysosomal compartment [348]. PS NPs stock dispersions were used as purchased (stock PS NPs) or pre-dialyzed for 24 hours to remove all labile dye already present in the NPs dispersions (pre-dialyzed PS NPs). Thereafter, PS NPs dispersions were dialyzed against citric acid – phosphate buffers with different acidity. The time kinetics of the dialyses were measured using fluorescence spectroscopy (Figure 4-7).

A limited amount of labile and free dye was present in the PS NP stock solutions. Pre-dialysis of the PS NP stock solutions, however, was not effective in reducing the further release of labile or free dye in the dialysate. No significant effect of acidification on leaching was found. To assess the potential impact of free dye on the observed interaction kinetics of the NPs in HPCs, cells were exposed to the free dye present the dialysate after 48 hours of dialysis at 37°C and 5% CO_2, or to corresponding amount of PS NPs (Figure 4-8). The free dye only comprised a small portion of the total fluorescence intensity compared to the PS NPs, which remained rather stable in function of the time. These data suggest minor impact of the free dye on the observed time kinetics of PS NPs in HPCs.

To investigate possible pH dependent changes in the fluorescence properties of the dyes embedded within or attached to the PS NPs fluorescence lifetime spectroscopy experiments were performed. The mean recovered fluorescence lifetime did not alter within the tested pH range of pH 5 to 7, indicating no significant change in the fluorescence properties of the fluorophores (Figure 4-9, Table 4-1).

Since PS NPs loading and release were shown to be strongly reduced when incubated at 4°C, the effect of temperature on the presence and release of labile and free dye was determined. This was achieved by dialysis at 4°C and compared to 37°C against a citric acid – phosphate buffer of pH 7 (data not shown). A slight difference between both conditions was found with 8% versus 12% of labile or free dye determined after 24 hours of dialysis at 4°C and 37°C respectively. These findings demonstrate that the arrest of the release phenomenon of HPCs due to cooling down to 4°C cannot be accredited to labile and free dye alone. As incubation of PS NPs at 4°C slows down the leaching only minimally, it would not be sufficient to retain the decay in GMFI of HPCs when the observed release process was due to a passive diffusion process such as dye leaching.

4.4.5 Negligible cell death and proliferation of HPCs and CD34-DC upon nanoparticle exposure

Cytotoxic effects as well as cell proliferation, in which the NP load will be divided over the daughter cells, could be another cause of the observed NP load [50, 343]. In order to investigate the presence of cytotoxicity, an Annexin V staining was performed after 24 hours of exposure to different doses of PS NPs. In addition, the cell number was determined in both HPCs and CD34-DCs (Figure 4-4). Since neither an increased apoptosis nor a pronounced proliferation was detected for both cell types, it is reasonable to conclude that the observed transient load is not a consequence of these processes.

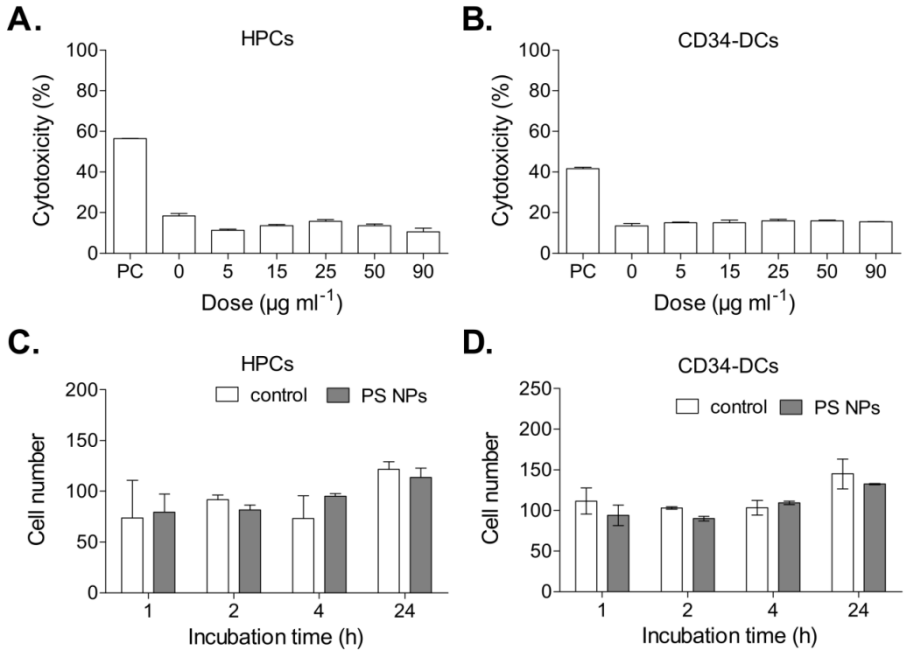

Figure 4-4: Assessment of apoptosis and cell proliferation of HPCs and CD34-DCs after exposure to 40 nm carboxylated PS NPs. HPCs (A) and CD34-DCs (B) were exposed for 24 hours to PS NPs at 37 °C and evaluated for induction of apoptosis using Annexin V staining. Staurosporine (0.1 µM) was used as a positive control (PC). Mean values ± SD of technical replicates (HPCs n=2; CD34-DC n=3) are shown. (C-D) Cell counting indicated a modest increase in the total cell number was found during the experimental time. Representative examples for HPCs (C) and CD34-DCs (D) are shown, with and without exposure to 50 µg ml^{-1} PS NPs. Mean values ± SD of 2 technical replicates.

4.4.6 Modelling the kinetics of cellular nanoparticle load

The dynamics of PS NPs in HPCs can be easily described mathematically. Denote the cellular NP load by the number of particles *N*, which is proportional to the experimental fluorescent signal measured by the flow cytometer (GMFI). To model the kinetics of *N* we assume that cell proliferation and cell death can be neglected, which is realistic for the experiments with HPCs and also for shorter time scales of CD34-DCs (Figure 4-4). Then, the time dependence of *N* is

determined by two competing contributions: a positive contribution due to the uptake of NPs from the extracellular medium increasing the cellular NP load and a negative contribution due to NPs released from the cell and entering the medium again. In its most simple form the time derivative of *N* can be modeled by:

$$\frac{dN}{dt} = R_{on}.c - R_{off}.N \qquad \text{(Eq. 4-1)}$$

in which *c* is the extracellular NP concentration, assumed to be a reservoir and hence constant, R_{on} and R_{off} are the rates of the competing processes.

If R_{on} is constant and R_{off} is zero, there is no NP release and *N* increases linearly in time. This behaviour is essentially observed in the CD34-DCs (Figure 4-2D) and many cell lines for short time scales [50]. Our experiments with HPCs exhibit clearly a different time dependent loading (Figure 4-2C), suggesting the presence of a release process, i.e. a positive R_{off} value with a NP release proportional to the load *N*. In this case the cellular NP load will experience a decreasing growth and will eventually saturate at a dynamic steady-state. However, if R_{off} is assumed to be a constant value, i.e. time-independent, *N* will be a monotonic function of time, which is clearly not what we observe. Our experiments show that the load *N* peaks within a time frame of one hour and decreases afterwards (Figure 4-2C). This suggests an active response in which the release rate increases over time. The experimental behaviour can be modelled by (Eq. 4-1) if we assume a time dependent R_{off} rate (Figure 4-5A). Figure 4-5B shows the estimations of R_{off} based on (Eq. 4-1) in which the time derivative is approximated by the finite time difference determined by the experimental measurement frequency. This time dependence can be used to numerically solve differential (Eq. 4-1) and it results in the simulated load presented in Figure 4-5A. This first model approach indicates that the release rate of the PS NPs increases in time; this result is rather robust and remains present also when e.g. a fixed background signal is subtracted from the NP load signal for instance due to the adhesion of NPs to the cell membrane.

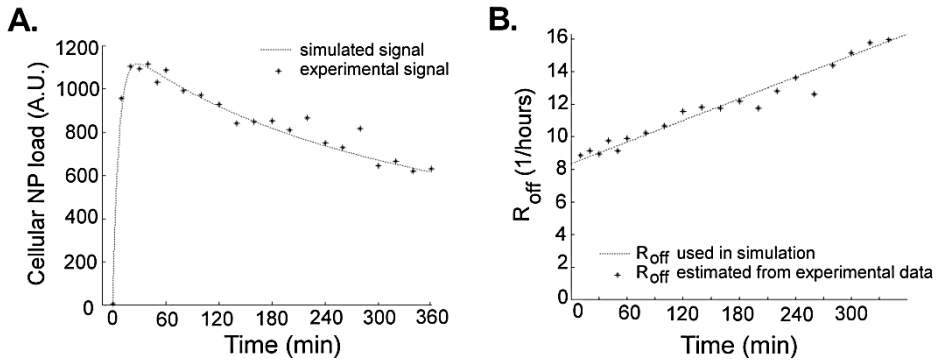

Figure 4-5: Model of the cellular load kinetics of PS NPs in HPCs describing the presence of a release process. The simulated and the experimentally obtained values of (a) The cellular NP load as a response to an exposure at a fixed NP concentration starting at time zero. (b) The release rate R_{off} as a function of time.

4.5 Conclusion

In the present study of interaction kinetics of carboxylated PS NPs, HPCs and CD34-DCs were observed to respond differently to identical NPs and under identical conditions. This could partially be explained by the difference in their cell physiology. CD34-DCs are more confined to and involved in antigen presentation and immune responses [340], whereas HPCs' main ability is to self-renew or multiply [327]. The differences in cell physiology are coupled with morphological differences. HPCs derived from cord blood have a high nucleus-cytoplasm ratio, with the cytoplasm poor in organelles, although a few mitochondria and endoplasmic reticulum cisternae can be seen [342]. In contrast, CD34-DCs have a relatively smaller nucleus/cytoplasm ratio, and thus, a cytoplasm containing significantly more organelles including endosomal vesicles [349]. The observations made in this study corroborate the involvement of active cellular processes in the newly observed transient load of HPCs. To our knowledge, this is the first time that this transient loading behaviour of HPCs with PS NPs has been reported. Brüstle *et al.* demonstrated the interaction of HPCs and PS NPs, where the uptake of 120-nm sized carboxylated PS NPs was evaluated after 24 hours of exposure and showed the presence of intracellular

vesicles containing NPs [350]. *Duinhouwer et al*. showed uptake of PGLA NPs in HPCs after 4 and 20 hours of exposure, without affecting their proliferation and differentiation capabilities [351]. Other studies in which iron oxide and Gd_2O_3 NPs by HPCs were used for MRI applications have reported solely their uptake and little effect on cellular function [333-335, 352, 353]. None of these preceding studies have reported the short-time kinetics of NPs in HPCs.

Transient loading of cells requires the release of the NPs, as we have described using the physics model. NP release has been reported before in multiple cell types and reviewed by *Sakhtianchi et al.* and *Oh et al.* [347, 354]. Internalized NPs are often delivered in early endosomes, which are considered as the main sorting station of the endocytic machinery [27, 58]. Although the majority of the NPs resides in the endolysosomal pathways, a fraction of the NPs is capable to escape to recycling endosomes and it is eventually released by cells [355, 356]. The NPs that are trapped in the endocytic machinery will end up in the lysosomal compartments. Some of the lysosomes are capable in undergoing exocytosis through fusion with the plasma membrane [198, 357]. In addition, NPs that have entered the endoplasmic reticulum of the Golgi apparatus may leave cells via vesicles related to the secretion system [358]. Also NPs that are present in the cytoplasm (e.g. NP uptake by diffusion or endolysosomal escape of NPs) can leave the cell as well through re-entry to the vesicular system or via unspecific mechanisms [354, 357]. Based on these reports, it is conceivable to have also an active release in HPCs.

Therapeutic strategies and transplantations using HSCs and HPCs may benefit from their remarkable response to NPs. The observed release mechanism opens new opportunities for the safe delivery of drugs or molecules of interest with limited bio-accumulation. However, further investigation is required to reveal how HPCs are capable in mediating the release and which cellular functions and associated dynamics are involved in this process. The effects of NP species, size, functionalization, administered dose, incubation time and intracellular fate should be carefully investigated as well. The resulting knowledge will allow us to exploit the full potential of NP applications in medicine.

4.6 Supplementary material

4.6.1 Nanoparticle uptake and uptake kinetics in HPCs and CD34-DC

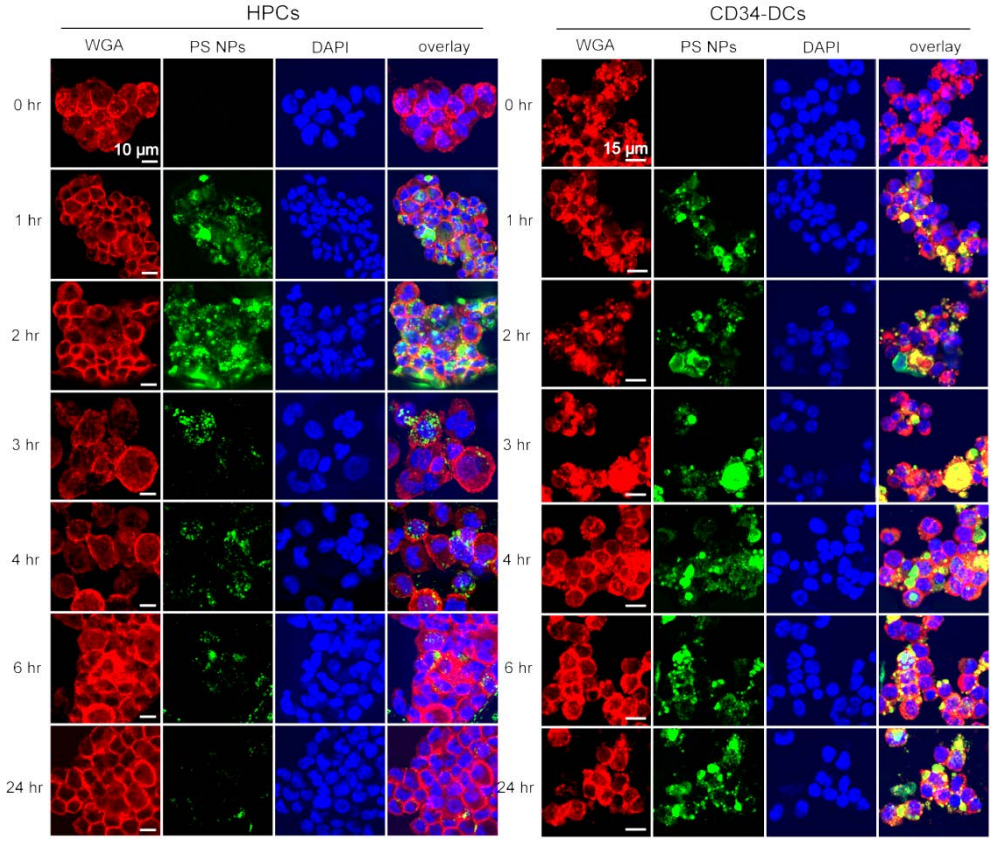

Figure 4-6: Uptake kinetics of 40-nm sized carboxylated PS NPs in HPCs and CD34-DCs. Microscopy images of time kinetics after exposure to 50 µg ml^{-1} uptake PS NPs (green). Nuclei of cells are labelled with DAPI (blue) and cell membranes labelled with Alexa Fluor® 555 conjugated WGA (red).

4.6.2 Dialysis of nanoparticles

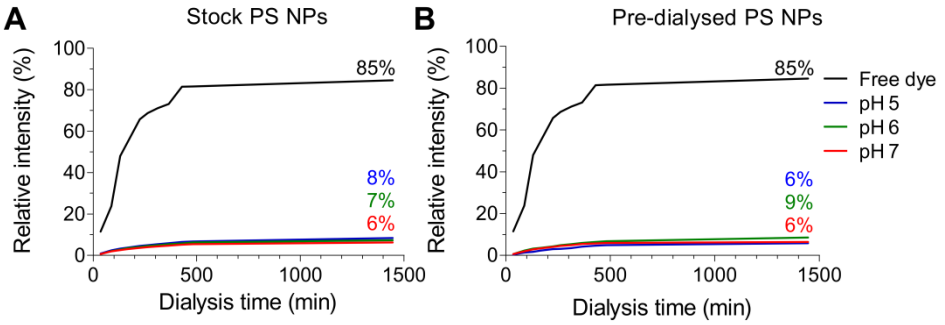

Figure 4-7: Normalized fluorescence intensity of dialysate after PS NPs or free dye dialysis at 37°C: (A) stock PS NPs and (B) pre-dialyzed PS NPs. Time kinetics of the normalized fluorescence intensity of the dialysate after dialysis of PS NPs or free dye against citric acid – phosphate buffers with different acidity. (A) PS NPs stock solutions were used as purchased (stock PS NPs) or (B) pre-dialyzed for 24 hours to remove all labile dye (pre-dialyzed PS NPs). Normalization was performed based on the fluorescence intensity of the PS NPs of free dye measured when diluted directly into the buffer (without dialysis).

4.6.3 Comparison between interaction kinetics of nanoparticles versus free dye in HPCs

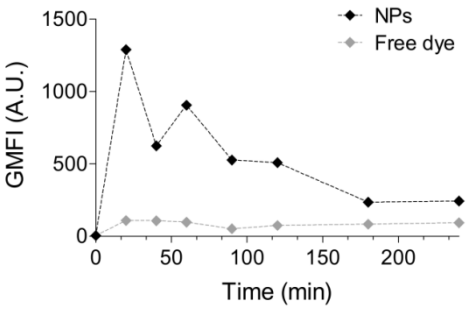

Figure 4-8: Loading kinetics of free dye and 40-nm sized carboxylated PS NPs in HPCs. Time kinetics of exposure to 50 µg ml^{-1} uptake PS NPs or exposure to the equivalent volume of free dye which was obtained by dialysis against PBS.

4.6.4 Fluorescence lifetime spectroscopy

The PS NPs stock solution was 100-fold diluted in citric acid – phosphate buffers of different pH (pH 5, 6 and 7). An identical microscope as used for imaging experiments was employed. The PS NPs were excited with a stationary femto-second pulsed laser (MaiTai DeepSee, Spectra-Physics) tuned at an output wavelength of 800 nm. The emission light was detected using non-descanned detection: the fluorescence was directed using a dichroic mirror KP650, a short-pass KP685 and a band-pass BP565-615 IR towards a photon-counting PMT (Hamamatsu 7422, Herrsching am Ammersee, Germany). This PMT was connected to an SPC830 card (Becker and Hickl, Berlin, Germany). For each buffer, minimum two time traces were collected in fifo mode for 60 s with a micro time resolution of 12 bit spread over 10 ns. The histogram of arrival times of the resulting data was analyzed using SPCImage utilizing an incomplete multi-exponential model consisting of two lifetime components. The mean lifetime τ_m was calculated using (Eq. 4-2):

$$\tau_m = \frac{\sum_{i=1}^{2} a_i \tau_i^2}{\sum_{i=1}^{2} a_i \tau_i} \qquad \text{(Eq. 4-2)}$$

where a_i and τ_i are respectively the amplitude and the lifetime of the i^{th} component.

Table 4-1: Fluorescence lifetime spectroscopy of PS NPs dispersed in citric acid – phosphate buffers with different acidity. The reduced χ^2 of the fit were all smaller than 1.7. No significant change in the mean fluorescence life time τ_m was found.

buffer acidity	a_1 [%]	τ_1 [ns]	a_2 [%]	τ_2 [ns]	τ_m [ns]
pH 5	68.5 ± 0.3	2.0376 ± 0.0007	31.5 ± 0.3	7.80 ± 0.03	5.705 ± 0.006
pH 6	71 ± 2	2.09 ± 0.04	29 ± 2	8.0 ± 0.1	5.72 ± 0.04
pH 7	72 ± 3	2.14 ± 0.08	28 ± 3	7.9 ± 0.2	5.6 ± 0.3

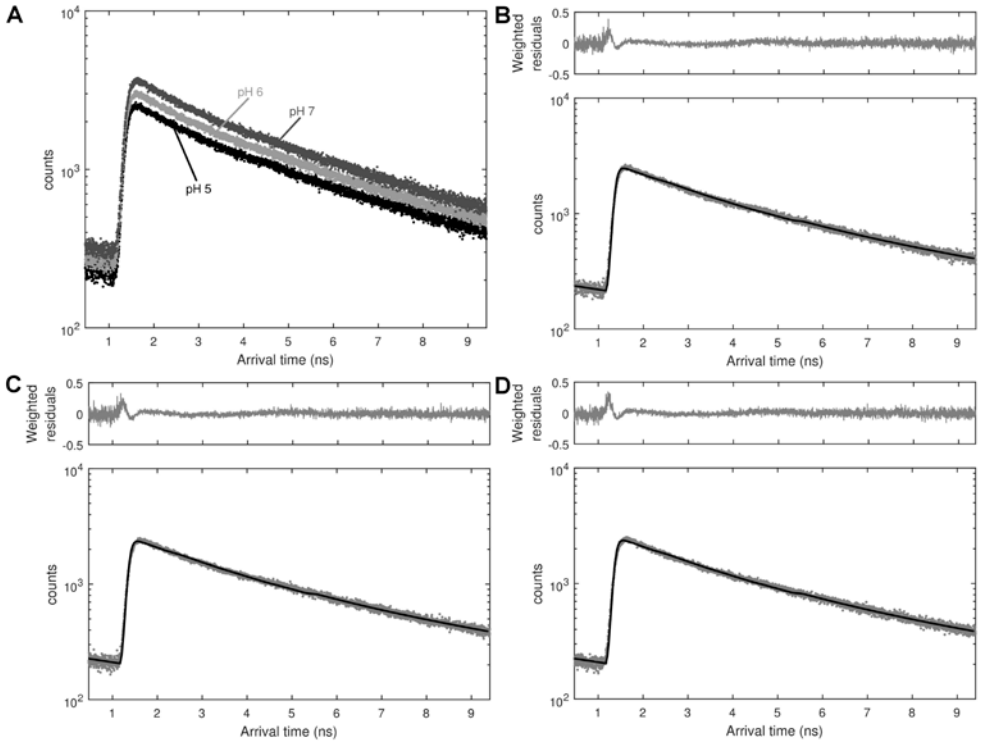

Figure 4-9: Histogram of the arrival times of fluorescence life time spectroscopy measurements of PS NPs dispersed in citric acid – phosphate buffers with different acidity. (a) Merged histograms; for visualization purposes, a multiplication of the recorded signals was performed: pH 5 × 1; pH 6 × 1.25 and pH 7 × 1.50. (b) pH 5. (c) pH 6. (d) pH 7. A representative example is shown with the recorded data in gray, the fit in black.

5 Interaction of gold nanoparticles and nickel (II) sulphate affects dendritic cell maturation

This chapter is based on:

I*nteraction of gold nanoparticles and nickel (II) sulphate affects dendritic cell maturation*

Sarah Deville, Birgit Baré, Jordi Piella, Kristof Tirez, Peter Hoet, Marco Monopoli, Kenneth Dawson, Victor Puntes, Inge Nelissen

Manuscript under review.

5.1 Abstract

Despite many investigations have focused on the pristine toxicity of GNPs, little is known about the outcome of co-exposure and interaction of GNPs with heavy metals which can possibly detoxify or potentiate them. Nickel is heavy metal with well document allergenic and carcinogenic potentials and it is one of the few materials that can form alloys with gold. The frequently occurring contamination of nickel in the environment can affect the GNPs toxicity as physicochemical interactions may either increase their persistence, change their bioavailability and/or alter their distribution and speciation. In present study the combined exposure of nickel (II) sulphate ($NiSO_4$) and GNPs on the maturation response of DCs was explored. In order to investigate whether GNPs interact with $NiSO_4$, citrate-stabilized 50-nm GNPs were dispersed in complex biological media and a detailed characterization of their possible interactions was performed using a broad range of experimental techniques including NTA, UV-Visible spectroscopy, ICP-MS, ζ-potential determination and proteomics. In addition, the effect of the co-exposure of GNPs on $NiSO_4$ allergenicity was assessed through *in vitro* studies in which immature myeloid CD34-DCs, differentiated from human cord blood-derived $CD34^+$ HPCs, were incubated in the presence of subtoxic concentrations of $NiSO_4$ and GNPs.

The physicochemical characterization of GNPs in complex media in the presence of $NiSO_4$ demonstrated a shift in protein corona composition, in which the attraction of low molecular weight proteins was favoured. No absorption of nickel(II) ions on the NPs' surface was detected. When CD34-DCs were treated with a mixture of $NiSO_4$ and GNPs, we observed a cell activation pattern that was significantly lower than the additive effect of both inducers with levels similar to those induced by $NiSO_4$ alone. ICP-MS analyses demonstrated a significant decrease in GNP uptake when $NiSO_4$ was present in the environment.

The presented results provide new insights in the interaction of heavy metals and NP on the maturation response of DCs. Moreover, this study highlights the necessity of mixture toxicology since these combined exposures are highly relevant for human subjection to NPs and risk assessment of nanomaterials.

5.2 Introduction

Although the nanotechnology industry is growing extremely fast, uncertainties concerning the interaction of NPs with their environment and their subsequent impact on biological systems still remain. Extensive investigations have focussed on the toxicity of single NPs, however, in the real-life environment NPs mostly occur in combinations with other particles, chemicals and/or biological compounds against a complex background. It is therefore more likely that humans and the environment eventually will be exposed to this cocktail of potential toxins. Indeed, NPs have been observed to be carriers for toxic ions, as in the case for radionuclei [359]. However, there is not only the transportation effect by NPs, but also transformations of NPs and ions when they mix. Recent studies have indicated that the interaction of NPs with heavy metals can possibly detoxify or potentiate their effects. For example, cell exposure to nanodiamonds and cupper(II) ions demonstrated a Trojan horse type effect, where adsorption of metal ions on the nanodiamonds' surface resulted in enhanced cytotoxic responses [360], and co-exposure of silica NPs and cadmium dichloride ($CdCl_2$) was reported to cause synergistically increased oxidative damage in the liver of mice [361], while arsene has been detoxified with iron oxide NPs [362]. These observations demonstrate the need to address interactions of living systems with NPs in the context of mixed exposure situations to adequately assess NPs' safety.

The application of GNPs is promising in a wide range of fields due to their chemical but not catalytic inertness, high biocompatibility and optical properties. Even though GNPs have been used since the ancient times, new applications of GNPs (e.g. the usage of GNPs in electronics [363, 364], sensors [365] and anticancer therapy [366-368]) are expanding tremendously during the last decade due to the advances in their controlled synthesis and surface functionalization [169, 369]. Although bulk gold is well known to be safe, at the nanoscale the surface chemical reactivity of GNPs (their catalytic effects due to the presence of low coordinated Au atoms at the surface of the NP) and the presence of stabilizing agents can cause toxic effects [370, 371]. Moreover, GNP

derivates have immunomodulatory properties in which both pro- and anti-inflammatory effects can be mediated through adjuvant effects or reduction of allergic responses [171, 372-374].

Nickel is a heavy metal with well documented allergenic and carcinogenic potential. Nevertheless, it is frequently used in industrial and consumer products, including stainless steel, alnico magnets, special alloys, coinage, jewellery and rechargeable batteries. The release of nickel ions from products may cause detrimental effects to the respiratory tract and the immune system, including allergic contact hypersensitivity and atopic dermatitis [375-377]. In addition to inducing cancer at high exposures [378], it contributes to the development of widespread allergic diseases which have become a serious health burden with a prevalence of more than 10% in the general population. Besides mercury, nickel is one of the few materials that forms alloys with gold. Direct interaction of GNPs and mercury(II) has already been observed by *Ojea-Jimenez et al*, who reported that GNPs are potent in the sequestration and removal of mercury(II) from aqueous solutions through chemisorption, followed by amalgam formation and mineral precipitation [379]. In those experiments, the elimination of mercury(II) caused large changes in the GNPs morphology and made them evolve into non-spherical coalescent NPs of increasing size, which were expulsed from the solution [379].

With the multiple applications of GNPs and the frequently occurring contamination of nickel in the environment, characterization of the combined exposure of living systems to GNPs and nickel becomes increasingly important. Until present, many studies have focused on the intrinsic immune toxicity of either GNPs or nickel. However, biological effects resulting from their interaction have not been addressed yet. Of special interest is the interaction of foreign matter with cells of the immune system, which are responsible to detect and categorize infections. Here, for the first time, we investigated the maturation effect of a mixture of GNPs and nickel(II) through an *in vitro* CD34-DC-based study. These CD34-DCs can reproduce the maturation process of skin LCs or interstitial DCs, which makes them highly relevant as a model system for *in vitro*

testing of allergenic compounds [380]. Nickel(II) sulphate ($NiSO_4$) was chosen as it is commonly used as a hapten for allergenic sensitization [381, 382]. Detailed characterization of GNPs –$NiSO_4$ interaction was performed in the *in vitro* exposure conditions, since biomolecules from the cell medium adsorb onto the GNPs' surface forming a biomolecule corona (known as the protein corona) and thus influence the bioreactivity of the NPs [20, 383]. The formation of a NP-corona complex is a multifactorial process, which is not only dependent on the characteristics of the NPs, but also depends on the interacting biomolecules, mainly proteins, and the surrounding medium (e.g. ionic strength, pH etc.) [384]. Here we showed that the presence of nickel(II) can change the GNPs' surface charge and consequently significantly alter the association of proteins (protein corona thickness and composition) in physiological media. Furthermore, our findings illustrate that the interaction of nickel(II) with GNPs results in a decreased maturation response in CD34-DCs.

5.3 Materials and methods

5.3.1 Nanoparticles and reagents

Citric acid stabilized GNPs supplied in 0.1 mM PBS with a nominal size of 50 nm were purchased from Cytodiagnostics Inc (Burlington, Canada). GNPs dispersions were made by diluting the stock solution in CCM, which is IMDM (Gibco, Paisley, UK) supplemented with 10% FBS (PAA laboratories, Pasching, Austria), 2% P/S (Gibco) and 1% BSA (Sigma-Aldrich), or 1.5% BSA in PBS, and vortexing for 30 seconds at full speed. Nickel sulphate ($NiSO_4.6H_2O$, Sigma-Aldrich, Steinheim, Germany) was diluted in CCM or 1.5% BSA. GNPs – $NiSO_4$ mixtures were prepared by diluting the GNPs' stock solution in CCM or 1.5% BSA containing $NiSO_4$. GNPs mixtures were characterized by NTA using NanoSight NS500 Instrument (NanoSight Ltd., Wiltshire, United Kingdom), zeta potential determination (Zeta PALS, Brookhaven Instruments corporation, Holtsville, USA), UV-Visible spectroscopy (Lambda 35, Perkin Elmer, Massachusetts, USA) and scanning electron microscopy (NanoSEM 450, FEI, Eindhoven, The

Netherlands). Sodium citrate and sodium hydroxide were purchased from Sigma-Aldrich.

5.3.2 Cell model

Immature CD34-DC, differentiated from human cord blood derived HPCs, were used as a highly relevant primary cell model showing in vivo-like DC characteristics [385]. $CD34^+$-HPC-cell isolation and culture procedures have been described previously [341]. Briefly, human cord blood samples were collected from umbilical blood vessels of placentas of full-term infants, born at the Heilig Hart hospital at Mol, Belgium and the St. Dimpna hospital at Geel, Belgium. Informed consent was given by the mothers and the study was approved by the ethical commission of both hospitals.

Mononuclear cells were separated from the cord blood by density gradient centrifugation (Ficoll-Paque™ plus, GE Healthcare, Uppsala, Sweden). Subsequently, $CD34^+$ HPCs were purified by EasySep® human CD34 positive selection kit (StemCELL Technologies Inc, Grenoble, France) according to the manufacturer's guidelines. $CD34^+$ HPCs cells were cultured at a cell concentration of 1×10^5 cells/ml for 12 days in CCM at 37 °C, 5% CO_2 and 95% humidity. GM-CSF (5000 U/ml; Gentaur, Brussels, Belgium), SCF (5 U/ml, Biosource, Nivelles, Belgium), TNF-α (250 U/ml, Roche, Basel, Switzerland), and IL-4 (1000 U/ml, Biosource) were added to the cultures. The immature DC phenotype was verified by means of flow cytometric analyses of selected surface markers (percentage positive cells for CD1a 10–30%; CD14 < 10%; CD83 1–5%; CD86 10–40% and HLA-DR 45–90%).

5.3.3 Dendritic cell maturation response

Immature CD34-DC were seeded in 24-well plates in 1 ml medium at a density of 1×10^6 cells/well. Cells were exposed to 6 pM GNPs (~ 4.4 µg/ml) and/or $NiSO_4$ mixtures (0.60 and 1.64 mM) for 24 hours. The maturation response of CD34-DC was measured by determination of cell surface expression of HLA-DR, CD80, CD83, CD86 and CD11c using flow cytometry (FACSCalibur™, Becton Dickinson, San Jose, California, USA). CD34-DC were identified by light scatter,

gates were set to exclude dead cells and cell debris. Light scattering profiles and fluorescence histograms were evaluated using CellQuest™ (Becton Dickinson). In order to account for the variability between different donors, the experiments were performed on 6 independent donors.

5.3.4 Assessment of uptake capacity of CD34-DCs upon maturation

In order to verify whether CD34-DCs NP uptake capacity was altered upon DC maturation, cells were artificially matured by adding 20 ng/ml TNF-α to the cultures on day 12 and incubated for 24 hours at 37°C and 5% CO2. Thereafter, immature and mature CD34-DCs were exposed to 50 µg/ml 40-nm sized carboxylated fluorescently stained polystyrene NPs (Dark red, Life Technologies) for 2 hours at 37°C and 5% CO2. Thereafter, cells were washed 3 times using PBS and NP uptake was determined by means of flow cytometry.

5.3.5 ICP-MS

In order to analyse if $NiSO_4$ was adsorbed to the GNP surface, GNPs together with 1.64 mM $NiSO_4$ were incubated in H_2O or CCM at 37°C and 5% CO_2 for 24 hours. GNPs were washed with PBS for 3 times at 3000×g for 40 minutes. Pellets were dissolved by adding 500 µl HCl Optima™ (Fisher Scientific, Erembodegem, Belgium) and 250 µl HNO3 OptimaTM (Fisher Scientific) and. In order to quantify GNP uptake, CD34-DCs incubated in CCM together with or without 0.60 mM and 1.64 mM $NiSO_4$ were collected after 24 hours. Cells were washed with PBS for 3 times at 300×g for 5 minutes. Pellets were dissolved by adding 750 µl HCl Optima™ and 250 µl HNO_3 Optima™. Thereafter, volumes were diluted in MilliQ ultrapure water (Millipore, Billerica, USA) and total nickel(II) or gold content was measured using a High Resolution ICP-MS (Element 2, Thermo Scientific, Waltham, USA). ICP-MS values for GNP uptake studies were corrected for cell death as determined by PI staining.

5.3.6 Protein corona

GNPs mixtures were incubated in either CCM or 1.5% BSA in PBS for 24 hours at 37°C, 5% CO_2. After incubation, GNPs were washed with PBS for 3 times in Protein LoBind Eppendorf tubes (Eppendorf AG, Hamburg, Germany) at 3000×g for 40 minutes as described before [386]. Thereafter, samples were diluted in Laemmli sample buffer (Bio-Rad Laboratories, Temse, Belgium) and heated for 5 minutes at 95°C. Beta galactosidase (Sigma-Aldrich) was added to the sample buffer as an internal loading control. Sodium dodecyl sulfate polyacrylamide gel electrophoresis (SDS-PAGE) was performed to characterize the protein corona (4-20% mini PROTEAN SFX, Bio-Rad) at 130 V for 1 hour. SDS-PAGE gels were imaged by the Stain-Free technology™, using a ChemiDoc XRS+ System (Bio-Rad) and quantified with the Image Lab Software (Bio-Rad). The total protein content was determined after GNP purification using the Micro BCA™ Protein Assay Kit (Pierce Biotechnology, Rockford, USA) according to the manufacturer's protocol. In order to quantify the thickness of the hard protein corona, disc centrifugation of the purified GNPs in CCM with or without nickel was performed using a CPS disc centrifuge (CPS Instruments Inc, Stuart, Florida, USA) with a 8-24% sucrose gradient (Merck, Darmstadt, Germany) and a rotation speed of 18 000 RPM. A core-shell method was used to analyse the DCS data as previously described [21, 386].

5.3.7 Statistical analysis

Statistical analyses were performed by GraphPad Prism version 5.00 (GraphPad Prism version 5.00 for Windows, San Diego, California, USA). Stimulation indices (SI) were calculated as:

$$\mathrm{SI} = \frac{\%\ \text{positive cells} \times \text{GMFI}}{\%\ \text{positive cells (control)} \times \text{GMFI (control)}}$$

Mean values of logarithmically transformed SI and SEM of N biologically independent experiments were calculated. Marker expression was considered significantly altered when $p < 0.05$ using a (paired) Student's t-test.

5.4 Results and discussion

5.4.1 Effects of co-exposure of GNPs and $NiSO_4$ on the sensitization response in CD34-DCs

In vitro studies were performed in order to investigate the potential interference of GNPs on the $NiSO_4$-induced sensitization response. Biologically relevant $NiSO_4$ concentrations were selected based on our previous studies [387, 388] and are appropriate for human $NiSO_4$ exposure as well [389, 390]. Immature myeloid CD34-DCs, differentiated from human cord blood-derived $CD34^+$ HPCs, were incubated in the presence of subtoxic concentrations of the chemical sensitizer $NiSO_4$ (0.60 and 1.64 mM) and 6 pM (3.5×10^9 NPs/ml, final exposure concentration) 50-nm citrate-stabilized GNPs for 24 hours, either as separate inducers or as a mixture (Figure 5-6). After exposure, CD34-DCs were harvested and analysed for surface marker expression. Altered expression of the treated cells *vs*. the solvent control was only considered as significant when the |SI| were larger than 1.5 (threshold for biological meaningful response). Exposure to GNPs resulted in a statistical significantly altered expression for CD80, CD83, CD86 and CD11c (Table 5-1). The observed cell activation pattern is in line with previous investigations on 40-nm sized GNPs exposure in bone marrow-derived DCs, which resulted in an increased secretion of the proinflammatory cytokines IL-6, IL-12 and GM-CSF [391].

In agreement with previous studies, the exposure of CD34-DCs to 0.60 mM $NiSO_4$ resulted in a significant upregulation of CD83, CD86 and HLA-DR, whereas 1.64 mM $NiSO_4$ caused the upregulation of CD83 and CD86 (Figure 5-1) [380, 387, 388].

The combined exposure of GNPs with 0.60 mM $NiSO_4$ led to a significant increase in CD80, CD83, CD86 and HLA-DR expression compared to untreated CD34-DCs, whereas GNPs and 1.64 mM $NiSO_4$ significantly altered the expression of CD83 and CD86 (Figure 5-1). However, the observed increase in the co-exposure sensitization response was remarkably lower than expected by adding the effects of both compounds. Rather a competitive response towards

the combined exposure was found, with a cell activation pattern most similar to this induced by $NiSO_4$ alone. These results are in agreement with our previous study using CD34-DCs in which 4 nm GNPs and 7 nm iron oxide NPs were co-incubated with a maturating cytokine mixture containing IL-1β and TNF-α [392]. Here, the NPs gave no additional enhancement or reduction of the DC sensitization response. Yet, others have reported an adjuvant activation of bone marrow-derived DCs by carbon black NPs [393, 394]. Discrepancies with preceding research can be attributed to the various NP-related factors such as differences in NP composition, NP size and contamination among others.

5.4.2 Co-exposure of NiSO4 interferes with GNP uptake in CD34-DCs

In order to evaluate if the cellular uptake by CD34-DCs of GNPs was altered during co-exposure to $NiSO_4$, ICP-MS analyses were performed. GNP uptake was evaluated after 24 hours of exposure. Remarkably, co-incubation of CD34-DCs together with NiSO4 resulted in a significant decrease in GNPs uptake (from 100 ± 4 % to 57 ± 5 % and 67 ± 5 % for 0.60 and 1.64 mM $NiSO_4$ resp.). DC maturation is known to inhibit of the cellular endocytosis processes [395]. In order to explore whether maturation of CD34-DC decreases their endocytic capacity, cells were artificially matured by TNF-α and exposed to 40-nm sized polystyrene NPs which are frequently used as model NPs. A non-significant decrease in NP internalization was observed upon maturation (from 100 ± 2% to 89 ± 14% for immature and mature CD34-DCs resp.).

5.4.3 Nickel(II) alters physicochemical GNPs properties in physiological media

Direct physicochemical interactions of GNPs and nickel(II) ions may increase their persistence, may mineralize them and make them no longer bioavailable and/or alter their biodistribution and speciation. In order to investigate the potential interactions of GNPs with nickel(II) ions, detailed characterization of 6 pM GNPs dispersed in 1.5% BSA in PBS or CCM containing $NiSO_4$ was performed. Effects were evaluated after 24 hours of incubation at 37°C and 5% CO_2.

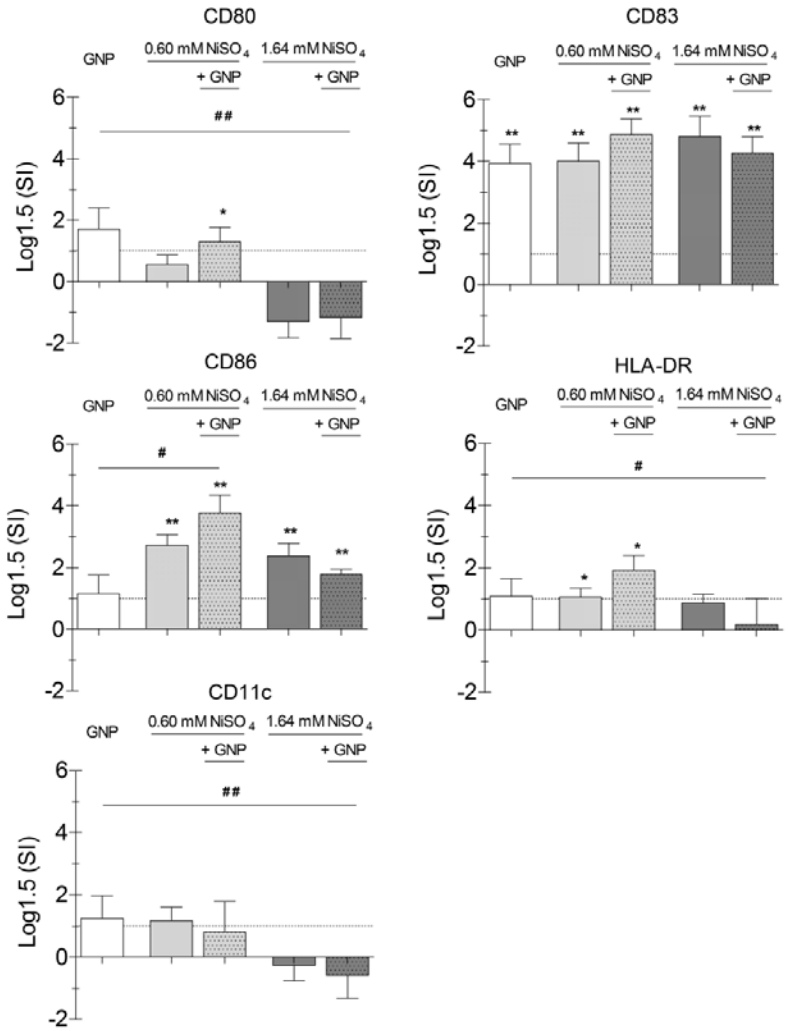

Figure 5-1: Mixture effects of GNPs and $NiSO_4$ on a sensitization response in CD34-DCs. Cells were exposed to 6 pM GNPs and $NiSO_4$ (0.60 and 1.64 mM) for 24 hours, harvested, and analysed for surface marker expression. Mean log1.5 SI ± SEM compared to the solvent control are shown (N = 6). Log1.5 of the solvent control was equal to 0. Significant altered expression compared to respective solvent control is indicated with * ($p < 0.05$) and ** ($p < 0.005$) only for conditions with $|SI| > 1.5$. Significant altered expression of the GNP treated cells compared to the GNPs together with $NiSO_4$ is indicated with # ($p < 0.05$) and ## ($p < 0.005$).

The size distribution of the GNPs – $NiSO_4$ mixtures was measured in water, BSA and CCM by NTA. GNPs' mean hydrodynamic size in water was 61 ± 3 nm, increasing to 80 ± 4 nm and 108 ± 9 nm when dispersed in BSA or CCM, respectively (Figure 5-2A, Figure 5-7). The increase of GNPs' size in biological fluid is related to the formation of a protein corona rather than NP aggregation, as that would show larger increases in NP size (vide infra) [20].

In a control experiment, addition of $NiSO_4$ to GNPs dispersed in water resulted in a fast, irreversible aggregation which may be due to the screening of the NP surface charge caused by the presence of ions in solution (Figure 5-3). When dispersed in BSA, the presence of 0.60 or 1.64 mM $NiSO_4$ did not significantly alter the GNPs' hydrodynamic size (from 80 ± 4 nm to 78 ± 3 nm and 74 ± 2 nm, resp.). In contrast, in CCM the presence of $NiSO_4$ significantly lowered the GNPs hydrodynamic size (from 108 ± 9 nm to 81 ± 5 nm ($p = 0.0019$) and 83 ± 5 nm ($p = 0.0021$), resp.).

UV-Visible spectroscopy measurements showed a shift of the surface plasmon resonance (SPR) peak of the GNPs in water from 535 ± 1 nm to 539 ± 1 nm and 543 ± 1 nm when GNPs were dispersed in BSA and CCM, resp. (Figure 5-2B). When $NiSO_4$ was present in the surrounding media, the SPR peak was not altered for BSA and was slightly lower for CCM (539 ± 1 nm for 0.60 and 1.64 mM $NiSO_4$ in BSA; 540 ± 2 nm and 541 ± 1 nm for 0.60 and 1.64 mM $NiSO_4$ in CCM). It is well known that the UV-Visible spectrum of GNPs is dominated by the SPR which is extremely sensitive to the aggregation state of the NPs, therefore, the observed small shifts of these peaks indicate that the size alterations are more related to the interaction of the NPs with the proteins rather than GNP aggregation.

The interactions of NPs with proteins and aggregation state can also be analysed with the NP surface charge. The surface charge of GNPs dispersed in water was -27 ± 1 mV (Figure 5-2C, Figure 5-8) close to the colloidal stability threshold (± -30 mV). Dispersion of the GNPs in BSA and CCM resulted in a less negative ζ-potential (-12 ± 1 mV and -7 ± 1 mV, resp.), indicating adsorption of bio-molecules on the GNPs' surface [20]. In BSA, the presence of $NiSO_4$ during the

incubation period did not remarkably alter the GNPs' charge (-13 ± 2 mV and -7 ± 2 mV for 0.60 and 1.64 mM $NiSO_4$, resp.). In contrast, co-incubation of GNPs with $NiSO_4$ in CCM resulted in a noteworthy more negative ζ-potential (-18 ± 2 mV and -20 ± 1 mV for 0.60 and 1.64 mM $NiSO_4$, resp.) compared to CCM without $NiSO_4$.

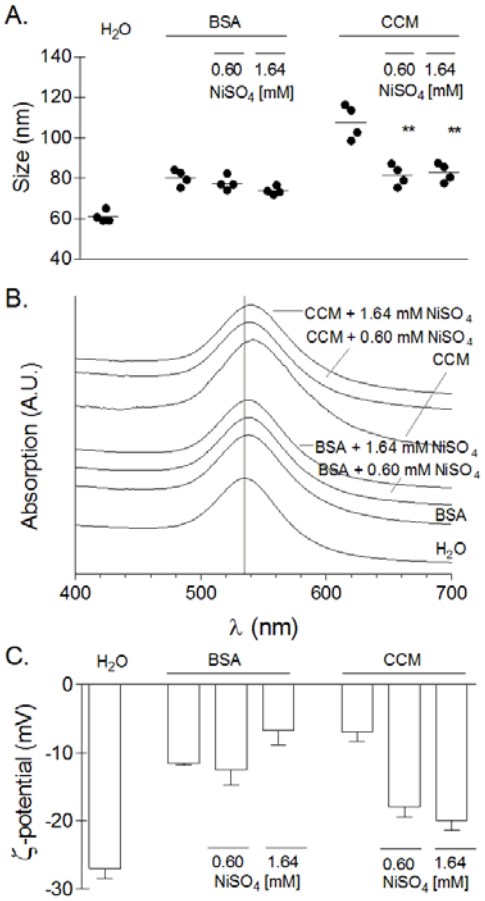

Figure 5-2: Physicochemical characterization of GNPs in water, BSA or CCM with or without $NiSO_4$ after 24 hours incubation at 37°C and 5% CO_2. (a) NTA indicating the mean hydrodynamic size. Significant differences to the control media containing no $NiSO_4$ are indicated with * ($p < 0.05$) and ** ($p < 0.005$). (b) UV-Visible spectroscopy after purification of the GNP mixtures. (c) Zeta potential determination after purification of the GNP mixtures.

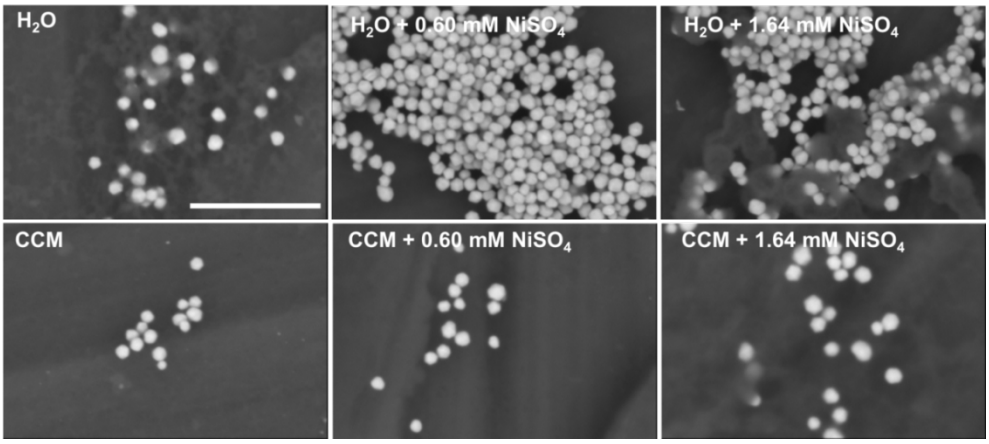

Figure 5-3: Scanning electron microscopy of GNPs in water and CCM, with or without $NiSO_4$, after 24 hours of incubation at 37°C and 5% CO_2. *Scale bar: 500 nm*

5.4.4 Complexation of nickel(II) by sodium citrate

To clarify whether the observed alterations were caused by the absorption of nickel(II) ions to the GNPs surface, ICP-MS analyses were performed on GNPs which were three times washed by centrifugation from GNP-$NiSO_4$ (1.64 mM) mixtures in water and CCM (note that 50 nm GNPs are very easily separated by centrifugation from the rest of the solution due to their high relatively mass). No significant amount of nickel(II) ions was detected on the isolated GNPs (data not shown). These findings are in contrast with previous research. *Ojea-Jimenez et al* demonstrated a deposition of mercury(II) ions on GNPs' surface [379]. Likewise, Fe_3O_4 nanodiamonds and silica NPs were shown to be potent in adsorbing metal ions [360, 361]. The GNPs used in present study were stabilized with sodium citrate (SC), a well-known chelating agent which is easily displaced by other biomolecules or ions in the surrounding solution. For that reason, the degree of nickel ions scavenged by citrate ions (SC) or BSA in the solution was evaluated in water or PBS using UV-Visible spectroscopy. A characteristic UV-Visible spectrum of 10 mM $NiSO_4$ dispersed in water and water with 10 mM NaOH is shown (Figure 5-4A). Addition of NaOH to the solution results in a high increase in the absorbance and a white-green precipitate of $Ni(OH)_2$ appears. This observation agrees with the formation, under alkaline conditions, of

insoluble $Ni(OH)_2$ in which its small aggregates act as scatter points for the light. The presence of 15 mM SC in this solution does not significantly alters the UV-Visible spectrum of the nickel(II) ions (Figure 5-4A). However, the addition of 10 mM NaOH does not result in the formation of a $Ni(OH)_2$ and no significant change in the absorbance occurs. These results agree with the complexation of nickel(II) ions by SC ions and the consequent stabilization of the nickel(II)-SC complex towards alkaline precipitation.

In order to better understand the complexation yield, additional experiments with varying SC concentrations were performed (Figure 5-4B). Generally, the characteristic peak of nickel(II) at 400 nm increases and slightly shifts to lower wavelengths with increasing SC concentrations. Addition of 10 mM NaOH results in an increase in absorbance in conditions with low SC concentrations, but not in conditions with a ratio of at least [nickel(II)]:[SC] < 2:1. Considering a complex Ni_3SC_2, commonly reported in the literature, the results show that the reaction is highly favourable and displaced towards the formation of the complex without requiring a large excess SC, in which all SC is complexing nickel(II). A characteristic UV-Vis spectrum of 10 mM $NiSO_4$ dispersed in PBS is shown (Figure 5-4C). The high absorbance together with the formation of a white-green precipitate in the solution indicates that nickel(II) is not stable in PBS and forms the insoluble $Ni_3P_2O_8$. In the presence of either SC or BSA, this precipitate is not observed. Thus, both may act as effective scavenging agents of nickel(II) ions, suggesting that both SC and BSA compete for the absorption of nickel(II) in complex biological media. As the concentration of SC in the GNP dispersion only 1.5 µM (information obtained from Cytodiagnostics Inc), most of the nickel(II) ions will bind to the proteins present in the complex media.

Figure 5-4 (p. 140): Complexation of nickel(II) by SC. (a)10 mM $NiSO_4$ in water and 15 mM SC before and after alkaline precipitation with 10 mM NaOH. (b) 10 mM in water with different concentrations of SC (0 – 15 mM) before and after alkaline precipitation. (c) 10 mM $NiSO_4$ in PBS before and in PBS with 1.5% BSA or 15 mM SC after alkaline precipitation.

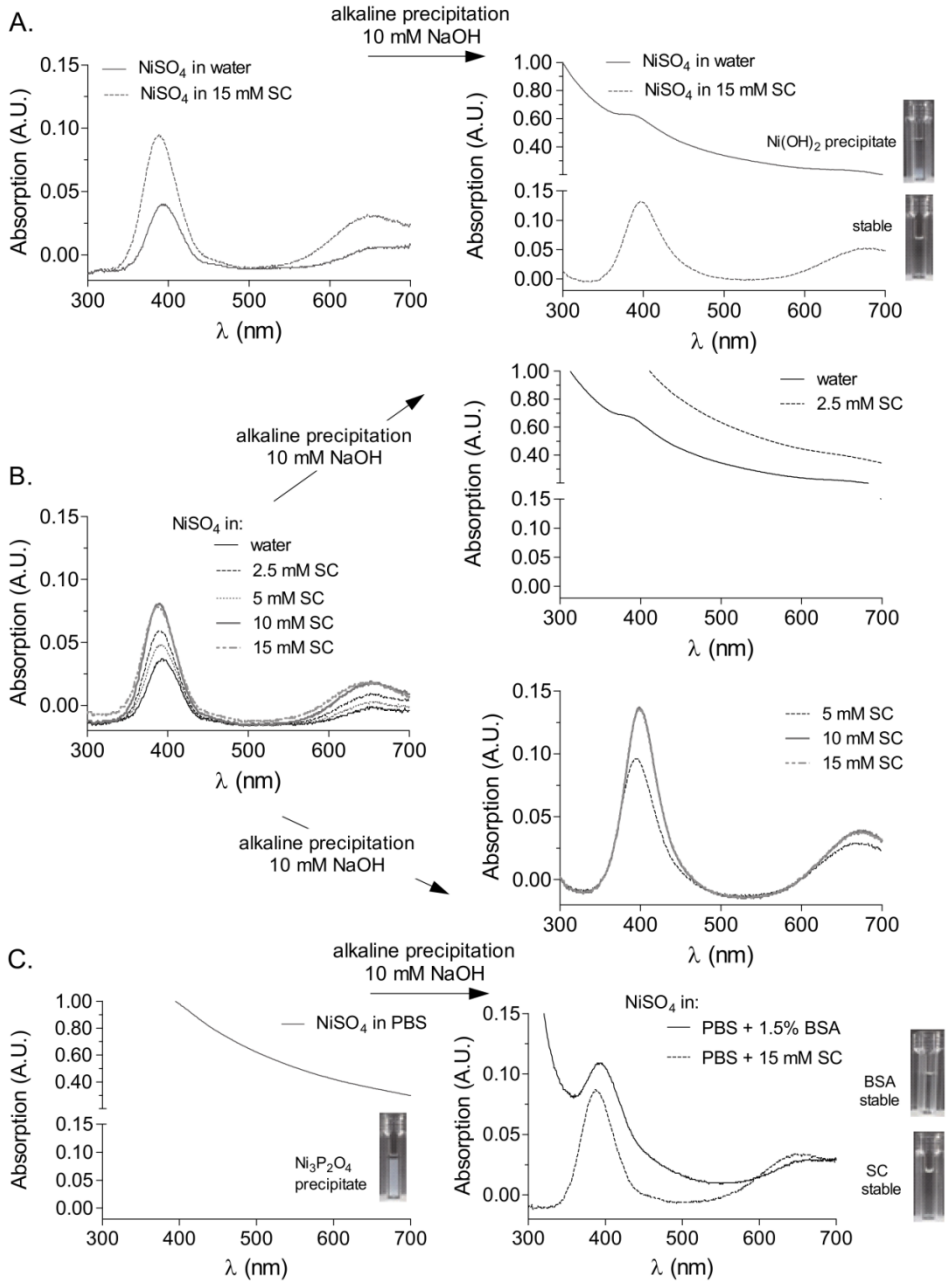
A.
alkaline precipitation
10 mM NaOH
NiSO4 in water
NiSO4 in 15 mM SC
Absorption (A.U.)
λ (nm)
Ni(OH)2 precipitate
stable
B.
alkaline precipitation
10 mM NaOH
NiSO4 in:
water
2.5 mM SC
5 mM SC
10 mM SC
15 mM SC
alkaline precipitation
10 mM NaOH
C.
alkaline precipitation
10 mM NaOH
NiSO4 in PBS
Ni3P2O4
precipitate
NiSO4 in:
PBS + 1.5% BSA
PBS + 15 mM SC
BSA
stable
SC
stable

5.4.5 Nickel(II) alters the GNP-adsorbed protein corona

In the previous experiments, while no direct interaction of the NP and nickel(II) was observed, clear and strong alteration of the NP protein interaction were clearly identified, deserving further investigation. Thus, the protein content of the GNPs–$NiSO_4$ mixtures was determined by Micro BCA™ Protein Assay Kit and evaluated to see whether the observed changes in size, charge and SPR peak could be attributed to a difference in the formation of the protein corona. Compared to the GNPs incubated in BSA, an increase in the total protein content in the presence of 1.64 mM $NiSO_4$ was found, although not significantly different (Figure 5-5A). On the contrary, GNPs incubated in CCM the presence of $NiSO_4$ had a significantly lower protein content compared to CCM without $NiSO_4$ ($p = 0.014$ and $p = 0.011$ for 0.60 and 1.64 mM $NiSO_4$ resp.).

In order to explore whether this decrease in protein content was coincident with a change in the thickness of the protein corona, disc centrifugation of the purified GNPs incubated in CCM with and without $NiSO_4$ was performed. Using a simple core-shell two-density model, as previously described [21, 386], the thickness of the GNPs corona after purification was computed. The corona thickness was significantly decreased in the presence of $NiSO_4$ (from 10.7 ± 1.6 nm for CCM without $NiSO_4$ to 7.1 ± 1.3 nm ($p = 0.0016$) and 7.1 ± 1.8 nm ($p = 0.0044$) for 0.60 and 1.64 mM $NiSO_4$ resp.) (Figure 5-5B).

In order to identify whether the composition (not only the amount) of protein corona also changed upon GNPs-$NiSO_4$ co-incubation in CCM, SDS-PAGE analysis was performed. Equal GNPs loading concentrations were determined by UV-visible spectroscopy and beta-galactosidase (molecular weight of 116 kDa) was added to the sample buffer as an internal loading control (Figure 5-5C). Seven distinguishable protein bands were detected, corresponding with a molecular weight of approximately 235, 116, 86, 70, 34, 26 and 15 kDa. The band densities were normalized against the internal loading control band within each lane and quantified relative to the GNPs in CCM without $NiSO_4$. A clear difference in the enrichment of various corona proteins adhered to GNPs upon $NiSO_4$ co-incubation was found. When GNPs were dispersed in CCM without $NiSO_4$, mainly

the enrichment of high molecular weight proteins was identified. However, the presence of $NiSO_4$ resulted in a shift towards attraction of low molecular weight proteins. Noteworthy band 4, which corresponds to BSA, is less abundant in the presence of $NiSO_4$ in CCM. This finding is in contrast with incubation in BSA alone in which 1.64 mM $NiSO_4$ increases GNPs protein content (Figure 5-5A). Apparently, when there is competition with other proteins in the surrounding media, interactions of nickel(II) and BSA binding to GNPs are different and, consequently, a smaller amount of BSA is bound to the GNPs.

Guo et al have described that co-incubation of silica NPs and $CdCl_2$ for 30 minutes at 4°C in complex biological media resulted in an increased binding of cadmium(II) ions to the proteins [361]. The binding of BSA to silica NPs in the presence of $CdCl_2$ was enhanced as binding with cadmium (II) ions favoured the electrostatic interaction with the silica NPs' surface, as in the well-known case of calcium(II) and magnesium(II). This observation co-incidences with a small increase in NPs size and a less negative ζ-potential. In the present study, as evidenced by the physicochemical characterization, only the GNPs incubated in BSA together with 1.64 mM $NiSO_4$ had a small increment of relative protein content and a less negative ζ-potential. GNPs incubated in CCM together with $NiSO_4$ showed a decrease in protein binding and ζ-potential. Nickel(II) ions are recognized to be capable to bind proteins and are potent oxidizers. Moreover, it was shown before that nickel(II) can induce conformational changes of proteins, alter their activity and contribute to the denaturation of proteins in the surrounding media [396, 397]. As a result, their affinity towards the GNPs surface can be changed [375, 398, 399]. Note that other bivalent ions as calcium(II) and magnesium(II) are known to interact with implanted surfaces and mediate the interaction of serum proteins with those implant surfaces [400, 401]. As shown by the SDS-PAGE, the absorbed proteins are smaller and, accordingly, form a more concise protein corona. This explains the observed changes in size and SPR peak as the hydrodynamic size of the GNPs was also reduced.

We demonstrated that the presence of increasing concentration of $NiSO_4$ induces gradual changes in the protein corona and charge of the GNPs. Protein adsorption and the protein corona of NPs is known to significantly impact on the cellular uptake of NPs[65, 70, 74]. The observed reduction in GNPs allergenicity during *in vitro* co-exposure may be explained by the decrease in GNP uptake in the presence of $NiSO_4$.

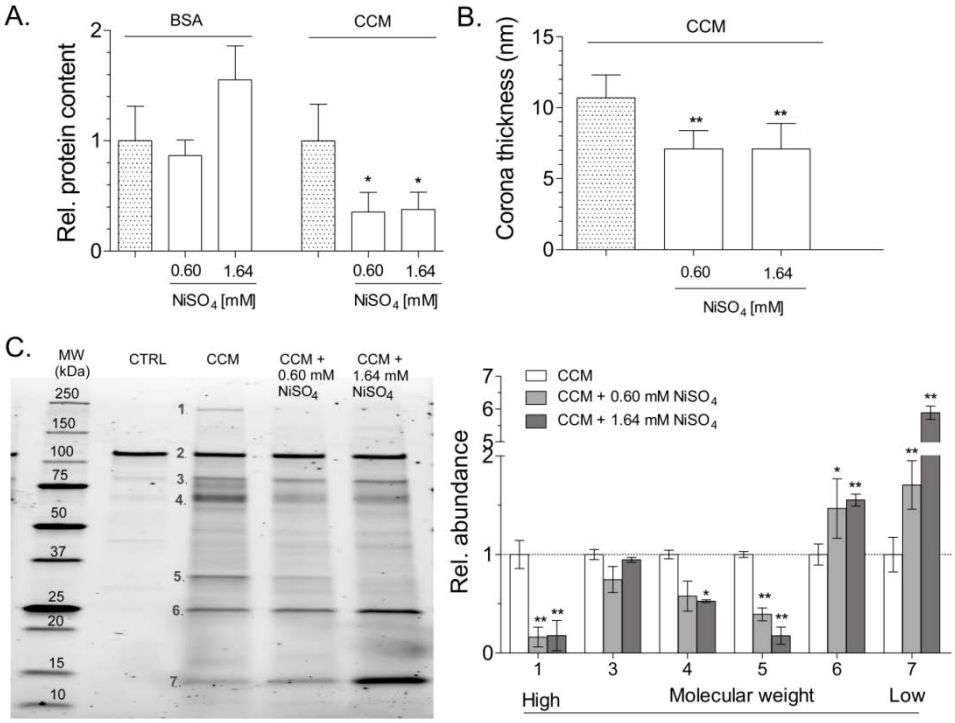

Figure 5-5: Nickel(II) alters the GNP-adsorbed protein corona. (a) Protein content ± SD absorbed to the GNPs surface compared to the control without $NiSO_4$. (b) Core shell estimations of GNPs' hard protein corona thickness in CCM with and without $NiSO_4$ (c) SDS-PAGE of the hard protein corona in CCM. Lanes are normalized to the reference band containing beta galactosidase (band 2) and bands are quantified relative to CCM without $NiSO_4$. The control of CCM without GNPs (CTRL) was performed to account for exclude centrifugation artefacts. Significant differences to the control media containing no $NiSO_4$ are indicated with * ($p < 0.05$) and ** ($p < 0.005$).

5.5 Conclusion

Despite many investigations have focused on the toxicity of GNPs, little is known about the interaction of GNPs with heavy metals and their effect on the immune system. In the present study, we explored for the first time the impact of mixtures of GNPs and $NiSO_4$ on the adaptive immune response, more specific the induction of an allergic sensitization response in human CD34-DCs. An interaction of GNPs with the $NiSO_4$ sensitization response of CD34-DCs was found which co-incidence with a decrease in GNP uptake. Although no adsorption of nickel(II) ions on the GNPs metallic surface could be detected, clear differences in the charge and protein corona of GNPs in the presence of $NiSO_4$ in complex biological media were observed, which may contribute to the observed decrease in GNPs' internalization and subsequent CD34-DC maturation. This study highlights both the complex interplay between NPs, proteins and ions, and the necessity of measuring and understanding toxicity of NPs in mixtures with other compounds, since combined exposures are highly relevant for human subjection to NPs and the risk assessment of nanomaterials.

5.6 Supplementary material

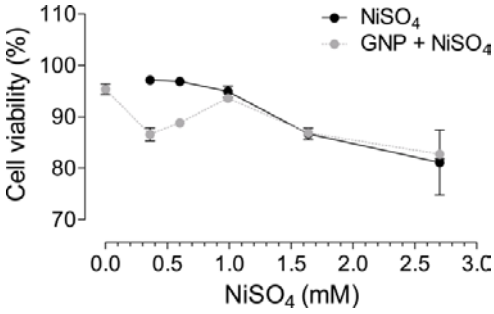

Figure 5-6: Effects of GNPs and $NiSO_4$ on cell viability in CD34-DCs. Cells were exposed to 6 pM GNPs and/or $NiSO_4$ for 24 hours, harvested, and analysed by flow cytometry using PI staining. Mean ± SD are shown. Data is shown representative to the solvent controls

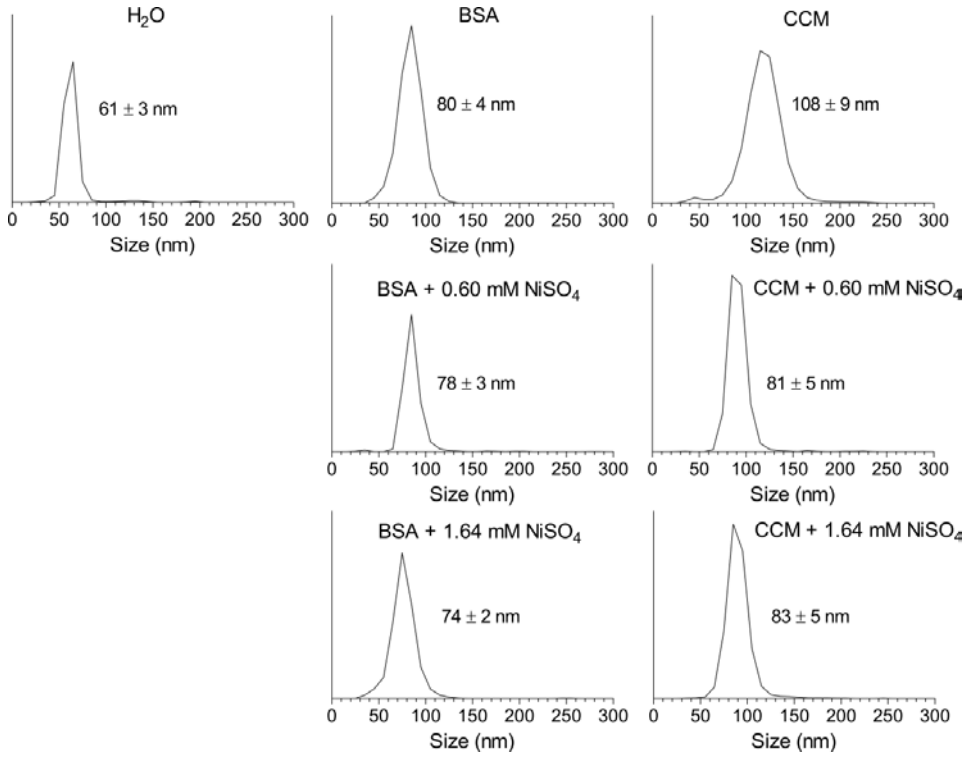

Figure 5-7: Size distribution of GNPs in water, BSA or CCM with or without NiSO4 after 24 hours incubation at 37°C and 5% CO2, obtained by NTA using NanoSight NS500 Instrument. Representative data of one measurement is shown, together with the mean ± SD of 4 measurements.

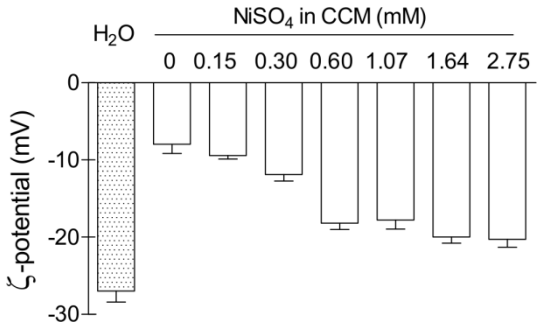

Figure 5-8: Zeta potential of GNPs in water and CCM, with various concentrations of $NiSO_4$ diluted in CCM after 24 hours incubation at 37°C and 5% CO_2.

Table 5-1: Effects of GNPs on a sensitization response in CD34-DCs. Cells (N = 11) were exposed to 6 pM GNPs for 24 hours, harvested, and analysed for surface marker expression. Significant altered expression was only considered when |SI|> 1.5. *Ns: not significant*

marker	control		GNPs		log1.5 (SI)	p value
	% pos. cells	GMFI	% pos. cells	GMFI		
CD80	18 ± 1	123 ± 16	26 ± 2	164 ± 19	1.85 ± 0.55	0.007
CD83	4 ± 0	101 ± 13	21 ± 3	140 ± 18	4.86 ± 0.53	< 0.001
CD86	22 ± 3	133 ± 17	28 ± 4	278 ± 70	1.74 ± 0.46	0.004
HLA-DR	57 ± 2	406 ± 63	61 ± 3	521 ± 84	0.74 ± 0.34	ns
CD11c	21 ± 3	170 ± 26	30 ± 2	171 ± 26	0.96 ± 0.15	< 0.001

6 Combined exposure to gold nanoparticles and house dust mite leads to altered sensitization response in vitro

This chapter is based on:

Combined exposure to gold nanoparticles and house dust mite leads to altered sensitization response in vitro

Sarah Deville, Nick Smisdom, An Jacobs, Jef Hooyberghs, Marcel Ameloot, Inge Nelissen.

Manuscript in preparation.

6.1 Abstract

The adjuvant activity of air pollution particles in allergic airway sensitization is well known, but a similar role of manufactured NPs in allergic sensitization has not been clarified. In present study the possible alteration of HDM-induced sensitization response by GNPs through *in vitro* studies was explored. Immature myeloid CD34-DCs, differentiated from human cord blood-derived $CD34^+$ HPCs, were incubated in the presence of HDM, as a model allergen, and citrate-stabilized 50-nm GNPs for 24 hours, either as separate inducers or as a mixture. Activation and maturation of CD34-DCs were studied as indicators of a sensitization response by measuring cell surface expression of the antigen-presenting HLA-DR receptor, the co-stimulatory molecules CD80, CD86 and CD83, and the integrin CD11c using flow cytometry. Exposure to the GNPs induced significant upregulation of the three co-stimulatory molecules. HDM did not stimulate any of the studied cell surface markers, but when co-incubated with the GNPs, it was observed to significantly inhibit NP-induced CD34-DC activation in a dose-dependent way. These results suggest that GNPs interfere with the allergens in the CD34-DC culture, resulting in decreased sensitizing effects. Uptake experiments of HDM and GNPs, and the physicochemical characterization of the GNP-HDM mixtures indicated that the GNPs and HDM are acting independently from each other. This suggests that the results may be explained by an immune regulatory mechanism. Further investigation will enhance our insight in the possible impact that NPs may pose to our health.

6.2 Introduction

Allergic diseases have risen dramatically in the past decades and have become a serious health burden with a prevalence of more than 10% in the general population. HDMs are one of the most common sources of airborne allergens worldwide. Sensitization to HDM triggers allergen-induced inflammation of the skin and airway mucosa, allergic rhinitis and asthma [402].

NPs are becoming more prevalent in industrial and commercial applications because of their unique size-related properties. The effect of NPs on the development of allergic disorders is not yet clarified. Previous investigations demonstrated an adjuvant activity of air pollution PM including UFP on allergic airway sensitization. UFP is typically composed from a carbonaceous core coated with metals, sulphates and polyaromatic hydrocarbons, and has the potential for binding allergens and absorbing lipopolysaccharides [159, 160]. Accordingly, UFP acts as an adjuvant in provoking primary allergic sensitization and are able to exacerbate secondary immune responses [161, 162]. Recent studies propose that NPs can exert similar effects on the immune system [166, 167]. For example, TiO_2 NPs have been shown to act as an adjuvant for the skin sensitizer DNCB, where it increases the dermal sensitization potency of DNCB [168]. In addition, both TiO_2 and GNPs aggravate the inflammatory response in a mouse model of diisocyanate-induced asthma [169].

There is still little known concerning the mixture effects of NPs and allergens. Recent studies have indicated that the interaction of NPs and other chemical/biological compounds can possibly result in additive, synergistic, inhibitory or potentiating effects. Interaction of NPs and heavy metals can enhance cytotoxic responses and increase oxidative damage [360, 361], but also detoxification can take place [362]. Adsorption of biomolecules and ions to the NPs' surface can result in Trojan horse type effects in which the NPs acts as vehicles for an increased intracellular delivery [360]. In addition, conjugation of allergens to NPs were shown to be potent in modulating the allergic responses. Here, the protease activity of Der p 1, the major allergen for HDM, was increased when attached to the GNPs' surface [403]. These observations make evident that it is necessary to address NPs interactions in the context of mixed exposure situations to adequately assess NPs' safety and allergenicity.

In our previous study, we have demonstrated that GNPs possess immunomodulatory properties on the allergic sensitization response of CD34-DCs. What is more, the combined exposure of GNPs and the known chemical sensitizer $NiSO_4$ significantly altered the allergenic response (Deville et al,

submitted). Here, substantial changes in the GNPs' protein corona formation and a decrease in GNP uptake were observed in the presence of $NiSO_4$. In present study we wanted to investigate whether co-exposure of the protein allergen HDM and GNPs also induces changes in the allergic sensitization response of CD34-DCs and if it can alter the protein corona formation and/or the GNPs' uptake. Therefore, we investigated the effect of co-exposure to GNPs and HDM on CD34-DC maturation, and performed an extensive physicochemical characterization of the GNPs in the presence of HDM in a complex physiological environment to investigate their potential interactions.

6.3 Materials and methods

6.3.1 Cell model

CD34-DCs which are differentiated from human cord blood-derived $CD34^+$ HPCs were used as a highly relevant primary cell model having in vivo-like DC characteristics [385]. $CD34^+$ HPCs isolation and culture procedures have been described before (Deville et al, submitted). Human cord blood samples were collected from umbilical blood vessels of placentas of full-term infants, born at the St. Dimpna hospital at Geel and Heilig Hart hospital at Mol (both Belgium). Informed consent was given by the mothers and the study was approved by the ethical commission of both hospitals. Mononuclear cells and subsequent $CD34^+$ HPCs were purified by density gradient centrifugation (Ficoll-Paque™ plus, GE Healthcare, Uppsala, Sweden) and EasySep® human CD34 positive selection kit (StemCELL Technologies Inc, Grenoble, France) respectively according to the manufacturer's guidelines. $CD34^+$ HPCs were cultured at a cell concentration of 1×10^5 cells/ml in cultured for 12 days in IMDM (Gibco, Paisley, UK) supplemented with 10% FBS (PAA laboratories, Pasching, Austria), 2% P/S (Gibco) and 1% BSA (Sigma-Aldrich, Bornem, Belgium) (CCM) at 37 °C, 5% CO_2 and 95% humidity. GM-CSF (5000 U/ml; Gentaur, Brussels, Belgium), SCF (5 U/ml, Biosource, Nivelles, Belgium), TNF-α (250 U/ml, Roche, Basel, Switzerland), and IL-4 (1000 U/ml, Biosource) were added to the cultures. Flow

cytometric analyses of selected surface markers was performed to verify the immature DC phenotype: percentage positive cells for CD1a 10–30%; CD14 < 10%; CD83 1–5%; CD86 10–40% and HLA-DR 45–90%.

6.3.2 Nanoparticles

Citric acid stabilized GNPs with a nominal size of 50 nm were purchased from Cytodiagnostics Inc (Burlington, Canada). GNPs dispersions were made by diluting the stock solution in CCM and vortexing for 30 seconds at full speed. GNPs dispersions were characterized by NTA using NanoSight NS500 Instrument (NanoSight Ltd., Wiltshire, United Kingdom), zeta potential determination (Zeta PALS, Brookhaven Instruments corporation, Holtsville, USA) and UV-Visible spectroscopy (Lambda 35, Perkin Elmer, Massachusetts, USA).

6.3.3 Cell viability, reactive oxygen species production and dendritic cell maturation response

Immature CD34-DCs were seeded in 24-well plates in 1 ml medium at a density of 1×10^6 cells/well. Cells were exposed to 6 pM GNPs (~ 4.4 µg/ml) and/or whole HDM Der p allergen mixture (GREER laboratories, Lenoir, USA) (20, 100 and 200 µg/ml) diluted in CCM. After 24 hours of exposure at 37°C and 5% CO_2 cell viability, ROS production and CD34-DC maturation response were determined using flow cytometry (FACSCalibur™, Becton Dickinson, San Jose, California, USA). CD34-DCs were identified by light scatter, gates were set to exclude dead cells and cell debris. Light scattering profiles and fluorescence histograms were evaluated using CellQuest™ (Becton Dickinson).

Cell viability was determined by a propidium iodide (PI, Sigma-Aldrich). CD34-DCs were collected and washed for three times with PBS (Gibco) and 20 µg/ml PI was applied immediately before flow cytometric analyses. ROS production was determined by using a CM-H_2DCFDA assay (Life Technologies, Paisley, UK) according to the manufacturer's guidelines. Briefly, cells were washed after exposure with Hank's Balanced Salt Solution (HBSS, Gibco) at room temperature for three times and collected in HBSS containing 2.5 µM CM-H_2DCFDA or CM-

H_2DCFDA and 0.5 mM of the positive control 3-morpholinosydnonimine hydrochloride (SIN-1, Calbiochem, San Diego, USA). Cells were incubated for 20 minutes at 37°C and 5% CO_2. Thereafter, they were washed for three times with HBSS at 4°C and immediately measured by flow cytometry.

The maturation response of CD34-DCs was evaluated by determination of cell surface expression of HLA-DR, CD80, CD83, CD86 and CD11c (Becton Dickinson) using flow cytometry according to the manufacturer's guidelines. SI were calculated as:

$$\mathrm{SI} = \frac{\%\ \text{positive cells} \times \text{GMFI}}{\%\ \text{positive cells (control)} \times \text{GMFI (control)}}$$

Mean values of logarithmically transformed SI and SEM of N biologically independent experiments were calculated. Statistical analyses were performed by GraphPad Prism version 5.00 (GraphPad Prism version 5.00 for Windows, San Diego, California, USA). Marker expression was considered significantly altered when $p < 0.05$ using a (paired) Student's t-test.

6.3.4 Labelling of HDM

HDM extract was fluorescently labelled with Rhodamine Green™ (RG) by means of RG carboylic acid, succinimidyl ester, hydrochloride (5(6)-CR-110, SE) (Life Technologies). HDM was dissolved in 0.1 M $NaHCO_3$ at a concentration of 10 mg/ml and 200 µg/ml of RG was added. The HDM-RG mixture was incubated for 2 hours at room temperature. Thereafter, unbound RG was removed by 5 ultrafiltration steps (Amicon Ultra 0.5, Millipore, Carrigtwohill, Ireland) and subsequently applied to dye removal columns (Fisher Scientific, Rockford, USA) according to the manufacturer's guidelines. Additionally, HDM extract was also biotinylated using the EZ-Link™ Sulfo-NHS-Biotinylation Kit (Thermo Scientific, Rockford, USA) according to the manufacturer's guidelines. A 20-fold molar excess of sulfo-NHS-Biotin was added to 2.5 mg/ml HDM extract and incubated for 2 hours on ice. Thereafter, the excess of biotin reagent was removed using a Zeba Spin Desalting Column (Thermo Scientific).

6.3.5 Cellular uptake of HDM and GNPs

The influence of GNPs on the cellular uptake of HDM was determined by means of flow cytometry. CD34-DCs were exposed to 6 pM GNPs and/or HDM-RG (20, 100 and 200 µg/ml) diluted in CCM for 24 hours. Thereafter, cells were washed for 3 times at 300×g for 5 minutes. Flow cytometric analyses were proceeded immediately. The effect of HDM on the uptake of the GNPs in CD34-DCs was investigated by ICP-MS. Cells were exposed to a mixture of 6 pM GNPs and/or HDM (20, 100 and 200 µg/ml) diluted in CCM for 24 hours. Thereafter, cells were washed for 3 times at 300×g for 5 minutes. Pellets were dissolved by adding 750 µl HCl Optima™ and 250 µl HNO_3 Optima™. Volumes were diluted in MilliQ ultrapure water (Millipore, Billerica, USA) and measured using a High Resolution ICP-MS (Element 2, Thermo Scientific, Waltham, USA).

6.3.6 Protein corona

GNPs and (biotin-labelled) HDM mixtures were incubated in CCM for 24 hours at 37°C, 5% CO_2. After incubation, the mixtures were washed with PBS for 3 times in Protein LoBind Eppendorf tubes (Eppendorf AG, Hamburg, Germany) at 3000×g for 40 minutes as described before [386]. Thereafter, samples were diluted in Laemmli sample buffer (Bio-Rad Laboratories, Temse, Belgium) and heated for 5 minutes at 95°C. SDS-PAGE was performed to characterize the protein corona (4-20% mini PROTEAN SFX, Bio-Rad) at 130 V for 1 hour. SDS-PAGE gels were imaged by the Stain-Free technology™, using a ChemiDoc XRS+ System (Bio-Rad) and quantified with the Image Lab Software (Bio-Rad). For detection of the biotin-labelled HDM, SDS-PAGE gels were blotted on a PVDF membrane using the Trans-Blot® Turbo™ Transfer pack and Blotting System (both Bio-Rad). Thereafter, membranes were washed with PBS containing 0.05% Tween®20 (PBS-T, Sigma) and blocked with 5% BSA in PBS-T. Thereafter, membranes were labelled with Pierce® High Sensitivity Streptavidin-HRP (0.05 µg/ml, Thermo Scientific) and Precision Protein™ StrepTactin-HRP Conjugate (Bio-Rad) for visualization of biotin-HDM and the protein ladder. Thereafter, membranes were washed and measured using Clarity Western ECL Substrate kit (Bio-Rad) according the manufacturer's guidelines.

6.4 Results and discussion

6.4.1 Co-exposure of GNPs and HDM decreases the GNP-induced cell activation response

The potential interference of HDM on the GNP-induced sensitization response was investigated through *in vitro* studies in immature myeloid CD34-DCs. CD34-DCs, which are differentiated from human cord blood-derived $CD34^+$ HPCs, were incubated in the presence of GNPs (4.4 µg/ml) or HDM (20, 100 or 200 µg/ml) either separate or as a mixture (Table 6-1). After 24 hours of exposure, CD34-DC were harvested and analysed for cell viability, ROS production and surface marker expression (Figure 6-1, Figure 6-5, Figure 6-6).

Exposure to GNPs and/or HDM did not cause a reduction in cell viability nor an increase in ROS production. On the other hand, noteworthy changes in cell activation markers were identified. Differences in surface marker expression of the treated cells *vs.* the solvent control were only considered as biologically significant when the |SI| were larger than 1.5. GNPs induced a significant upregulation of the CD80, CD83 and CD86 surface markers, which are costimulatory molecules involved in DC activation and its effector function. These findings are in agreement with previous investigations demonstrating the immunomodulatory properties of these GNPs (Deville et al, submitted) [391]. Exposure to HDM, however, did not induce any significant maturation response in CD34-DCs. Combined exposure to both GNPs and HDM resulted in a dose dependent decrease in the cell activation pattern compared to GNPs alone. Remarkably, exposure of GNPs and high levels of HDM led to a downregulation of CD34-DCs maturation with levels similar to the solvent control alone. These results are in line with a previous study in which peripheral blood-derived DCs were co-exposed to UFP and HDM, this resulted in a lower cytokine production compared to the cytokine production induced by the separate inducers [404].

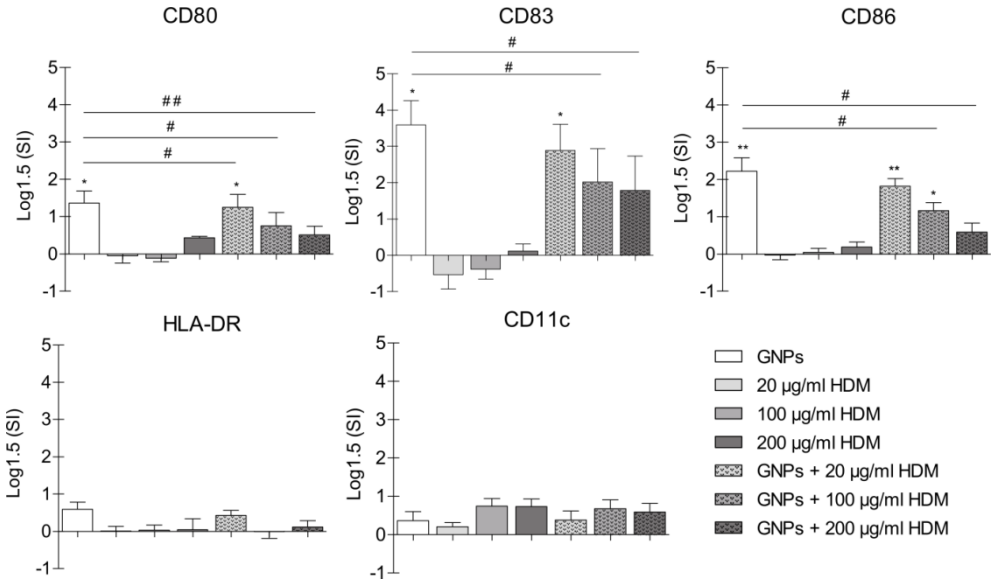

Figure 6-1: Mixture effects of GNPs and HDM on a sensitization response in CD34-DCs. Cells were exposed to 6 pM (4.4 µg/ml) GNPs and 20, 100 or 200 µg/ml HDM for 24 hours, harvested, and analysed for surface marker expression. Mean log1.5 SI ± SEM are shown (n =5). Log1.5 of the solvent control was equal to 0. Significant altered expression compared to respective solvent control is indicated with * ($p < 0.05$) and ** ($p < 0.005$). Significant altered expression of the GNP treated cells compared to the GNPs together with HDM is indicated with # ($p < 0.05$) and ## ($p < 0.005$). Only for conditions with |SI|> 1.5 were considered biologically relevant.

6.4.2 Independent uptake of HDM and GNPs by CD34-DCs

These results propose that the uptake of GNPs and HDM responses are in competition with each other. For that reason, the uptake of fluorescently labelled HDM and GNPs by CD34-DCs was investigated and compared under co-exposure conditions (Figure 6-2). A dose dependent increase in HDM was found when CD34-DCs were exposed to 20, 100 and 200 µg/ml. However, the presence of GNPs in the cellular environment did not affect the uptake of HDM. Correspondingly, the uptake of GNPs was similar with or without HDM to be present in the environment. These observations put forward that the uptake of HDM and GNPs by CD34-DCs are independently taking place from each other.

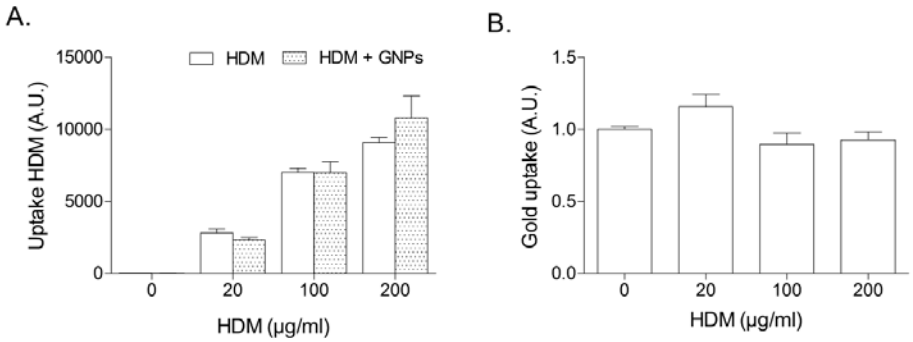

Figure 6-2: Uptake of HDM and GNPs in CD34-DCs was not altered during co-exposure. Cells were exposed to 6 pM GNPs and 20, 100 or 200 µg/ml fluorescently labelled HDM for 24 hours (n = 4). (A) Uptake of HDM was measured by means of flow cytometry. (B) ICP-MS analyses of gold content from cells exposed to HDM. *A.U.: arbitrary units*

6.4.3 HDM changes GNPs' protein corona composition

When GNPs are presented in a physiological environment, they selectively absorb biomolecules on their surface which forms a biomolecular corona. This interface can be divided into the 'hard' and 'soft' corona, depending on the binding strength and exchange rates of the molecules. The 'hard' corona consists of molecules with a high affinity for the NPs surface. However, molecules which are loosely bound to the NPs surface are connected with the 'hard' corona through electrostatic, protein – protein interactions, form the 'soft' corona [405]. Interaction of HDM with the GNPs and, consequently, enrichment and incorporation in the GNPs' corona can modulate the co-exposure response of the CD34-DCs by altering its uptake mechanism or changing the proteolytic activity of HDM affecting the immunomodulatory properties of the GNPs [403]. For that reason, proteomic analyses of the hard protein corona were performed with the unlabelled and biotinylated HDM (biotin-HDM) (Figure 6-3, Figure 6-4). Changes in the protein corona composition were found when HDM was present in the environment. There is a shift from high molecular weight proteins to low molecular weight proteins present upon co-exposure of GNPs with HDM in CCM.

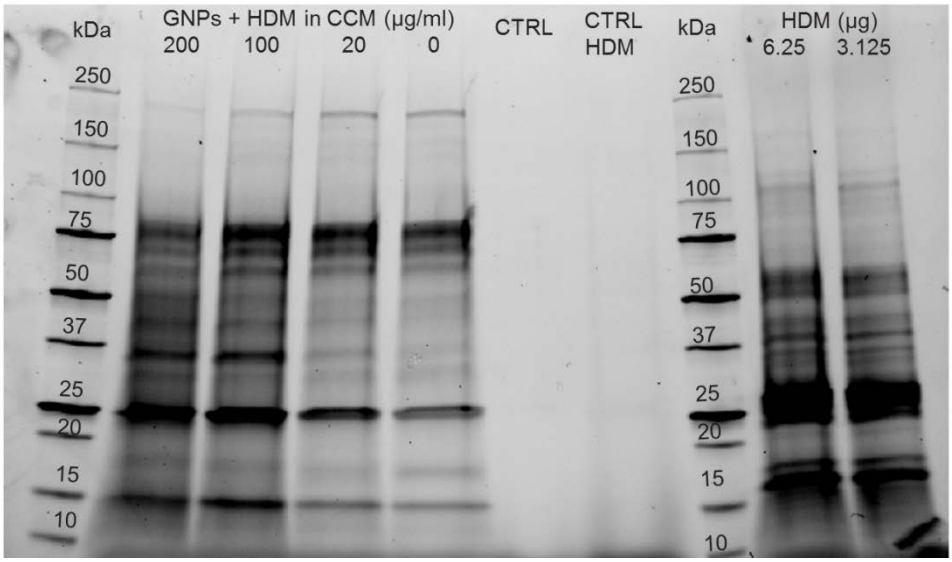

Figure 6-3: Changes in the hard protein corona of GNPs in the presence of HDM. SDS-PAGE of the isolated hard protein corona of GNPs treated with HDM in CCM for 24 hours. To have a high enough protein content to be visible on the gel, a total volume of 30 ml of the GNPs-HDM in CCM dispersions was incubated, the resulting protein corona was isolated and loaded on the gel. In addition, CCM (CTRL) and CCM with 200 µg/ml HDM (CTRL HDM) without GNPs were processed similar to the samples with the addition of GNPs and loaded on the gel to account for centrifugation artefacts. HDM extract (6.25 µg and 3.125 µg) was directly loaded on the gel as a control.

Moreover, a more intense staining of the unresolved bands is noticeable. We hypothesize that there is a change in protein content and that the proteolytic activity of HDM influences the formation of the protein corona. Quantification of the total amount of protein present in the protein corona and investigation of the proteolytic activity of HDM (with or without GNPs) should be further explored. Using Western blot analyses, the presence of biotin-HDM was identified in the hard protein corona (Figure 6-4). The amount of biotin-HDM conjugated with the GNPs was semi-quantitatively determined using densitometry: for 20 µg/ml less than 0.1 µg/ml, for 100 µg/ml 0.47 ± 0.21 µg/ml HDM and for 200 µg/ml 0.77 ± 0.37 µg/ml HDM were attached to 6 pM of GNPs. This data illustrates that only a small fraction of the total available amount of HDM is incorporated in the GNPs' protein corona.

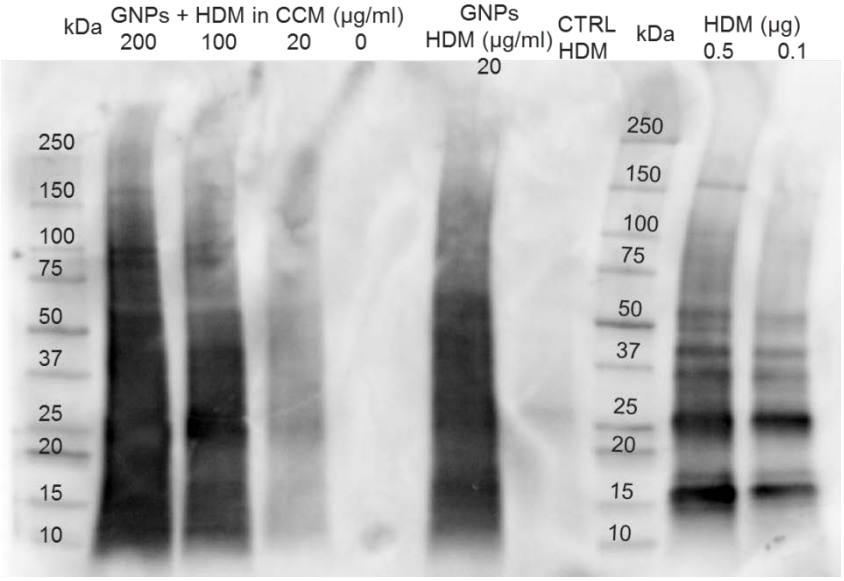

Figure 6-4: Enrichment of biotinylated HDM in the hard protein corona of GNPs. Western blot of the isolated hard protein corona of GNPs treated with the biotin-HDM in CCM for 24 hours. Note that the western blot detection has a much higher sensitivity in comparison with the hard corona determination by SDS-PAGE, only 1 ml of the GNPs-biotin-HDM mixture in CCM was used here for the purification of the protein corona. GNPs with 20 µl/ml represents a control sample in which the GNPs were incubated without serum proteins, and CCM with biotin-HDM (CTRL HDM) represent a control without GNPs. Both were processed similar to the GNPs + HDM in CCM and loaded on the gel. Pure biotin-HDM extract (0.5 µg and 0.1 µg) was directly loaded on the gel as a control.

6.5 Conclusion

Combined exposure of HDM and GNPs can significantly inhibit NP-induced CD34-DC activation in a dose-dependent way. Uptake experiments of HDM and GNPs, and the physicochemical characterization of the GNP-HDM mixtures indicated that the GNPs and HDM are predominantly acting independently from each other. However, an enrichment of HDM in and alteration of the resulting protein corona of the GNPs was identified. Further investigation will need to be performed to elucidate the underlying mechanism.

6.6 Supplementary material

Table 6-1: Physicochemical characterization of GNPs (± SD) after 24 hours incubation in water or CCM containing 20, 100 or 200 µg/ml HDM at 37°C and 5% CO_2.

	Size [a] (nm)	Charge [b] (mV)	SPR peak (nm)
Water	61 ± 3	-27 ± 1	535 ± 1
CCM	108 ± 9	-7 ± 1	540 ± 1
CCM + 20 µg/ml HDM	128 ± 18	-7 ± 3	539 ± 1
CCM + 100 µg/ml HDM	125 ± 8	-9 ± 2	539 ± 1
CCM + 200 µg/ml HDM	113 ± 3	-8 ± 2	539 ± 1

[a] Hydrodynamic diameter obtained by NTA

[b] Zeta potential determination

[c] SPR peak measured by UV-Visible spectroscopy

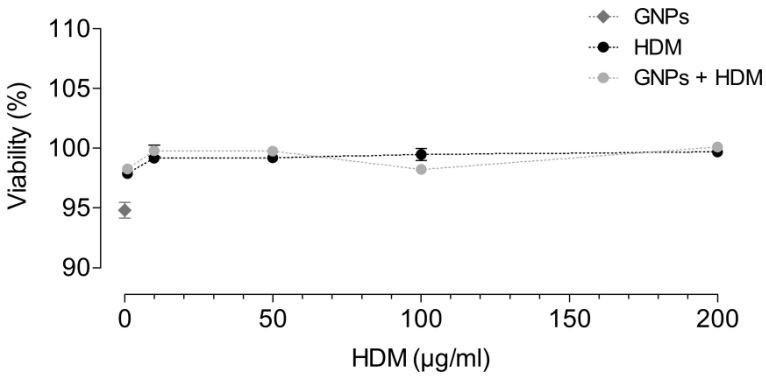

Figure 6-5: No effects of 6 pM GNPs and/or HDM on cell viability in CD34-DCs after 24 hours of exposure at 37°C and 5% CO_2. Cells were harvested after exposure and analysed by flow cytometry using PI staining. Mean ± SD are shown. Data is shown relative to the respective solvent controls.

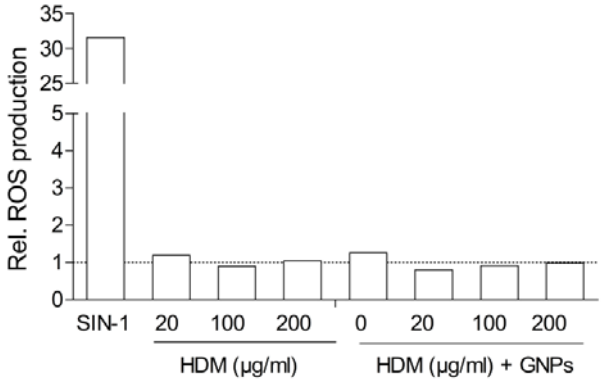

Figure 6-6: No increase of ROS production by CD34-DCs after 24 hours of exposure to 6 pM GNPs and/or HDM at 37°C and 5% CO_2. ROS production was measured by flow cytometry by means of a CM-H2DCFDA assay. SIN-1 (0.5 mM) was used as a positive control for ROS. Data is shown relative to the respective solvent controls.

7 General discussion

In the first part of this dissertation, the aim was to investigate whether advanced fluorimetric techniques are suitable to retrieve quantitative information on the uptake, the intracellular behaviour and the fate of NPs in biological cells. The applicability of these techniques were examined and broadened for evaluating the nano-bio interaction. Various aspects on evaluating NP uptake, their intracellular trafficking and their potential release remain largely unknown. Progress was achieved through a careful investigation of these nano-bio interactions. By using microfluorimetric techniques, the intracellular dynamics of NPs and the cotransport of the NPs with cell organelles were identified and quantified. Additionally, the uptake and release of drug-loaded nanocarriers were also monitored. Furthermore, flow cytometry was applied to gain new insights in the uptake kinetics of NPs in HPCs and CD34-DCs.

In the second part, the aim was to examine the impact of NPs on the biological function of DCs. Effects of GNPs on the allergen-induced DC sensitization were identified. Insights were also gained on the importance of mixture toxicology for the evaluation of functional effects of NPs on biological cells. For this, we focused our study on the characterization of the NPs in a biological context and performed a detailed physicochemical characterization.

The obtained results and findings in this dissertation are in line with an increasing awareness that an appropriate characterization of the NPs is extremely important. The previous chapters already contained in depth discussions of the obtained results, therefore, this chapter provides a more general discussion with a focus on the potential pitfalls in the evaluation of nano-bio interactions and the precautions to be taken. Besides, the remaining questions of the presented research are also discussed. To end with, an outlook for the future development of the field is provided.

7.1 Characterization of nano-bio interactions in a biological context

7.1.1 Characterization of nanoparticles in a complex physiological environment

When NPs interact with biological matter the NP size and stability are significantly altered due to the formation of the protein corona. The stability can be impaired, resulting in a time-dependent variability in the NPs' size distribution [406]. Therefore, it is crucial to perform a time-dependent physicochemical characterization in the physiological media in which the NPs are applied.

In **chapter 4** we performed a characterization of the PS NPs over time to evaluate the stability of the NPs in a complex physiological environment. These results demonstrated that although the dispersions reached a zeta potential close to neutrality, the NPs remained stable over the complete duration of the experiments and beyond.

In **chapter 5** a detailed physicochemical characterization of the interaction between GNPs and $NiSO_4$ was performed in order to reveal whether GNPs and nickel(II) ions interact with each other in a complex, physiological mixture. Whereas electron microscopy and UV-Visible spectroscopy demonstrated the absence of NP aggregation, no changes in NP shape and no NP dissolution, NTA and DCS demonstrated that the protein corona formation of the GNPs was hampered when nickel(II) ions were present in the environment. Through ICP-MS analyses the interaction of nickel(II) ions with the GNPs' surface was monitored over time. The results proved the absence of a direct interaction between the GNPs and $NiSO_4$. Moreover, additional experiments revealed that the overall charge of the NPs (obtained through ζ-potential determination) and the composition of the protein corona (SDS-page) was significantly different in $NiSO_4$ containing media most likely to be explained by an interaction of nickel(II) ions and the proteins present in the surrounding media.

In **chapter 6** physicochemical characterizations of the GNPs and HDM in a complex physiological environment showed that the presence of HDM could affect the protein corona composition. Note that for visualization purposes, HDM was modified through fluorescent conjugation and biotinylation. Therefore this modification might have repercussions on the biological effects. It is necessary to validate whether the co-exposure of GNPs with modified HDM has similar effects on the maturation response of CD34-DC compared to the unmodified HDM.

For both $NiSO_4$ and HDM contaminations in the GNPs' environment, the observed NP-allergen interactions give rise to a new biological identity of the NPs which may be responsible for the observed changes in their biological activity. Future experiments are necessary to elucidate whether the altered corona alone is sufficient in changing the NPs' uptake and allergenicity e.g. by administering the isolated NP-corona mixtures to the cells. In addition, the role of the NP surface functionalization, NP dimension and NP composition should be performed to identify whether the observed phenomenon is general or specific for the presented cases.

The combination of different characterization methods allowed to build a more comprehensive picture of the concerned events by removing the uncertainties associated with individual methods.

7.1.2 Stability of nanoparticles

Maintaining and characterizing the physical and chemical stability of NPs is a crucial requirement for correctly assessing their biological effects. Instability of the NPs can result in altered nano-bio interactions, and also complicates the interpretation of their outcome. Evaluating the uptake and release of NPs using fluorescence-based techniques is often problematic by the presence of residual free dye or labile dye within the NP dispersion [50, 345].

In **chapter 4** the uptake of 40-nm sized fluorescently stained PS NPs was studied in $CD34^+$ HPCs and $CD34^+$ derived DCs using flow cytometry and CLSM. HPCs showed a transient association with the PS NPs, whereas the CD34-DCs

displayed a monotonic increase of NP load over time. This novel observation suggests that HPCs are capable in releasing their cargo over time and offers a unique approach to transiently equip them with active cargo. However, it is very difficult to establish that this phenomenon is solely attributed to a specific cellular behaviour because of the possibility of technical artefacts which may influence the observations and the limitations of the available techniques. Although flow cytometry has proven its value in many NP uptake studies, the presence of residual free dye can strongly influence the NP uptake profile [50, 345]. CLSM cannot distinguish free dye from PS NPs. Moreover, as the HPCs are relatively small and have a high nucleus to cytoplasm volume ratio, the diffraction-limited resolution of a confocal microscope does not allow to determine the difference between internalized NPs or NPs associated with the cell membrane due to the small cytoplasm of the HPCs.

In order to explore whether a significant proportion of the dye was released from the PS NPs under biological conditions, HPCs and CD34-DCs were exposed under energy-depleted conditions. These experiments demonstrated that the uptake and/or release of PS NPs were energy-dependent. This cannot be explained when the observed process was purely credited to dye leaching and diffusion of the labile dye from the NPs. Moreover, the transient behaviour was not attributed to HPCs proliferation in which NPs divide over the daughter cells or through the induction of apoptotic cell death in which the NPs may leave the cell through the release of apoptotic bodies. In order to exclude that the observed transient loading behaviour of HPCs was caused through dye leaching, the extent of free dye or labile dye present in the NP mixture was determined through dialysis experiments under the experimental conditions (i.e. in a pH range between 5 and 7 analogous to the acidity of the endolysosomal compartment and cell culture medium, respectively). Approximately 10% of free or labile dye was present in the dialysate of the NPs' stock solution, which was independent from the pH of the solution. Next, cells were exposed to the PS NPs' isolated dye in order to investigate whether they were capable in producing the observed effects. These results demonstrated that the free dye only comprised a small fraction of the total fluorescence intensity compared to the fluorescence

intensity obtain when cells were exposed to PS NPs. Moreover, the intensity profile remained rather stable as a function of time. These results suggest that the impact of residual free dye or labile dye on the cells is rather limited. Nevertheless, it is very difficult to establish this without any doubt e.g. some reports have demonstrated that polymeric NPs which do not appear to leach under aqueous solutions in contrary can leach dye when their become in contact with the hydrophobic environment of the cell [50, 345, 407].

In order to validate if there is indeed an active excretion of the PS NPs by HPCs over time, the intracellular and time-dependent PS NPs content should ideally be monitored. Electron microscopy is frequently used to demonstrate the intracellular localization of NPs, however, as PS NPs are lucent under these conditions they can be confused with spherical vesicular structures with the risk that changes in cellular structures are mistaken for changes in the intracellular accumulation of PS NPs in HPCs [408]. Moreover, as PS NPs are composed of organic materials, they cannot be measured using ICP-MS analysis. For that reason, it is highly necessary that those observations are being reproduced with other NPs having a similar size, charge and protein corona composition, but different core which allows to validate the observation of NP release using other, more direct quantitative approaches such as ICP-MS or electron microscopy.

In the case of drug delivery, the primary goal of the used nanocarriers is the transport of the cargo to the intracellular environment where it can be released in a controlled manner. It is crucial that the contents of the NPs are not passively carried over to the cell. In **chapter 3**, the uptake, the intracellular dynamics and the intracellular degradation of biodegradable PLLA nanocarriers containing Hypericin and Coumarin-6 were investigated. Here, efforts were made to explore if the hydrophobic cargo of these nanocarriers could possibly unintendedly be transported directly to the cell surface and deliver the dyes directly into the cell through a kiss-and-run mechanism between the nanocarriers and the cell membrane [309]. To confirm this, a cell-free model system was used in which DOPC/DMPC microbubbles simulate the hydrophobic cell membrane. In this way, the hydrophobic interactions between the PLLA

nanocarriers and the cells were investigated under the *in vitro* exposure conditions. Incubation of the PLLA-Cou-Hyp NPs with the microbubbles did not cause a premature release of the cargo, which allowed to corroborate that the release of Hypericin and Coumarin-6 indeed occurred within the intracellular environment.

7.1.3 Kinetic behaviour of nanoparticles in the cell

The complexity of the movements of fluorescently stained NPs inside the cell can be characterized by a multitude of microfluorimetric methods. Ideally, the applied methods should be non-invasive, i.e. the measurements should not interfere with the NP dynamics, and relatively fast in order to follow up the NP dynamics in real-time. In **chapter 2** and **chapter 3** ICS based techniques and SPT were performed in order to evaluate the intracellular trafficking of PS NPs and PLLA nanocarriers loading with Hypericin and/or Coumarin-6. For this, confocal image time-series were recorded to measure the NP dynamics. The implemented ICS based techniques were STICS, TICS and STICCS, in which fluctuations of the fluorescence intensity are used to monitor the dynamics within an area of the cell. STICS and TICS involve the correlation analysis of the fluctuations of the fluorescently stained NPs in space and/or time. In order to assess the dynamics of the associated motions of two populations (i.e. NPs and cell organelles), STICS was used via cross-correlation analyses (STICCS) of the two fluorescence detection channels. In addition, NPs were tracked frame by frame from the image time-series and their trajectories were analysed by SPT, revealing information on the transport mode/coefficients.

The applied methods were able to provide insights into the inherent transport characteristics of the NPs and the involved cellular organelles. However, thorough knowledge of the analysis algorithms is necessary to put the obtained quantitative extraction in the right perspective. Discrepancies were found between the results obtained by STICCS, in which the obtained values provide information on the co-transport of the NPs with the cell organelle of interest, and STICS, which provides information on the total NPs dynamics. This observation is due to the averaging effects inherent to ICS based methods. Cautions should

be taken in the interpretation of the results obtained by STICS and STICCS as one could corroborate from this observation that the NPs within the cell organelles represent a subpopulation which display a much larger transport velocity compared to the NPs which are not associated with the cell organelle of interest. However, with those kind of data analyses, it is not possible to draw any conclusions on this and thus illustrating the importance of knowledge on the analysis algorithms to put this data in the right perspective.

In this work, the kinetic behaviour of fluorescently stained NPs was studied. However, as mentioned before, due to the difficulties associated with them (i.e. the presence of free dye or dye leaching), new approaches are emerging to track the dynamics of non-fluorescent NPs based on their intrinsic photophysical properties. NPs which are large enough can be detected through Rayleigh intensity scattering (e.g. 200-nm sized latex, polystyrene or silica NPs) [409]. Metal NPs – typically larger than 40 nm – can be imaged using optical microscopy including with dark field illumination [410, 411] and with total internal reflection [412]. Inorganic NPs comprised of non-centrosymmetric and highly polarized structures, can generate an optical second harmonic signal [413]. In addition, photothermal imaging can be used to observe GNPs based on the absorbing properties of the material [414].

7.2 Impact of nanoparticles on function of dendritic cells

Understanding the behaviour of NPs in DCs is important in order to understand their associated health effects and to determine their potential for new therapeutic approaches, but this is also challenging. Uptake of NPs may modify the DC functionality [171] and, vice versa, NP-induced DC maturation can change the NPs' uptake efficiency [395].

In **chapter 5** and **chapter 6** the effect of 50-nm sized GNPs on DCs was investigated. Identification of the cell surface marker expression after exposure revealed DC activation and maturation upon NP exposure. In order to investigate whether the observed immunomodulatory properties interfere with the sensitization responses, DCs were exposed to two major allergens $NiSO_4$ and

HDM in combination with GNPs. Nickel(II) allergy is an inflammatory disease, which is categorized as a delayed-type (type IV) hypersensitivity reaction. Exposure to HDM allergens can induce a type I hypersensitivity response. Both $NiSO_4$ and HDM are frequently found in the environment and represent realistic situations for a combined exposure together with nanomaterials. Accordingly, before NPs enter the biological system they can easily be polluted with biomolecules and/or contaminants present in the environment. Co-exposure of DCs to a mixture of GNPs and $NiSO_4$ demonstrated a competitive effect between both on the DC activation. However, the physicochemical characterization demonstrated that GNPs and $NiSO_4$ – as discussed before – have an indirect influence on each other. This complicates the interpretation of the results as the biological identity of the GNPs was changed in the presence of $NiSO_4$. The protein corona is important in determining the NP uptake mechanism and uptake rate, and thereby the change of the GNPs' identity can possibly explain the observed effects.

On the other hand, co-exposure of DCs to a mixture of GNPs and HDM resulted in a HDM-dependent inhibition of the DC activation. Here, changes in the protein corona composition were identified, but they did not interfere with each other's uptake. These results suggests that GNPs and HDM interact at the cell signalling level, presumably through activation of multiple intracellular pathways – for instance cascades involving the innate and adaptive immune responses.

For both allergens, profound molecular studies are needed to further explore the origin of those mixture effects. Furthermore, as mentioned before the role of the NP concentration, surface functionalization, dimension and composition should be investigated to identify whether the observed phenomenon is general or specific for the presented allergens. In order to further explore the impact of the observed immunomodulatory effects by GNPs on DCs, future research should investigate whether the capabilities of these DCs to direct T-cell proliferation and differentiation are also altered in the presence of GNPs and/or $NiSO_4$ and HDM, but also the effect of the protein corona should be further elucidated.

7.3 Future perspectives

Nanotechnology and the development of novel NPs based approaches are promising for diagnostics and therapeutics. However, there is still limited knowledge with regard to their toxicological risk, their specificity or optimal functions [415-417]. Despite the advances in the last year, the nano-bio interaction is often evaluated under conditions that do not reflect the complexity of the physiological environment. However, understanding these nano-bio interactions is extremely important to further increase the development of the field.

One of the biggest challenges is the protein corona formation around NPs and the interfering interactions of environmental contaminants. The complex interplay of the proteins with the NPs surface through numerous weak interactions make it difficult to predict its final identity which will interact with the cellular machinery. In the past, the focus of the nanotechnology was primarily on the physicochemical properties of the NPs itself, the chemically attached biomolecules to the NPs' surface and the biomolecule binding target. However, it has now been recognized that under real-life biological conditions protein coronas are formed spontaneously and that this needs to be accounted for [415, 416, 418]. Interestingly, the concept of the personalized protein corona has been introduced recently, taking into account that the protein corona composition is strongly dependent on the protein source of the individual [419]. Consequently, patients with different diseases can form a different protein corona when exposed to the same NPs due to individual differences in their serum profile, changing the NPs' identity and behaviour and thus complicating further the picture.

In addition, more emphasis should be put on a more realistic evaluation of the toxicity and potential effects of NPs e.g. under several conditions in their life cycle. NPs can change over time, due to biological and environmental processes (e.g. adsorption of proteins or endotoxins) but also through chemical reactions (e.g. dissolution and surface reactions). Accordingly, the effects of NPs during their entire life cycle has to be taken into account.

In order to make significant progress in the nanomedical field, it is necessary that technologies and methods for characterization of the nano-bio interactions are implemented and applied under conditions which reflect the real-life and personalized complexity of the physiological environment in a clinical setting. Moreover, by developing new and more advanced methods the interaction of proteins with the NP and, consequently, their interactions with the cells can be further explored.

Reference list

1. Strambeanu, N., L. Demetrovici, and D. Dragos, *Natural Sources of Nanoparticles*, in *Nanoparticles' Promises and Risks*, M. Lungu, et al., Editors. 2015, Springer International Publishing. p. 9-19.
2. Heiligtag, F.J. and M. Niederberger, *The fascinating world of nanoparticle research.* Materials Today, 2013. **16**(7–8): p. 262-271.
3. Horikoshi, S. and N. Serpone, *Introduction to Nanoparticles*, in *Microwaves in Nanoparticle Synthesis*. 2013, Wiley-VCH Verlag GmbH & Co. KGaA. p. 1-24.
4. Sciau, P., *Nanoparticles in Ancient Materials: The Metallic Lustre Decorations of Medieval Ceramics*. The Delivery of Nanoparticles, ed. A.A. Hashim. 2012: InTech.
5. Santamaria, A., *Historical Overview of Nanotechnology and Nanotoxicology*, in *Nanotoxicity*, J. Reineke, Editor. 2012, Humana Press. p. 1-12.
6. *Commision recommendation of 18 October 2011 on the definition of nanomaterial (2011/696/EU)*. 2011, Official Journal of the European Union. p. 38-40.
7. Buzea, C., I. Pacheco, and K. Robbie, *Nanomaterials and nanoparticles: Sources and toxicity.* Biointerphases, 2007. **2**(4): p. MR17-MR71.
8. Nel, A., et al., *Toxic potential of materials at the nanolevel.* Science, 2006. **311**(5761): p. 622-7.
9. Oberdörster, G., E. Oberdörster, and J. Oberdörster, *Nanotoxicology: An Emerging Discipline Evolving from Studies of Ultrafine Particles.* Environ Health Perspect, 2005. **113**(7): p. 823-839.
10. Roduner, E., *Size matters: why nanomaterials are different.* Chem Soc Rev, 2006. **35**(7): p. 583-592.
11. Gallego, O. and V. Puntes, *What can nanotechnology do to fight cancer?* Clin Transl Oncol, 2006. **8**(11): p. 788-95.
12. Masotti, A., *Multifuntional nanoparticles: preparation and applications in biomedicine and in non-invasive bioimaging.* Recent Pat Nanotechnol, 2010. **4**(1): p. 53-62.
13. Lundqvist, M., et al., *The evolution of the protein corona around nanoparticles: a test study.* ACS Nano, 2011. **5**(9): p. 7503-9.
14. Nienhaus, G.U., P. Maffre, and K. Nienhaus, *Studying the protein corona on nanoparticles by FCS.* Methods Enzymol, 2013. **519**: p. 115-37.
15. Fröhlich, E. and E. Roblegg, *Models for oral uptake of nanoparticles in consumer products.* Toxicology, 2012. **291**(1-3): p. 10-17.
16. Cedervall, T., et al., *Understanding the nanoparticle-protein corona using methods to quantify exchange rates and affinities of proteins for nanoparticles.* Proc Natl Acad Sci U S A, 2007. **104**(7): p. 2050-5.
17. Vroman, L., et al., *Interaction of high molecular weight kininogen, factor XII, and fibrinogen in plasma at interfaces.* Blood, 1980. **55**(1): p. 156-9.
18. Tenzer, S., et al., *Rapid formation of plasma protein corona critically affects nanoparticle pathophysiology.* Nat Nano, 2013. **8**(10): p. 772-781.

19. Tenzer, S., et al., *Nanoparticle size is a critical physicochemical determinant of the human blood plasma corona: a comprehensive quantitative proteomic analysis.* ACS Nano, 2011. **5**: p. 7155 - 7167.
20. Casals, E., et al., *Time Evolution of the Nanoparticle Protein Corona.* ACS Nano, 2010. **4**(7): p. 3623-3632.
21. Monopoli, M.P., et al., *Physical–Chemical Aspects of Protein Corona: Relevance to in Vitro and in Vivo Biological Impacts of Nanoparticles.* J Am Chem Soc, 2011. **133**(8): p. 2525-2534.
22. Luyts, K., et al., *How physico-chemical characteristics of nanoparticles cause their toxicity: complex and unresolved interrelations.* Env Sci Process Impact, 2013. **15**(1): p. 23-38.
23. Lundqvist, M., et al., *Nanoparticle size and surface properties determine the protein corona with possible implications for biological impacts.* Proc Natl Acad Sci U S A, 2008. **105**(38): p. 14265-70.
24. Milani, S., et al., *Reversible versus irreversible binding of transferrin to polystyrene nanoparticles: soft and hard corona.* ACS Nano, 2012. **6**(3): p. 2532-41.
25. Walczyk, D., et al., *What the cell "sees" in bionanoscience.* J Am Chem Soc, 2010. **132**(16): p. 5761-8.
26. Nel, A.E., et al., *Understanding biophysicochemical interactions at the nano-bio interface.* Nat Mater, 2009. **8**(7): p. 543-557.
27. dos Santos, T., et al., *Effects of transport inhibitors on the cellular uptake of carboxylated polystyrene nanoparticles in different cell lines.* PLoS One, 2011. **6**(9): p. e24438.
28. Hillaireau, H. and P. Couvreur, *Nanocarriers' entry into the cell: relevance to drug delivery.* Cell Mol Life Sci, 2009. **66**(17): p. 2873-2896.
29. Aderem, A. and D.M. Underhill, *Mechanisms of phagocytosis in macrophages.* Annu Rev Immunol, 1999. **17**: p. 593-623.
30. Rabinovitch, M., *Professional and non-professional phagocytes: an introduction.* Trends Cell Biol, 1995. **5**(3): p. 85-7.
31. Owens, D.E., 3rd and N.A. Peppas, *Opsonization, biodistribution, and pharmacokinetics of polymeric nanoparticles.* Int J Pharm, 2006. **307**(1): p. 93-102.
32. Vonarbourg, A., et al., *Parameters influencing the stealthiness of colloidal drug delivery systems.* Biomaterials, 2006. **27**.
33. Stern, S.T., P.P. Adiseshaiah, and R.M. Crist, *Autophagy and lysosomal dysfunction as emerging mechanisms of nanomaterial toxicity.* Part Fibre Toxicol, 2012. **9**(1): p. 1-17.
34. Bareford, L.M. and P.W. Swaan, *Endocytic mechanisms for targeted drug delivery.* Adv Drug Deliv Rev, 2007. **59**.
35. Conner, S.D. and S.L. Schmid, *Regulated portals of entry into the cell.* Nature, 2003. **422**.
36. Hillaireau, H., et al., *Hybrid polymer nanocapsules enhance in vitro delivery of azidothymidine-triphosphate to macrophages.* J Control Release, 2006. **116**(3): p. 346-52.
37. Mayor, S. and R.E. Pagano, *Pathways of clathrin-independent endocytosis.* Nat Rev Mol Cell Biol, 2007. **8**(8): p. 603-12.

38. Wang, T., et al., *Cellular uptake of nanoparticles by membrane penetration: a study combining confocal microscopy with FTIR spectroelectrochemistry.* ACS Nano, 2012. **6**(2): p. 1251-9.
39. Rothen-Rutishauser, B.M., et al., *Interaction of fine particles and nanoparticles with red blood cells visualized with advanced microscopic techniques.* Environ Sci Technol, 2006. **40**(14): p. 4353-9.
40. Treuel, L., X. Jiang, and G.U. Nienhaus, *New views on cellular uptake and trafficking of manufactured nanoparticles.* J R Soc Interface, 2013. **10**(82): p. 20120939.
41. Verma, A., et al., *Surface-structure-regulated cell-membrane penetration by monolayer-protected nanoparticles.* Nat Mater, 2008. **7**(7): p. 588-95.
42. Zhang, X. and S. Yang, *Nonspecific adsorption of charged quantum dots on supported zwitterionic lipid bilayers: real-time monitoring by quartz crystal microbalance with dissipation.* Langmuir, 2011. **27**(6): p. 2528-35.
43. Dif, A., et al., *Interaction between water-soluble peptidic CdSe/ZnS nanocrystals and membranes: formation of hybrid vesicles and condensed lamellar phases.* J Am Chem Soc, 2008. **130**(26): p. 8289-96.
44. Leroueil, P.R., et al., *Nanoparticle Interaction with Biological Membranes: Does Nanotechnology present a Janus Face?* Acc Chem Res, 2007. **40**(5): p. 335-342.
45. Laurencin, M., et al., *Interactions between giant unilamellar vesicles and charged core-shell magnetic nanoparticles.* Langmuir, 2010. **26**(20): p. 16025-30.
46. Roiter, Y., et al., *Interaction of nanoparticles with lipid membrane.* Nano Lett, 2008. **8**(3): p. 941-4.
47. Leroueil, P.R., et al., *Wide varieties of cationic nanoparticles induce defects in supported lipid bilayers.* Nano Lett, 2008. **8**(2): p. 420-4.
48. Kostarelos, K., et al., *Cellular uptake of functionalized carbon nanotubes is independent of functional group and cell type.* Nat Nanotechnol, 2007. **2**(2): p. 108-13.
49. Yu, J., S.A. Patel, and R.M. Dickson, *In vitro and intracellular production of peptide-encapsulated fluorescent silver nanoclusters.* Angew Chem Int Ed Engl, 2007. **46**(12): p. 2028-30.
50. Salvati, A., et al., *Experimental and theoretical comparison of intracellular import of polymeric nanoparticles and small molecules: toward models of uptake kinetics.* Nanomedicine, 2011. **7**(6): p. 818-826.
51. Kuhn, D.A., et al., *Different endocytotic uptake mechanisms for nanoparticles in epithelial cells and macrophages.* Beilstein J Nanotechnol, 2014. **5**: p. 1625-1636.
52. Iversen, T.G., N. Frerker, and K. Sandvig, *Uptake of ricinB-quantum dot nanoparticles by a macropinocytosis-like mechanism.* J Nanobiotechnology, 2012. **10**: p. 33.

53. Vranic, S., et al., *Deciphering the mechanisms of cellular uptake of engineered nanoparticles by accurate evaluation of internalization using imaging flow cytometry.* Part Fibre Toxicol, 2013. **10**(1): p. 1-16.
54. Firdessa, R., T.A. Oelschlaeger, and H. Moll, *Identification of multiple cellular uptake pathways of polystyrene nanoparticles and factors affecting the uptake: relevance for drug delivery systems.* Eur J Cell Biol, 2014. **93**(8-9): p. 323-37.
55. Shang, L., K. Nienhaus, and G. Nienhaus, *Engineered nanoparticles interacting with cells: size matters.* J Nanobiotechnol, 2014. **12**(1): p. 5.
56. Albanese, A., P.S. Tang, and W.C. Chan, *The effect of nanoparticle size, shape, and surface chemistry on biological systems.* Annu Rev Biomed Eng, 2012. **14**: p. 1-16.
57. Lunov, O., et al., *Modeling receptor-mediated endocytosis of polymer-functionalized iron oxide nanoparticles by human macrophages.* Biomaterials, 2011. **32**(2): p. 547-55.
58. dos Santos, T., et al., *Quantitative Assessment of the Comparative Nanoparticle-Uptake Efficiency of a Range of Cell Lines.* Small, 2011. **7**(23): p. 3341-3349.
59. Rejman, J., et al., *Size-dependent internalization of particles via the pathways of clathrin- and caveolae-mediated endocytosis.* Biochem J, 2004. **377**(1): p. 159-169.
60. Chithrani, B.D., A.A. Ghazani, and W.C. Chan, *Determining the size and shape dependence of gold nanoparticle uptake into mammalian cells.* Nano Lett, 2006. **6**(4): p. 662-8.
61. Andar, A.U., et al., *Microfluidic preparation of liposomes to determine particle size influence on cellular uptake mechanisms.* Pharm Res, 2014. **31**(2): p. 401-13.
62. Lu, F., et al., *Size Effect on Cell Uptake in Well-Suspended, Uniform Mesoporous Silica Nanoparticles.* Small, 2009. **5**(12): p. 1408-1413.
63. Osaki, F., et al., *A Quantum Dot Conjugated Sugar Ball and Its Cellular Uptake. On the Size Effects of Endocytosis in the Subviral Region.* J Am Chem Soc, 2004. **126**(21): p. 6520-6521.
64. Wang, S.-H., et al., *Size-dependent endocytosis of gold nanoparticles studied by three-dimensional mapping of plasmonic scattering images.* J Nanobiotechnol, 2010. **8**(1): p. 33.
65. Brun, E. and C.c. Sicard ? Roselli, *Could nanoparticle corona characterization help for biological consequence prediction?* Cancer Nanotechnol, 2014. **5**(1): p. 7.
66. Wang, G., et al., *Gold-peptide nanoconjugate cellular uptake is modulated by serum proteins.* Nanomed Nanotechnol Biol Med, 2012. **8**: p. 822 - 832.
67. Patel, P., et al., *Scavenger receptors mediate cellular uptake of polyvalent oligonucleotide-functionalized gold nanoparticles.* Bioconj Chem, 2010. **21**: p. 2250 - 2256.
68. Jiang, X., et al., *Quantitative analysis of the protein corona on FePt nanoparticles formed by transferrin binding.* J R Soc Lond Interface, 2010. **7**(Suppl 1): p. S5 - S13.

69. Treuel, L., et al., *Impact of protein modification on the protein corona on nanoparticles and nanoparticle-cell interactions.* ACS Nano, 2014. **8**: p. 503 - 513.
70. Lesniak, A., et al., *Effects of the presence or absence of a protein corona on silica nanoparticle uptake and impact on cells.* ACS Nano, 2012. **6**: p. 5845 - 5857.
71. Lesniak, A., et al., *Nanoparticle adhesion to the cell membrane and its effect on nanoparticle uptake efficiency.* J Am Chem Soc, 2013. **135**: p. 1438 - 1444.
72. Lunov, O., et al., *Differential uptake of functionalized polystyrene nanoparticles by human macrophages and a monocytic cell line.* ACS Nano, 2011. **5**: p. 1657 - 1669.
73. Peng, Q., et al., *Preformed albumin corona, a protective coating for nanoparticles based drug delivery system.* Biomaterials, 2013. **34**: p. 8521 - 8530.
74. Lesniak, A., et al., *Serum heat inactivation affects protein corona composition and nanoparticle uptake.* Biomaterials, 2010. **31**: p. 9511 - 9518.
75. Maiorano, G., et al., *Effects of cell culture media on the dynamic formation of protein-nanoparticle complexes and influence on the cellular response.* ACS Nano, 2010. **4**: p. 7481 - 7491.
76. Yan, Y., et al., *Differential roles of the protein corona in the cellular uptake of nanoporous polymer particles by monocyte and macrophage cell lines.* ACS Nano, 2013. **7**: p. 10960 - 10970.
77. Prapainop, K., D. Witter, and P. Wentworth, *A chemical approach for cell-specific targeting of nanomaterials: small-molecule-initiated misfolding of nanoparticle corona proteins.* J Am Chem Soc, 2012. **134**: p. 4100 - 4103.
78. Krais, A., et al., *Targeted uptake of folic acid-functionalized iron oxide nanoparticles by ovarian cancer cells in the presence but not in the absence of serum.* Nanomed Nanotechnol Biol Med, 2014. **?**: p.?
79. Maynard, A. and D.H. Pui, *Nanotechnology and occupational health: New technologies – new challenges.* J Nanopart Res, 2007. **9**(1): p. 1-3.
80. Giles, J., *Nanotechnology: what is there to fear from something so small?* Nature, 2003. **426**(6968): p. 750.
81. Soenen, S.J., et al., *Cellular toxicity of inorganic nanoparticles: Common aspects and guidelines for improved nanotoxicity evaluation.* Nano Today, 2011. **6**(5): p. 446-465.
82. Stroh, A., et al., *Iron oxide particles for molecular magnetic resonance imaging cause transient oxidative stress in rat macrophages.* Free Radic Biol Med, 2004. **36**(8): p. 976-84.
83. Jain, T.K., et al., *Biodistribution, clearance, and biocompatibility of iron oxide magnetic nanoparticles in rats.* Mol Pharm, 2008. **5**(2): p. 316-27.
84. Soto, K., K.M. Garza, and L.E. Murr, *Cytotoxic effects of aggregated nanomaterials.* Acta Biomater, 2007. **3**(3): p. 351-8.
85. Fu, P.P., et al., *Mechanisms of nanotoxicity: Generation of reactive oxygen species.* J Food Drug Anal, 2014. **22**(1): p. 64-75.

86. Halliwell, B. and O.I. Aruoma, *DNA damage by oxygen-derived species Its mechanism and measurement in mammalian systems.* FEBS Lett, 1991. **281**(1–2): p. 9-19.
87. Meng, H., et al., *A Predictive Toxicological Paradigm for the Safety Assessment of Nanomaterials.* ACS Nano, 2009. **3**(7): p. 1620-1627.
88. Valko, M., et al., *Free radicals, metals and antioxidants in oxidative stress-induced cancer.* Chem Biol Interact, 2006. **160**(1): p. 1-40.
89. Valko, M., et al., *Free radicals and antioxidants in normal physiological functions and human disease.* Int J Biochem Cell Biol, 2007. **39**(1): p. 44-84.
90. Stadtman, E.R. and B.S. Berlett, *Reactive Oxygen-Mediated Protein Oxidation in Aging and Disease.* Chem Res Toxicol, 1997. **10**(5): p. 485-494.
91. Butterfield, D.A. and J. Kanski, *Brain protein oxidation in age-related neurodegenerative disorders that are associated with aggregated proteins.* Mech Ageing Dev, 2001. **122**(9): p. 945-62.
92. Poon, H.F., et al., *Free radicals and brain aging.* Clin Geriatr Med, 2004. **20**(2): p. 329-59.
93. Poli, G., et al., *Oxidative stress and cell signalling.* Curr Med Chem, 2004. **11**(9): p. 1163-82.
94. Evans, M.D., M. Dizdaroglu, and M.S. Cooke, *Oxidative DNA damage and disease: induction, repair and significance.* Mutat Res, 2004. **567**(1): p. 1-61.
95. Shi, H., L.G. Hudson, and K.J. Liu, *Oxidative stress and apoptosis in metal ion-induced carcinogenesis.* Free Radic Biol Med, 2004. **37**(5): p. 582-593.
96. Wang, F., et al., *Oxidative stress contributes to silica nanoparticle-induced cytotoxicity in human embryonic kidney cells.* Toxicol In Vitro, 2009. **23**(5): p. 808-15.
97. Huang, D.M., et al., *The promotion of human mesenchymal stem cell proliferation by superparamagnetic iron oxide nanoparticles.* Biomaterials, 2009. **30**(22): p. 3645-51.
98. Schafer, R., et al., *Transferrin receptor upregulation: in vitro labeling of rat mesenchymal stem cells with superparamagnetic iron oxide.* Radiology, 2007. **244**(2): p. 514-23.
99. Pisanic, T.R., 2nd, et al., *Nanotoxicity of iron oxide nanoparticle internalization in growing neurons.* Biomaterials, 2007. **28**(16): p. 2572-81.
100. Daniels, P.J., et al., *Mammalian metal response element-binding transcription factor-1 functions as a zinc sensor in yeast, but not as a sensor of cadmium or oxidative stress.* Nucleic Acids Res, 2002. **30**(14): p. 3130-3140.
101. Ferré-D'Amaré, A. and W.C. Winkler, *The roles of metal ions in regulation by riboswitches.* Met Ions Life Sci, 2011. **9**: p. 141-173.
102. van Aerle, R., et al., *Molecular Mechanisms of Toxicity of Silver Nanoparticles in Zebrafish Embryos.* Environ Sci Technol, 2013. **47**(14): p. 8005-8014.

103. Soenen, S.J., et al., *Intracellular nanoparticle coating stability determines nanoparticle diagnostics efficacy and cell functionality.* Small, 2010. **6**(19): p. 2136-45.
104. Kedziorek, D.A., et al., *Gene expression profiling reveals early cellular responses to intracellular magnetic labeling with superparamagnetic iron oxide nanoparticles.* Magn Reson Med, 2010. **63**(4): p. 1031-43.
105. Chen, M. and A. von Mikecz, *Formation of nucleoplasmic protein aggregates impairs nuclear function in response to SiO2 nanoparticles.* Exp Cell Res, 2005. **305**.
106. Park, H.J., et al., *Silver-ion-mediated reactive oxygen species generation affecting bactericidal activity.* Water Res, 2009. **43**(4): p. 1027-32.
107. Kwakye-Awuah, B., et al., *Antimicrobial action and efficiency of silver-loaded zeolite X.* J Appl Microbiol, 2008. **104**(5): p. 1516-24.
108. Saptarshi, S., A. Duschl, and A. Lopata, *Interaction of nanoparticles with proteins: relation to bio-reactivity of the nanoparticle.* J Nanobiotechnol, 2013. **11**: p. 26.
109. Linse, S., et al., *Nucleation of protein fibrillation by nanoparticles.* Proc Natl Acad Sci U S A, 2007. **104**(21): p. 8691-6.
110. Baglioni, S., et al., *Prefibrillar amyloid aggregates could be generic toxins in higher organisms.* J Neurosci, 2006. **26**(31): p. 8160-7.
111. Dempsey, P.W., S.A. Vaidya, and G. Cheng, *The art of war: Innate and adaptive immune responses.* Cell Mol Life Sci, 2003. **60**(12): p. 2604-21.
112. Amodio, G. and S. Gregori, *Dendritic cells a double-edge sword in autoimmune responses.* Front Immunol, 2012. **3**: p. 233.
113. Banchereau, J. and R.M. Steinman, *Dendritic cells and the control of immunity.* Nature, 1998. **392**(6673): p. 245-52.
114. Lambrecht, B.N. and H. Hammad, *The role of dendritic and epithelial cells as master regulators of allergic airway inflammation.* Lancet, 2010. **376**(9743): p. 835-43.
115. Laskarin, G., et al., *Antigen-presenting cells and materno-fetal tolerance: an emerging role for dendritic cells.* Am J Reprod Immunol, 2007. **58**(3): p. 255-67.
116. Merad, M., F. Ginhoux, and M. Collin, *Origin, homeostasis and function of Langerhans cells and other langerin-expressing dendritic cells.* Nat Rev Immunol, 2008. **8**(12): p. 935-47.
117. Rescigno, M. and A. Di Sabatino, *Dendritic cells in intestinal homeostasis and disease.* J Clin Invest, 2009. **119**(9): p. 2441-50.
118. van Spriel, A.B. and E.C. de Jong, *Dendritic cell science: more than 40 years of history.* J Leukoc Biol, 2013. **93**(1): p. 33-8.
119. Wu, L. and A. Galy, *Chapter 1 - The development of dendritic cells from hematopoietic precursors*, in *Dendritic Cells (Second Edition)*, M.T.L.W. Thomson, Editor. 2001, Academic Press: London. p. 3-I.
120. Saha, P. and F. Geissmann, *Toward a functional characterization of blood monocytes.* Immunol Cell Biol, 2011. **89**(1): p. 2-4.
121. Breton, G., et al., *Defining human dendritic cell progenitors by multiparametric flow cytometry.* Nat Protoc, 2015. **10**(9): p. 1407-1422.

122. Lee, J., et al., *Restricted dendritic cell and monocyte progenitors in human cord blood and bone marrow.* J Exp Med, 2015. **212**(3): p. 385-99.
123. Breton, G., et al., *Circulating precursors of human CD1c+ and CD141+ dendritic cells.* J Exp Med, 2015. **212**(3): p. 401-13.
124. Vu Manh, T.-P., et al., *Investigating evolutionary conservation of dendritic cell subset identity and functions.* Front Immunol, 2015. **6**.
125. Qu, C., et al., *Monocyte-derived dendritic cells: targets as potent antigen-presenting cells for the design of vaccines against infectious diseases.* Int J Infect Dis, 2014. **19**: p. 1-5.
126. Leon, B., M. Lopez-Bravo, and C. Ardavin, *Monocyte-derived dendritic cells.* Sem Immunol, 2005. **17**(4): p. 313-8.
127. Leon, B. and C. Ardavin, *Monocyte-derived dendritic cells in innate and adaptive immunity.* Immunol Cell Biol, 2008. **86**(4): p. 320-324.
128. Manh, T.-P.V., et al., *Plasmacytoid, conventional, and monocyte-derived dendritic cells undergo a profound and convergent genetic reprogramming during their maturation.* Eur J Immunol, 2013. **43**(7): p. 1706-1715.
129. Krishnaswamy, J.K., T. Chu, and S.C. Eisenbarth, *Beyond pattern recognition: NOD-like receptors in dendritic cells.* Trends Immunol, 2013. **34**(5): p. 224-233.
130. Trombetta, E.S. and I. Mellman, *Cell biology of antigen processing in vitro and in vivo.* Annu Rev Immunol, 2005. **23**: p. 975-1028.
131. Villadangos, J.A. and P. Schnorrer, *Intrinsic and cooperative antigen-presenting functions of dendritic-cell subsets in vivo.* Nat Rev Immunol, 2007. **7**(7): p. 543-555.
132. Roche, P.A. and K. Furuta, *The ins and outs of MHC class II-mediated antigen processing and presentation.* Nat Rev Immunol, 2015. **15**(4): p. 203-216.
133. Munz, C., R.M. Steinman, and S. Fujii, *Dendritic cell maturation by innate lymphocytes: coordinated stimulation of innate and adaptive immunity.* J Exp Med, 2005. **202**(2): p. 203-7.
134. Iwasaki, A. and R. Medzhitov, *Toll-like receptor control of the adaptive immune responses.* Nat Immunol, 2004. **5**(10): p. 987-995.
135. West, M.A., et al., *Enhanced dendritic cell antigen capture via toll-like receptor-induced actin remodeling.* Science, 2004. **305**(5687): p. 1153-7.
136. Verdijk, P., et al., *Morphological changes during dendritic cell maturation correlate with cofilin activation and translocation to the cell membrane.* Eur J Immunol, 2004. **34**(1): p. 156-64.
137. Dalod, M., et al., *Dendritic cell maturation: functional specialization through signaling specificity and transcriptional programming.* The EMBO Journal, 2014. **33**(10): p. 1104-1116.
138. Lipscomb, M.F. and B.J. Masten, *Dendritic Cells: Immune Regulators in Health and Disease.* Physiol Rev, 2002. **82**(1): p. 97-130.
139. Austyn, J., *Antigen-presenting Cells.* Am J Respir Crit Care Med, 2000. **162**(supplement_3): p. S146-S150.

140. Banchereau, J., et al., *Immunobiology of dendritic cells.* Annu Rev Immunol, 2000. **18**: p. 767-811.
141. Reis e Sousa, C., A. Sher, and P. Kaye, *The role of dendritic cells in the induction and regulation of immunity to microbial infection.* Curr Opin Immunol, 1999. **11**(4): p. 392-9.
142. Stockwin, L.H., et al., *Dendritic cells: immunological sentinels with a central role in health and disease.* Immunol Cell Biol, 2000. **78**(2): p. 91-102.
143. Steinman, R.M. and J. Banchereau, *Taking dendritic cells into medicine.* Nature, 2007. **449**(7161): p. 419-426.
144. Drakesmith, H., B. Chain, and P. Beverley, *How can dendritic cells cause autoimmune disease?* Immunol Today, 2000. **21**(5): p. 214-7.
145. Hardin, J.A., *Dendritic cells: potential triggers of autoimmunity and targets for therapy.* Ann Rheum Dis, 2005. **64**(suppl 4): p. iv86-iv90.
146. Pinzon-Charry, A., T. Maxwell, and J.A. Lopez, *Dendritic cell dysfunction in cancer: A mechanism for immunosuppression.* Immunol Cell Biol, 2005. **83**(5): p. 451-461.
147. e Silva, R.d.F., M.C.A.B. de Castro, and V.R.A. Pereira, *Dendritic cells based approaches in the fight against diseases.* Front Immunol, 2014. **5**.
148. Delamarre, L. and I. Mellman, *Harnessing dendritic cells for immunotherapy.* Sem Immunol, 2011. **23**(1): p. 2-11.
149. Fajardo-Moser, M., S. Berzel, and H. Moll, *Mechanisms of dendritic cell-based vaccination against infection.* Int J Med Microbiol, 2008. **298**(1–2): p. 11-20.
150. Galluzzi, L., et al., *Trial watch: Dendritic cell-based interventions for cancer therapy.* Oncoimmunology, 2012. **1**(7): p. 1111-1134.
151. Lion, E., et al., *NK cells: key to success of DC-based cancer vaccines?* Oncologist, 2012. **17**(10): p. 1256-70.
152. Ricupito, A., et al., *Boosting anticancer vaccines: Too much of a good thing?* Oncoimmunology, 2013. **2**(7): p. e25032.
153. McCurry, K.R., et al., *Regulatory dendritic cell therapy in organ transplantation.* Transpl Int, 2006. **19**(7): p. 525-38.
154. Lambrecht, B. and H. Hammad, *Lung Dendritic Cells: Targets for Therapy in Allergic Disease*, in *Dendritic Cells*, G. Lombardi and Y. Riffo-Vasquez, Editors. 2009, Springer Berlin Heidelberg. p. 99-114.
155. Li, H. and B. Shi, *Tolerogenic dendritic cells and their applications in transplantation.* Cell Mol Immunol, 2015. **12**(1): p. 24-30.
156. Moghimi, S.M., A.C. Hunter, and J.C. Murray, *Nanomedicine: current status and future prospects.* FASEB J, 2005. **19**(3): p. 311-330.
157. Duschl, A., *Chapter 4 - Nanoparticles and Allergy*, in *Nanoparticles and the Immune System*, D. Boraschi and A. Duschl, Editors. 2014, Academic Press: San Diego. p. 55-68.
158. Klippstein, R. and D. Pozo, *Nanotechnology-based manipulation of dendritic cells for enhanced immunotherapy strategies.* Nanomedicine, 2010. **6**(4): p. 523-9.
159. Valavanidis, A., K. Fiotakis, and T. Vlachogianni, *Airborne particulate matter and human health: toxicological assessment and importance of size and composition of particles for oxidative damage and carcinogenic*

mechanisms. J Environ Sci Health C Environ Carcinog Ecotoxicol Rev, 2008. **26**(4): p. 339-62.
160. Hopke, P.K. and A. Rossner, *Exposure to airborne particulate matter in the ambient, indoor, and occupational environments.* Clin Occup Environ Med, 2006. **5**(4): p. 747-71.
161. Li, N., et al., *Ambient ultrafine particles provide a strong adjuvant effect in the secondary immune response: implication for traffic-related asthma flares.* Am J Physiol Lung Cell Mol Physiol, 2010. **299**(3): p. L374-83.
162. Evans, K.A., et al., *Increased ultrafine particles and carbon monoxide concentrations are associated with asthma exacerbation among urban children.* Environ Res, 2014. **129**: p. 11-9.
163. Hardy, C.L., et al., *Inert 50-nm polystyrene nanoparticles that modify pulmonary dendritic cell function and inhibit allergic airway inflammation.* J Immunol, 2012. **188**(3): p. 1431-41.
164. Lovik, M., et al., *Diesel exhaust particles and carbon black have adjuvant activity on the local lymph node response and systemic IgE production to ovalbumin.* Toxicology, 1997. **121**(2): p. 165-78.
165. Ghio, A.J. and R.B. Devlin, *Inflammatory lung injury after bronchial instillation of air pollution particles.* Am J Respir Crit Care Med, 2001. **164**(4): p. 704-8.
166. Brandenberger, C., et al., *Engineered silica nanoparticles act as adjuvants to enhance allergic airway disease in mice.* Part Fibre Toxicol, 2013. **10**: p. 26.
167. Kroker, M., et al., *Preventing carbon nanoparticle-induced lung inflammation reduces antigen-specific sensitization and subsequent allergic reactions in a mouse model.* Part Fibre Toxicol, 2015. **12**(1): p. 20.
168. Hussain, S., et al., *Nano-titanium dioxide modulates the dermal sensitization potency of DNCB.* Part Fibre Toxicol, 2012. **9**: p. 15.
169. Hussain, S., et al., *Lung exposure to nanoparticles modulates an asthmatic response in a mouse model.* Eur Respir J, 2011. **37**(2): p. 299-309.
170. Villiers, C., et al., *Analysis of the toxicity of gold nano particles on the immune system: effect on dendritic cell functions.* J Nanopart Res, 2010. **12**(1): p. 55-60.
171. Tomić, S., et al., *Size-Dependent Effects of Gold Nanoparticles Uptake on Maturation and Antitumor Functions of Human Dendritic Cells In Vitro.* PLoS One, 2014. **9**(5): p. e96584.
172. Frick, S.U., et al., *Functionalized polystyrene nanoparticles trigger human dendritic cell maturation resulting in enhanced CD4+ T cell activation.* Macromol Biosci, 2012. **12**(12): p. 1637-47.
173. Blank, F., et al., *Biomedical nanoparticles modulate specific CD4+ T cell stimulation by inhibition of antigen processing in dendritic cells.* Nanotoxicology, 2011. **5**(4): p. 606-21.
174. Zupke, O., et al., *Preservation of dendritic cell function upon labeling with amino functionalized polymeric nanoparticles.* Biomaterials, 2010. **31**(27): p. 7086-95.

175. Mottram, P.L., et al., *Type 1 and 2 immunity following vaccination is influenced by nanoparticle size: formulation of a model vaccine for respiratory syncytial virus.* Mol Pharm, 2007. **4**(1): p. 73-84.
176. Broos, S., et al., *Immunomodulatory nanoparticles as adjuvants and allergen-delivery system to human dendritic cells: Implications for specific immunotherapy.* Vaccine, 2010. **28**(31): p. 5075-85.
177. Seong, S.Y. and P. Matzinger, *Hydrophobicity: an ancient damage-associated molecular pattern that initiates innate immune responses.* Nat Rev Immunol, 2004. **4**(6): p. 469-78.
178. Palucka, K. and J. Banchereau, *Cancer immunotherapy via dendritic cells.* Nat Rev Cancer, 2012. **12**(4): p. 265-77.
179. Sehgal, K., et al., *Nanoparticle-mediated combinatorial targeting of multiple human dendritic cell (DC) subsets leads to enhanced T cell activation via IL-15-dependent DC crosstalk.* J Immunol, 2014. **193**(5): p. 2297-305.
180. Ballester, M., et al., *Nanoparticle conjugation enhances the immunomodulatory effects of intranasally delivered CpG in house dust mite-allergic mice.* Sci Rep, 2015. **5**: p. 14274.
181. Kenyon, N.J., et al., *Self-assembling nanoparticles containing dexamethasone as a novel therapy in allergic airways inflammation.* PLoS One, 2013. **8**(10): p. e77730.
182. Look, M., et al., *The nanomaterial-dependent modulation of dendritic cells and its potential influence on therapeutic immunosuppression in lupus.* Biomaterials, 2014. **35**(3): p. 1089-95.
183. Weiss, R., et al., *New approaches to transcutaneous immunotherapy: targeting dendritic cells with novel allergen conjugates.* Curr Opin Allergy Clin Immunol, 2013. **13**(6): p. 669-76.
184. Kawasaki, N., et al., *Targeted delivery of mycobacterial antigens to human dendritic cells via Siglec-7 induces robust T cell activation.* J Immunol, 2014. **193**(4): p. 1560-6.
185. Pavot, V., et al., *Directing vaccine immune responses to mucosa by nanosized particulate carriers encapsulating NOD ligands.* Biomaterials, 2016. **75**: p. 327-39.
186. Nagatomo, D., et al., *Cholesteryl Pullulan Encapsulated TNF-alpha Nanoparticles Are an Effective Mucosal Vaccine Adjuvant against Influenza Virus.* Biomed Res Int, 2015. **2015**: p. 471468.
187. Xiang, S.D., et al., *Nanoparticles modify dendritic cell homeostasis and induce non-specific effects on immunity to malaria.* Trans R Soc Trop Med Hyg, 2015. **109**(1): p. 70-6.
188. Yuan, B., et al., *A novel nanoparticle containing MOG peptide with BTLA induces T cell tolerance and prevents multiple sclerosis.* Mol Immunol, 2014. **57**(2): p. 93-9.
189. Yeste, A., et al., *Nanoparticle-mediated codelivery of myelin antigen and a tolerogenic small molecule suppresses experimental autoimmune encephalomyelitis.* Proc Natl Acad Sci U S A, 2012. **109**(28): p. 11270-5.
190. Shang, L. and G.U. Nienhaus, *Small fluorescent nanoparticles at the nano–bio interface.* Materials Today, 2013. **16**(3): p. 58-66.

191. Hötzer, B., I.L. Medintz, and N. Hildebrandt, *Fluorescence: Fluorescence in Nanobiotechnology: Sophisticated Fluorophores for Novel Applications (Small 15/2012).* Small, 2012. **8**(15): p. 2290-2290.
192. Mailander, V. and K. Landfester, *Interaction of nanoparticles with cells.* Biomacromolecules, 2009. **10**(9): p. 2379-400.
193. Schumann, C., et al., *A correlative approach at characterizing nanoparticle mobility and interactions after cellular uptake.* J Biophotonics, 2012. **5**(2): p. 117-27.
194. Zhang, L.W. and N.A. Monteiro-Riviere, *Use of confocal microscopy for nanoparticle drug delivery through skin.* J Biomed Opt, 2012. **18**(6): p. 061214-061214.
195. Hearnden, V., S. MacNeil, and G. Battaglia, *Tracking nanoparticles in three-dimensional tissue-engineered models using confocal laser scanning microscopy.* Methods Mol Biol, 2011. **695**: p. 41-51.
196. Alvarez-Roman, R., et al., *Skin penetration and distribution of polymeric nanoparticles.* J Control Release, 2004. **99**(1): p. 53-62.
197. Shang, L., et al., *Microwave-assisted rapid synthesis of luminescent gold nanoclusters for sensing Hg2+ in living cells using fluorescence imaging.* Nanoscale, 2012. **4**(14): p. 4155-4160.
198. Jiang, X., et al., *Endo- and exocytosis of zwitterionic quantum dot nanoparticles by live HeLa cells.* ACS Nano, 2010. **4**(11): p. 6787-97.
199. Hell, S.W., *Far-field optical nanoscopy.* Science, 2007. **316**(5828): p. 1153-8.
200. Huang, B., H. Babcock, and X. Zhuang, *Breaking the diffraction barrier: super-resolution imaging of cells.* Cell, 2010. **143**(7): p. 1047-58.
201. Schübbe, S., et al., *Size-Dependent Localization and Quantitative Evaluation of the Intracellular Migration of Silica Nanoparticles in Caco-2 Cells.* Chem Mater, 2012. **24**(5): p. 914-923.
202. Peuschel, H., et al., *Quantification of Internalized Silica Nanoparticles via STED Microscopy.* Biomed Res Int, 2015. **2015**: p. 16.
203. Parhamifar, L. and S.M. Moghimi, *Total internal reflection fluorescence (TIRF) microscopy for real-time imaging of nanoparticle-cell plasma membrane interaction.* Methods Mol Biol, 2012. **906**: p. 473-82.
204. Aaron, J.S., et al., *Nanotoxicology: Advanced Optical Imaging Reveals the Dependence of Particle Geometry on Interactions Between CdSe Quantum Dots and Immune Cells (Small 3/2011).* Small, 2011. **7**(3): p. 333-333.
205. Suh, J., D. Wirtz, and J. Hanes, *Real-time intracellular transport of gene nanocarriers studied by multiple particle tracking.* Biotechnol Prog, 2004. **20**(2): p. 598-602.
206. Lai, S.K., et al., *Characterization of the intracellular dynamics of a non-degradative pathway accessed by polymer nanoparticles.* J Control Release, 2008. **125**(2): p. 107-11.
207. Deville, S., et al., *Intracellular dynamics and fate of polystyrene nanoparticles in A549 Lung epithelial cells monitored by image (cross-) correlation spectroscopy and single particle tracking.* Biochim Biophys Acta, 2015. **1853**(10 Pt A): p. 2411-9.

208. Rossow, M., W.W. Mantulin, and E. Gratton, *Spatiotemporal image correlation spectroscopy measurements of flow demonstrated in microfluidic channels.* J Biomed Opt, 2009. **14**(2): p. 024014.
209. Coppola, S., et al., *Quantitative measurement of intracellular transport of nanocarriers by spatio-temporal image correlation spectroscopy.* Method Appl Fluoresc, 2013. **1**(1).
210. Penjweini, R., et al., *Transport and accumulation of PVP-Hypericin in cancer and normal cells characterized by image correlation spectroscopy techniques.* Biochim Biophys Acta, 2014. **1843**(5): p. 855-65.
211. Penjweini, R., et al., *Intracellular localization and dynamics of Hypericin loaded PLLA nanocarriers by image correlation spectroscopy.* J Control Release, 2015. **218**: p. 82-93.
212. Hemmerich, P.H. and A.H. von Mikecz, *Defining the subcellular interface of nanoparticles by live-cell imaging.* PLoS One, 2013. **8**(4): p. e62018.
213. Murray, R.A., et al., *A Quantitative Study of the Intracellular Dynamics of Fluorescently Labelled Glyco-Gold Nanoparticles via Fluorescence Correlation Spectroscopy.* Small, 2014. **10**(13): p. 2602-2610.
214. Lai, S.K., et al., *Privileged delivery of polymer nanoparticles to the perinuclear region of live cells via a non-clathrin, non-degradative pathway.* Biomaterials, 2007. **28**(18): p. 2876-84.
215. Sundara Rajan, S. and T.Q. Vu, *Quantum dots monitor TrkA receptor dynamics in the interior of neural PC12 cells.* Nano Lett, 2006. **6**(9): p. 2049-59.
216. Ruan, G., et al., *Imaging and tracking of tat peptide-conjugated quantum dots in living cells: new insights into nanoparticle uptake, intracellular transport, and vesicle shedding.* J Am Chem Soc, 2007. **129**(47): p. 14759-66.
217. Sandin, P., et al., *High-speed imaging of Rab family small GTPases reveals rare events in nanoparticle trafficking in living cells.* ACS Nano, 2012. **6**(2): p. 1513-21.
218. Vercauteren, D., et al., *Dynamic Colocalization Microscopy To Characterize Intracellular Trafficking of Nanomedicines.* ACS Nano, 2011. **5**(10): p. 7874-7884.
219. Shao, L., et al., *Studies on interaction of CdTe quantum dots with bovine serum albumin using fluorescence correlation spectroscopy.* J Fluoresc, 2009. **19**(1): p. 151-7.
220. Maffre, P., et al., *Effects of surface functionalization on the adsorption of human serum albumin onto nanoparticles – a fluorescence correlation spectroscopy study.* Beilstein J Nanotechnol, 2014. **5**: p. 2036-2047.
221. Varela, J.A., et al., *Quantifying size-dependent interactions between fluorescently labeled polystyrene nanoparticles and mammalian cells.* J Nanobiotechnology, 2012. **10**: p. 39.
222. Martens, T.F., et al., *An ex vivo assay to measure the intravitreal mobility of nanomedicines for retinal gene therapy.* Acta Ophthalmol, 2012. **90**: p. 0-0.
223. Forier, K., et al., *Lipid and polymer nanoparticles for drug delivery to bacterial biofilms.* J Control Release, 2014. **190**: p. 607-23.

224. Shapiro, H.M., *How Flow Cytometers Work*, in *Practical Flow Cytometry*. 2005, John Wiley & Sons, Inc. p. 101-223.
225. Shapero, K., et al., *Time and space resolved uptake study of silica nanoparticles by human cells.* Mol Biosyst, 2011. **7**(2): p. 371-378.
226. Kim, J.A., et al., *Low Dose of Amino-Modified Nanoparticles Induces Cell Cycle Arrest.* ACS Nano, 2013.
227. Ojea-Jimenez, I., et al., *Engineered inorganic nanoparticles for drug delivery applications.* Curr Drug Metab, 2013. **14**(5): p. 518-30.
228. Boczkowski, J. and P. Hoet, *What's new in nanotoxicology? Implications for public health from a brief review of the 2008 literature.* Nanotoxicology, 2010. **4**(1): p. 1-14.
229. Frohlich, E., et al., *Action of polystyrene nanoparticles of different sizes on lysosomal function and integrity.* Part Fibre Toxicol, 2012. **9**: p. 26.
230. Soldati, T. and M. Schliwa, *Powering membrane traffic in endocytosis and recycling.* Nat Rev Mol Cell Biol, 2006. **7**(12): p. 897-908.
231. Panariti, A., G. Miserocchi, and I. Rivolta, *The effect of nanoparticle uptake on cellular behavior: disrupting or enabling functions?* Nanotechnol Sci Appl, 2012. **5**: p. 87-100.
232. Petersen, N.O., et al., *Quantitation of membrane receptor distributions by image correlation spectroscopy: concept and application.* Biophys J, 1993. **65**(3): p. 1135-46.
233. Wiseman, P.W., *Image correlation spectroscopy: mapping correlations in space, time, and reciprocal space.* Methods Enzymol, 2013. **518**: p. 245-67.
234. Wiseman, P.W. and N.O. Petersen, *Image correlation spectroscopy. II. Optimization for ultrasensitive detection of preexisting platelet-derived growth factor-beta receptor oligomers on intact cells.* Biophys J, 1999. **76**(2): p. 963-77.
235. Kolin, D.L., S. Costantino, and P.W. Wiseman, *Sampling effects, noise, and photobleaching in temporal image correlation spectroscopy.* Biophys J, 2006. **90**(2): p. 628-39.
236. Hebert, B., S. Costantino, and P.W. Wiseman, *Spatiotemporal image correlation spectroscopy (STICS) theory, verification, and application to protein velocity mapping in living CHO cells.* Biophys J, 2005. **88**(5): p. 3601-14.
237. Kulkarni, R.P., et al., *Quantitating intracellular transport of polyplexes by spatio-temporal image correlation spectroscopy.* Proc Natl Acad Sci U S A, 2005. **102**(21): p. 7523-8.
238. Toplak, T., et al., *STICCS reveals matrix-dependent adhesion slipping and gripping in migrating cells.* Biophys J, 2012. **103**(8): p. 1672-82.
239. Zagato, E., et al., *Single-particle tracking for studying nanomaterial dynamics: applications and fundamentals in drug delivery.* Nanomedicine (Lond), 2014. **9**(6): p. 913-27.
240. Bove, J., et al., *Magnitude and direction of vesicle dynamics in growing pollen tubes using spatiotemporal image correlation spectroscopy and fluorescence recovery after photobleaching.* Plant Physiol, 2008. **147**(4): p. 1646-1658.

241. Wiseman, P.W., et al., *Spatial mapping of integrin interactions and dynamics during cell migration by image correlation microscopy.* J Cell Sci, 2004. **117**(Pt 23): p. 5521-34.
242. Comeau, J.W., D.L. Kolin, and P.W. Wiseman, *Accurate measurements of protein interactions in cells via improved spatial image cross-correlation spectroscopy.* Mol Biosyst, 2008. **4**(6): p. 672-85.
243. Kolin, D.L. and P.W. Wiseman, *Advances in image correlation spectroscopy: measuring number densities, aggregation states, and dynamics of fluorescently labeled macromolecules in cells.* Cell Biochem Biophys, 2007. **49**(3): p. 141-64.
244. Delon, A., et al., *Photobleaching, mobility, and compartmentalisation: inferences in fluorescence correlation spectroscopy.* J Fluoresc, 2004. **14**(3): p. 255-67.
245. Manders, E.M.M., F.J. Verbeek, and J.A. Aten, *Measurement of co-localization of objects in dual-colour confocal images.* J Microsc, 1993. **169**(3): p. 375-382.
246. Bolte, S. and F.P. Cordelières, *A guided tour into subcellular colocalization analysis in light microscopy.* J Microsc, 2006. **224**(3): p. 213-232.
247. Crocker, J.C. and D.G. Grier, *Methods of Digital Video Microscopy for Colloidal Studies.* J Colloid Interface Sci, 1996. **179**(1): p. 298-310.
248. Schmidt, T., et al., *Imaging of single molecule diffusion.* Proc Natl Acad Sci U S A, 1996. **93**(7): p. 2926-9.
249. Notelaers, K., et al., *Analysis of alpha3 GlyR single particle tracking in the cell membrane.* Biochim Biophys Acta, 2014. **1843**(3): p. 544-53.
250. Coue, M., et al., *Inhibition of actin polymerization by latrunculin A.* FEBS Lett, 1987. **213**(2): p. 316-8.
251. Nan, X., et al., *Observation of individual microtubule motor steps in living cells with endocytosed quantum dots.* J Phys Chem B, 2005. **109**(51): p. 24220-4.
252. Gambin, Y., et al., *Lateral mobility of proteins in liquid membranes revisited.* Proc Natl Acad Sci U S A, 2006. **103**(7): p. 2098-102.
253. Saffman, P.G. and M. Delbruck, *Brownian motion in biological membranes.* Proc Natl Acad Sci U S A, 1975. **72**(8): p. 3111-3.
254. Einstein, A., *Über die von der molekularkinetischen Theorie der Wärme geforderte Bewegung von in ruhenden Flüssigkeiten suspendierten Teilchen.* Ann Phys, 1905. **322**(8): p. 549-560.
255. Zajac, A.L., et al., *Local cytoskeletal and organelle interactions impact molecular-motor- driven early endosomal trafficking.* Curr Biol, 2013. **23**(13): p. 1173-80.
256. Trybus, K.M., *Intracellular transport: the causes for pauses.* Curr Biol, 2013. **23**(14): p. R623-5.
257. Beckerle, M.C., *Microinjected fluorescent polystyrene beads exhibit saltatory motion in tissue culture cells.* J Cell Biol, 1984. **98**(6): p. 2126-32.
258. Mallik, R., et al., *Building Complexity: An In Vitro Study of Cytoplasmic Dynein with In Vivo Implications.* Curr Biol, 2005. **15**(23): p. 2075-2085.

259. Hirokawa, N., *Kinesin and dynein superfamily proteins and the mechanism of organelle transport.* Science, 1998. **279**(5350): p. 519-26.
260. Pollard, T.D. and J.A. Cooper, *Actin, a central player in cell shape and movement.* Science, 2009. **326**(5957): p. 1208-12.
261. Chen, H., et al., *Cholesterol Level Regulates Endosome Motility via Rab Proteins.* Biophys J 2008. **94**(4): p. 1508-1520.
262. Gasman, S., Y. Kalaidzidis, and M. Zerial, *RhoD regulates endosome dynamics through Diaphanous-related Formin and Src tyrosine kinase.* Nat Cell Biol, 2003. **5**(3): p. 195-204.
263. Esner, M., et al., *Development of a Kinetic Assay for Late Endosome Movement.* J Biomol Screen, 2014.
264. Bandyopadhyay, D., et al., *Lysosome Transport as a Function of Lysosome Diameter.* PLoS One, 2014. **9**(1): p. e86847.
265. Szymanski, C.J., W.H.t. Humphries, and C.K. Payne, *Single particle tracking as a method to resolve differences in highly colocalized proteins.* Analyst, 2011. **136**(17): p. 3527-33.
266. Balint, S., et al., *Correlative live-cell and superresolution microscopy reveals cargo transport dynamics at microtubule intersections.* Proc Natl Acad Sci U S A, 2013. **110**(9): p. 3375-80.
267. Guduru, R., et al., *Magneto-electric nanoparticles to enable field-controlled high-specificity drug delivery to eradicate ovarian cancer cells.* Sci Rep, 2013. **3**: p. 2953.
268. Petros, R.A. and J.M. DeSimone, *Strategies in the design of nanoparticles for therapeutic applications.* Nat Rev Drug Discov, 2010. **9**(8): p. 615-27.
269. Xie, J., S. Lee, and X. Chen, *Nanoparticle-based theranostic agents.* Adv Drug Deliv Rev, 2010. **62**(11): p. 1064-79.
270. Sutradhar, K.B. and M.L. Amin, *Nanotechnology in Cancer Drug Delivery and Selective Targeting.* ISRN Nanotechnology, 2014. **2014**: p. 12.
271. Liu, Y., et al., *Intracellular dynamics of cationic and anionic polystyrene nanoparticles without direct interaction with mitotic spindle and chromosomes.* Biomaterials, 2011. **32**(32): p. 8291-303.
272. Huang, F., et al., *Quantitative nanoparticle tracking: applications to nanomedicine.* Nanomedicine (Lond), 2011. **6**(4): p. 693-700.
273. Kim, A.J., et al., *Non-degradative intracellular trafficking of highly compacted polymeric DNA nanoparticles.* J Control Release, 2012. **158**(1): p. 102-7.
274. Martens, T.F., et al., *Coating nanocarriers with hyaluronic acid facilitates intravitreal drug delivery for retinal gene therapy.* J Control Release, 2015. **202**: p. 83-92.
275. Culic-Viskota, J., et al., *Surface functionalization of barium titanate SHG nanoprobes for in vivo imaging in zebrafish.* Nat Protoc, 2012. **7**(9): p. 1618-33.
276. Hofmann, D. and V. Mailander, *Pharmacology of nanocarriers on the microscale: importance of uptake mechanisms and intracellular trafficking for efficient drug delivery.* Nanomedicine (Lond), 2013. **8**(3): p. 321-3.

277. Kumari, A., S.K. Yadav, and S.C. Yadav, *Biodegradable polymeric nanoparticles based drug delivery systems.* Colloids Surf B Biointerfaces, 2010. **75**(1): p. 1-18.
278. Guo, S. and L. Huang, *Nanoparticles containing insoluble drug for cancer therapy.* Biotechnol Adv, 2013.
279. Hofmann, D., et al., *Mass spectrometry and imaging analysis of nanoparticle-containing vesicles provide a mechanistic insight into cellular trafficking.* ACS Nano, 2014. **8**(10): p. 10077-88.
280. Zhou, K., et al., *Tunable, ultrasensitive pH-responsive nanoparticles targeting specific endocytic organelles in living cells.* Angew Chem Int Ed Engl, 2011. **50**(27): p. 6109-14.
281. Marin, M.J., et al., *Localized intracellular pH measurement using a ratiometric photoinduced electron-transfer-based nanosensor.* Angew Chem, 2012. **124**: p. 9795-99.
282. Nafee, N., et al., *Antibiotic-free nanotherapeutics: hypericin nanoparticles thereof for improved in vitro and in vivo antimicrobial photodynamic therapy and wound healing.* Int J Pharm, 2013. **454**(1): p. 249-58.
283. Lima, A.M., et al., *Hypericin encapsulated in solid lipid nanoparticles: phototoxicity and photodynamic efficiency.* J Photochem Photobiol B, 2013. **125**: p. 146-54.
284. Zeisser-Labouebe, M., et al., *Hypericin-loaded nanoparticles for the photodynamic treatment of ovarian cancer.* Int J Pharm, 2006. **326**(1-2): p. 174-81.
285. Jichlinski, P. and D. Jacqmin, *Photodynamic Diagnosis in Non-Muscle-Invasive Bladder Cancer.* Eur Urol Suppl, 2008. **7**(7): p. 529-535.
286. Jocham, D., H. Stepp, and R. Waidelich, *Photodynamic Diagnosis in Urology: State-of-the-Art.* Eur Urol, 2008. **53**(6): p. 1138-1150.
287. Zhu, T.C., B. Liu, and R. Penjweini, *Study of tissue oxygen supply rate in a macroscopic photodynamic therapy singlet oxygen model.* J Biomed Opt, 2015. **20**(3): p. 38001.
288. Penjweini, R., et al., *Long-term monitoring of live cell proliferation in presence of PVP-Hypericin: a new strategy using ms pulses of LED and the fluorescent dye CFSE.* J Microsc, 2012. **245**(1): p. 100-108.
289. Penjweini, R., et al., *Optimizing the antitumor selectivity of PVP-Hypericin re A549 cancer cells and HLF normal cells through pulsed blue light.* Photodiagnosis Photodyn Ther, 2013. **10**(4): p. 591-599.
290. Makadia, H.K. and S.J. Siegel, *Poly Lactic-co-Glycolic Acid (PLGA) as Biodegradable Controlled Drug Delivery Carrier.* Polymers (Basel), 2011. **3**(3): p. 1377-1397.
291. Xie, J. and C.H. Wang, *Self-assembled biodegradable nanoparticles developed by direct dialysis for the delivery of paclitaxel.* Pharm Res, 2005. **22**(12): p. 2079-90.
292. Nobs, L., et al., *Biodegradable nanoparticles for direct or two-step tumor immunotargeting.* Bioconj Chem, 2006. **17**(1): p. 139-45.
293. Han, S., et al., *Efficient Delivery of Antitumor Drug to the Nuclei of Tumor Cells by Amphiphilic Biodegradable Poly(L-Aspartic Acid-co-Lactic*

Acid)/DPPE Co-Polymer Nanoparticles. Small, 2012. **8**(10): p. 1596-1606.
294. Barthel, A.K., et al., *Imaging the intracellular degradation of biodegradable polymer nanoparticles.* Beilstein J Nanotechnol, 2014. **5**: p. 1905-17.
295. Geissbuehler, M., et al., *Nonlinear correlation spectroscopy (NLCS).* Nano Lett, 2012. **12**(3): p. 1668-72.
296. Ries, J. and P. Schwille, *Fluorescence correlation spectroscopy.* Bioessays, 2012. **34**(5): p. 361-8.
297. Liu, J., et al., *Study of interaction of hypericin and its pharmaceutical preparation by fluorescence techniques.* J Biomed Opt, 2009. **14**(1): p. 014003.
298. Almutairi, A., et al., *Monitoring the biodegradation of dendritic near-infrared nanoprobes by in vivo fluorescence imaging.* Mol Pharm, 2008. **5**(6): p. 1103-10.
299. Ethirajan, A., et al., *Biodegradable Polymeric Nanoparticles as Templates for Biomimetic Mineralization of Calcium Phosphate.* Macromol Chem Physic, 2011. **212**(9): p. 915-925.
300. Musyanovych, A., et al., *Preparation of biodegradable polymer nanoparticles by miniemulsion technique and their cell interactions.* Macromol Biosci, 2008. **8**(2): p. 127-39.
301. Rivolta, I., et al., *Cellular uptake of coumarin-6 as a model drug loaded in solid lipid nanoparticles.* J Physiol Pharmacol, 2011. **62**(1): p. 45-53.
302. Xiao, X., et al., *Exosomes: decreased sensitivity of lung cancer A549 cells to cisplatin.* PLoS One, 2014. **9**(2): p. e89534.
303. Shindo-Okada, N., et al., *Establishment of cell lines with high and low metastatic potential from A549 human lung adenocarcinoma.* Jpn J Cancer Res, 2002. **93**(1): p. 50-60.
304. Penjweini, R., et al., *Modifying excitation light dose of novel photosensitizer PVP-Hypericin for photodynamic diagnosis and therapy.* J Photochem Photobiol B, 2013. **120**: p. 120-129.
305. Kubin, A., et al., *How to make hypericin water-soluble.* Die Pharmazie, 2008. **63**(4): p. 263-269.
306. Endo, K., et al., *Nocodazole induces mitotic cell death with apoptotic-like features in Saccharomyces cerevisiae.* FEBS Lett, 2010. **584**(11): p. 2387-92.
307. Rocheleau, J.V., P.W. Wiseman, and N.O. Petersen, *Isolation of bright aggregate fluctuations in a multipopulation image correlation spectroscopy system using intensity subtraction.* Biophys J, 2003. **84**(6): p. 4011-22.
308. Huntosova, V., et al., *Cell death response of U87 glioma cells on hypericin photoactivation is mediated by dynamics of hypericin subcellular distribution and its aggregation in cellular organelles.* Photochem Photobiol Sci, 2012. **11**(9): p. 1428-36.
309. Hofmann, D., et al., *Drug delivery without nanoparticle uptake: delivery by a kiss-and-run mechanism on the cell membrane.* Chem Commun (Camb), 2014. **50**(11): p. 1369-71.

310. Furse, K.E. and S.A. Corcelli, *The dynamics of water at DNA interfaces: computational studies of Hoechst 33258 bound to DNA.* J Am Chem Soc, 2008. **130**(39): p. 13103-9.
311. Inokuchi, Y., et al., *Physicochemical properties affecting retinal drug/coumarin-6 delivery from nanocarrier systems via eyedrop administration.* Invest Ophthalmol Vis Sci, 2010. **51**(6): p. 3162-70.
312. Jones, G., 2nd and J.A. Jimenez, *Azole-linked coumarin dyes as fluorescence probes of domain-forming polymers.* J Photochem Photobiol B, 2001. **65**(1): p. 5-12.
313. Eriksson, E.S.E., et al., *Properties and Permeability of Hypericin and Brominated Hypericin in Lipid Membranes.* J Chem Theory Comput, 2009. **5**(12): p. 3139-3149.
314. Burel, L.a.J., P., *Homo-association of hypericin in water and consequences on its photodynamic properties.* J Chim Phys, 1996. **93**: p. 300-316.
315. Van de Putte, M., et al., *Hypericin as a marker for determination of tissue viability after intratumoral ethanol injection in a murine liver tumor model.* Acad Radiol, 2008. **15**(1): p. 107-13.
316. Miskovsky, P., *Hypericin--a new antiviral and antitumor photosensitizer: mechanism of action and interaction with biological macromolecules.* Curr Drug Targets, 2002. **3**(1): p. 55-84.
317. Taroni, P., et al., *Time-resolved microspectrofluorimetry and fluorescence lifetime imaging of hypericin in human retinal pigment epithelial cells.* Photochem Photobiol, 2005. **81**(3): p. 524-8.
318. Das, K., et al., *Photophysics of hypericin and hypocrellin A in complex with subcellular components: interactions with human serum albumin.* Photochem Photobiol, 1999. **69**(6): p. 633-45.
319. Garrison, A.K., et al., *Visualization and analysis of microtubule dynamics using dual color-coded display of plus-end labels.* PLoS One, 2012. **7**(11): p. e50421.
320. Jordan, M.A., D. Thrower, and L. Wilson, *Effects of vinblastine, podophyllotoxin and nocodazole on mitotic spindles. Implications for the role of microtubule dynamics in mitosis.* J Cell Sci, 1992. **102 (Pt 3)**: p. 401-16.
321. Quintero, O.A., et al., *Human Myo19 is a novel myosin that associates with mitochondria.* Curr Biol, 2009. **19**(23): p. 2008-13.
322. Ceresa, B.P., M. Lotscher, and S.L. Schmid, *Receptor and membrane recycling can occur with unaltered efficiency despite dramatic Rab5(q79l)-induced changes in endosome geometry.* J Biol Chem, 2001. **276**(13): p. 9649-54.
323. Seachrist, J.L., P.H. Anborgh, and S.S. Ferguson, *beta 2-adrenergic receptor internalization, endosomal sorting, and plasma membrane recycling are regulated by rab GTPases.* J Biol Chem, 2000. **275**(35): p. 27221-8.
324. Pfeffer, S.R., *Rab GTPase regulation of membrane identity.* Curr Opin Cell Biol, 2013. **25**(4): p. 414-9.

325. Herman, B. and D.F. Albertini, *A time-lapse video image intensification analysis of cytoplasmic organelle movements during endosome translocation.* J Cell Biol, 1984. **98**(2): p. 565-76.
326. Mukherjee, P., et al., *Accumulation and interaction of hypericin in low-density lipoprotein--a photophysical study.* Photochem Photobiol, 2008. **84**(3): p. 706-12.
327. Woods, N.B., A. Ooka, and S. Karlsson, *Development of gene therapy for hematopoietic stem cells using lentiviral vectors.* Leukemia, 2002. **16**(4): p. 563-9.
328. Edmundson, M., N.T. Thanh, and B. Song, *Nanoparticles based stem cell tracking in regenerative medicine.* Theranostics, 2013. **3**(8): p. 573-82.
329. Lu, R., et al., *Tracking single hematopoietic stem cells in vivo using high-throughput sequencing in conjunction with viral genetic barcoding.* Nat Biotechnol, 2011. **29**(10): p. 928-33.
330. Kay, M.A., *State-of-the-art gene-based therapies: the road ahead.* Nat Rev Genet, 2011. **12**(5): p. 316-328.
331. Stuckey, D.W. and K. Shah, *Stem cell-based therapies for cancer treatment: separating hope from hype.* Nat Rev Cancer, 2014. **14**(10): p. 683-691.
332. Lee, D.E., et al., *Multifunctional nanoparticles for multimodal imaging and theragnosis.* Chem Soc Rev, 2012. **41**(7): p. 2656-72.
333. England, T.J., et al., *Hematopoietic stem cell (CD34+) uptake of superparamagnetic iron oxide is enhanced by but not dependent on a transfection agent.* Cytotherapy, 2013. **15**(3): p. 384-90.
334. Daldrup-Link, H.E., et al., *Targeting of hematopoietic progenitor cells with MR contrast agents.* Radiology, 2003. **228**(3): p. 760-7.
335. Daldrup-Link, H.E., et al., *Migration of iron oxide-labeled human hematopoietic progenitor cells in a mouse model: in vivo monitoring with 1.5-T MR imaging equipment.* Radiology, 2005. **234**(1): p. 197-205.
336. Hedlund, A., et al., *Gd(2)O(3) nanoparticles in hematopoietic cells for MRI contrast enhancement.* Int J Nanomedicine, 2011. **6**: p. 3233-40.
337. McNeer, N.A., et al., *Nanoparticles deliver triplex-forming PNAs for site-specific genomic recombination in CD34+ human hematopoietic progenitors.* Mol Ther, 2011. **19**(1): p. 172-80.
338. McNeer, N.A., et al., *Systemic delivery of triplex-forming PNA and donor DNA by nanoparticles mediates site-specific genome editing of human hematopoietic cells in vivo.* Gene Ther, 2013. **20**(6): p. 658-69.
339. Fifis, T., et al., *Size-dependent immunogenicity: therapeutic and protective properties of nano-vaccines against tumors.* J Immunol, 2004. **173**(5): p. 3148-54.
340. Diwan, M., et al., *Biodegradable nanoparticle mediated antigen delivery to human cord blood derived dendritic cells for induction of primary T cell responses.* J Drug Target, 2003. **11**(8-10): p. 495-507.
341. Schoeters, E., et al., *Microarray analyses in dendritic cells reveal potential biomarkers for chemical-induced skin sensitization.* Mol Immunol, 2007. **44**(12): p. 3222-3233.

342. Deliliers, G.L., et al., *Ultrastructural Features of CD34+ Hematopoietic Progenitor Cells from Bone Marrow, Peripheral Blood and Umbilical Cord Blood.* Leuk Lymphoma, 2001. **42**(4): p. 699-708.
343. Kim, J.A., et al., *Role of cell cycle on the cellular uptake and dilution of nanoparticles in a cell population.* Nat Nanotechnol, 2012. **7**(1): p. 62-8.
344. Rode, M., T. Berg, and T. Gjøen, *Effect of Temperature on Endocytosis and Intracellular Transport in the Cell Line SHK-1 Derived from Salmon Head Kidney.* Comp Biochem Physiol A Mol Integr 1997. **117**(4): p. 531-537.
345. Tenuta, T., et al., *Elution of Labile Fluorescent Dye from Nanoparticles during Biological Use.* PLoS One, 2011. **6**(10): p. e25556.
346. Iversen, T.-G., T. Skotland, and K. Sandvig, *Endocytosis and intracellular transport of nanoparticles: Present knowledge and need for future studies.* Nano Today, 2011. **6**(2): p. 176-185.
347. Oh, N. and J.-H. Park, *Endocytosis and exocytosis of nanoparticles in mammalian cells.* Int J Nanomedicine, 2014. **9**(Suppl 1): p. 51-63.
348. Hara-Chikuma, M., et al., *ClC-3 chloride channels facilitate endosomal acidification and chloride accumulation.* J Biol Chem, 2005. **280**(2): p. 1241-7.
349. Clark, E.M., et al., *Ultrastructural basis of enhanced antitumor cytotoxicity of cord blood-derived CTLs: a comparative analysis with peripheral blood and bone marrow.* Int J Oncol, 2010. **37**(3): p. 645-53.
350. Brüstle, I., et al., *Hematopoietic and mesenchymal stem cells: polymeric nanoparticle uptake and lineage differentiation.* Beilstein J Nanotechnol, 2015. **6**: p. 383-395.
351. Duinhouwer, L.E., et al., *Magnetic Resonance Detection of CD34+ Cells from Umbilical Cord Blood Using a 19-F Label.* PLoS One, 2015. **10**(9): p. e0138572.
352. Maxwell, D.J., et al., *Fluorophore-conjugated iron oxide nanoparticle labeling and analysis of engrafting human hematopoietic stem cells.* Stem Cells, 2008. **26**(2): p. 517-24.
353. Arbab, A.S., et al., *Labeling of cells with ferumoxides-protamine sulfate complexes does not inhibit function or differentiation capacity of hematopoietic or mesenchymal stem cells.* NMR Biomed, 2005. **18**(8): p. 553-9.
354. Sakhtianchi, R., et al., *Exocytosis of nanoparticles from cells: role in cellular retention and toxicity.* Adv Colloid Interface Sci, 2013. **201-202**: p. 18-29.
355. Stayton, I., et al., *Study of uptake and loss of silica nanoparticles in living human lung epithelial cells at single cell level.* Anal Bioanal Chem, 2009. **394**(6): p. 1595-1608.
356. Chu, Z., et al., *Cellular uptake, evolution, and excretion of silica nanoparticles in human cells.* Nanoscale, 2011. **3**(8): p. 3291-9.
357. Panyam, J. and V. Labhasetwar, *Dynamics of endocytosis and exocytosis of poly(D,L-lactide-co-glycolide) nanoparticles in vascular smooth muscle cells.* Pharm Res, 2003. **20**(2): p. 212-20.
358. Cartiera, M.S., et al., *The uptake and intracellular fate of PLGA nanoparticles in epithelial cells.* Biomaterials, 2009. **30**(14): p. 2790-8.

359. Schafer, T., et al., *Nanoparticles and their influence on radionuclide mobility in deep geological formations.* Appl Geochem, 2012. **27**(2): p. 390-403.
360. Zhu, Y., et al., *Nanodiamonds act as Trojan horse for intracellular delivery of metal ions to trigger cytotoxicity.* Part Fibre Toxicol, 2015. **12**(1): p. 2.
361. Guo, M., et al., *In vivo biodistribution and synergistic toxicity of silica nanoparticles and cadmium chloride in mice.* J Hazard Mater, 2013. **260**: p. 780-8.
362. Yavuz, C.T., et al., *Low-Field Magnetic Separation of Monodisperse Fe3O4 Nanocrystals.* Science, 2006. **314**(5801): p. 964-967.
363. Gutiérrez-Sánchez, C., et al., *Gold Nanoparticles as Electronic Bridges for Laccase-Based Biocathodes.* J Am Chem Soc, 2012. **134**(41): p. 17212-17220.
364. Osorio, H.M., et al., *Preparation of nascent molecular electronic devices from gold nanoparticles and terminal alkyne functionalised monolayer films.* J Mater Chem C, 2014. **2**(35): p. 7348-7355.
365. Saha, K., et al., *Gold Nanoparticles in Chemical and Biological Sensing.* Chem Rev, 2012. **112**(5): p. 2739-2779.
366. Mukherjee, P., et al., *Potential therapeutic application of gold nanoparticles in B-chronic lymphocytic leukemia (BCLL): enhancing apoptosis.* J Allergy Clin Immunol, 2007. **5**: p. 4-4.
367. Curry, D., et al., *Adsorption of doxorubicin on citrate-capped gold nanoparticles: insights into engineering potent chemotherapeutic delivery systems.* Nanoscale, 2015. **7**(46): p. 19611-9.
368. Amreddy, N., et al., *Tumor-targeted and pH-controlled delivery of doxorubicin using gold nanorods for lung cancer therapy.* Int J Nanomedicine, 2015. **10**: p. 6773-88.
369. Bastús, N.G., J. Comenge, and V. Puntes, *Kinetically Controlled Seeded Growth Synthesis of Citrate-Stabilized Gold Nanoparticles of up to 200 nm: Size Focusing versus Ostwald Ripening.* Langmuir, 2011. **27**(17): p. 11098-11105.
370. Alkilany, A.M. and C.J. Murphy, *Toxicity and cellular uptake of gold nanoparticles: what we have learned so far?* J Nanopart Res, 2010. **12**(7): p. 2313-2333.
371. Vijayakumar, S. and S. Ganesan, *In Vitro Cytotoxicity Assay on Gold Nanoparticles with Different Stabilizing Agents.* J Nanomater, 2012. **2012**: p. 9.
372. Comenge, J., et al., *Detoxifying Antitumoral Drugs via Nanoconjugation: The Case of Gold Nanoparticles and Cisplatin.* PLoS One, 2012. **7**(10): p. e47562.
373. Almeida, J.P.M., E.R. Figueroa, and R.A. Drezek, *Gold nanoparticle mediated cancer immunotherapy.* Nanomedicine, 2014. **10**(3): p. 503-514.
374. Bastús, N.G., et al., *Homogeneous Conjugation of Peptides onto Gold Nanoparticles Enhances Macrophage Response.* ACS Nano, 2009. **3**(6): p. 1335-1344.

375. Das, K.K., S.N. Das, and S.A. Dhundasi, *Nickel, its adverse health effects & oxidative stress.* Indian J Med Res, 2008. **128**(4): p. 412-25.
376. Denkhaus, E. and K. Salnikow, *Nickel essentiality, toxicity, and carcinogenicity.* Crit Rev Oncol Hematol, 2002. **42**(1): p. 35-56.
377. Torres, F., et al., *Management of contact dermatitis due to nickel allergy: an update.* Clin Cosmet Investig Dermatol, 2009. **2**: p. 39-48.
378. Shen, H.M. and Q.F. Zhang, *Risk assessment of nickel carcinogenicity and occupational lung cancer.* Environ Health Perspect, 1994. **102**(Suppl 1): p. 275-282.
379. Ojea-Jimenez, I., et al., *Citrate-coated gold nanoparticles as smart scavengers for mercury(II) removal from polluted waters.* ACS Nano, 2012. **6**(3): p. 2253-60.
380. Nelissen, I., et al., *MUTZ-3-derived dendritic cells as an in vitro alternative model to CD34+ progenitor-derived dendritic cells for testing of chemical sensitizers.* Toxicol In Vitro, 2009. **23**(8): p. 1477-81.
381. Kot, M., et al., *Contact hypersensitivity to haptens of the European standard series and corticosteroid series in the population of adolescents and adults with atopic dermatitis.* Dermatitis, 2014. **25**(2): p. 72-6.
382. Rustemeyer, T., et al., *Human T lymphocyte priming in vitro by haptenated autologous dendritic cells.* Clin Exp Immunol, 1999. **117**(2): p. 209-16.
383. Cedervall, T., et al., *Detailed identification of plasma proteins adsorbed on copolymer nanoparticles.* Angew Chem Int Ed Engl, 2007. **46**(30): p. 5754-6.
384. Saptarshi, S.R., A. Duschl, and A.L. Lopata, *Interaction of nanoparticles with proteins: relation to bio-reactivity of the nanoparticle.* J Nanobiotechnol, 2013. **11**: p. 26-26.
385. Lundberg, K., et al., *Transcriptional profiling of human dendritic cell populations and models--unique profiles of in vitro dendritic cells and implications on functionality and applicability.* PLoS One, 2013. **8**(1): p. e52875.
386. Pitek, A.S., et al., *Transferrin Coated Nanoparticles: Study of the Bionano Interface in Human Plasma.* PLoS One, 2012. **7**(7): p. e40685.
387. Schoeters, E., et al., *Gene expression signatures in CD34+-progenitor-derived dendritic cells exposed to the chemical contact allergen nickel sulfate.* Toxicol Appl Pharmacol, 2006. **216**(1): p. 131-149.
388. Lambrechts, N., et al., *Gene markers in dendritic cells unravel pieces of the skin sensitization puzzle.* Toxicol Lett, 2010. **196**(2): p. 95-103.
389. Nestle, F.O., H. Speidel, and M.O. Speidel, *Metallurgy: High nickel release from 1- and 2-euro coins.* Nature, 2002. **419**(6903): p. 132-132.
390. Thyssen, J.P., et al., *Assessment of nickel and cobalt release from 200 unused hand-held work tools for sale in Denmark - Sources of occupational metal contact dermatitis?* Sci Total Environ, 2011. **409**(22): p. 4663-6.
391. Niikura, K., et al., *Gold nanoparticles as a vaccine platform: influence of size and shape on immunological responses in vitro and in vivo.* ACS Nano, 2013. **7**(5): p. 3926-38.

392. Pfaller, T., et al., *The suitability of different cellular in vitro immunotoxicity and genotoxicity methods for the analysis of nanoparticle-induced events.* Nanotoxicology, 2010. **4**(1): p. 52-72.
393. de Haar, C., et al., *Lung dendritic cells are stimulated by ultrafine particles and play a key role in particle adjuvant activity.* J Allergy Clin Immunol, 2008. **121**(5): p. 1246-54.
394. Koike, E., et al., *Carbon black nanoparticles promote the maturation and function of mouse bone marrow-derived dendritic cells.* Chemosphere, 2008. **73**(3): p. 371-6.
395. Garrett, W.S., et al., *Developmental control of endocytosis in dendritic cells by Cdc42.* Cell, 2000. **102**(3): p. 325-34.
396. Tayefi-Nasrabadi, H., E. Keyhani, and J. Keyhani, *Conformational changes and activity alterations induced by nickel ion in horseradish peroxidase.* Biochimie, 2006. **88**(9): p. 1183-97.
397. Mahmoudi, A., et al., *Effect of Mn2+, Co2+, Ni2+, and Cu2+ on horseradish peroxidase: activation, inhibition, and denaturation studies.* Appl Biochem Biotechnol, 2003. **104**(1): p. 81-94.
398. Roediger, B. and W. Weninger, *How nickel turns on innate immune cells.* Immunol Cell Biol, 2011. **89**(1): p. 1-2.
399. Heiss, K., et al., *Subproteomic analysis of metal-interacting proteins in human B cells.* Proteomics, 2005. **5**(14): p. 3614-22.
400. Ellingsen, J.E., *A study on the mechanism of protein adsorption to TiO2.* Biomaterials, 1991. **12**(6): p. 593-6.
401. Ji, Z., et al., *Dispersion and Stability Optimization of TiO(2) Nanoparticles in Cell Culture Media.* Environ Sci Technol, 2010. **44**(19): p. 7309-7314.
402. Jacquet, A., *Innate Immune Responses in House Dust Mite Allergy.* ISRN Allergy, 2013. **2013**: p. 18.
403. Radauer-Preiml, I., et al., *Nanoparticle-allergen interactions mediate human allergic responses: protein corona characterization and cellular responses.* Part Fibre Toxicol, 2016. **13**(1): p. 1-15.
404. Matthews, N.C., et al., *Urban Particulate Matter-activated Human Dendritic Cells Induce the Expansion of Potent Inflammatory Th1, Th2 and Th17 Effector Cells.* Am J Respir Cell Mol Biol, 2015.
405. Winzen, S., et al., *Complementary analysis of the hard and soft protein corona: sample preparation critically effects corona composition.* Nanoscale, 2015. **7**(7): p. 2992-3001.
406. Treuel, L., et al., *Physicochemical characterization of nanoparticles and their behavior in the biological environment.* Phys Chem Chem Phys, 2014. **16**(29): p. 15053-15067.
407. Pietzonka, P., et al., *Transfer of lipophilic markers from PLGA and polystyrene nanoparticles to caco-2 monolayers mimics particle uptake.* Pharm Res, 2002. **19**(5): p. 595-601.
408. Mühlfeld, C., et al., *Visualization and quantitative analysis of nanoparticles in the respiratory tract by transmission electron microscopy.* Part Fibre Toxicol, 2007. **4**(1): p. 1-17.

409. Cognet, L., C. Leduc, and B. Lounis, *Advances in live-cell single-particle tracking and dynamic super-resolution imaging.* Curr Opin Chem Biol, 2014. **20C**: p. 78-85.
410. Schultz, S., et al., *Single-target molecule detection with nonbleaching multicolor optical immunolabels.* Proc Natl Acad Sci U S A, 2000. **97**(3): p. 996-1001.
411. Hu, M., et al., *Dark-field microscopy studies of single metal nanoparticles: understanding the factors that influence the linewidth of the localized surface plasmon resonance.* J Mater Chem, 2008. **18**(17): p. 1949-1960.
412. Sönnichsen, C., et al., *Spectroscopy of single metallic nanoparticles using total internal reflection microscopy.* Appl Phys Lett, 2000. **77**(19): p. 2949-2951.
413. Hsieh, C.L., et al., *Second harmonic generation from nanocrystals under linearly and circularly polarized excitations.* Opt Express, 2010. **18**(11): p. 11917-32.
414. Nieves, D.J., et al., *Photothermal raster image correlation spectroscopy of gold nanoparticles in solution and on live cells.* R Soc Open Sci, 2015. **2**(6).
415. Mahmoudi, M., et al., *Crucial role of the protein corona for the specific targeting of nanoparticles.* Nanomedicine (Lond), 2015. **10**(2): p. 215-26.
416. Hamad-Schifferli, K., *How can we exploit the protein corona?* Nanomedicine (Lond), 2013. **8**(1): p. 1-3.
417. Cho, E.J., et al., *Nanoparticle characterization: state of the art, challenges, and emerging technologies.* Mol Pharm, 2013. **10**(6): p. 2093-110.
418. Monopoli, M., et al., *Physical-chemical aspects of protein corona: relevance to in Vitro and in Vivo biological impacts of nanoparticles.* J Am Chem Soc, 2011. **133**: p. 2525 - 2534.
419. Hajipour, M.J., et al., *Personalized protein coronas: a "key" factor at the nanobiointerface.* Biomater Sci, 2014. **2**(9): p. 1210-1221.

Summary

In the last decade, the usage of nanoparticles for biomedical and commercial applications is expanding extensively. Nanotechnology offers the unprecedented capacity to manipulate cells with nanoscale precision, opening up tremendous opportunities to exploit the interactions at the nano-bio interface for therapeutic purposes. In order to take full advantage of this promise, it is necessary that the interactions of nanoparticles and living cells are characterized in advance. This allows the assessment of the safety of nanotechnology-based applications, but also provides insights to the nano-bio interactions for preventive health strategies and future health applications.

Recent investigations have shown that nanoparticles can interfere with the immune system, which can result in adverse immune reactions including the development and/or progression of allergic responses. In contrast, the specific targeting of nanoparticles to the cells of the immune system can be used to modulate the immune response for therapeutic approaches. Dendritic cells, one of the key players of the immune system, act as specialized sentinel cells that scan the interfaces of the body which are in contact with the external environment. From this point of view, they are expected to encounter the nanoparticles in the human body. Since dendritic cells are involved in many diseases, they also provide a target for disease prevention and therapy.

Although efforts have been made in understanding how nanoparticles interact with biological systems, significant progresses are prevented because of the lack of well-adjusted tools to evaluate the nano-bio interaction. For that reason, part of this dissertation focuses on the implementation of technologies to assess this interaction. In that part, advanced fluorimetric techniques are used to study the uptake, the intracellular behaviour and the fate of nanoparticles in biological cells. In the second part, the impact of nanoparticles on the biological function of dendritic cells is investigated. This dissertation is a composition of 5 manuscripts, preceded by an **introduction** and followed by a general discussion. In **chapter 2** and **chapter 3** the intracellular behaviour and fate of nanoparticles are investigated using advanced microfluorimetric techniques in human lung cancer cells, which act as a model system. The results demonstrate

that image correlation spectroscopy based techniques and single particle tracking are applicable to study the dynamic processes of nanoparticles in biological cells and to study their interactions with intracellular targets. Furthermore, the uptake and release of hypericin-loaded nanoparticles are studied in human lung cancer cells. In **chapter 4** the uptake and uptake kinetics of nanoparticles in hematopoietic progenitor cells and hematopoietic progenitor-derived dendritic cells are investigated. Here, a different cellular uptake between both cell types is identified. In **chapter 5** and **chapter 6** the influence of nanoparticles on the allergic sensitization response of dendritic cells is explored. The results demonstrate that both the uptake of nanoparticles and the immune response against nanoparticles can be influenced when other bio-active molecules are present in the environment. The results demonstrate the importance of mixture toxicology for the risk assessment of nanomaterials since these exposures are the most relevant for the human situation. The **general discussion** first handles the applications and conclusions with regard to the characterization of the nano-bio interactions. Thereafter the interactions of nanoparticles on biological function of dendritic cells are discussed. Finally, a section is devoted to the future perspectives with regard to nano-bio interaction studies.

Nederlandse samenvatting

In de laatste tien jaar heeft de ontwikkeling van nanodeeltjes voor biomedische en commerciële toepassingen een dramatische expansie ondervonden. Omwille van hun grootte-afhankelijke eigenschappen worden nanodeeltjes in tal van consumentenproducten gebruikt, nl. omwille van hun antimicrobiële en zelfreinigende eigenschappen, hun duurzaamheid en hun resistentie tegen omgevingsfactoren. Daarnaast biedt nanotechnologie ook de mogelijkheid om biologische materie op de nanoschaal te gaan manipuleren. Dit genereert tal van opportuniteiten om de interacties tussen nanodeeltjes en biologische materie te sturen voor therapeutische doeleinden. Om het potentieel van nanodeeltjes volledig te gebruiken, maar ook om gezondheidsproblemen geassocieerd met de blootstelling aan nanomaterialen te voorkomen, is het belangrijk dat de interacties tussen nanodeeltjes en biologische cellen op voorhand gekarakteriseerd worden. Deze inzichten kunnen mogelijkheden bieden voor veilig nanoproductontwerp, preventieve gezondheidsmaatregelen en toekomstige gezondheidstoepassingen.

Recent onderzoek heeft aangetoond dat nanodeeltjes in staat zijn om te interfereren met het immuunysteem. Dit kan leiden tot ongewenste immuunreacties waaronder het ontstaan of verergeren van allergische reacties. In tegenstelling, het specifiek richten van nanodeeltjes naar de cellen van het immuunsysteem kan gebruikt worden om immuunreacties voor therapeutische doeleinden te moduleren. Dendrietcellen, één van de sleutelspelers van het immuunsysteem, kunnen als gespecialiseerde schildwachters werken waarbij ze de grenzen van het lichaam die in contact staan met de externe omgeving scannen. Vanuit dit perspectief wordt verwacht dat dendrietcellen de nanodeeltjes kunnen tegenkomen in het menselijk lichaam. Aangezien dendrietcellen betrokken zijn bij tal van ziektes, kunnen zij ook als aanknopingspunt dienen voor ziektepreventie en therapie.

Hoewel er pogingen gedaan zijn om te begrijpen hoe de interactie is tussen nanodeeltjes en biologische systemen, wordt aanzienlijke vooruitgang verhinderd door het ontbreken van goed aangepaste methodologieën om de interactie tussen beide te evalueren. Daarom zal er een deel van

doctoraatsproefschrift specifiek gefocust worden op de implementatie van biomedische technieken om deze interactie te evalueren. Daarnaast wordt de invloed van nanodeeltjes op de biologische functie van dendrietcellen bestudeerd. Dit proefschrift is een samenstelling van 5 manuscripten, voorafgegaan door een **inleiding**, en gevolgd door een algemene discussie. In **hoofdstuk 2** en **hoofdstuk 3** wordt in een humane longkankercellijn, als modelsysteem, het intracellulair transport en het lot van nanodeeltjes onderzocht door middel van geavanceerde beeldvormingstechnieken. De resultaten wijzen erop dat *image correlation spectroscopy*-gebaseerde technieken en *single particle tracking* bruikbaar zijn om de dynamische processen van nanodeeltjes in biologische cellen en hun interacties met intracellulaire doelwitten te bestuderen. Daarnaast wordt de opname en vrijgave van *hypericine*-geladen nanodeeltjes bestudeerd in een humane longkankercellijn. In **hoofdstuk 4** wordt de opname van nanodeeltjes in humane hematopoëtische progenitorcellen en de daaruit gedifferentieerde dendrietcellen opgevolgd. Hier wordt voor beide celtypes een afzonderlijk opnamemechanisme vastgesteld. In **hoofdstuk 5** en **hoofdstuk 6** wordt nagegaan of de interactie tussen nanodeeltjes en dendrietcellen de allergische sensitisatie-respons kan beïnvloeden. De resultaten wijzen erop dat de opname van nanodeeltjes enerzijds en de immuunrespons ten aanzien van nanodeeltjes anderzijds opmerkelijk kan veranderen wanneer er andere bioactieve moleculen in de omgeving aanwezig zijn. Deze resultaten duiden bovendien op het belang van het toepassen van gecombineerde blootstellingsexperimenten voor de risicobepaling van nanomaterialen. Bovendien zijn deze gecombineerde blootstellingen ook het meest relevant voor de humane situatie.

De **algemene discussie** behandelt de toepassingen en conclusies met betrekking tot de karakterisatie van de nano-bio-interacties, daarna worden de interactie van nanodeeltjes op de biologische functie van dendrietcellen besproken. Ten slotte wordt een sectie gewijd aan de toekomstperspectieven met betrekking tot nano-bio-interactie studies.

Curriculum vitae

Sarah Deville was born on October 2nd 1989 in Bilzen. In 2007 she obtained her degree General Secondary Education (*Algemeen Secundair Onderwijs*) in the study option Sciences-Mathematics at *Heilig-Grafinstuut* in Bilzen. In the same year she began her studies at Hasselt University where she graduated *magna cum laude* in 2012 as Master of Biomedical Sciences with specialization Clinical Molecular Sciences. Her thesis entitled 'The influence of aquaporin-4 isoform interaction on supramolecular water channel assembly in astrocytoma cells' was executed in the Biophysics group of prof. dr. Marcel Ameloot (Biomedical Research Institute, Hasselt University, Diepenbeek) in collaboration with prof. dr. Raf De Jongh (Ziekenhuis Oost-Limburg, Genk). In October 2012 she started her PhD at Hasselt University and Flemish Institute for Technological Research (VITO). During this period, she participated in various assignments and courses framed within the *Doctoral School for Medicine and Life Sciences*, and she helped to organize the third µFIBR symposium. The results obtained during her PhD were partially published in international journals and presented at various (inter)national congresses.

Bibliography

Publications

Publications from this work

- **Deville, S.**, Penjweini, R., Smisdom, N., Notelaers, K., Nelissen, I., Hooyberghs, J., & Ameloot, M. (2015). Intracellular dynamics and fate of polystyrene nanoparticles in A549 Lung epithelial cells monitored by image (cross-) correlation spectroscopy and single particle tracking. *Biochimica et Biophysica Acta (BBA) - Molecular Cell Research, 1853*(10), 2411-2419.
- Penjweini, R., **Deville, S.**, D'Olieslaeger, L., Berden, M., Ameloot, M., & Ethirajan, A. (2015). Intracellular localization and dynamics of Hypericin loaded PLLA nanocarriers by image correlation spectroscopy. *Journal of Controlled Release, 218*, 82-93.
- **Deville, S.**, Baré, B., Piella, J., Tirez, K., Hoet, P., Monopoli, M., Dawson, K., Puntes, V.F., Nelissen, I. Interaction of gold nanoparticles and nickel (II) sulphate affects dendritic cell maturation. *Submitted*

Publications from collaborative projects

- Penjweini, R., Smisdom, N., **Deville, S.**, & Ameloot, M. (2014). Transport and accumulation of PVP-Hypericin in cancer and normal cells characterized by image correlation spectroscopy techniques. *Biochimica et Biophysica Acta (BBA) - Molecular Cell Research, 1843*(5), 855-865.
- Vlassaks, E., Gavilanes, A.W., Vles, J.S., **Deville, S.**, Kramer, B.W., Strackx, E. & Martinez-Martinez, P. (2012). The effects of fetal and perinatal asphyxia on neural cytokine levels and ceramide metabolism in adulthood. *Journal of Neuroimmunology*, *255(1-2)*, 97-101.

Selected oral presentations

- *Safety characterization of gold nanoparticles in complex mixtures*
  Deville, S., Baré, B., Piella, J., Tirez, K., Hoet, P., Puntes, V.F., Nelissen, I.

The safety of nanomaterials: opportunities & challenges
BelTox and INVITROM Joint annual meeting
Antwerp, Belgium, November 26, 2015

Workshop Nano in Belgium: FPS Health, Food Chain Safety and Environment, the FPS Employment, Labour and Social Dialogue and the FPS Economy, SMEs, Self-Employed and Energy
Brussels, Belgium, October 22, 2015

- *Intracellular dynamics and fate of nanoagents in lung epithelial cells, monitored by image (cross-) correlation spectroscopy and single particle tracking*
  Deville, S., Penjweini, R.

  µFiBR 2014 - A series of tutorial lectures on Optical Imaging in Biomedical Nanotechnology
  Diepenbeek, Belgium, October 3, 2014

- *Investigation of intracellular nanoparticle transport and fate by image correlation spectroscopy*
  Deville, S., Penjweini, R., Smisdom, N., Notelaers, K., Nelissen, I., Hooyberghs, J., Ameloot, M.

  BioMiMedics Science meeting
  Maastricht, Netherlands, December 12, 2013

  NanoSafety 2013
  Saarbrucken, Germany, November 21, 2013

Selected poster presentations

- *Reduced sensitization response by mixed exposure to nickel(II) sulphate and gold nanoparticles*
  Deville, S., Baré, B., Piella, J., Hoet, P., Puntes, V.F., Nelissen, I.

  BioNanoMed 2015
  Graz, Austria, April 7-10, 2015

- *Monitoring the intracellular dynamics of polystyrene nanoparticles in lung epithelial cells monitored by image (cross-) correlation spectroscopy and single particle tracking*

  Deville, S., Penjweini, R., Smisdom, N., Notelaers, K., Nelissen, I., Hooyberghs, J., Ameloot, M.

  Workshop Nano in Belgium: FPS Health, Food Chain Safety and Environment, the FPS Employment, Labour and Social Dialogue and the FPS Economy, SMEs, Self-Employed and Energy
  Brussels, Belgium, October 22, 2015

  NanoBio&Med
  Barcelona, Spain, November 17-20, 2014

- *Uptake kinetics of polystyrene nanoparticles in CD34$^+$ hematopoietic stem cells and CD34-derived dendritic cells*

  Deville, S., Baré, B., Ameloot, M., Nelissen, I., Hooyberghs, J.

  ESTIV 2014
  Egmond aan Zee, Netherlands, June 10-13, 2014

  NanoSafety 2013
  Saarbrucken, Germany, November 20-22, 2013

  Intracellular nanoparticle dynamics investigated by image correlation spectroscopy

  Deville, S., Penjweini, R., Smisdom, N., Nelissen, I., Hooyberghs, J., Ameloot, M.

  SEURAT summer school
  Egmond aan Zee, Netherlands, June 8-10, 2014

  European Materials Research Society Spring meeting
  Strasbourg, France, May 27-31, 2013

  Focus on Microscopy
  Maastricht, Netherlands, March 24-27, 2013

Grants

- International mobility grant 2013 from Hasselt University (03/12/2013)
- Transnational Access grant 2014 from EU FP7 QualityNano (23/12/2014)

Dankwoord

En tot slot…

Zonder de hulp van velen zou ik niet op deze laatste bladzijden beland zijn. Daarom wil ik in dit laatste deel graag iedereen bedanken voor zijn of haar bijdrage in dit proefschrift.

Ongeveer 4 jaar geleden kreeg ik de mogelijkheid van mijn toenmalige masterproef-promoter, prof. dr. Marcel Ameloot, om een doctoraatsvoorstel in te dienen voor een positie in samenwerking met het Vlaams Instituut voor Technologisch Onderzoek (VITO). Na het uitschrijven en het succesvol verdedigen van het project, heb ik op 1 oktober 2012 onder zijn promotorschap de eerste stappen in mijn doctoraat gezet. Graag wil ik de instellingen erkennen die het mogelijk gemaakt hebben om de gepresenteerde doctoraatsstudie uit te voeren, namelijk de Universiteit Hasselt en VITO.

Eerst een woord van dank voor mijn promoter prof. dr. Marcel Ameloot. Na mijn masterstage bij de onderzoeksgroep Biofysica wist ik dat ik hier graag aan een doctoraat wilde beginnen. Marcel, ik wil jou graag bedanken voor de fijne samenwerking en voor alle kansen die ik van jou kreeg om mijn doctoraatsonderzoek uit te voeren. Jouw kennis en ideeën hebben me altijd gestimuleerd om bij te leren en verder te zoeken naar oplossingen als het onderzoek vastliep. Ik heb ontzettend veel geleerd van jou, zowel op wetenschappelijk als persoonlijk vlak. Daarnaast wil ik graag mijn co-promoter prof. dr. Jef Hooyberghs bedanken voor de fijne samenwerking. Jef, jij hebt altijd geboeid geluisterd en meegedacht over de vooruitgang van het project. Bovendien heeft jouw kritische blik en jouw wiskundige benadering van biologische problemen mij geleerd om op een andere manier naar mijn onderzoeksresultaten te kijken. Ook mag ik dr. Inge Nelissen niet vergeten. Inge, jij hebt mij alle aspecten van de interactie van nanodeeltjes in een biologische omgeving bijgebracht. Vaak heb ik aan jouw deur gestaan met vragen of bezorgdheden. Ook maakte je altijd tijd voor het bespreken van de laatste onderzoeksresultaten, voor het doornemen van posters en artikels, of voor een leuke babbel. Marcel, Jef en Inge, ik kon altijd bij jullie terecht, oprecht bedankt voor alles!

Graag wil ik prof. dr. Ivo Lambrichts, prof. dr. Niels Hellings, prof. dr. Milos Nesladek, prof. dr. Peter Hoet en dr. Anna Salvati bedanken voor hun rol in mijn doctoraatsjury, in het bijzonder voor het lezen en kritisch becommentariëren van mijn doctoraatsproefschrift. Jullie opbouwende commentaren en adviezen hebben de kwaliteit van het onderzoek en mijn thesis versterkt.

Werken op twee locaties, in Diepenbeek en in Mol, was niet altijd even praktisch. Het vergde vaak inspanningen om toch maar alles zo goed mogelijk te kunnen combineren. Regelmatig leek het een kleine verhuizing om alle spullen van de ene locatie naar de andere locatie te vervoeren, of om in de vroege uurtjes te beginnen om zo tijdig te kunnen vertrekken om die belangrijke vergadering op de andere instelling bij te wonen. Gelukkig had ik op beide plaatsen ontzettend veel mensen waar ik op kon rekenen en die me hielpen om dit praktisch allemaal mogelijk te maken.

Allereerst wil ik Petra Bex en Jo Janssen van Universiteit Hasselt bedanken voor de praktische ondersteuning in het celkweeklabo. Bedankt voor de vele malen dat ik op jullie hulp mocht rekenen en voor het oogje in het zeil te houden als mijn stagestudenten aan het werk waren. Ook wil ik graag Veronique Pousset bedanken om alle administratieve beslommeringen voor jouw rekening te nemen en in het bijzonder voor de hulp tijdens de eindfase van mijn doctoraat. Bovendien wil ik ook de *Doctoral School of Medicine and Life Sciences* bedanken, met name Stefanie Kerkhofs, voor de assistentie bij de registratie van certificaten en het voorzien van de nodige handtekeningen.

Graag wil ik ook mijn collega's van Universiteit Hasselt bedanken voor de leuke samenwerking. Toen ik in 2012 startte bestond de Biofysica groep uit Nick Smisdom, Rozhin Penjweini, Ben De Clercq, Kristof Notelaers, Rik Paesen en Kathleen Sanen. Later werd de groep uitgebreid met Hannelore Bové, Eli Slenders, Daniel Hadraba, Martin van de Ven en Srujan Cheruku. Vaak heb ik jullie hulp gekregen als er problemen waren met de confocale microscoop, maar ook wanneer mijn programmeerskills in MATLAB het weer eens lieten afweten. Naast de wetenschappelijke samenwerking waren er ook de verscheidene Biofysica teambuildingsactiveiten waaronder spelletjesavonden, boerengolf,

lasergamen, bowlen, steengrillen etc. Bedankt voor de fijne groepsfeer, ik wens jullie allen heel veel succes met jullie toekomstplannen! Er zijn enkele Biofysica-collega's die in het bijzonder een speciaal extra dankwoordje verdienen voor de samenwerking tijdens de afgelopen jaren.

Rozhin, when I started my PhD in October 2012, you recently joined the Biophysics group as a post-doctoral researcher. We started working together from the beginning of my PhD. We worked as a team in which our competences complemented each other. We mastered a lot of experiments, data analyses and students together. Although we had many time-consuming experiments and worked so many evenings and week-ends, we were always able to convert the necessary to a pleasure. The experiences with a terrifying cold confocal room were often treated with lots of hot chocolate, chocolates and other sweets. I will also never forget our research stay in Barcelona and the pleasant off-work activities we did together. Although you left the group to go to the United States in September 2014, we kept contact and are still collaborating together. I want to thank you for all your help in the last four years and for being such as great friend to me. I wish you a lot of success with your future life!

Nick, tijdens mijn masterproef heb ik je leren kennen als een gedreven onderzoeker. Tijdens mijn doctoraat kon ik steeds op je hulp rekenen. Toen je een jaar na mij ook op VITO aanbelandde, zaten we plots in het zelfde UHasselt/VITO schuitje en werd onze samenwerking nog sterker. Bedankt voor het delen van maar al je (wetenschappelijke) ervaringen en de kilo's chocolade die je mee naar het werk nam! Ik wens je heel veel succes in de komende jaren en ik ben er van overtuigd dat je het zeer goed gaat doen!

Kristof, als begeleider tijdens mijn masterthesis en daarna als Biofysica-collega heb ik steeds op jou kunnen rekenen. Bedankt voor mij altijd te motiveren, voor je goede raad, maar ook je wetenschappelijke bijdrage aan mijn doctoraat! Ik wens jou ook veel succes in je verdere carrière.

Daarnaast wil ik ook graag al de studenten die onder mijn begeleiding in het labo hebben gestaan bedanken. Jullie hebben allen op jullie eigen manier een steentje bijgedragen en meegeholpen om vorm te geven aan dit onderzoek!

Ook wil ik de collega's van de onderzoeksgroepen Fysiologie en Morfologie bedanken voor jullie hulp en ondersteuning in het labo, maar ook voor de leuke babbels tijdens het wachten tussen de experimenten door. Daarnaast wil ik Christoffer De Dobbelaere en Ken Elen van Anorganische en Fysische Chemie bedanken voor het delen van jullie chemische expertise, maar ook voor de goede samenwerking tijdens de gezamelijke studentenprojecten die we uitgevoerd hebben.

Ook op VITO kon ik steeds terugvallen op mijn collega's binnen de groep Milieurisico & Gezondheid. Graag wil ik dr. Rudi Torfs bedanken om mij de kans te geven mijn doctoraatsonderzoek hier uit te voeren en voor de financiële ondersteuning van mijn onderzoek. Daarnaast wil ik iedereen van ABS bedanken voor jullie steun en interesse in mijn werk, en natuurlijk ook voor de leuke sfeer tijdens de koffiepauzes!

Toen ik startte op VITO, mocht ik het kantoor delen met Birgit Baré en Wahyu Wijaya Hadiwikarta. Birgit, bedankt om me alle kneepjes van het vak te leren maar ook om me op de hoogte te brengen van het reilen en zeilen binnen de groep. Ook kon ik steeds bij jou terecht om mijn hart te luchten en om naast het werk samen iets leuks te doen! Ik wens je veel succes in de toekomst! Wahyu, thanks for being a great colleague and friend! It was a pleasure to share the office with you. Your mathematic and ICT skills (and your patience) enabled me to find my way through the data analyses. I also want to thank you for reminding me when there were birthday treats! In 2015 en 2016 kwamen Bart Wathiong en Eline Oeyen ons kantoor vervoegen. In de afgelopen jaren zijn jullie allen zoveel meer dan alleen collega's geworden. Ik wil jullie dan ook bedanken voor de leuke sfeer die er altijd was.

An Jacobs en Karen Hollanders, bedankt voor alle hulp die ik van jullie gekregen heb in het labo en voor jullie geduld voor de zovele malen dat ik aan jullie deur heb gestaan. Graag wil ik ook Marie Pierre Goyvaerts en Pascale Berckmans bedanken voor de kwaliteitsvolle werkomgeving. Eddy Janssens en Daniëlla Ooms wil ik graag bedanken voor hun inspanningen om iedere dag weer stalen te gaan ophalen in de ziekenhuizen in Mol en Geel!

Ook wil ik graag An Kestens en Els Kenis bedanken voor jullie ondersteuning. Voor alle vragen kon ik bij jullie terecht. Ook als er problemen waren zoals dringende of verloren bestellingen, zoekgeraakte pakketjes of betalingen, dan konden jullie me altijd helpen om naar een oplossing te zoeken. Door jullie hulp werd een grote last van mijn schouders genomen en kon ik me volledig toeleggen op het wetenschappelijk werk.

In addition, I would like to express my gratitude to my co-workers from other national and international research groups, and especially to Prof. dr. Victor Puntes, Jordi Piella and Sofia Rubio: muchas gracias por la excelente cooperación y hospitalidad en Barcelona!

Tot slot wil ik mijn familie bedanken voor alle steun die ik voor en tijdens mijn doctoraat heb gekregen. Mama en papa, bedankt voor alle kansen die jullie mij gegeven hebben, jullie stonden altijd klaar voor mij en zorgden voor de nodige afleiding als ik er nood aan had. Opa, ook wil ik jou bedanken omdat je altijd in mij geloofd hebt. Ben en Lies, bedankt om altijd voor mij klaar te staan met een luisterend oor, raad en daad. Ooms en tantes, neven en nichten, bedankt voor jullie interesse en steun. Mijn schoonfamilie inclusief kleine Axel, wil ik ook bedanken voor de leuke activiteiten tijdens het afgelopen jaar! Ik wens jullie allen veel (baby)geluk en levensvreugde. Natuurlijk wil ik ook een zeer speciaal iemand bedanken die een plekje in mijn hart heeft veroverd. Remy, bedankt om aan mijn zijde te staan. Je was er steeds om me uit de dipjes te halen en er iedere keer weer voor mij te zijn. Ik kijk uit naar onze toekomst samen!